Beyond Λ and CDM: interacting scalar fields for dark sector cosmology

Gaspard Poulot

Cosmology, Relativity and Gravitation group
School of Mathematical and Physical Sciences
The University of Sheffield

A dissertation submitted in candidature for the degree of
Doctor of Philosophy at the University of Sheffield,
Supervised by Prof. Carsten van de Bruck

2025

Declaration

I declare that, unless otherwise stated, the work presented in this thesis is my own. This includes co-authored research papers for which I played a major role in the analytical and numerical calculations as well as writing up.

No part of this thesis has been accepted or is currently being submitted for any other qualification at the University of Sheffield or elsewhere.

The following chapters are based wholly or in part on previous publications:

- Chapter 5 is based on [1], co-authored with Carsten van de Bruck and Elsa Teixeira. Elsa Teixeira is credited for Figures 5.3-5.7 as well as numerical implementation of the model. This work has been published in JCAP.

- Chapter 6 is based on [2], co-authored with Elsa Teixeira, Carsten van de Bruck, Eleonora Di Valentino and Vivian Poulin. Elsa Teixeira is credited for Figures 6.1, 6.5, 6.6 as well as running the MCMC analysis. This work is currently being peer-reviewed for publication in Physical Review D.

- Chapter 7 is based on [3], co-authored with Elsa Teixeira, Carsten van de Bruck and Nelson Nunes. This work is currently being peer-reviewed for publication in JCAP.

- Chapter 8 is based on ongoing work in collaboration with Carsten van de Bruck, Eleonora Di Valentino, Nelson Nunes and Elsa Teixeira. This work is as of yet unpublished.

Acknowledgements

First, I would like to thank Prof. Carsten van de Bruck. You have helped me so much along the way, always happy to provide guidance and support when it was needed.

Next, I want to thank all my collaborators: Dr. Eleonora Di Valentino, Dr. Nelson Nunes, Dr. Vivian Poulin and especially Dr. Elsa Teixeira.

The CRAG group has been a big part of why I have enjoyed my PhD, and for this I want to thank all current and former members, academics, postdocs and fellow PhD students I had the chance to interact with. Special thanks to Adam Smith for proofreading this thesis and providing feedback.

Importantly I want to thank my family – Mum and Dad, Violette and Aloïse – for being with me through my whole academic journey.

Finally, thank you to Evie for being a continuous source of encouragement, laughs and adventures.

Abstract

Since its modern inception in the early twentieth century, cosmology has developed drastically due to new observational methods. With this, our understanding of the Universe has changed accordingly, requiring new theoretical insights. For the past twenty-five years, ΛCDM has been considered the standard model of cosmology. However, with ever-increasing observational precision, new tensions in the data have emerged. There are many hints that this crisis in cosmology should be addressed by considering alternatives to ΛCDM, especially the dark energy 'Λ' and the cold dark matter 'CDM' components. These two highly studied but scarcely understood energy sources form what we refer to as the dark sector. Dark sector physics often results in novel phenomenology that can alleviate cosmological tensions whilst also providing a robust theoretical framework.

In this thesis, we will first review the basics of modern cosmology, culminating in the description of the ΛCDM and cosmological tensions. We then introduce alternative dark sector models from the literature, focusing on scalar fields. The bulk of this work focuses on studying new models of interacting scalar field dark matter (DM) and dark energy (DE). We study a model inspired by hybrid inflation, obtaining a previously unknown form of dark energy-dark matter coupling. By comparing this model to cosmological data we conclude that it can alleviate the H_0 tension. We also propose a framework for DM-DE scalar fields based on effective field theory. This results in the DM component developing a negative equation of state at late times. We look for evidence of this new signature in cosmological observations and find that whilst this model can reduce the S_8 tension, new data will be needed to establish whether this model is fully viable.

Contents

Figures

Tables

Chapter 1

Introduction

Cosmology is the branch of science which aims to explain the past, present and future of our universe. Since it is concerned with *everything*, understanding cosmology requires concepts from all areas of physics, from gravity to quantum theory to thermodynamics to astronomy and more. It is now widely accepted that the universe began in a condensed, hot state and cooled down rapidly through expansion, in a process called the hot big bang. From this, it follows that cosmology deals with some of the most extreme phenomena in all of physics, all the way from localised high-energy interactions to large-scale processes at record-low temperatures.

Being one of the oldest sciences, cosmology has evolved over the centuries thanks to technological and theoretical progress; and while some of its considerations remain in the realm of metaphysics, it is now based on solid theoretical grounds and a plethora of reliable astronomical observations. The main theoretical breakthrough – which cemented cosmology as a science – came from Einstein's theory of general relativity (GR) in 1915 [31]. Using Einstein's insights, Friedmann, Lemaître, Robertson and Walker (FLRW) independently developed a mathematical description of our universe in the 1920's and 1930's [32–35]. This was based on the assumptions that our universe is homogeneous - it looks the same wherever you are observing from - and isotropic - it looks the same no matter which direction you look in. On the observational side, Hubble's 1929 observation of receding galaxies [7] was the first evidence that our universe is in fact expanding, and a confirmation of the FLRW solution which typically predicts an expanding universe.

Since these early developments, cosmology has developed rapidly, driven by new observations. A unique challenge of cosmology comes from its very nature: since we are concerned with studying the universe as a whole, observations are non-replicable due to the cosmic scales involved. Thankfully, due to the sheer size of the universe, there are many instances of objects in a given class – galaxies, stars etc. – and so cosmology relies heavily on statistics to draw conclusions. The uncertainties in cosmological observations come not only from standard systematics, but also from the fact that we can only observe one realisation of the universe. The latter phenomenon is usually referred to as cosmic variance. Despite these limitations, cosmology has evolved in under a century from a lack of observations with prohibitively large errors to now being considered a precision science [36], with a number of state of the art telescopes and percent level uncertainties. This increase in the quality of observations has led to many theoretical breakthroughs to explain them, culminating in the currently accepted standard model of cosmology, ΛCDM, which we will describe in Chapter 3.

In this thesis, we will first review the relevant background to understand modern cosmology. We will then go beyond the standard model, and describe new models which aim to solve some outstanding problems emerging both from theoretical and observational considerations. In particular, we will focus on the nature of dark matter (DM) and dark energy (DE) and their possible joint origin.

The thesis is organised as follows: Chapter 2 introduces the mathematical foundations of cosmology, including Einstein's general relativity and the basics of physical cosmology. These concepts come together with observational cosmological methods in Chapter 3, culminating with a description of the ΛCDM model and its challenges. In Chapter 4 we present alternatives to ΛCDM, focussing on scalar fields and their use to model dark matter and dark energy. After this, all material presented is new, independent research. Chapter 5 proposes a new model for DM and DE based on two scalar fields interacting through the hybrid inflation [37] potential. In Chapter 6 we constrain the parameters of the hybrid dark sector model by comparing its theoretical predictions to cosmological observables. In Chapter 7 we introduce an interacting scalar fields framework for DM and DE based on effective field theory. The model has the interesting property of yielding a negative equation of state for DM at late times. We study in detail a simplified model based on this framework in Chapter 8, including the behaviour of perturbations and a Bayesian analysis of the parameters preferred by cosmological data. In this thesis we will work in units where $\hbar = c = 1$ and adopt the $(-,+,+,+)$ metric signature.

Chapter 2

Mathematical foundations of cosmology

The interplay between geometry and physics is central to our understanding of the universe. In this chapter, we will see how the foundations of general relativity – introduced in Section 2.1 – can naturally lead to a theory of an expanding universe and therefore cosmology (in Section 2.2).

2.1 General relativity

In order to describe the evolution of our universe, we need the physical and mathematical framework of general relativity. Developed by Albert Einstein in 1915 [31], general relativity is a geometric theory of gravity. At its core, it explains what we call gravity as the curvature of spacetime. The curvature of spacetime is influenced by any matter present in the spacetime, and that matter evolves according to the curvature. This holds true in cosmology, where the contents of the universe directly influence how the universe evolves.

2.1.1 Einstein's GR basics

The central degree of freedom in GR is the metric tensor $g_{\mu\nu}$ [38–40], which allows us to define physical distances between points in spacetime, and in turn make sense of causality in the universe. The metric is conventionally written as a line element ds^2, which represents the length of an infinitesimal displacement vector:

$$ds^2 = g_{\mu\nu}\mathrm{d}x^\mu\mathrm{d}x^\nu, \tag{2.1}$$

where $\mathrm{d}x^{\mu}$ is a basis covector.

To formalise the notion of curvature, we need to generalise the concept of a derivative in curved spacetime. This is provided by a connection ∇, which evaluates the rate of change of a tensor between two neighbouring points and is defined as such for an arbitrary tensor of rank (k, l):

$$\begin{aligned}\nabla_{\mu} T^{\nu_1 \ldots \nu_k}_{\rho_1 \ldots \rho_l} &= \partial_{\mu} T^{\nu_1 \ldots \nu_k}_{\rho_1 \ldots \rho_l} \\ &+ \Gamma^{\nu_1}_{\mu\lambda} T^{\lambda \ldots \nu_k}_{\rho_1 \ldots \rho_l} + \ldots + \Gamma^{\nu_k}_{\mu\lambda} T^{\nu_1 \ldots \lambda}_{\rho_1 \ldots \rho_l} \\ &- \Gamma^{\lambda}_{\mu\rho_1} T^{\nu_1 \ldots \nu_k}_{\lambda \ldots \rho_l} - \ldots - \Gamma^{\lambda}_{\mu\rho_l} T^{\nu_1 \ldots \nu_k}_{\rho_1 \ldots \lambda},\end{aligned} \tag{2.2}$$

where we have introduced the Christoffel symbols $\Gamma^{\mu}_{\nu\rho}$. In GR, we require that the connection satisfy two extra conditions [38]:

- it is torsion free: $\Gamma^{\mu}_{\nu\rho} = \Gamma^{\mu}_{\rho\nu}$
- it is metric compatible: $\nabla_{\rho} g_{\mu\nu} = 0$.

It turns out there is only one such connection, called the Levi-Civita connection and defined as follows:

$$\Gamma^{\rho}_{\mu\nu} = \frac{1}{2} g^{\rho\lambda} (\partial_{\mu} g_{\nu\lambda} + \partial_{\nu} g_{\lambda\mu} - \partial_{\lambda} g_{\mu\nu}). \tag{2.3}$$

Next, we can introduce curvature in the form of the Riemann tensor, which is related to the change in a vector after having been parallel transported around a loop:

$$R^{\sigma}{}_{\rho\mu\nu} \equiv \partial_{\mu} \Gamma^{\sigma}_{\nu\rho} - \partial_{\nu} \Gamma^{\sigma}_{\mu\rho} + \Gamma^{\sigma}_{\mu\lambda} \Gamma^{\lambda}_{\nu\rho} - \Gamma^{\sigma}_{\nu\lambda} \Gamma^{\lambda}_{\mu\rho}. \tag{2.4}$$

The Riemann tensor has multiple algebraic symmetries and it obeys a differential constraint, the Bianchi identity:

$$\nabla_{[\lambda} R_{\rho\sigma]\mu\nu} = 0, \tag{2.5}$$

where indices in square brackets are antisymmetrised. We now define useful contractions of the Riemann tensor: the Ricci tensor

$$R_{\mu\nu} \equiv R^{\lambda}{}_{\mu\lambda\nu}, \tag{2.6}$$

which is symmetric, and the Ricci scalar

$$R \equiv R_{\mu\nu} g^{\mu\nu}. \tag{2.7}$$

From there we define the Einstein tensor

$$G_{\mu\nu} \equiv R_{\mu\nu} - \frac{1}{2} R g_{\mu\nu}, \tag{2.8}$$

which is symmetric and covariantly conserved, meaning its covariant derivative vanishes:

$$\nabla^{\mu} G_{\mu\nu} = 0. \tag{2.9}$$

We now seek to find an equation which describes the dynamics of a generic spacetime containing some matter or energy (the case of a vacuum spacetime follows straightforwardly). In order to do this, we first need to model the matter [1] in our spacetime. To do this we define the energy-momentum (EM) tensor $T^{\mu\nu}$ which heuristically is "the flux of four-momentum p^{μ} across a surface of constant x^{ν}" [38]. To generalise conservation of energy-momentum to curved spacetime, the following covariant conservation law applies to all non-interacting energy-momentum tensors:

$$\nabla^{\mu} T_{\mu\nu} = 0. \tag{2.10}$$

It is common in cosmology to model a group of particles as a fluid, in which case the components of the energy-momentum tensor have a straightforward physical interpretation in the fluid's rest frame:

- T^{00} represents the energy density ρ,
- T^{i0} is the momentum density,
- T^{ii} give the x, y, z components of the pressure[2],
- T^{ij} for $i \neq j$ describe shear stress.

A simple but useful special case is that of perfect fluids, which can be described with only two degrees of freedom: the energy density ρ and the pressure p (notice in this case the pressure is the same in all directions). Perfect fluids have no shear stress in the frame where momentum density vanishes. Their EM tensor can generally be written as

$$T^{\mu\nu} = (\rho + p) u^{\mu} u^{\nu} + p g^{\mu\nu} \tag{2.11}$$

---

[1] Here we use matter in a loose sense to mean any form of stress-energy present in the universe. Later, in the context of cosmology, matter will refer to presureless dust.

[2] No sum is implied here.

where u^μ is the four-velocity of the fluid.

Now back to our main problem. We need an equation relating gravity (the metric) to whatever 'stuff' is in our spacetime (the energy-momentum). Einstein's insight (one of many!) was to see that whatever the actual description of gravity was, it had to agree with Newton's on appropriately small scales. By deriving the Newtonian limit of GR and comparing it to Poisson's equation, the simplest second-order set of equations corresponding to these constraints are Einstein's equations:

$$R_{\mu\nu} - \frac{1}{2} R g_{\mu\nu} = 8\pi G T_{\mu\nu}, \tag{2.12}$$

where G is Newton's gravitational constant. The neat tensor notation hides 10 non-linear equations which in general are very difficult to solve. Nevertheless, Einstein's equations encompass the deep fundamental fact that the curvature of spacetime (and hence what we perceive as gravity) is influenced by, and influences, the energy-momentum present in the spacetime. In cosmology, we will solve these equations by assuming some physically motivated symmetries present in our universe, as well as specifying the energy contents of the universe. Before we do this, however, let us take a detour and derive Eq. (2.12) from a different approach, namely that of the principle of least action.

2.1.2 The Einstein-Hilbert action

In order to understand GR as a classical field theory, we now seek an action which can yield Einstein's equations. Along with being an elegant formulation of GR, this approach makes it easier to modify Einstein's original theory by adding extra ingredients and couplings - one might, for example, want to combine electrodynamics and GR. The degree of freedom which we will vary according to the principle of least action is the metric itself, $g_{\mu\nu}$. This action will necessarily be of the form

$$\mathcal{S}_{\mathcal{H}} = \int d^4x \sqrt{-g}\, \mathcal{L}_{\mathcal{H}} \tag{2.13}$$

where $\mathcal{L}_{\mathcal{H}}$ is a Lorentz scalar which we will call the Lagrangian[3], and the extra factor of $\sqrt{-g}$ is necessary to keep the volume element invariant under coordinate transformations.

A non-trivial scalar $\mathcal{L}$ must be at least second order in derivatives of the metric[4] [40]. At second order, the only possible scalar is the Ricci scalar R . For simplicity's sake (i.e.

---

[3] Strictly speaking, this is the Lagrangian density.

[4] We discuss the cosmological constant in the next section.

avoiding higher derivatives orders), Hilbert proposed the following action

$$\mathcal{S}_{\mathcal{H}} = \frac{1}{16\pi G}\int d^4x\sqrt{-g}\,R, \tag{2.14}$$

which turns out to be the right one. To see this, we can first compute the variation in the action $\delta\mathcal{S}_{\mathcal{H}}$ caused by a small variation in the metric $\delta g^{\mu\nu}$. The principle of least action then tells us that the equation of motion is obtained by taking this variation and setting it to 0, in other words:

$$\frac{\delta\mathcal{S}_{\mathcal{H}}}{\delta g^{\mu\nu}} = 0 \tag{2.15}$$

We omit the full derivation here but the upshot is the following:

$$\frac{\delta\mathcal{S}_{\mathcal{H}}}{\delta g^{\mu\nu}} = \sqrt{-g}\left[R_{\mu\nu} - \frac{1}{2}Rg_{\mu\nu}\right] = 0 \tag{2.16}$$

which is precisely Einstein's equations in vacuum. In order to add matter, we define a new action

$$\mathcal{S} = \frac{1}{16\pi G}\mathcal{S}_{\mathcal{H}} + \mathcal{S}_M \tag{2.17}$$

where $\mathcal{S}_M$ is the action for matter. By defining the energy-momentum tensor as

$$T_{\mu\nu} = -2\frac{1}{\sqrt{-g}}\frac{\delta\mathcal{S}_M}{\delta g^{\mu\nu}}, \tag{2.18}$$

we recover the full Einstein equations after varying $\mathcal{S}$.

2.1.3 The cosmological constant

As we will see in detail in Section 2.2.5, Einstein's equations admit solutions describing a dynamical (usually expanding) universe. In the early 20th century, the idea that our universe might be expanding was an eccentric one, and the fact that his theory of gravitation allowed for this was a difficult pill to swallow for Einstein. To ensure a static universe solution, he decided to modify his field equations in the most minimal way possible whilst still preserving most of its properties, by adding a linear combination of the metric to the original tensor. What results, as was proved by Lovelock in 1971 [41], is the most generic two-index symmetric tensor equation constructed in 4D from the metric with up to second-order derivatives and is divergence free. The action required to obtain the modified equations is the following:

$$\mathcal{S} = \int d^4x\sqrt{-g}\left(\frac{1}{16\pi G}\left(R-2\Lambda\right)+\mathcal{L}_M\right), \tag{2.19}$$

where Λ is a constant, usually referred to as the cosmological constant (CC), and $\mathcal{L}_M$ is the matter Lagrangian. The corresponding equations of motion obtained after varying this action are the Einstein equations with a cosmological constant:

$$R_{\mu\nu} - \frac{1}{2}Rg_{\mu\nu} + \Lambda g_{\mu\nu} = 8\pi G T_{\mu\nu}. \tag{2.20}$$

It turns out that the static solution obtained by adding the CC is unstable to small perturbations in the curvature or the matter density. Moreover, Hubble's observations of receding galaxies in 1929 [7], suggesting the universe was in fact expanding, prompted Einstein to label this as his "greatest blunder" [42]. We will come back to the issue of the cosmological constant in Section 2.2.4 and evaluate whether this was indeed such a massive blunder on Einstein's part.

2.2 Cosmology

Solving the Einstein equations is hard. It is hard in vacuum, and it is even harder in the presence of mass-energy. We know that the universe is full of *stuff*, and therefore we will focus on the latter case. In order to make progress, we will have to make use of the powerful concept of symmetries, motivated by physical observations.

2.2.1 The cosmological principle

Whilst it may seem counter-intuitive at first, the cornerstone of modern cosmology is the assumption that our universe is spatially homogeneous and isotropic, also called the cosmological principle. Broadly speaking, this states that on large enough scales, the universe looks the same to an observer wherever they are (homogeneity) and whichever direction they look (isotropy). Of course, we know from everyday life that the universe is neither of these things on our planetary scale, hence the importance of specifying that we are talking about large scales. Still, we know that there are lots of galaxies far away in the universe, and that they surely do not all look the same. On top of that, how can we know what the universe looks like to a different observer, since no human has even left our solar system?

First, let us consider isotropy. There is strong evidence that the universe looks the same in all directions, mainly coming from the cosmic microwave background (CMB). We will discuss this in more detail later, but the CMB is a relic radiation emitted around 300,000 years after the Big Bang, which certainly represents a large enough scale. Statistically, the CMB radiation looks the same (i.e. each photon is the same temperature) regardless of direction. This isotropy is remarkably only broken at a scale of one part in around 10^5 (see Fig. 5.7), and these anisotropies are the seeds of all the structure we observe today in the universe.

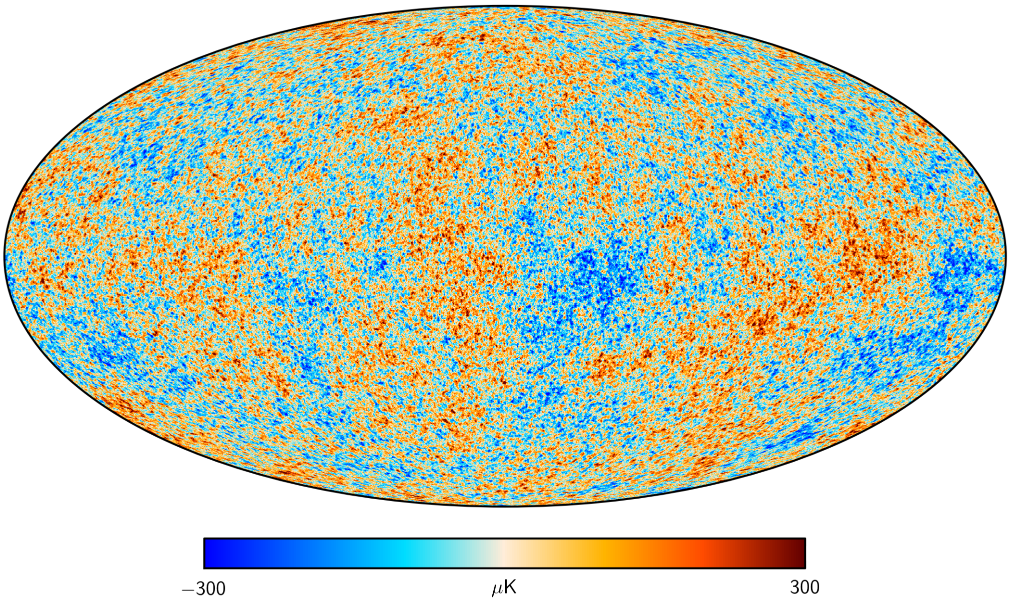

Figure 2.1: Sky map of the CMB temperature anisotropy from the Planck Collaboration [4, 5].

Homogeneity is trickier to prove, since we only have one place from which to observe the universe. If we invoke the Copernican principle and assume that we are not in a special place in the universe, isotropy for us would imply isotropy everywhere in the universe. Remarkably, isotropy at every point in spacetime necessarily implies homogeneity [43]. Observationally, we can rely on galaxy surveys (see Fig. 2.2) to probe homogeneity in our universe: if the statistical properties of galaxy distribution in a given volume are independent of their location in the universe, then the universe can be considered to be homogeneous. Recent galaxy surveys suggest that the universe starts to look homogeneous at around 100 Mpc [44].

Now that we are happy to consider that the universe is broadly speaking homogeneous and isotropic, we will take this as a fact and explore what it means mathematically. The idea is to consider a spatially homogeneous and isotropic background spacetime on which

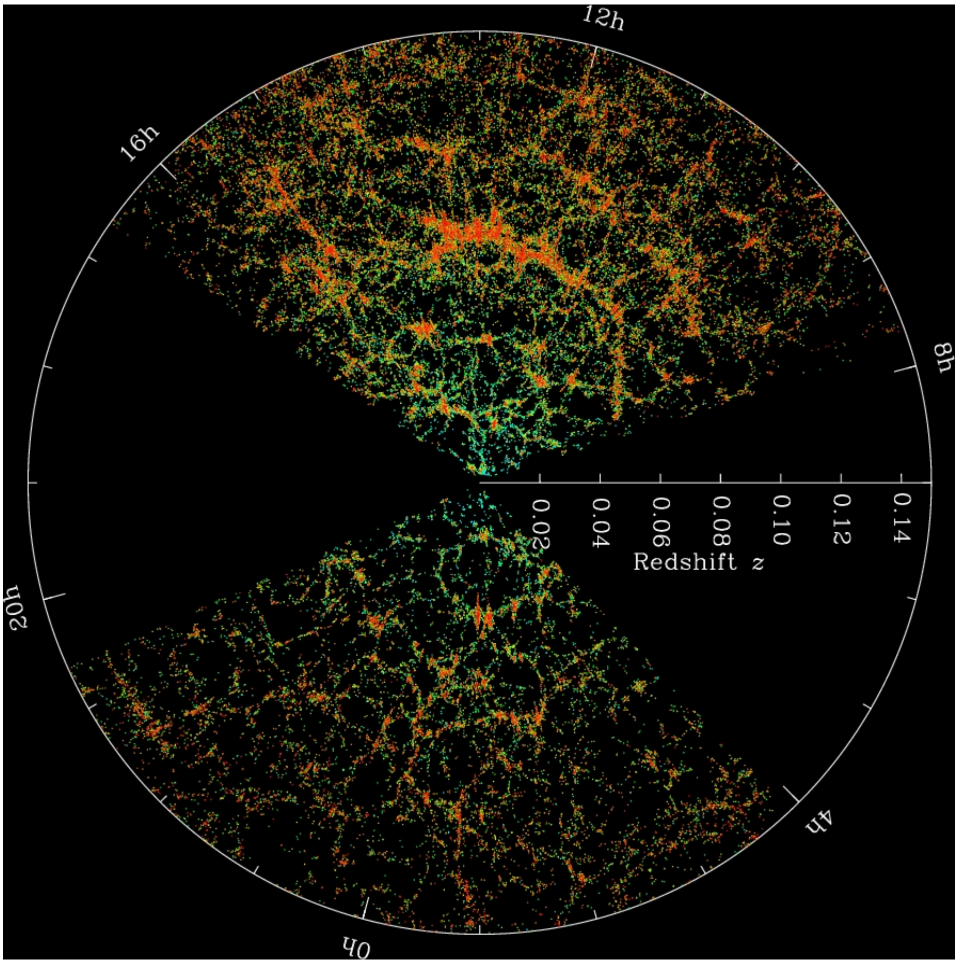

Figure 2.2: The map of the universe from the Sloane Digital Sky Survey (SDSS) [6]. Each dot represents a galaxy, coloured according to the age of their stars. Redder, more strongly clustered galaxies contain older stars. The missing directions in the wedge were not observed due to foreground dust. Image credit M. Blanton and SDSS collaboration `https://www.sdss4.org/science/orangepie/`.

we can study small perturbations which introduce inhomogeneity and anisotropy. These small perturbations will then be the seeds of the structure we observe today.

In short, we want to foliate our spacetime with spacelike hypersurfaces - that is, associate a spacelike hypersurface with each point in time, where time is described by a continuous parameter. In other words, at each moment in time we associate a hypersurface representing space. This hypersurface must be both rotationally invariant (isotropic) and translationally invariant (homogeneous) - such a 3-space is said to be maximally symmetric. These conditions imply that the components of the metric can only depend on time and that the spatial curvature must be constant throughout space.

2.2.2 The Friedmann-Lemaitre-Robertson-Walker metric

Putting all the insights from the previous sections together, the most general metric exhibiting spatial isotropy and homogeneity is the Friedmann-Lemaitre-Robertson-Walker metric:

$$ds^2 = -\mathrm{d}t^2 + a^2(t)\gamma_{ij}\mathrm{d}x^i\mathrm{d}x^j. \tag{2.21}$$

The coordinates we choose are standard in cosmology and are as follows: t is called cosmic time and represents the proper time of an observer with no peculiar velocity in a spatially isotropic and homogeneous universe. It is a preferred time coordinate in our spacetime. The spatial coordinates $\{x, y, z\}$ denote comoving coordinates. These spatial coordinates evolve along with the expansion of the universe, meaning that the comoving distance between two points remains constant throughout cosmic history. Physical distances are proportional to the scale factor $a(t)$ and so evolve with time. Proper distance can be recovered through $x^i_{\text{phys}}(t) = a(t)x^i$. The scale factor is a dimensionless quantity related to the relative size of the universe, so it is a direct measure of its expansion and evolution. Finally, γ_{ij} represents the metric for a maximally symmetric 3-space. Since curvature is constant on the 3-space, it is sufficient to consider 3 distinct cases, depending on whether the curvature K is positive, negative or zero.

- If $K > 0$, the spacelike hypersurface is the 3-sphere and the universe is **closed**.
- If $K = 0$, the 3-space is simply Euclidean space and the universe is **flat**.
- If $K < 0$ the spatial slices are hyperboloids and the universe is **open**.

In comoving spherical coordinates, the spatial metric can be written as

$$\gamma_{ij}\mathrm{d}x^i\mathrm{d}x^j = \frac{\mathrm{d}r^2}{1 - Kr^2} + r^2(\mathrm{d}\theta^2 + \sin^2\theta\mathrm{d}\varphi^2). \tag{2.22}$$

Note that $\{r, \theta, \varphi\}$ are derived from the comoving spatial coordinates $\{x, y, z\}$ hence they are also comoving. The above metric can be rewritten in terms of a new radial coordinate χ, defined as

$$\mathrm{d}\chi \equiv \frac{\mathrm{d}r}{\sqrt{1 - Kr^2}}. \tag{2.23}$$

Integrating yields $r = S_k(\chi)$, where [38]

$$S_k(\chi) \begin{cases} \sin\chi \text{ for } K > 0 \\ \chi \text{ for } K = 0 \\ \sinh\chi \text{ for } K < 0, \end{cases} \tag{2.24}$$

and so the spatial metric can be rewritten as

$$\gamma_{ij}\mathrm{d}x^i\mathrm{d}x^j = \mathrm{d}\chi^2 + S_k^2(\chi)(\mathrm{d}\theta^2 + \sin^2\theta\mathrm{d}\varphi^2). \tag{2.25}$$

There is a common alternate time coordinate called conformal time τ, defined as $dt = ad\tau$. Writing the FLRW metric with $K = 0$ in conformal time yields

$$ds^2 = a^2(t)\left(-\mathrm{d}\tau^2 + \gamma_{ij}\mathrm{d}x^i\mathrm{d}x^j\right), \tag{2.26}$$

i.e. $g_{\mu\nu} = a(t)\eta_{\mu\nu}$ where $\eta_{\mu\nu}$ is the Minkowski metric of special relativity – a flat, static spacetime. We will denote derivatives with respect to conformal time with a $'$ symbol, i.e. $f' \equiv \frac{df}{d\tau}$

Let us now consider the implications of the spacetime symmetries on the energy-momentum tensor introduced in Section 2.1.1 [45]. Let us decompose our EM tensor into a scalar T_{00}, a 3-vector $T_{i0} = T_{0i}$ and a 3-tensor T_{ij}. Now, we know from homogeneity that any scalar must be a function of time only, and from isotropy that any 3-vector must vanish (since there are no preferred directions). Moreover, it can be shown that isotropy forces the element of a 3-tensor to be proportional to the 3-metric, with homogeneity again requiring that the constant of proportionality be only a function of time. We can therefore write the components of $T_{\mu\nu}$ as

- $T_{00} = \rho(t)$,
- $T_{i0} = T_{0i} = 0$,
- $T_{ij} = p(t)g_{ij}$.

Note that the symmetries do not allow for momentum density or shear stress, and force the pressure to be the same in every direction. In a comoving frame, the fluid is at rest and so

$$u^\mu = (1, 0, 0, 0), \tag{2.27}$$

which means the EM tensor for a fluid in a homogeneous and isotropic universe can be written as

$$T_{\mu\nu} = (\rho + p)u_\mu u_\nu + pg_{\mu\nu}. \tag{2.28}$$

The above equation is exactly Eq. (2.11), meaning that the spacetime symmetries imposed by the cosmological principle have picked out the perfect fluid as the only allowed form of fluid mass-energy.

For completeness, we also include the trace of the EM tensor

$$T = T^\mu_\mu = -\rho + 3p, \tag{2.29}$$

which can be a useful quantity.

2.2.3 The Friedmann equations

Equipped with the metric and the energy-momentum tensor, we are now ready to write down the Einstein equations. Note that the use of symmetry has greatly reduced the number of degrees of freedom in the metric from 10 (since the Einstein tensor is symmetric) to just one: the scale factor $a(t)$. Let us start by calculating the Einstein tensor in an FLRW spacetime. Following symmetry arguments, we know that the $G_{i0} = G_{0i}$ components vanish, and that $G_{ij} \propto g_{ij}$. After some calculations we are left with

$$G_{00} = 3\left[\left(\frac{\dot{a}}{a}\right)^2 + \frac{K}{a^2}\right] \tag{2.30}$$

$$G_{ij} = -\left[2\frac{\ddot{a}}{a} + \left(\frac{\dot{a}}{a}\right)^2 + \frac{K}{a^2}\right] g_{ij}, \tag{2.31}$$

where we use the overdot to refer to cosmic time derivative, i.e. $\dot{f} \equiv \frac{df}{dt}$ For reference, the Ricci scalar reduces to

$$R = 6\left[\frac{\ddot{a}}{a} + \left(\frac{\dot{a}}{a}\right)^2 + \frac{K}{a^2}\right]. \tag{2.32}$$

Now, plugging in Eqs. (2.30), (2.31) into the Einstein equations and doing some rearranging, we obtain the Friedmann equations:

$$\left(\frac{\dot{a}}{a}\right)^2 = \frac{8\pi G}{3}\rho - \frac{K}{a^2}, \tag{2.33}$$

$$\frac{\ddot{a}}{a} = -\frac{4\pi G}{3}(\rho + 3p), \tag{2.34}$$

where it is to be understood that ρ and p correspond to the sum of the energy density and pressure of all types of mass-energy in the universe (we will describe the contents of our universe in Section 2.2.4). These equations allow us to solve for the scale factor and so for the evolution of the universe. There is, however, a caveat. We have two Friedmann equations for 3 variables, $a(t)$, $\rho(t)$ and $p(t)$. In order to close this system, we must introduce an equation of state (EoS) for the fluid, that is a relation between the energy density and the pressure $p = p(\rho)$. For a linear barotropic fluid, this is given by

$$p = w\rho, \tag{2.35}$$

where w is the constant equation of state. We will relax the assumption that w is a constant later in this thesis.

We define the Hubble parameter,

$$H(t) \equiv \frac{\dot{a}}{a}, \tag{2.36}$$

which is used to describe the expansion rate of the universe at a given time. In an expanding universe, $H(t)$ is necessarily positive. In terms of conformal time, we define

$$\mathcal{H}(\eta) \equiv \frac{a'}{a}. \tag{2.37}$$

We can derive another useful cosmological equation from the conservation of energy-momentum, Eq. (2.10). Plugging in our FLRW metric, we obtain the simple expression

$$\dot{\rho} + 3H(\rho + p) = 0. \tag{2.38}$$

Note that the first Friedmann equation, Eq. (2.33), in conjunction with the energy-momentum conservation equation, Eq. (2.38), are equivalent to the two Friedmann equations – Eqs. (2.33), (2.34). We will generally use the former combination in the rest of this work, and refer to Eq. (2.33) simply as the Friedmann equation.

Finally, let us introduce the density parameter $\Omega(t)$, which is used to describe the fractional density of different energy components in the universe. This is defined as

$$\Omega \equiv \frac{8\pi G}{3H^2}\rho = \frac{\rho}{\rho_{\text{crit}}}, \tag{2.39}$$

where we have defined ρ_{crit} the critical density, which is the density required to keep the universe flat at any given time. This can be seen by rewriting the Friedmann equation as

$$\Omega - 1 = \frac{K}{a^2H^2}, \tag{2.40}$$

which shows that if the energy density is equal to the critical density, the spatial curvature is necessarily zero.

2.2.4 Mass-energy in the universe

Now that we have developed the mathematical machinery to describe our universe, let us see in detail how the mass-energy content of the universe influences its evolution. To this end, we will first solve Eq. (2.38) for a linear barotropic fluid. In this case the equation simplifies to

$$\dot{\rho} + 3H\rho(1+w) = 0, \tag{2.41}$$

which can be straightforwardly integrated to yield

$$\rho(t) = \rho_i \left(\frac{a(t)}{a_i}\right)^{-3(1+w)}, \tag{2.42}$$

where the subscript i denotes the value of the functions at some initial time t_i. Note that here we have assumed there is only one fluid species in the universe, which we will justify in a moment.

Clearly, which equation of state one chooses for their perfect fluid directly changes how the universe evolves. In order to restrict which values of w are allowed, we turn to the energy conditions. In short, these are mathematical constraints on the EM tensor constructed in an effort to make the mass-energy content of spacetime physically realistic. Energy conditions provide a relativistic, coordinate-invariant generalisation of the idea that energy density should not be negative. Here we describe the main energy conditions, in the case of a linear barotropic perfect fluid [5]:

- The null energy condition (NEC) requires $\rho + p \geq 0$.

---

[5] See [38] for fully covariant formulation

- The weak energy condition (WEC) requires $\rho \geq 0$, $\rho + p \geq 0$.
- The dominant energy condition (DEC) requires $\rho \geq |p|$.
- The strong energy condition (SEC) requires $\rho + p \geq 0$, $\rho + 3p \geq 0$.

For now we will adopt the weak energy condition, which means that we will consider perfect fluids with positive energy density and $w \geq -1$.

Let us discuss the main three sources of mass-energy we will encounter in cosmology:

Matter Also called dust, matter is the most familiar (although not most abundant, see Section 3.2.2) source of mass-energy in our universe. Physically it is defined as a fluid made up of non-relativistic, non-interacting particles such that their pressure is negligible. In practice, this means that $w = 0$ and so their energy density evolves as $\rho \propto a^{-3}$. This is in keeping with the expectation that the number density dilutes inversely proportional to the volume of the universe as it expands, and the mass of the particles stays unchanged. Dust is used to model[6] all baryonic and leptonic matter that make up gases, stars and galaxies, as well as cold dark matter (CDM) which we will discuss in Section 3.1.2.

Radiation This term is used to describe either actual electromagnetic radiation (photons) or massive relativistic particles (neutrinos). Their equation of state is $w = 1/3$. This can be seen by taking the EM tensor of Maxwell's electromagnetic theory and showing its trace is equal to 0. Equating this to the trace of a perfect fluid EM tensor (Eq. (2.29)), we see that $p = \rho/3$ [38]. Solving the continuity equation Eq. (2.41), we get $\rho \propto a^{-4}$. Radiation dilutes quicker than matter in an expanding universe. This is because the number density of the photons evolves with the volume of the universe, photons also lose energy at a rate of a^{-1} due to redshift, which we will discuss in more detail in Section 2.2.6.

Vacuum energy Let us go back to the cosmological constant from Eq. (2.20). If one moves this contribution to the right hand side and considers it as a source of mass-energy, we find that this corresponds to the energy-momentum tensor of a perfect fluid with $p = -\rho$, or $w = -1$. The energy density is $\rho = \frac{\Lambda}{8\pi G}$ which in principle can be positive or negative depending on the sign of Λ (although adopting the WEC restricts it to positive values). One interpretation for the cosmological constant is that it represents a vacuum energy of the universe, constant at every point in spacetime.

---

[6] On large scales.

Most models for realistic universes will include a combination of all three components described above, as well as curvature. Since they decay at different rates, it is common to divide the history of the universe into separate epochs, when a particular component dominates the sum of energy densities. Radiation decays quickest, and so can only dominate at early times if its initial energy density is high enough. At some later point, matter might take over and the universe becomes matter dominated. The vacuum energy, being constant, will always come to dominate regardless of how small it is, as long as there is no collapse. There is also a possibility that the curvature contribution will become dominant. Indeed, looking at Eq. (2.33), the K term is proportional to a^{-2} and so decays slower than matter. Since the behaviour of ρ directly enters into the Friedmann equation, we shall see next how the universe (i.e. the scale factor) evolves in each epoch.

2.2.5 Dynamics of the universe

We can now solve the Friedmann equation (Eq. (2.33)) throughout the history of the universe, by adopting the simplifying assumption of a single-component universe. Indeed, as mentioned in the previous section, since all types of mass-energy decay at different rates in a dynamical universe, there will be stretches of time where one component comes to dominate the energy-momentum of the universe, and so we can ignore the other components at that point. For a perfect fluid with equation of state $p = w\rho$, the Friedmann equation can be solved exactly in terms of cosmic time

$$a(t) \propto \begin{cases} t^{2/(3(1+w))} \text{ if } w \neq -1 \\ e^{Ht} \text{ if } w = -1, \end{cases} \tag{2.43}$$

and in conformal time

$$a(\tau) \propto \begin{cases} \tau^{2/(1+3w)} \text{ if } w \neq -1 \\ |\tau|^{-1} \text{ if } w = -1. \end{cases} \tag{2.44}$$

A few interesting things to note: first, the scale factor grows quicker in matter domination (MD) than in radiation domination (RD), but it expands quickest during vacuum energy domination (ΛD). Next, it is easy to see by looking at Eq. (2.33) that the Hubble rate $H(t)$ decreases during RD and MD, while it stays constant in ΛD. Finally, looking at Eq. (2.34), we can see that the expansion of the universe accelerates ($\ddot{a} > 0$) for $w \leq -1/3$, meaning that it is actually decelerating during RD and MD, but accelerating during ΛD.

In the above discussion we have neglected curvature. Indeed, as mentioned earlier a universe with a cosmological constant will necessarily end up in ΛD, but depending on the size of the K term in Eq. (2.40) curvature may influence the dynamics. The sign of K is crucial to the type of evolution it yields. Suppose there is no cosmological constant [7], then curvature will become dominant after MD. If the universe is open ($K < 0$), then there will just be a new expanding epoch with $\rho \propto a^{-2}$ and $a(t) \propto t$. The universe will expand at a steady rate ($\ddot{a} = 0$) forever. However, if the universe is closed ($K > 0$), when curvature takes over the contribution will now be negative. The expansion will then slow down until the matter energy density is equal to the curvature contribution, at which point the rhs of Eq. (2.33) will become 0. It is of course not possible for this to go negative as it must be equal to H^2, but H itself will become negative, meaning that the universe will start contracting instead of expanding! This may result in what we call a big crunch, when the universe shrinks back to a singularity at $a = 0$ [8].

2.2.6 Cosmological redshift and measuring distances

One of the main ways we gather information about our universe is by observing distant objects such as stars and galaxies. In order to use these observations, we will be interested in working out how far these objects are from us. Here we develop the mathematical machinery to understand distances in cosmology.

First, let us discuss photons, since electromagnetic radiation is how we typically observe astronomical objects. As photons travel to reach observers on Earth, their wavelength gets stretched due to the expansion of the universe. Formally, the momentum p of photons is proportional to $a^{-1}(t)$, and the relation to the wavelength is given by $\lambda = h/p$ (where h is the Planck constant) hence $\lambda \propto a(t)$:

$$\lambda(t_0) = \frac{a(t_0)}{a(t_1)}\lambda(t_1). \tag{2.45}$$

We define the redshift z as the fractional change in photon wavelength between the source (where the photon was emitted) and the observer:

$$z \equiv \frac{\lambda_{\text{obs}} - \lambda_{\text{em}}}{\lambda_{\text{em}}}. \tag{2.46}$$

Plugging in Eq. (2.45) and assuming the common convention of setting the present-day

---

[7] It is also possible that curvature takes over after ΛD if there exists a mechanism for the cosmological constant to decay.

[8] Note that the expanding universe models also suffer from a singularity at $a = 0$. This would have happened in the past, at which point all energy densities diverge.

scale factor to 1 (a_0=1), we obtain the following important relation between redshift and scale-factor:

$$a(t) = \frac{1}{1+z} \tag{2.47}$$

where we have generalised the emitted time $t_{\rm em}$ to be any value of t. The equation above means that the observed redshift of an object tells us when the photon was emitted.

For small redshifts ($z \ll 1$), it is common to associate cosmological redshift with standard Doppler-effect redshift, and hence the receding velocity of a nearby object is simply $v = z$ in natural units. At larger scales, the curvature of spacetime becomes important and this simplification does not hold any more.

Expanding the scale factor for a nearby source around $a(t_0) \equiv a_0$, we get

$$\begin{aligned} a(t) &= a_0 + (t-t_0)\dot{a}(t_0) + \mathcal{O}\left((t-t_0)^2\right) + \dots \\ &\approx a_0\left[1 + (t-t_0)H_0\right] \end{aligned} \tag{2.48}$$

where H_0 is the Hubble rate today.

Now we define the comoving distance d_c, which remains constant between two objects as the universe expands [45]:

$$d_c = \int_t^{t_0} \frac{dt'}{a(t')}, \tag{2.49}$$

as well as the particle horizon (often just referred to as the horizon)

$$d_h(t) = \int_0^t \frac{dt'}{a(t')}, \tag{2.50}$$

which represents the maximum size of a causally-connected patch at a given (conformal) time. In a standard cosmology, the horizon is roughly equal to $d_h \sim (aH)^{-1}$.

The proper distance d_p is the distance between two objects in a reference frame with constant cosmological time:

$$d_p = a(t)\chi(r) \tag{2.51}$$

where χ was defined in Eq. (2.24). For objects at low redshift, comoving and proper distances agree and so $d_c \approx d_p \approx (t_0 - t) \equiv d$. Plugging the definition of redshift into Eq. (2.48), we get

$$v \approx z \approx H_0 d. \tag{2.52}$$

This is Hubble's law, which states that the redshift of a nearby object is proportional to its distance and the constant of proportionality is precisely the Hubble rate today[9].

At higher redshifts, when we cannot take a simple first order approximation, we have to define new distance measures which are compatible with the curvature of spacetime. First, we generalise the idea of using luminosity L (which is intrinsic to a bright object) and flux F (which is the signal we observe in units of energy per time per area) in order to find the distance. We define the luminosity distance d_L:

$$d_L^2 \equiv \frac{L}{4\pi F}. \tag{2.53}$$

The general equation for flux in euclidean space is $F = L/A$ where A is the area of a sphere centred at the source. In an expanding universe however, this relationship will not be as straightforward. Indeed, we have to account for the fact that the photons will be redshifted and so their observed energy will be perceived as less than it was when emitted. Also, due to time dilation the rate at which the photons are observed is also reduced by the same factor of redshift. In total, the observed flux is therefore

$$F = \frac{L}{(1+z)^2 A}. \tag{2.54}$$

If the source is situated at a comoving distance χ, the area A defined above is given as

$$A = 4\pi S_k^2(\chi), \tag{2.55}$$

which in the end gives the the following expression for the luminosity distance:

$$d_L = (1+z) S_k(\chi). \tag{2.56}$$

We now explore a second way of measuring distances to far-away objects. If we know the intrinsic size of an object - for simplicity we will call this the diameter D - then by comparing this length to its observed angular size $\delta\theta$ in the sky it is possible to infer its distance. Following our intuition from Euclidean space for a small angular size, we define the angular diameter distance d_A:

$$d_A \equiv \frac{D}{\delta\theta}. \tag{2.57}$$

Using the FLRW metric we find that $D = a(t) S_k(\chi)\delta\theta$, and so the angular diameter

---

[9] Note that this assumes that there is no peculiar velocity component, i.e. any velocity of the object is due to the expansion of the universe with no other, non-comoving, motion.

distance is

$$d_A = \frac{S_k(\chi)}{1+z} = \frac{d_L}{(1+z)^2}. \tag{2.58}$$

2.3 Cosmological perturbation theory

We have seen so far that on large scales the universe can be well approximated as being homogeneous and isotropic. However, it also remains true that when we look out into the night sky, we see direct proof that these assumptions do not hold true for smaller scales. Indeed, the structure in the universe such as galaxies and clusters seems to break the symmetry. This implies that our first order approximation for the background universe does not hold everywhere, and on smaller scales we shall look for a more refined approach. The framework we use is that of perturbation theory, where we assume a background maximally symmetric universe on top of which we introduce some small perturbations. We will keep to linear perturbations in this work, but in order to study structure formation it is often necessary to go to higher orders.

2.3.1 The metric and the energy-momentum tensor

The question remains of what we mean by perturbations of the background. In Einstein's equations we had two ingredients: the metric, and the EM tensor. We will simply introduce some small perturbations in these two components, which will break isotropy and homogeneity [46]. We only consider perturbations around the flat FLRW metric, as we will not need the fully general equations in the rest of this work. Expanding the metric and EM tensor in this way we get:

$$g_{\mu\nu} = \bar{g}_{\mu\nu} + \delta g_{\mu\nu} \tag{2.59}$$

$$T_{\mu\nu} = \bar{T}_{\mu\nu} + \delta T_{\mu\nu}, \tag{2.60}$$

where the over-bar signifies the background quantity and δ indicates the perturbation. The Einstein equation for the perturbations are simply

$$\delta G_{\mu\nu} = 8\pi G \delta T_{\mu\nu}, \tag{2.61}$$

where we have decomposed the Einstein tensor into a background part and a perturbed part by plugging in Eq. (2.59).

Let us look at the perturbed metric in more detail. In conformal time, we rewrite

Eq. (2.59) as

$$g_{\mu\nu} = a^2(\tau)(\eta_{\mu\nu} + h_{\mu\nu}), \tag{2.62}$$

which defines $h_{\mu\nu}$. Before we write down the components of $h_{\mu\nu}$, let us consider the following: remember we arrived at the background FLRW metric by imposing spatial homogeneity and isotropy. It is therefore interesting to ask ourselves what happens to $h_{\mu\nu}$ when we apply spatial rotations to the whole metric. It turns out that the h_{00} component behaves as a scalar under these transformations, h_{i0} behaves as a vector and h_{ij} behaves as a tensor. It is possible to decompose the last two sets of components into scalar, vector and tensor parts. For our purposes, we will only be interested in the scalar part of the perturbed FLRW metric[10], and so we write this as:

$$h_{00} = -2\Phi \tag{2.63}$$

$$h_{i0} = \nabla_i B \tag{2.64}$$

$$h_{ij} = -2(\delta_{ij}\Psi - \nabla_i\nabla_j E), \tag{2.65}$$

where Φ, B, Ψ, E are scalar functions of conformal time and comoving spatial coordinates.

Let us now discuss the perturbed EM tensor. To this end, let us perturb the energy density, pressure and velocity of the fluid:

$$\rho = \bar{\rho} + \delta\rho \tag{2.66}$$

$$p = \bar{p} + \delta p \tag{2.67}$$

$$u_i = \delta u_i. \tag{2.68}$$

We also define what we will refer to as the velocity perturbation v_i:

$$v_i \equiv a u_i, \tag{2.69}$$

as well as the density contrast δ:

$$\delta \equiv \frac{\delta\rho}{\bar{\rho}}. \tag{2.70}$$

Keeping only the scalar part of the perturbations, we get the following components for

---

[10] Remarkably, the scalar, vector and tensor parts of the perturbation decouple at linear order, which makes it possible to consider only scalar perturbations [46].

the perturbed EM tensor:

$$\delta T^0{}_0 = -\delta\rho \tag{2.71}$$
$$\delta T^0{}_i = -(\bar{\rho}+\bar{p})\nabla_i(v-B) \tag{2.72}$$
$$\delta T^i{}_0 = (\bar{\rho}+\bar{p})\nabla_i v \tag{2.73}$$
$$\delta T^i{}_j = \delta p \delta^i_j + (\partial^i\partial_j - \frac{1}{2}\delta^i_j\nabla^2)\Sigma, \tag{2.74}$$

where v is the scalar part of the velocity perturbation v_i, Σ is the scalar part of the anisotropic stress Σ_{ij}. We will usually assume no anisotropic stress and so set $\Sigma = 0$.

2.3.2 Gauge transformations

So far we have ignored an important subtlety of perturbing our background FLRW metric. In order for us to be able to decompose spacetime into a background part and a perturbed part, the two have to share the same coordinate system. Because of the extra freedom (reduced symmetry) in the perturbed spacetime, there are many choices of coordinates in the perturbed spacetime that are equivalent at the background level. In this context, we will refer to a choice of coordinates as a *gauge*, and going from one allowed gauge to another will be referred to as a *gauge transformation*. In practice, gauge transformations are those coordinate transformations for which Eq. (2.59) still holds. We will go from one gauge to another via the following transformation:

$$\tilde{x}^\alpha = \hat{x}^\alpha + \xi^\alpha, \tag{2.75}$$

where $\tilde{x}^\alpha$ are the coordinates in the new gauge, $\hat{x}^\alpha$ are the coordinates in the original gauge and ξ^α is a linear-order vector defining the gauge transformation. Under this transformation, background quantities remain unchanged but perturbed ones change. For the scalar metric perturbations, a gauge transformation induces the following:

$$\tilde{\Phi} = \Phi - \xi^{0\prime} - \frac{a'}{a}\xi^0 \tag{2.76}$$
$$\tilde{B} = B + \xi' + \xi^0 \tag{2.77}$$
$$\tilde{\Psi} = \Psi - \frac{1}{3}\nabla^2\xi + \frac{a'}{a}\xi^0 \tag{2.78}$$
$$\tilde{E} = E + \xi, \tag{2.79}$$

where ξ is the scalar part of the spatial component, i.e. $\xi_i = \nabla_i \xi$. For the EM tensor scalar perturbations, the gauge transformation laws are:

$$\tilde{\delta\rho} = \delta\rho - \bar{\rho}'\xi^0 \tag{2.80}$$

$$\tilde{\delta} = \delta - \frac{\bar{\rho}'}{\bar{\rho}}\xi^0 \tag{2.81}$$

$$\tilde{\delta p} = \delta p - \bar{p}\xi^0 \tag{2.82}$$

$$\tilde{v} = v + \xi' \tag{2.83}$$

$$\tilde{\Sigma} = \Sigma. \tag{2.84}$$

Two gauges are worth mentioning as examples. First, the so-called Newtonian gauge is one in which $B^N = E^N = 0$ (the superscript N denotes the Newtonian gauge). The exact form of the gauge transformation as per Eq. (2.75) is the following:

$$\xi = -E \tag{2.85}$$

$$\xi^0 = -B + E'. \tag{2.86}$$

We will use mainly the synchronous gauge in this work, for numerical convenience. It is defined by the requirement that $\Phi^S = B^S = 0$, where the subscript S denotes the synchronous gauge. Formally it is obtained by setting

$$\xi^{0\prime} + \mathcal{H}\xi^0 = \Phi \tag{2.87}$$

$$\xi' = -\xi^0 - B, \tag{2.88}$$

which, since it is a set of differential equation, only specifies the gauge up to an integration constant. We follow Ma & Bertschinger's [47] notation and define

$$h \equiv -6\Psi^S \tag{2.89}$$

$$\eta \equiv \Psi^S + \frac{1}{3}\nabla^2 E^S \tag{2.90}$$

$$\mu \equiv 2E^S. \tag{2.91}$$

2.3.3 Equations of motion for a perturbed universe

Taking the components of the perturbed metric and EM tensor, it is straightforward (if tedious!) to work out the components of the perturbed Einstein tensor and therefore write down the Einstein equations. To simplify notation, we will choose to show the equations in the synchronous gauge and in Fourier space. We use the following Fourier space conventions: we expand scalar functions as

$$f(\tau, \vec{x}) = \int d^3x f_k(\tau) e^{i\vec{k}\cdot\vec{x}} \tag{2.92}$$

where $\vec{x} = (x, y, z)$ and $\vec{k}$ is a comoving wave vector. It is therefore straightforward to go from coordinate space to Fourier space by using the following dictionary:

$$\begin{aligned} \partial_i &\to ik_i \\ \nabla^2 &\to -k^2. \end{aligned}$$

Additionally, we adopt the convention of Liddle & Lyth [48] and include the following factors of k when defining the Fourier components of B and E:

$$\begin{aligned} B &\to \frac{B_k}{k} \\ E &\to \frac{E_k}{k^2}. \end{aligned}$$

In general this convention also holds for any other scalar constructed by decomposing a vector (extra $1/k$ factor) or a tensor (extra $1/k^2$ factor).

We can now write down Einstein's equations at linear order in perturbation theory:

$$\begin{aligned} k^2\eta - \frac{1}{2}\mathcal{H}h' &= -4\pi G a^2 \delta\rho \qquad (2.93)\\ k^2\eta' &= 4\pi G a^2 (\bar{\rho} + \bar{p}) k v \qquad (2.94)\\ h'' + 2\mathcal{H}h' - 2k^2\eta &= -24\pi G a^2 \delta p \qquad (2.95)\\ h'' + 6\eta'' + 2\mathcal{H}h' + 12\mathcal{H}\eta' - 2k^2\eta &= -16\pi G a^2 \Sigma. \qquad (2.96) \end{aligned}$$

Similarly to the background case, conservation of energy-momentum leads to useful equations at first order, here written in a general gauge:

$$\begin{aligned} \delta\rho' =& -3\mathcal{H}(\delta\rho + \delta p) + (\bar{\rho} + \bar{p})(3\Psi' + E' - kv) \qquad (2.97)\\ (\bar{\rho} + \bar{p})(v - B)' =& -(\bar{\rho} + \bar{p})'(v - B) - 4\mathcal{H}(\bar{\rho} + \bar{p})(v - B)\\ & + k\delta p - \frac{2}{3}k\Sigma + k(\bar{\rho} + \bar{p})\Phi. \qquad (2.98) \end{aligned}$$

Once again, we need to specify some extra information about our fluid in order to solve the above equation. There are two analogues to the EoS at perturbative level: the adiabatic sound-speed, defined as

$$c_a^2 \equiv \frac{\dot{\bar{p}}}{\dot{\bar{\rho}}}, \tag{2.99}$$

and the effective sound-speed:

$$c_s^2 \equiv \frac{\delta p}{\delta \rho}. \tag{2.100}$$

For perfect fluids, the two sound-speeds are equal to the equation of state w. However we will consider fluids which break this assumption in Chapter 7.

2.4 Summary

In this chapter we have introduced the fundamentals of GR, developing this framework in order to describe our own universe. This led us to cosmology by assuming homogeneity and isotropy. We discussed the expansion of the universe, and how it is influenced by its energy content. We described different distance measures in cosmology before moving on to linear perturbation theory, which explains the seeds of the large-scale structure we observe in our universe today. In the next chapter we will make use of these concepts along with observations to draw conclusions on the nature of our universe.

Chapter 3

ΛCDM: the standard model of cosmology

Cosmology is the branch of astrophysics that aims to study our universe as a whole. It is concerned with the evolution of the universe, from its earliest moments to its current state as well as its future fate. Having introduced the theoretical foundations of cosmology in the previous chapter, we will now explore the various observations that tell us about the contents of our universe. In doing this, we will arrive at the standard model of cosmology, ΛCDM, and describe its features, successes and shortcomings. This chapter is organised thus: Section 3.1 describes key concepts in observational cosmology. Section 3.2 introduces the standard model of cosmology, ΛCDM, and Section 3.3 discusses limitations of this model.

3.1 Observational cosmology

In this section, we review the historical developments of observational cosmology, and how this field has helped us understand the contents of our universe.

3.1.1 The expanding universe

The notion of an expanding universe was first explored in the framework of GR by de Sitter in 1917 [49], and then further by Friedmann and Lemaitre in the 1920's [32, 33]. Around this time, work from Slipher [50] showed that far away galaxies exhibited a red Doppler shift, as if they were receding away from us. Definitive evidence that the universe is expanding was provided by Edwin Hubble in 1929 [7] when he observed that further away galaxies receded quicker than closer ones. He discovered that the relation between redshift, or recessional velocity, and the distance to the galaxy was linear, which is precisely what would later be called Hubble's law as introduced in Eq. (2.52). His measurement of $H_0 = 500\text{km/s/Mpc}$ was off by a factor of 7 compared to the modern accepted value which has settled around $H_0 \approx 70\text{km/s/Mpc}$, as we will see in Section 3.3.2. The original Hubble diagram (distance against velocity) from that paper is shown in Fig. 3.1. Measuring the redshift of galaxies is done by observing galaxy spectra, finding recognisable transition lines in those spectra and comparing their wavelength to the expected value. In order to find the distance, we use so-called *standard candles* - bright objects for which we know the intrinsic luminosity based on some physical or observational arguments. In particular, Hubble used a class of standard candles known as Cepheid variables. These are stars that pulsate periodically, changing their luminosity in the process. There is a known relationship between the period and the luminosity, meaning that by observing the period of brightness change one can infer the star's intrinsic luminosity. From this, one can use the luminosity distance measure to establish the distance to that star. Hubble chose galaxies which contained such Cepheid variable stars in order to estimate their distance to Earth. Since his original paper, there

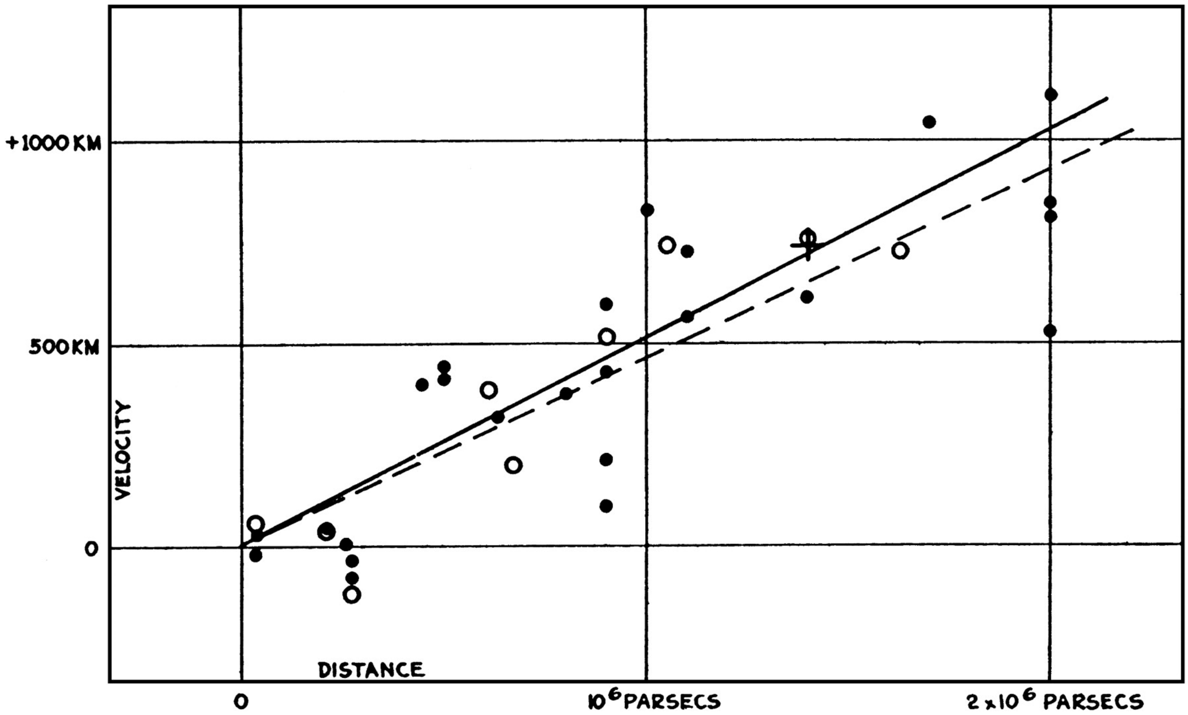

Figure 3.1: The original Hubble diagram, showing distance against velocity (with the original wrong units!). Taken from [7].

have been a multitude of further studies confirming Hubble's conclusion regarding the expansion of the universe, and the value of the Hubble constant is now determined at around the percent level, although as we will see in Section 3.3.2 results from different observations seem to disagree with each other.

3.1.2 Dark matter

We now turn our attention to a type of matter we have not encountered so far, and yet is incredibly important in our current understanding of the universe. When we look out to the sky, most of the light we observe originates directly from baryonic matter [1], either from planets, stars, galaxies or the interstellar gas medium. It would be reasonable to expect that most of the mass-energy in the universe comes from these, but an ever increasing amount of observational evidence tells us otherwise.

The first hints that there might be more than meets the eye in our universe came in the 1930's from Fritz Zwicky and Sinclair Smith [51]. They took observations of the Virgo cluster and estimated the total mass made up by all the galaxies inside it. Using the virial theorem, it was then possible to estimate the average velocity dispersion of galaxies inside the cluster, and compare it to the observed velocities. The results hinted that to obtain the correct velocity dispersion, one would need much more mass in the cluster than was observed. One hypothesis was that the cluster was full of extra matter that was not visible with telescopes - *dark matter*. However, the smoking gun for dark matter did not come until the 1970's. Vera Rubin and others observed anomalies in the rotation curves of galaxies [52]; given their luminosity, they could infer their masses using stellar mass estimates. From there, it was then possible to predict the rotation velocity as a function of their radii simply using Newtonian dynamics. The observations found that the galaxies were rotating too fast at large radii when compared to theoretical predictions, meaning that there must be extra gravitational matter located in galactic halos. This kind of matter is usually called dark matter (DM) due to the fact that it does not interact electromagnetically, and therefore cannot be detected by standard telescopes. The existence of cold dark matter – cold referring to it being non-relativistic – is now widely accepted in the scientific community as a key ingredient in the universe. Modern observations suggest that DM makes up around 30% of the total energy density in the universe today [8].

From a theoretical point of view, it is necessary to model CDM to integrate it within

---

[1] Strictly speaking, baryonic matter should only refer to things made up of protons and neutrons, but in cosmology this loosely refers to all atoms and ions, neglecting the mass contributions from electrons.

our general relativity, FLRW framework. In its simplest form, CDM can be thought of as a non-relativistic, non-interacting and therefore pressureless perfect fluid. This means the equation of state of CDM is simply $w = 0$, and it behaves exactly as standard baryonic matter on cosmological scales[2].

3.1.3 Dark energy and late-time acceleration

After the discovery of DM, estimates for the total energy density pointed at the fact that there did not seem to be enough matter in the universe to reach critical density (i.e. $\Omega < 1$). This meant that either the universe was open, or there was more CDM as yet undetected, or there was some other source of mass-energy in the universe causing it to be flat. This conundrum was resolved in 1998, when the Supernova Cosmology Project [53] and the High-Z Supernova Search team [54] independently presented groundbreaking observations suggesting that the universe was expanding in an accelerated fashion. They did this by observing type Ia supernovae (SN-Ia), which are standardisable candles. These supernova (SN) explosions peak at a specific luminosity which is believed to be the same for the whole star population. Since these objects are farther away than Cepheid variables, they probe the luminosity distance beyond the linear approximation described in Section 2.2.6. The luminosity distance in this case is approximately

$$d_L(z) = \frac{1+z}{H_0} \int_0^z \frac{dz'}{\sqrt{\Omega_m (1+z')^3 + \Omega_\Lambda}}, \tag{3.1}$$

where Ω_m and Ω_Λ are the fractional energy densities of matter and dark energy, respectively. This means it is possible to determine the relative abundance of matter (both dark and baryonic) and of a hypothetical cosmological constant[3].

These observations showed that far-away supernovae were fainter than expected in a matter-dominated (decelerating) universe, meaning the expansion of the universe must be accelerating. Indeed, [54] found that $\Omega_\Lambda > 0$ at over 3σ significance level, and a preference for a flat universe (when combining with CMB data). It can be seen from Eq. (2.34) that a universe dominated by a CC will be accelerating.

It is now widely accepted that the universe is currently dominated by a *dark energy* (DE) component which behaves like a cosmological constant, i.e. $p = -\rho$.

Type Ia supernovae surveys have continually progressed in the past 30 years or so,

---

[2] This is true at background level, however at linear perturbation level the non-gravitational interactions of baryons result in different dynamics to CDM.

[3] Here we have written the above equation in a convenient way, already assuming that a CC was the correct form of mass-energy to include.

and there are now several state of the art collaborations such as Pantheon+ [55], Dark Energy Survey (DES) [56] and Union3 [57]. The data from these allows one to constrain Ω_m in an independent fashion, assuming a flat universe with cosmological constant.

3.1.4 The cosmic microwave background

We now discuss the crown jewel of observational cosmology, the single observation which tells us the most about our universe. The cosmic microwave background (CMB) consists of relic radiation (i.e. photons) emitted around the time of recombination. Around $300,000$ years after the big bang, the scattering rate between photons and electrons became smaller than the expansion rate, leading to photons being free to travel and rendering the universe transparent (as opposed to its previous opaque stage due to the mean-free-path of photons being too small). Photons we observe today that were emitted at the time of decoupling are said to come from the spherical surface of last scattering. These highly energetic photons travelled through the expanding universe and lost energy to cosmological redshift, reaching us at a temperature of 2.726 K.

This remarkable feature was first observed by Wilson and Penzias in 1964 [58] by accident. They found an extra background noise in their radio antenna when pointing it at the sky. After eliminating any external sources of error, they realised that this corresponded to an isotropic signal in the radio frequency. It was suggested by Dicke, Peebles and Wilkinson [59] that this might be a remnant radiation from the big bang. Remarkably, the signal was the same in all directions, providing early evidence of isotropy in the universe. Later, in 1989, the COBE satellite was launched in order to observe the CMB without having to deal with atmospheric effects. COBE confirmed the original observation that the CMB was isotropic, and also showed its spectrum was that of a perfect (or as close as one can be) black-body radiation [60]. Its most significant discovery, however, was that there were actually small temperature anisotropies present in the CMB, at roughly one part in 10^5. Newer generations of CMB space satellites like WMAP [12] and the state of the art Planck [8], as well as ground based telescopes like ACT [10] and SPT [61] have since then pushed the precision with which the anisotropies are observed, allowing cosmologists to constrain model parameters with high precision (below percent level for H_0 with Planck).

The main observable for the CMB anisotropies is the temperature power spectrum, also called the TT power spectrum. We define the dimensionless temperature fluctuation as [62–64]

$$\Theta(\theta,\varphi) \equiv \frac{\delta T(\theta,\varphi)}{\langle T\rangle} \equiv \frac{T(\theta,\varphi)-\langle T\rangle}{\langle T\rangle}, \tag{3.2}$$

where θ is the polar angle, φ is the azimuthal angle, $\langle T\rangle$ is the average temperature over the whole sky, whilst $T(\theta,\varphi)$ is the temperature at any given point in the sky. Since the temperature fluctuations are defined on the surface of a sphere, it is common to expand these in spherical harmonics $Y_{lm}(\theta,\varphi)$:

$$\Theta(\theta,\varphi) = \sum_{l=0}^{\infty}\sum_{m=-l}^{l} a_{lm}Y_{lm}(\theta,\varphi), \tag{3.3}$$

where a_{lm} are the coefficients of the expansion. In order to extract information from the anisotropies, we will be interested in the correlation function, describing the average product of the temperature fluctuation for two points on the sphere separated by a given angle. In other words, this is a measure of the average temperature anisotropy for a certain scale in the CMB. We define the correlation function as

$$C^{TT}(\theta) = \big\langle\Theta(\hat{n})\Theta(\hat{n}')\big\rangle, \tag{3.4}$$

where $\hat{n},\hat{n}'$ are vectors from the observer to the last scattering surface such that $\cos\theta = \hat{n}\cdot\hat{n}'$, and the angle brackets denote averaging over all possible points separated by an angle θ. Due to angular resolution limitations, in practice it is impossible to obtain $C^{TT}(\theta)$ for all angles and it is again more convenient to expand into spherical harmonics:

$$C^{TT}(\theta) = \frac{1}{4\pi}\sum_{\ell=0}^{\infty}(2\ell+1)C_\ell^{TT}\mathcal{P}_\ell(\cos\theta), \tag{3.5}$$

where C_ℓ are the multipole moments and $\mathcal{P}_\ell$ are the Legendre polynomials. It can be shown that the following relation holds:

$$\langle a_{\ell m}a^*_{\ell' m'}\rangle = \delta_{\ell\ell'}\delta_{mm'}C_\ell. \tag{3.6}$$

It is possible to invert Eq. (3.3) to obtain an explicit form for $a_{\ell m}$. From there, the C_ℓ^{TT} coefficients can be written as:

$$C_\ell^{TT} = \frac{2}{\pi}\int_0^\infty dk\, k^2|\Theta_\ell(k)|^2, \tag{3.7}$$

where we have defined $\Theta_\ell(k)$ as

$$\Theta_\ell(k) \equiv \frac{1}{(-i)^\ell} \int_{-1}^{1} \frac{d\mu}{2} \mathcal{P}_\ell(\mu)\Theta(k,\mu) \tag{3.8}$$

In the above equation, $\Theta(k,\mu)$ is the Fourier transform of $\Theta(\theta,\varphi)$ and $\mu = \hat{k}\cdot\hat{p}$ where $\hat{k}$ is the normalised photon wavenumber and $\hat{p}$ is the direction of propagation of the photon. Finally, it is conventional to define the following quantity when plotting the CMB power spectrum:

$$D_\ell^{TT} \equiv \frac{\ell(\ell+1)}{2\pi} C_\ell^{TT}. \tag{3.9}$$

From a theoretical point of view, we want to compute the C_ℓ^{TT} coefficients for a given cosmological model, varying its parameters and comparing these results with the observed power spectrum. There are two important aspects to consider when computing the value of Θ_ℓ today. First, the initial conditions of the perturbations are set by inflation (see more in Section 3.2.1). Second, the evolution of the photon perturbations, as they travel from the surface of last scattering to present day, depends on the other perturbed quantities in the universe. Indeed, the photons' energy will change as they travel through gravitational wells, and so the path they take influences their final state. In order to model these effects, we adopt the line-of-sight integral approach [65] which expresses $\Theta_\ell(k,\eta_0)$ as

$$\Theta_\ell(k,\eta_0) = \int_0^{\eta_0} d\eta\, S(k,\eta) j_\ell[k(\eta_0-\eta)], \tag{3.10}$$

where we denote conformal time as η for the rest of this discussion and η_0 is the conformal time today. The j_ℓ are spherical Bessel functions, and $S(k,\eta)$ is the so-called *source function*:

$$S(k,\eta) \approx g(\eta)[\Theta_0(k,\eta)+\Psi(k,\eta)] + \frac{i}{k}[v_b(k,\eta)g(\eta)]' + e^{-\tau}[\Psi'(k,\eta)-\Phi'(k,\eta)], \tag{3.11}$$

where Θ_0 is the temperature monopole and v_b is the baryon peculiar velocity. In the above equation we have ignored small polarisation effects and defined the optical depth τ:

$$\tau(\eta) \equiv \int_\eta^{\eta_0} d\eta'\, n_e \sigma_T a, \tag{3.12}$$

where n_e is the electron number density and σ_T is the Compton scattering cross section, as well as the visibility function $g(\eta)$:

$$g(\eta) \equiv -\tau'(\eta)e^{-\tau(\eta)}. \tag{3.13}$$

The optical depth is a measure of the line-of-sight opacity of the free electrons for CMB photons. In other words, τ is large when the free electron density is high and the photons scatter off them at a high rate, causing photon perturbations to wash out. This is the case at early times before recombination. The visibility function models the probability density of a photon to have been last scattered at conformal time η. This function is sharply peaked around recombination, although it can also tell us about reionisation[4] in the form of a second peak [66, 67]. Indeed, after reionisation photons can scatter off electrons again, which can reduce the perturbations at late-times. We now describe the physical interpretation of each term in the source function, Eq. (3.11):

- The first term is the so-called *Sachs-Wolfe* effect. This term represents the extra perturbation from the gravitational potential: At recombination, photons inside a gravitational well will have to climb out, losing energy to redshift. This term is therefore an effective temperature anisotropy due to inhomogeneities in the gravitational potential at recombination. Due to the visibility function multiplying it, this is only relevant around recombination and so these give an indication of the perturbations that froze in after last scattering.

- The second term is a Doppler effect due to the baryon velocity v_b, which are tightly coupled to the CMB photons before decoupling.

- The third term is the *integrated Sachs-Wolfe* (ISW) effect. This takes into account the dynamical nature of the gravitational potentials as photons travel through them to reach observers on Earth. It is a post-recombination effect which encompasses the late-time evolution of perturbations in the universe.

So far we have focused on the temperature power spectrum C_ℓ^{TT}, however there is more information in the CMB still. Photons exhibit polarisation, and this polarisation changes when interacting with electrons via Compton scattering. This means that recombination may leave a net polarisation imprint on CMB photons. There are two types of polarisation modes: E-modes are due to scalar perturbations and are about 10 times smaller in magnitude than temperature anisotropies. B-mode polarisation is mainly created by gravitational waves, so is a tensor perturbation effect. These create a much smaller signal that has not been detected yet[5]. The E-modes produce a pattern of anisotropies that can be observed from the CMB and turned into a power spectrum

---

[4] See Section 3.2.1 for a description of recombination and reionisation.

[5] Although they were thought to have been discovered by the BICEP collaboration [68] in 2014, the conclusion was ruled out and explained by foreground effects [69].

C_ℓ^{EE}. Taking cross correlations between temperature and polarisation anisotropies yields the C_ℓ^{TE} spectrum.

As photons travel from the last scattering surface to reach us, massive objects along their path will deviate their trajectories according to gravitational lensing. This means that large scale structure (LSS) affects the CMB anisotropies. It is possible to obtain a lensing map from the temperature and polarisation maps by comparing the size of specific hot and cold spots to the average. This creates a new observable, the lensing spectrum $C_\ell^{\phi\phi}$ which provides additional information about the late universe. All spectra discussed in this section are shown from Planck in Fig. 3.2.

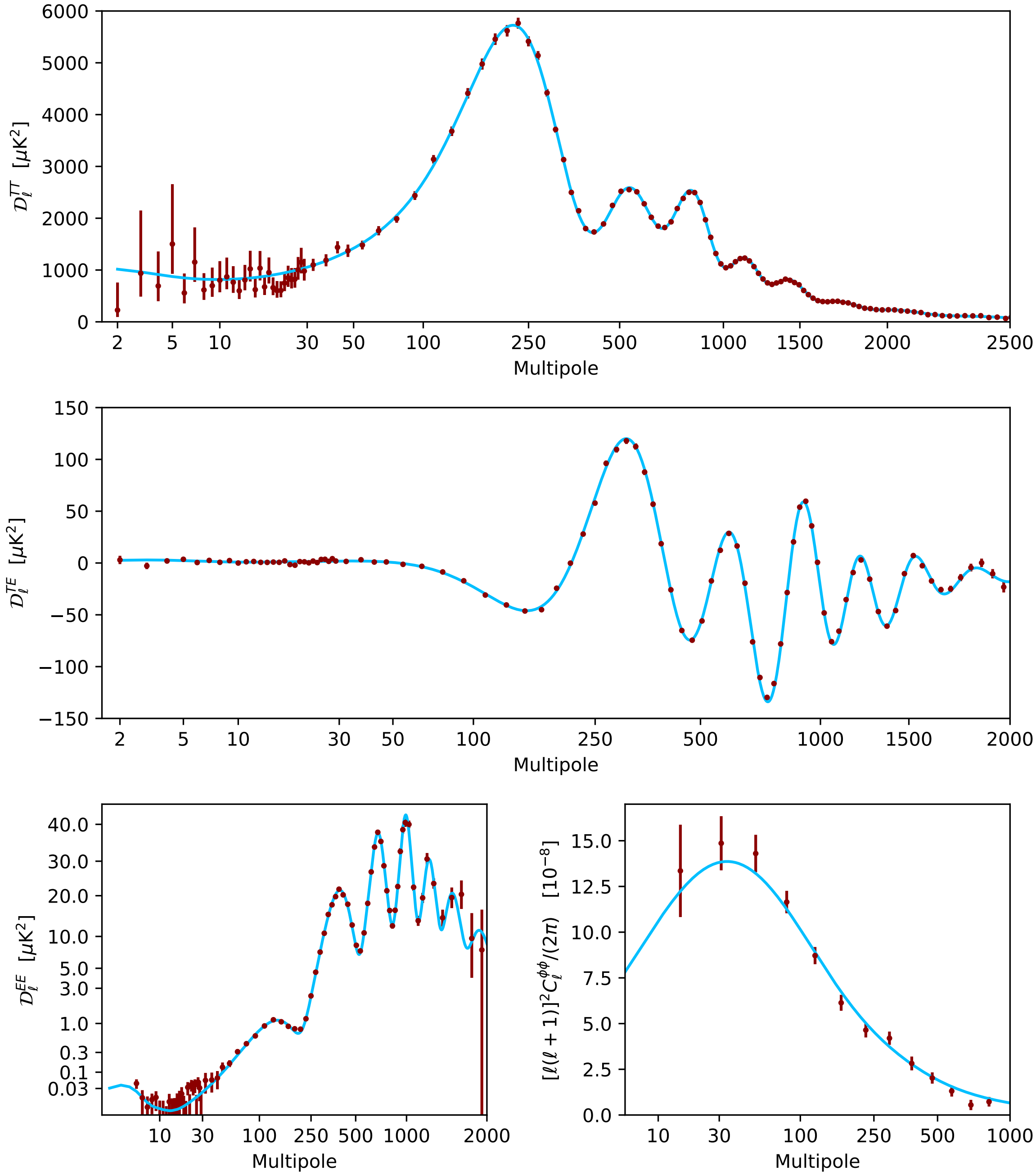

Figure 3.2: Figure showing all Planck power spectra from the 2018 data release, including the observed data points for the TT, TE, EE and lensing spectra, as well as the ΛCDM best fit model in solid blue. Taken from `https://www.cosmos.esa.int/web/planck/picture-gallery` [8].

3.1.5 Baryonic acoustic oscillations

Before recombination, the universe was made up of a hot baryon-photon plasma. Gravity drove baryons to cluster together, but radiation pressure forced them outwards. The interplay of these two forces created acoustic waves that travelled from overdensities and expanded outward in the plasma. These waves are akin to sound waves, and have a sound speed c_s that can be expressed as [64, 70]

$$c_s = \frac{1}{\sqrt{3\left(1 + \frac{3\rho_b}{4\rho_\gamma}\right)}}, \tag{3.14}$$

where ρ_b is the baryon energy density and ρ_γ is the photon energy density. After recombination and decoupling, baryons no longer interact with photons at a high enough rate to be tightly coupled - the name for this period is the drag epoch. At this point, the acoustic oscillations freeze and imprint a specific pattern of perturbations. There is a preferred scale separating overdensities corresponding to the comoving distance a sound wave could have travelled by the time of decoupling. This quantity is known as the sound horizon r_s:

$$r_s(z) = \int_z^\infty \frac{c_s(z')}{H(z')} dz'. \tag{3.15}$$

This physical phenomenon leaves an imprint in the CMB photons in the form of the relative amplitudes of the peaks in the C_ℓ^{TT}'s. It also follows that the baryon perturbations should be imprinted by the baryon acoustic oscillations (BAO). Since baryons interact through gravity with CDM, the overdensities left over by BAO end up accruing DM, which means later down the line cosmological structure. The upshot is that BAO predicts galaxies to be more correlated on the sound horizon scale.

In practice there are two possible measurements when observing galaxy distributions. One might observe a strong correlation in the transverse direction, meaning in terms of angular separation. In this case what is measured is the angular separation $\theta_s(z)$ at a particular redshift

$$\theta_s(z) \equiv \frac{r_s(z_{\rm drag})}{d_M(z)}, \tag{3.16}$$

where we have defined the comoving angular diameter distance $d_M(z) \equiv (1+z)d_A(z)$ and the sound horizon is evaluated at the drag epoch [71–73]. If the correlation is in the line-of-sight direction, the relevant observable is the redshift separation $\Delta z_s(z)$:

$$\Delta z_s(z) \equiv \frac{r_s(z_{\rm drag})}{d_H(z)} \tag{3.17}$$

where we defined $d_H(z) \equiv 1/H(z)$ in natural units. In other words the preferred redshift separation imprinted by BAO probes the Hubble parameter. There is a final distance measure that is also used in BAO experiments: for observations with low signal-to-noise ratio, it is common to combine d_M and d_H to obtain a spherically angle-averaged distance d_V:

$$d_V(z) \equiv (d_M^2 d_H)^{1/3}. \tag{3.18}$$

BAO observations such as SDSS [6] and DESI [13] use the statistics of galaxy distributions to determine θ_s and Δz_s. By calibrating r_s from the Planck CMB observations or big bang nucleosynthesis (BBN) observations [74], it is therefore possible to constrain d_M, d_H and d_V, which tell us much about the evolution of our universe - especially constraining Ω_m and H_0.

3.1.6 The matter power spectrum

We can define a similar quantity to the CMB power spectra in terms of the matter fluctuations. Indeed, we have seen in Section 2.3 that the matter perturbations are important due to their influence on the evolution of the gravitational potentials. The amplitude of the density contrast is directly related to the observed clustering of large scale structure. One way to measure clustering is by observing the two-point correlation function for galaxies. Physically, it can be thought of as the probability of a galaxy being found a distance $|\mathbf{x} - \mathbf{x}'|$ from a given galaxy located at $\mathbf{x}'$ [75]. The two-point function is defined as [45]:

$$\xi(|\mathbf{x} - \mathbf{x}'|) \equiv \langle \delta(\mathbf{x}) \delta(\mathbf{x}') \rangle, \tag{3.19}$$

where $\delta(\mathbf{x})$ is the three-dimensional Dirac delta function. In Fourier space, the two-point function is

$$\langle \delta(\mathbf{k}) \delta(\mathbf{k}') \rangle \equiv (2\pi)^3 \delta(\mathbf{k} - \mathbf{k}') \mathcal{P}(k), \tag{3.20}$$

where $\mathcal{P}(k)$ is the matter power spectrum which can be defined through $\xi(r)$ as

$$\mathcal{P}(k) = \frac{4\pi}{k} \int_0^\infty dr \; r \sin{(kr)} \xi(r). \tag{3.21}$$

In essence, the matter power spectrum is the Fourier transform of the two-point correlation function. A higher value of the power spectrum corresponds to more clustering at a given scale k.

Schematically, the power spectrum behaves in the following way [45]:

$$\mathcal{P}(k) \propto \begin{cases} k^{n_s} \text{ for } k < k_{eq} \\ k^{n_s - 4} \text{ for } k > k_{eq}, \end{cases} \tag{3.22}$$

where the spectral index n_s is a dimensional quantity close to one[6] and $k_{eq} \equiv a_{eq} H_{eq}$ is the wave-number of modes which enter the horizon at matter-radiation equality.

3.2 Towards a standard model of cosmology

We now put all the previous sections together and introduce the accepted standard model of cosmology, describing the history of our universe.

3.2.1 A brief history of our universe

Following the observations described in Section 3.1, we know that the universe is expanding. We have developed a mathematical framework to describe how this evolution behaves, characterised by the scale factor $a(t)$. It is straightforward to see that as $t \to 0$ and $a \to 0$, $\rho \to \infty$. This implies a singularity in the energy density as the scale factor goes to 0. Applying the laws of thermodynamics to an expanding universe, it can be shown that the photon temperature goes as $T \propto a^{-1}$, which also implies that the temperature diverges at early times. These findings lead to the natural conclusion that the universe started from an initial singularity with a small scale factor, high temperature and high energy density. From there, it expanded and cooled down eventually reaching the stage that we find ourselves in. This is the *hot big bang* theory. We will now describe the evolution of the universe [48, 76] since the big bang, which we will take as its starting point.

The early universe and inflation

We know little of the very first instants of the universe, and a complete understanding would require a fully fledged theory of quantum gravity due to interactions taking place at very small scales and high energies during this epoch. However, we know that at some

---

[6] See Section 3.2.2 for more details on n_s.

point in the early universe the temperature dropped enough for the electroweak force to no longer be unified with the strong force. Around this time, before around 10^{-36}s (or about 10^{16}GeV in terms of energy scales) after the big bang, the universe enters an inflationary epoch. This is a period of quasi[7] de Sitter expansion, i.e. exponential accelerated growth similar to the late-time dark energy epoch. Such an epoch is needed to address two theoretical problems present in the standard evolution history of the universe:

1. The flatness problem states roughly that if the universe is close to being flat today, it had to have been even closer to flat in the past. Consider Eq. (2.40) and set the current universe to be close to but not quite flat – say, $|1-\Omega_0| < 10^{-1}$. Propagating the equations backwards in time through matter and radiation domination leads to the fact that at early times, the quantity $|1-\Omega(t)|$ would have had to be much, much smaller. Plugging in the numbers, at around the Planck time $t \approx 5 \times 10^{-44}$s we would need the universe to be flat at around 1 part in 10^{60}. This amount of fine-tuning is not attractive from a theoretical point of view, and so prompted cosmologists to look for a solution.

2. The horizon problem stems from the observation that the universe is homogeneous and isotropic on large scales. This leads to the problem that two points on the celestial sphere might be separated by a distance greater than the horizon distance, meaning they would have never been in causal contact. This problem is glaring in the CMB, where points separated by more than about 2° would have not have been in causal contact at the time of recombination. It seems unlikely that the CMB could be uniform up to 10^{-5}K when most parts of it were never in causal contact.

The inflation solution, first proposed by Alan Guth in 1981 [77] solves both problems: the accelerated period of expansion drives the universe to flatness, regardless of initial condition, and increases the size of the horizon exponentially since H stays constant but a increases by several orders of magnitude (a might grow between 20 and 30 orders of magnitude, depending on the specific inflation model).

The physics of inflation are often described by a slow rolling scalar field (see Chapter 4). Remarkably, due to the rapid growth of the universe, quantum fluctuations of this field get blown up to macroscopic scales during inflation and provide the seeds for the

---

[7] It is only 'quasi' de Sitter because this period needs to end for our universe to develop into what we know.

inhomogeneities at recombination observed in the CMB (see Section 3.1.4). In this sense, we say that inflation sets the initial conditions for perturbations in the universe. After inflation, the inflaton field eventually decays into standard model particles, transferring its energy to relativistic particles. This process is called reheating [78] and starts the radiation domination epoch.

Radiation domination

After inflation finishes, radiation becomes the dominant form of energy-density, made up of photons as well as relativistic particles. Around 150 GeV ($\sim 10^{-12}$ s), the electroweak phase transition takes place, leaving the weak force and the electromagnetic force separate, and particles acquire mass via the Higgs mechanism. At this point, the universe is made up of a quark-gluon plasma, as the energies are too high for hadrons (made up of quarks in a bound state) to form.

After around 1 to 10 s, at an energy scale of around 1-10 MeV, big bang nucleosynthesis starts to take place. This means free protons and neutron bind together into nuclei for the first time, mainly forming into hydrogen and helium-4.

Matter domination

Matter-radiation equality, the epoch when the energy density of radiation decayed enough to match that of matter, happens after around 10^4 years, or a redshift of $z \sim 10^4$.

The universe remains a plasma of photons, nuclei and electrons until around $300,000$ years after the Big Bang, at a temperature of around 3000K. At this point, the temperature has become low enough for nuclei and electrons to form atoms. This is recombination. Shortly after this, as the universe becomes less and less ionised (since most of the free electrons pair up with nuclei), the interaction rate between photons and electrons drops until the photons become free streaming. This is decoupling. Before this, the universe was effectively opaque as the mean-free-path of photons was very short due to high interactions. Photons which became free after decoupling make up the CMB radiation.

After recombination, a long time goes before the formation of stars, and not much is known about this era. Recent observations have revealed the oldest known galaxy has a redshift of about $z \sim 14$ [79], which would make it almost 300 million years old. From then on, reionisation takes place, during which the mostly neutral atoms in the universe become ions once more. Structure continues to form into what we observe today.

Dark energy domination

The final step in our universe's history is the start of dark energy domination, beginning the accelerated expansion of the universe. Whilst this seems like a recent occurrence in terms of redshift, $z \sim 0.4$ or less, in cosmic time this happened a whopping 10 billion years after the start of the universe. This is also roughly when our solar system formed. The universe today is believed to be about 13.8 billion years old.

3.2.2 The ΛCDM model

We can now finally formulate the standard model of cosmology, which has been established since the start of the century, and is built on all the previously mentioned observational evidence, as well as theoretical breakthroughs.

The ΛCDM model can be summarised thus:

- The theoretical cornerstone of the standard model is Einstein's general relativity, coupled with the cosmological principle. This leads, as we saw, to the FLRW metric, the linear perturbations of which can explain the anisotropies in the CMB.
- A period of inflation in the early universe is required to solve the horizon and flatness problems, as well as set the initial conditions for the perturbations.
- The universe is populated with relativistic species like photons and neutrinos [8] – the sum of all neutrino species masses is taken to be $\sum m_\nu = 0.06$eV – as well as ordinary baryonic matter such as protons and neutrons.
- A cold dark matter component – the 'CDM' in ΛCDM – is present in the universe, modelled as pressureless dust.
- Dark energy is modelled as a cosmological constant Λ, i.e. a perfect fluid with equation of state $w = -1$.

The ΛCDM model can be characterised by 6 parameters only, and these are constrained using cosmological data[9]:

$\boldsymbol{\Omega_c h^2}$ parametrises the CDM energy density in the universe, where $h = H_0/(100\,\mathrm{km\,s^{-1}\,Mpc^{-1}})$.

$\boldsymbol{\Omega_b h^2}$ parametrises the energy density of baryons.

---

[8] Strictly speaking neutrinos are only relativistic in the early universe since they are massive.

[9] See Appendix A for more details.

$\boldsymbol{\theta_s(z_*)}$ is the angular scale of the sound horizon, $\theta_s(z_*) = r_s(z_*)/d_M(z_*)$, where z_* is the redshift at recombination. This is well constrained by the acoustic peaks in the CMB, and through its dependence on angular distance constrains the fractional energy density of the curvature of the universe Ω_k.

$\boldsymbol{\tau_{\mathrm{reio}}}$ is the optical depth to reionisation. It provides insight on when reionisation took place. A higher τ_{reio} yields to a suppression of anisotropies on small scales $\ell \gtrsim 100$ since photons scatter off electrons more, smoothing out anisotropies.

$\boldsymbol{A_s}$ is the square of the typical curvature perturbations generated during inflation. It also governs the amplitude of the C_ℓ^{TT}'s.

$\boldsymbol{n_s}$ is the spectral index of primordial perturbations. It describes how primordial perturbations depend on scale k, and how C_ℓ^{TT} behaves at small-scale.

Table 3.1 shows the best fit values for the ΛCDM parameters from the Planck CMB data.

Parameter	Best-fit value
$\Omega_c h^2$	0.1198 ± 0.0012
$\Omega_b h^2$	0.02233 ± 0.00015
$100\theta_s$	1.04108 ± 0.00031
τ_{rei}	0.0540 ± 0.0074
$\log(10^{10} A_s)$	3.043 ± 0.014
n_s	0.9652 ± 0.0042

Table 3.1: ΛCDM parameter constraints from Planck18, using the combined `Plik` and `CamSpec` likelihoods [8].

Overall, the ΛCDM model is a great triumph for cosmology, as it is able to successfully explain observations from BBN, the CMB, all the way to large-scale structure and the late time acceleration of our universe.

3.3 Limitations of ΛCDM

Despite its ability to describe a wide range of cosmological observations, the ΛCDM model is not without its challenges. Theoretical concerns and observational discrepancies have emerged, prompting ongoing debate and further research exploration. Some of these stem from the fundamental assumptions of the model, while others arise from tensions between different measurements of key cosmological parameters. Understanding these limitations is essential to determining whether ΛCDM needs to simply be improved upon (with, say, a more robust theoretical foundation) or if entirely new physics might be required to fully explain the universe.

3.3.1 Theoretical issues

Whilst ΛCDM provides a strong framework, it only prescribes the contents of the universe in a superficial way, with no explanation for their origin. To this day, the nature of dark matter and dark energy remain an open problem in cosmology, along with the very first instants of the universe.

The cosmological constant

First, the so-called cosmological constant problem highlights the theoretical difficulty of justifying the observed value of Λ. Current observations indicate that the energy density contributed by the cosmological constant is very small [8], $\rho_\Lambda \approx 10^{-47}\,\mathrm{GeV}^4$. On the other hand, we know from quantum field theory (QFT) that vacuum fluctuations of fields create a zero-point energy which should contribute to the cosmological constant. However, theoretical calculations of the vacuum energy from QFT yield results that are over a 100 orders of magnitude too large[10] [80]! This is a serious fundamental problem that has so far not been resolved (and that we will not try to resolve in this work). Attempts to address the cosmological constant problem include supersymmetry, which predicts the vacuum energy to be zero through a cancellation of terms between fermions and bosons [81]. However, we do not observe supersymmetry at our energy scales which means that it must be broken (if it was there in the first place) at low energies, leading to a non-zero cosmological constant once more.

Another issue related to Λ is the so-called cosmological coincidence problem. This can essentially be stated by asking the question ‘Why now?’; we currently live in an era when the energy density of matter is of the same order of magnitude as that of the cosmological constant [82]. We know that this was not the case for most of the universe’s history, and that this therefore requires a high degree of fine tuning in the initial conditions. One possible solution is to employ anthropic arguments [83] – to say that, somehow, this situation is most ‘likely’ given that we can observe it.

---

[10] One might argue that such a calculation should only be valid when worked through from a fundamental theory of quantum gravity rather than QFT.

The two problems discussed above hint at the fact that the origin of dark energy might be dynamical, instead of simply emerging from a cosmological constant. Indeed, if there is a fundamental cancellation that solves the cosmological constant problem, dark energy has to emerge from a different theoretical mechanism. Moreover, if DE is dynamical, there could be a mechanism explaining the coincidence of density ratios. One way to obtain such suitable solutions is by modifying the gravitational sector of the theory [84], that is to alter the Einstein field equations which dictate the dynamics of the universe. We will focus on a class of alternative methods which postulate the existence of a new kind of matter in the universe called quintessence [85]. As we will see in more detail in Section 4.1.2, this consists of a scalar field slowly rolling along its potential with a time-varying equation of state, meaning that it does not necessarily behave like a cosmological constant outside of the current era.

Cold Dark Matter

While ΛCDM requires the existence of cold dark matter, it does not specify its fundamental nature. Indeed, the pressureless fluid approximation does not describe the microscopic physics that may explain DM. There are DM candidates at virtually all mass scales, ranging from ultra light particles to primordial black holes [86], but most models rely on the presence of a DM fermionic particle which interacts mainly gravitationally. The most widely studied scenario is that of Weakly Interacting Massive Particles (WIMPs) [87] which have been the subject of many experimental detection attempts, both directly or indirectly. Another popular class of candidates are the axions, or axion-like particles (ALPs). These are pseudo-scalar particles which are generally very light, weakly interacting and couple to the electromagnetic sector. Axions were originally introduced as a solution to the strong CP problem in quantum chromodynamics (QCD) [88], but have since been studied extensively in a cosmological setting [89] after it was proposed that CDM could be explained by considering light bosons [90]. In this case, the DM is a bosonic wave-like state (also sometimes called fuzzy) that behaves like one would expect CDM to on large scales. In this work, we will consider a generalisation of the axion model and simply consider scalar-field dark matter.

Early universe

It is standard to consider ΛCDM to include some mechanism for inflation, in order to solve the flatness and horizon problems as well as set the initial conditions for the CMB. There is no single prescription for this however, and there are many inflationary models, from modified gravity to multi-scalar field models [91]. Unfortunately, it is not clear whether observations will ever be able to narrow down the possibilities to just one model [92, 93].

Going back even further than inflation, we have seen in Section 2.2.5 that the FLRW metric leads to a singularity at $t = 0$. Modifications to the standard expansion history have been proposed to avoid the singularity by adding a period of contraction prior to the big bang, leading to a *big bounce* instead [94]. In these scenarios, the scale factor never reaches 0 thus avoiding the singularity. Another avenue is that taken by quantum gravity. Indeed, it is reasonable to expect quantum effects to take over when the universe is sufficiently small and highly energetic, at which point the GR description breaks down. Whilst much research has been conducted in this field, it seems we are not currently close to reaching a consensus or a complete description of quantum gravity [95].

3.3.2 Cosmological tensions

High-precision observations have revealed inconsistencies in key cosmological measurements, such as the Hubble constant and the distribution of matter. These discrepancies challenge the internal consistency of ΛCDM and may indicate the need for new physics, unless they are caused by systematics.

The Hubble tension

Measuring the expansion rate today H_0 has been a main aim of modern cosmology ever since Hubble's first observations mentioned in Section 3.1.1. Since then, the precision with which we can determine H_0 has increased manifold, down to around the percent level [8]. There are two main ways to obtain H_0 from measurements: one follows Hubble's original method, using standard candles to fit Hubble's law, and the other takes advantage of the CMB observations to statistically determine the best fit H_0. The former method is a local measurement dependent on astrophysical physical assumptions, whilst the latter is an early-time measurement which depends on the cosmological model assumed (in this case ΛCDM). The Hubble tension can be summarised as the fact that the late-time standard candle measurements of H_0 disagree with the early time CMB value by more than 5σ [14]. This is indeed a problem, as one would expect these values to agree regardless of what data they are extracted from, considering H_0 is a constant. Before describing possible explanations or solutions for the Hubble tension, let us first describe how the H_0 measurements are made in the first place.

The state of the art for determining H_0 from local probes is the so-called cosmic distance ladder method. The idea is to build a robust Hubble diagram using different standard candles. The first 'rung' of the ladder is built using geometric measurements. The distance to close bright objects can be determined using parallax. These measurements are then used to calibrate the luminosity of Cepheid variables, which form the second rung of the ladder. These are used up to distances of 10-40 Mpc. The third rung of the ladder consists of type Ia supernovae. These are calibrated using Cepheid variables in the same host galaxies, at low redshift. Once calibrated, it is possible to use further away SN-Ia in the Hubble flow and get a good estimate of the Hubble constant. Each rung yields an absolute magnitude M used to calibrate the next rung. This absolute magnitude is related to the luminosity distance in Mpc via

$$m - M = 5 \log d_L \,[\mathrm{Mpc}] + 25, \tag{3.23}$$

where m is the apparent magnitude, which measures an object's brightness reverse logarithmically and d_L was defined in Section 2.2.6. The distance ladder is illustrated in Fig. 3.3.

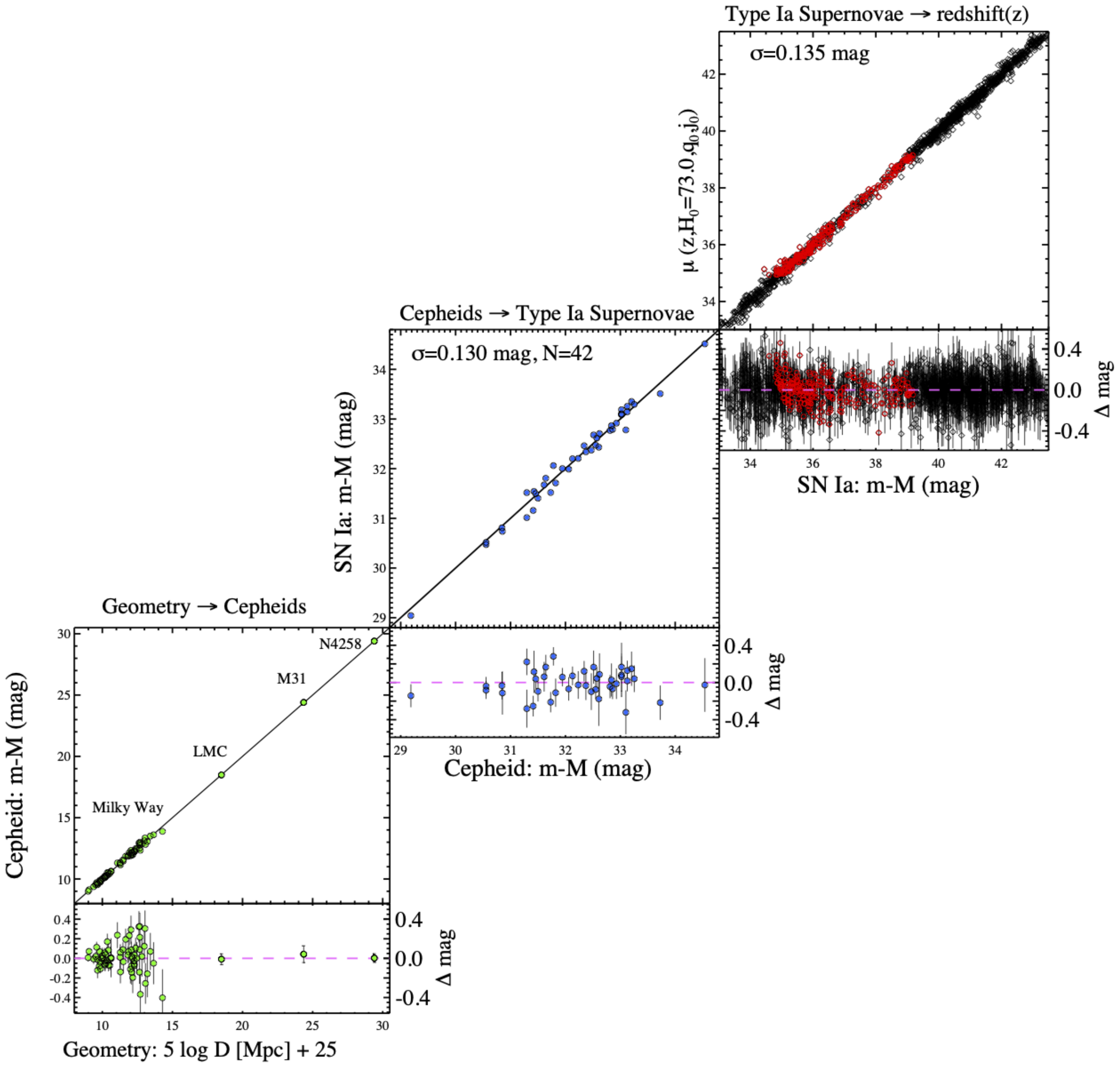

Figure 3.3: The cosmic distance ladder, from [9]. Each rung is shown, along with magnitude residuals – i.e. deviations from the straight line relationship of Eq. (3.23).

The current best estimate for the Hubble constant from local measurements comes from the SH0ES collaboration, which report a value of $H_0 = 73.04 \pm 1.04$ km s^{-1} Mpc^{-1} [14]. It is important to note that there are other methods used to construct the distance ladder. In particular, the Chicago-Carnegie Hubble Program (CCHP) collaboration use tip of the red giant branch (TRGB) stars to calibrate the SN-Ia instead of Cepheids. Their latest reported value[11] is $H_0 = 69.96 \pm 2.17$ km s^{-1} Mpc^{-1} [16].

We have seen in Section 3.1.4 that the CMB is an incredibly powerful measurement

---

[11] Note this paper [15] by the SH0ES collaboration which claims that the lower H_0 value reported by CCHP is due to a selection effect from using a smaller supernovae sample.

when it comes to constraining our cosmology. Remarkably, even though the CMB was emitted at recombination, it still contains information about the path the photons took to reach us, and therefore can tell us about the rate of expansion today. To do this, however, one must provide a cosmological model. Indeed, a specific cosmological model will predict power spectra for a given set of parameters, and these power spectra can be compared to the observed data points. The best-fit parameters then tell us about the cosmology of our universe, including H_0. The best-fit value obtained by the final Planck data release is $H_0 = 67.27 \pm 0.6$ km s^{-1} Mpc^{-1} [8], which is in over 5σ tension with the SH0ES result. It is also possible to use other CMB observations such as ACT, SPT and WMAP, as well as BAO observations calibrated with BBN in order to constrain H_0. All these early-time probes are in various levels of tension with the late-time observations. A summary of the different values of the Hubble constant is provided in Fig. 3.4.

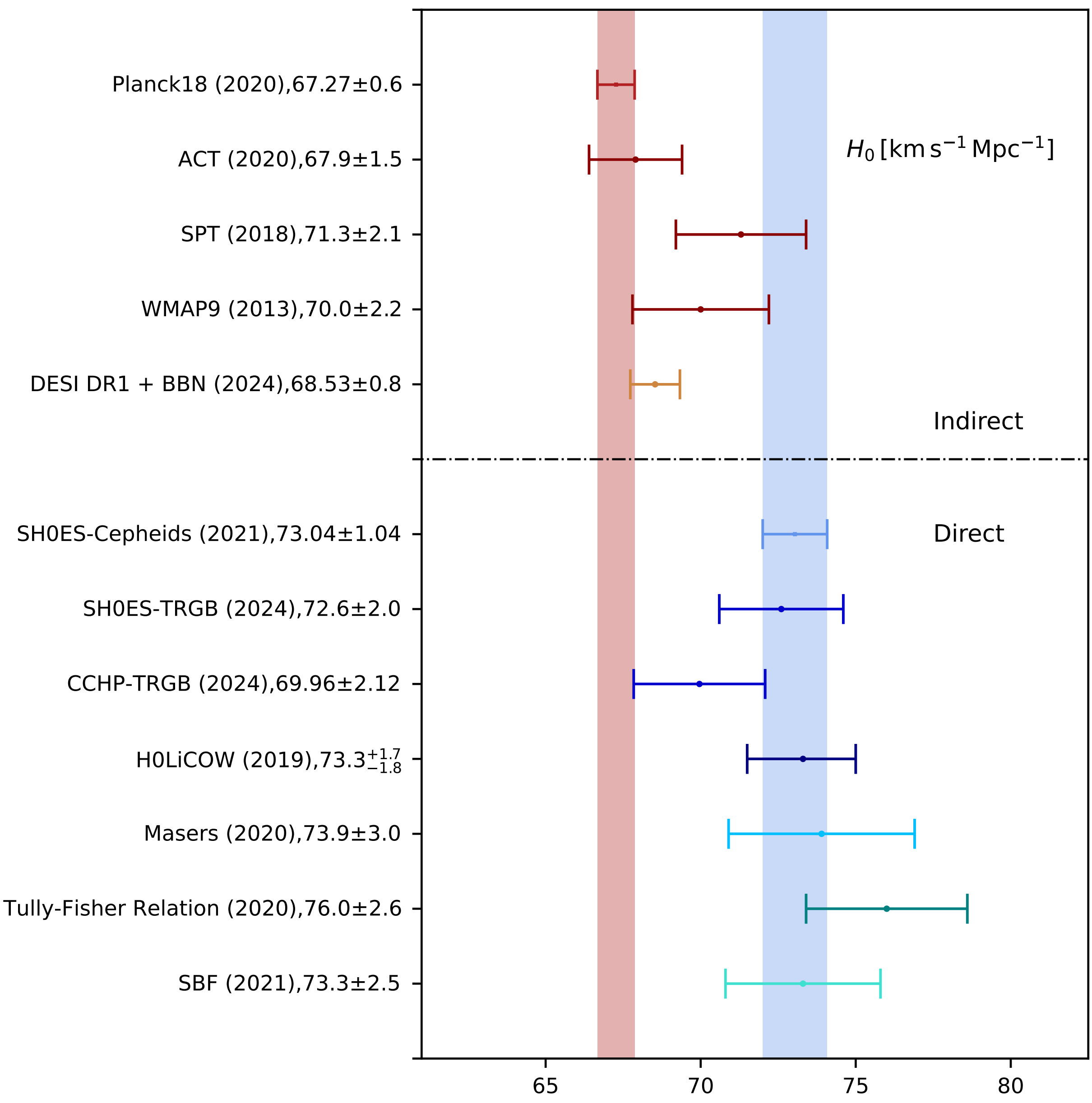

Figure 3.4: Whisker plot showing different observed values of the Hubble constant. The red band corresponds to the Planck 2018 best-fit value, while the blue band is the SH0ES measurement. The values are taken in order from [8, 10–20]. SBF stands for Surface Brightness Fluctuation. This figure was produced using code provided in [21].

Two main possibilities arise when trying to explain the source of the tension. First, there might be some unaccounted for systematic errors in the data, coming from either Planck or late-time observations, be it from the actual observation or from the astrophysics assumptions (in the late-time case) made to arrive at the result. Many discussions have been made on this topic, and both sides (Planck and SH0ES) claim to have a strong handle on systematics [21]. The only remaining option, and perhaps most interesting one, is that ΛCDM might not be the best way to describe our universe. Indeed, since H_0 from Planck is model-dependent, one can imagine modifying ΛCDM in order to obtain a higher value. This is currently a strong driving force in theoretical cosmology, where a lot of model building is now motivated by the need to solve the Hubble tension.

Broadly the proposed solutions – none of which fully satisfactorily solve the tension at the time of writing – can be divided into two categories: early-time and late-time solutions. The idea behind early-time solutions is to modify physics around the recombination era in order to affect the CMB. The angular scale of the sound horizon $\theta_s(z_*)$ is tightly constrained by the CMB, and so the sound horizon $r_s(z_*)$ is free to change as long as the comoving angular distance d_M changes accordingly too. Since $r_s \sim 1/H(z_*)$ from Eq. (3.15) and $d_M \sim 1/H_0$, it is in principle possible to increase H_0 to its SH0ES value by decreasing the sound horizon at last scattering [96]. Such models include early dark energy [97], modified radiation contents (N_{eff}) [98] and modified recombination (such as time-varying electron mass) [99]. Late-time solutions modify the expansion history of the universe post recombination, by introducing a dynamical DE component, introducing new interactions [100] or modifying gravity (see [101] and references therein). For extensive reviews of possible solutions to the Hubble tension, see [21, 102].

The S_8 tension

The S_8 tension is another inconsistency between the CMB and late-time probes, concerning the amount of clustering in the universe. Formally, the S_8 parameter is defined as

$$S_8 \equiv \sigma_8 \sqrt{\frac{\Omega_m}{0.3}}, \tag{3.24}$$

where we have introduced σ_8, the root mean squared matter density fluctuation in a sphere of comoving radius $R = 8h^{-1}$ Mpc [64]:

$$\sigma_8 \equiv \langle \delta^2_{m,8}(\mathbf{x}) \rangle. \tag{3.25}$$

In the above,

$$\delta_{m,8}(\mathbf{x}) \equiv \int d^3x' \delta_m(\mathbf{x'}) W_8(|\mathbf{x} - \mathbf{x'}|) \tag{3.26}$$

where $W_8(x)$ is the following top-hat function :

$$W_8(x) = \begin{cases} 3/(4\pi R^3) \text{ if } x < R \\ 0 \text{ otherwise,} \end{cases} \tag{3.27}$$

for $R = 8h^{-1}$ Mpc. The σ_8 parameter also describes the amplitude of the matter power spectrum at scales of $8h^{-1}$ Mpc.

Low redshift measurements of S_8 are obtained by studying gravitational weak lensing or redshift-space galaxy clustering [103]. The former uses the lensing of distant galaxies by foreground matter to estimate the amount of structure in the universe. The latter uses the galaxy power spectrum to infer σ_8 and Ω_m and therefore S_8.

On the other hand, S_8 can also be estimated from the CMB by similar methods to the H_0 measurements. Values of S_8 obtained from CMB experiments seem in $2-3\sigma$ tension compared to low-redshift measurements which prefer lower values of S_8 [104]. It is important to note that both CMB and late-time measurements are cosmological model-dependent, and so the values quoted are for ΛCDM only. Fig. 3.5 shows a selection of S_8 measurements, highlighting the tension between early and late-time probes.

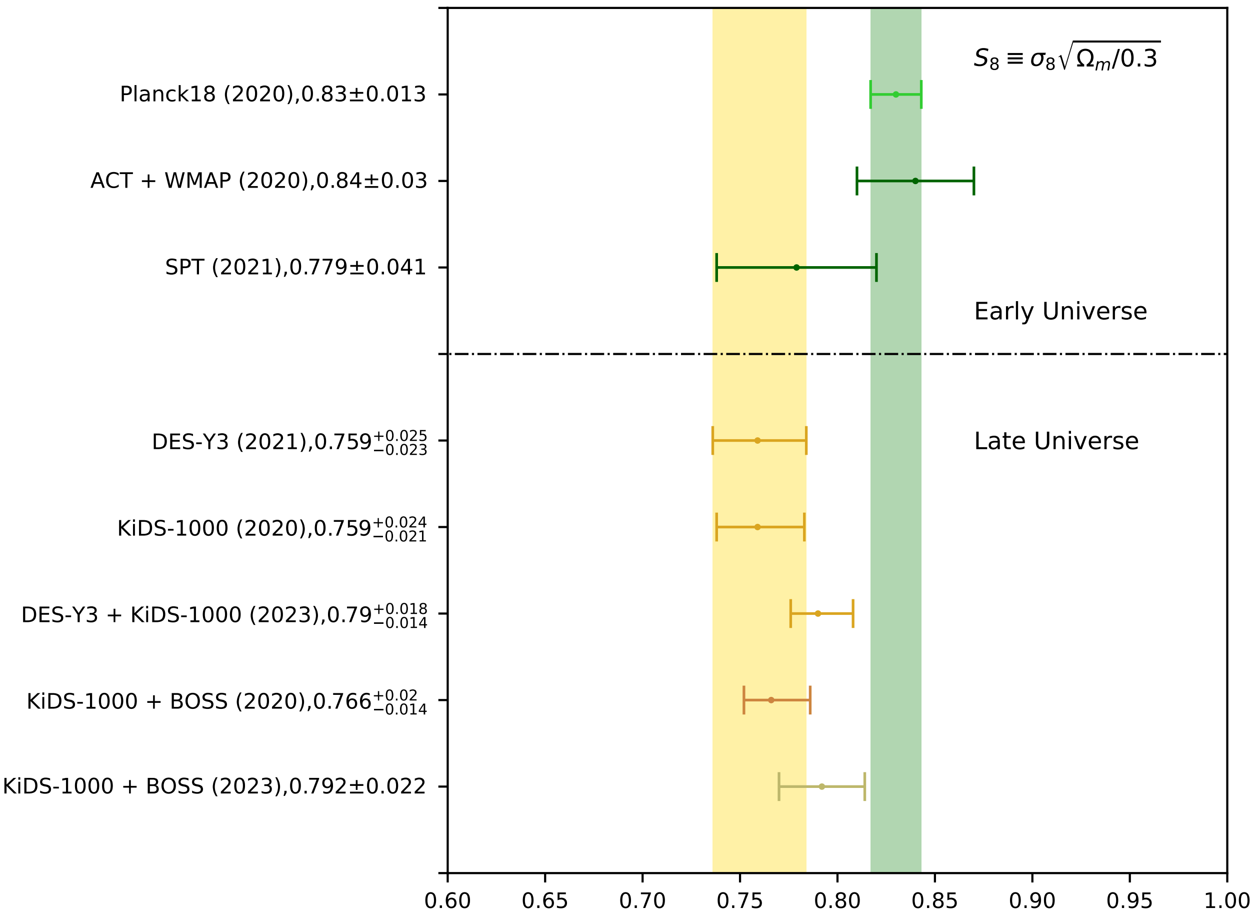

Figure 3.5: Whisker plot showing different observed values of S_8. The green band corresponds to the Planck 2018 best-fit value, while the yellow band is the DES-Y3 measurement. The values are taken in order from [8,10,22–27]. This figure was produced using code provided in [21].

Other observational anomalies

Despite H_0 and S_8 being the most established tensions in ΛCDM, there are other anomalies arising from different observations in cosmology. Here we will simply provide a short list with references for the interested reader.

- The CMB lensing anomaly refers to a possible internal inconsistency with the Planck data. To see this, one introduces an A_{lens} parameter which scales by hand the effect of gravitational lensing on the CMB – $A_{\text{lens}} < 1$ means less lensing than in GR, $A_{\text{lens}} > 1$ means more lensing. When leaving this free to vary in the Planck analysis, the data actually prefers a value larger than 1 [8, 105]. Note, however, that this preference goes away when using an alternate likelihood for the Planck data [106, 107], and it is also not present in ACT data [108].

- The sound horizon problem is closely related to the H_0 tension. As discussed in Section 3.1.5, BAO data provides distance information if it is calibrated with a value for the sound horizon. At the same time, SN-Ia also provide distance information after being calibrated with a H_0 value. The distance data obtained by BAO calibrated by Planck disagrees significantly with that from Pantheon+ SN-Ia calibrated with SH0ES [96, 109]. This inconsistency between late-time probes is caused by a tension between early and late-time calibrators, possibly hinting at some new physics pre-recombination.

3.4 Summary

In this chapter we reviewed the historical developments of observational cosmology, starting from the discovery of the expansion of the universe, through to dark matter and dark energy. We then discussed modern observational probes such as the CMB, BAO and the matter power spectrum. To finish, we introduced the standard model of cosmology ΛCDM, covering its triumphs as well as its limitations – with a particular focus on cosmological tensions. In the next chapter we will look to extend our model beyond ΛCDM by considering alternative formulations of DE and DM.

Chapter 4

Beyond Λ and CDM

We have seen in the previous chapter that although very successful, the ΛCDM model is under scrutiny due to theoretical shortcomings as well as tensions in the observed data. The accumulation of these reasons is a strong motivator to consider modifications to the standard cosmological history. In this chapter we will focus on extensions of ΛCDM pertaining to CDM and DE. Since not much is known about these exotic sources of matter, it is possible to come up with models which deviate from ΛCDM while still being allowed by data. In particular, in Section 4.1 we will discuss the use of scalar fields for DM and DE, and in Section 4.2 cover interactions in the dark sector (i.e. between DM and DE).

4.1 Scalar fields in cosmology

Scalar fields are ubiquitous in all areas of physics, and cosmology is no exception. When exploring physics beyond the standard model, scalar fields are often the simplest and most natural extension to consider, as they introduce new dynamical degrees of freedom without the complications of higher-spin fields or additional symmetries. In cosmology, scalar fields have mostly been used to describe inflation, dark energy and dark matter. These scalar fields can can exhibit a wide range of dynamical behaviours, leading to a rich phenomenology.

4.1.1 Scalar fields basics

We modify the Einstein-Hilbert action in the following way by adding the standard Lagrangian for a canonical scalar field ϕ to the matter Lagrangian of the theory:

$$S = \int d^4x\sqrt{-g}\left[\frac{1}{2}M_{Pl}^2 R - \frac{1}{2}(\partial\phi)^2 - V(\phi)\right], \tag{4.1}$$

where $V(\phi)$ denotes the potential of the scalar field and $\mathrm{M}_{\mathrm{Pl}}^2$ is the reduced Planck mass, defined as $\mathrm{M}_{\mathrm{Pl}}^2 = \frac{1}{8\pi G}$.

Varying the above action with respect to ϕ, we obtain the Klein-Gordon (KG) equation:

$$\nabla^\mu\nabla_\mu\phi - \frac{\partial V}{\partial\phi} = 0, \tag{4.2}$$

and varying the scalar field part of the action with respect to the metric as in Eq. (2.18) we get the EM tensor for a general scalar field:

$$T_{\mu\nu}^{(\phi)} = \nabla_\mu\phi\nabla_\nu\phi - g_{\mu\nu}\left(\frac{1}{2}g^{\alpha\beta}\nabla_\alpha\phi\nabla_\beta\phi + V(\phi)\right). \tag{4.3}$$

So far the discussion has been general and applies for scalar fields in any GR metrics. In practice, the scalar field acts as a source of matter and shows up on the right hand side of the Einstein equations as part of the energy-momentum tensor. To specialise to cosmology, we need to use the flat FLRW metric. Doing this yields the KG equation

$$\ddot{\phi} + 3H\dot{\phi} + V_{,\phi} = 0, \tag{4.4}$$

which dictates the dynamics of the scalar field. Note the presence of H in the second term on the lhs: this leads to damping in an expanding universe ($H > 0$), and is a driving term in a collapsing universe ($H < 0$).

Inserting the flat FLRW metric, Eq. (4.3) yields the components of the EM tensor in an expanding universe:

- $T_{00}^{(\phi)} = \frac{1}{2}\dot{\phi}^2 + V(\phi)$,
- $T_{i0}^{(\phi)} = T_{0i}^{(\phi)} = 0$,
- $T_{ij}^{(\phi)} = \left(\frac{1}{2}\dot{\phi}^2 - V(\phi)\right)g_{ij}$.

Comparing this to the energy momentum of a generic fluid (see Section 2.2.2), it is natural to associate an energy density and pressure to the scalar field in the following way[1] [111]:

$$\rho = \frac{1}{2}\dot{\phi}^2 + V(\phi) \tag{4.5}$$

$$p = \frac{1}{2}\dot{\phi}^2 - V(\phi). \tag{4.6}$$

Using the definitions above, it is straightforward to see that the KG equation is equivalent to the fluid continuity equation (Eq. (2.38)). We thus see that for positive potentials, the equation of state can take any value between $-1 \leq w \leq 1$. The specific dynamics of the scalar field will be determined by its potential, as well as the expansion of the universe (i.e. the other matter sources in the universe). For our purpose, we will be mostly interested in the cases with $w = -1$ (DE) and $w = 0$ (DM).

We now discuss linear perturbations of the scalar field ϕ. Following the approach in Section 2.3, we write ϕ as

$$\phi = \bar{\phi} + \delta\phi, \tag{4.7}$$

where the bar denotes the background quantity, and the perturbation $\delta\phi$ depends on both time and spatial coordinates. In the rest of this chapter we omit the over-bar notation and simply denote the background field as ϕ. It is then possible to plug in the expanded ϕ as well as the expanded metric into Eq. (4.2) and linearise to obtain the following perturbed KG equation in general gauge (see Section 2.3 for definitions of the various terms below) :

$$\delta\ddot{\phi} + 3H\delta\dot{\phi} + \frac{k^2}{a^2}\delta\phi + V_{,\phi\phi}\delta\phi = \dot{\phi}\left(\dot{\Phi} + 3\dot{\Psi} - \frac{k}{a}B + \dot{E}\right) + 2(\ddot{\phi} + 3H\dot{\phi})\Phi. \tag{4.8}$$

Similarly, we can expand the EM tensor from Eq. (4.3) to linear order to get the perturbed EM tensor. As for the background, it is then possible to compare the components to those of the EM tensor for a perfect fluid, and obtain the following dictionary linking scalar field perturbations to fluid perturbations [111]:

$$\delta\rho = \dot{\phi}\delta\dot{\phi} - \dot{\phi}^2\Phi + V_{,\phi}\delta\phi, \tag{4.9}$$

$$\delta p = \dot{\phi}\delta\dot{\phi} - \dot{\phi}^2\Phi - V_{,\phi}\delta\phi, \tag{4.10}$$

$$\frac{a}{k}(\rho + p)(v - B) = \dot{\phi}\delta\phi. \tag{4.11}$$

Since ϕ is a scalar, its perturbations change in the following way under a gauge trans-

---

[1] Note that these equalities hold more generally in GR, see [110]

formation [112]:

$$\tilde{\delta\phi} = \delta\phi - \bar{\phi}'\xi^0, \tag{4.12}$$

similar to energy density perturbations.

4.1.2 Quintessence

We now turn to describing dark energy dynamics with a scalar field. Such a field needs an equation of state close to $w \approx -1$ in order to behave like dark energy. To be precise, to ensure an accelerated expansion the scalar field has to have $w < -1/3$.

Looking at Eqs. (4.5), (4.6), it is possible to obtain a DE-like EoS if

$$\frac{1}{2}\dot{\phi}^2 \ll V(\phi). \tag{4.13}$$

In that case, $\rho \approx -p$ and the energy density is nearly constant. This particular regime is usually referred to as *slow-roll*, referencing the small kinetic contribution to the energy density. In general this is achieved by having a shallow potential, preventing the field from rolling down and accruing kinetic energy [113].

Broadly, there are two classes of basic quintessence models.

- Freezing models start with a EoS $w \neq -1$ at early-times, and eventually reaches $w \approx -1$ at late-time. The field slows down as the universe expands, eventually effectively freezing. These models can be obtained with inverse power law potentials $V \propto \phi^{-n}$ [114] and exponential potentials $V \propto e^{-\lambda\phi}$ [73, 115]. Interestingly, exponential potentials exhibit scaling behaviour, meaning their EoS scales in the same way as the dominant component in the universe for $\lambda^2 > 3(1+w_d)$ where w_d is the EoS of the dominant species.

- Thawing models, on the contrary, start-off non-dynamical with $w \approx -1$ and begin rolling down their potential at late-times. Such behaviour can be obtained with a simple massive scalar field with potential $V = \frac{1}{2}m^2\phi^2$ [116]. We will study this in more detail when discussing scalar dark matter, but a light scalar field of mass around 10^{-33}eV will be held by Hubble friction until late-times and so behave close to a cosmological constant. Even lighter fields will still be frozen today.

Whilst quintessence does not offer a solution for the cosmological constant problem, it is built on the assumption that if some physical mechanism solves it, then the observed cosmological constant needs to be explained somehow. However, the dynamical nature of the dark energy in the quintessence scenario can help alleviate the coincidence problem. This is especially true for scaling solutions, where the DE density parameter need not have been so unnaturally small before DE domination.

4.1.3 Scalar field dark matter

The notion that scalar fields might be used to model dark matter dates back to Michael Turner's seminal 1983 paper [117]. In his study he proved that a coherently oscillating massive scalar field behaved like dark matter on large timescales. The idea is that the scalar field is oscillating in its ϕ^2 potential but is also being damped by the expansion of the universe (the $3H\dot{\phi}$ term in Eq. (4.2)). This damping leads to a decaying envelope in addition to the oscillations. On large timescales, the oscillations are not necessarily resolved and it is convenient to average them out over a period of oscillation. Once this is done, the behaviour of the scalar field fluid is approximately that of pressureless dust. We will see that at linear perturbation level the story is slightly different, and this leads to modified structure formation in the late universe.

First, let us prove that a massive oscillating scalar field behaves like matter in an expanding universe. Since $V(\phi) = \frac{1}{2}m^2\phi^2$, the KG equation becomes

$$\ddot{\phi} + 3H\dot{\phi} + m^2\phi = 0. \tag{4.14}$$

Ignoring the Hubble term, this is simply the equation for a harmonic oscillator. We therefore expect the solution to display damped oscillations. There are two regimes of interest: if $H > m$, the Hubble friction is so large that the field is stuck [118] - the friction term dominates over the mass term and so ϕ is constant. This is the dark energy regime described in the previous section. If $H < m$, the field thaws and starts feeling the effect of its potential. The dynamics of the field then will be to roll down towards the minimum of its potential. Due to the parabolic nature of V, ϕ will start to oscillate around the minimum, with some extra damping due to the friction term.

Let us solve this equation for a given epoch, characterised by the equation of state w_d. According to Eq. (2.43), the Hubble rate is simply

$$H = \frac{2}{3(1+w_d)}\frac{1}{t}, \tag{4.15}$$

and so the KG equation becomes

$$\ddot{\phi} + \frac{2}{1+w_d}\frac{1}{t}\dot{\phi} + m^2\phi = 0. \tag{4.16}$$

To solve this, let us change variables and write $\phi \equiv \varphi t^{-\alpha}$, where

$$\alpha \equiv \frac{1}{1+w_d} - \frac{1}{2}. \tag{4.17}$$

The equation then becomes

$$t^2\ddot{\varphi} + t\dot{\varphi} + \varphi(m^2t^2 - \alpha^2) = 0. \tag{4.18}$$

The general solution for φ is a linear combination of Bessel functions of the first kind $J_\alpha(mt)$ and second kind $Y_\alpha(mt)$, both of order α. Therefore the solution for ϕ is [119,120]

$$\phi(t) = t^{-\alpha}\left[C\,J_\alpha(mt) + D\,Y_\alpha(mt)\right], \tag{4.19}$$

where C, D are integration constants. In matter domination, this reduces exactly to

$$\phi(t) = \left(\frac{a_0}{a}\right)^{\frac{3}{2}}[\phi_+\cos(mt) + \phi_-\sin(mt)], \tag{4.20}$$

where ϕ_+ and ϕ_- are related to C and D. In fact we will use this approximation throughout rather than the exact Bessel solution. Indeed, Bessel functions tend to sin and cos functions for $mt \gg 1$. Since we are assuming $m > H$ and $H \propto 1/t$, $mt \gg 1$ is satisfied as long as $m \gg H$. Therefore a good approximation at first order in H/m is Eq. (4.20) for all relevant epochs.

We will now take Eq. (4.20), plug it into the definition of the energy density and pressure, Eqs. (4.5), (4.6) and average these quantities over a period of oscillation. This means we want to compute

$$\langle\rho\rangle = \frac{1}{2}\langle\dot{\phi}^2\rangle + \frac{1}{2}m^2\langle\phi^2\rangle, \tag{4.21}$$
$$\langle p\rangle = \frac{1}{2}\langle\dot{\phi}^2\rangle - \frac{1}{2}m^2\langle\phi^2\rangle. \tag{4.22}$$

Here, the angle brackets denote the following time averaging:

$$\langle f(t)\rangle \equiv \frac{1}{T}\int_t^{t+T} f(t')dt' \tag{4.23}$$

for a periodic function $f(t)$ with period T. In the case of the massive scalar field, $T = 2\pi/m$. Treating the oscillation envelope as constant over a period of oscillation – this means we can take out the factor of $a^{-3/2}$ from the integral, treating the oscillation timescale as much smaller than cosmological timescales – we obtain the following averaged quantities:

$$\langle\phi\rangle = 0, \tag{4.24}$$

$$\langle\dot{\phi}\rangle = 0, \tag{4.25}$$

$$\langle\phi^2\rangle = \frac{1}{2}(\phi_+^2 + \phi_-^2)\left(\frac{a_0}{a}\right)^{-3}, \tag{4.26}$$

$$\langle\dot{\phi}^2\rangle = \frac{1}{2}m^2(\phi_+^2 + \phi_-^2)\left(\frac{a_0}{a}\right)^{-3}. \tag{4.27}$$

Plugging these back into Eqs. (4.5), (4.6), we get

$$\langle\rho\rangle = \frac{1}{2}m^2(\phi_+^2 + \phi_-^2)\left(\frac{a_0}{a}\right)^{-3}, \tag{4.28}$$

$$\langle p\rangle = 0, \tag{4.29}$$

showing that $\langle\rho\rangle \propto a^{-3}$ behaves like matter and consistently $\langle w\rangle \equiv \frac{\langle p\rangle}{\langle\rho\rangle} = 0$. It is possible to generalise the above result to all (positive) power-law potentials of the form $V(\phi) \propto \phi^n$: in that case [117], $\langle w\rangle = \frac{n-2}{n+2}$.

Whilst the background behaviour of a massive scalar field can be well approximated by pressureless dust (for a more accurate fluid approximation scheme see [121]), things change at linear order in perturbation theory. In particular, the sound speed of perturbations is non-zero for light scalar field dark matter, which is different to CDM (in which case it is 0). To see this, we follow the original derivation by Hwang and Noh [122].

First, we come up with an ansatz to solve Eq. (4.8):

$$\delta\phi(k,t) = \delta\phi_+(k,t)\sin(mt) + \delta\phi_-(k,t)\cos(mt), \tag{4.30}$$

where $\delta\phi_+$, $\delta\phi_-$ are slowly varying functions (compared to the scale of oscillation). To simplify calculations we now move to the axion-comoving gauge, which sets us in the rest frame of the axion. This means that after time-averaging,

$$\langle T^0_i\rangle = 0. \tag{4.31}$$

This is achieved by setting $v = B = 0$. Plugging Eq. (4.30) into Eq. (4.8) and looking at terms multiplying $\cos(mt)$[2], we get

$$\delta\ddot{\phi}_+ + 2\delta\dot{\phi}_- m + 3H\left(\delta\phi_- m + \delta\dot{\phi}_+\right) + \delta\phi_+\frac{k^2}{a^2} = (\dot{\phi}_+ + \phi_- m)\left(\dot{\Phi} + 3\dot{\Psi} + \dot{E}\right) - 2m^2\phi_+\Phi. \tag{4.32}$$

We now solve this equation at leading order in H/m, since we are considering fast oscillations compared to the expansion of the universe. Since our ansatz separates the fast oscillations from the slower timescale evolution, we can say that $\delta\dot{\phi}_\pm \sim H$ and $\delta\ddot{\phi}_\pm \sim H^2$. Further, the derivatives of the metric components are also varying on Hubble timescales, so for our purposes $\dot{\Phi} \sim \dot{\Psi} \sim \dot{E} \sim H$. The leading order is therefore the 0th order in H/m. Discarding higher order terms leads to the following solution:

$$\Phi = -\frac{a^{\frac{3}{2}}}{2}\frac{\delta\phi_+}{\phi_+}\frac{k^2}{m^2a^2}. \tag{4.33}$$

From Eq. (4.11) we see that in the comoving gauge

$$\langle\dot{\phi}\delta\phi\rangle = 0. \tag{4.34}$$

Since

$$\langle\dot{\phi}\delta\phi\rangle = a^{-\frac{3}{2}}m[\delta\phi_+\phi_- - \delta\phi_-\phi_+], \tag{4.35}$$

our choice of gauge implies

$$\delta\phi_+\phi_- = \delta\phi_-\phi_+. \tag{4.36}$$

Furthermore, applying our gauge condition to Eq. (2.98) yields

$$\Phi = -\frac{\langle\delta p\rangle}{\langle\rho + p\rangle}. \tag{4.37}$$

Recall

$$\langle\rho + p\rangle = \langle\dot{\phi}^2\rangle = \frac{m^2}{2}(\phi_+^2 + \phi_-^2)\left(\frac{a_0}{a}\right)^3, \tag{4.38}$$

so combining Eqs. (4.33), (4.37) we get

$$\langle\delta p\rangle = \frac{a^{-\frac{3}{2}}}{4}(\phi_+^2 + \phi_-^2)\frac{\delta\phi_+}{\phi_+}m^2\left[\frac{k^2}{a^2m^2}\right]. \tag{4.39}$$

We can now compute $\langle\delta\rho\rangle$ in order to obtain the sound speed $c_s^2 \equiv \langle\delta p\rangle/\langle\delta\rho\rangle$. First we

---

[2] The result is the same for terms proportional to $\sin(mt)$.

compute the individual terms:

$$\langle \dot{\phi}\delta\dot{\phi} \rangle = \frac{a^{-\frac{3}{2}}}{2} m[\delta\dot{\phi}_- \phi_+ - \delta\dot{\phi}_+ \phi_- + m(\delta\phi_- \phi_- + \delta\phi_+ \phi_+)] \tag{4.40}$$

$$\langle \phi\delta\phi \rangle = \frac{a^{-\frac{3}{2}}}{2} (\delta\phi_+ \phi_+ + \delta\phi_- \phi_-). \tag{4.41}$$

Dropping higher order terms in H/m like $\delta\dot{\phi}_+$ and $\delta\dot{\phi}_-$ and using Eq. (4.36) we get

$$\langle \delta\rho \rangle = \frac{a^{-\frac{3}{2}}}{2} (\phi_+^2 + \phi_-^2) \frac{\delta\phi_+}{\phi_+} m^2 \left[\frac{1}{2} \frac{k^2}{a^2 m^2} + 2 \right]. \tag{4.42}$$

Putting it all together, we get the sound-speed in comoving gauge:

$$c_s^2 = \frac{\frac{1}{2}\frac{k^2}{a^2m^2}}{\frac{1}{2}\frac{k^2}{a^2m^2} + 2}. \tag{4.43}$$

There are two main regimes of note for this:

- If $k \gg ma$, $c_s^2 \approx 1$ and structure formation is suppressed due to the extra pressure contribution. This happens on small scales at early times for small scalar field mass.
- If $k \ll ma$, $c_s^2 \approx k^2/(4a^2m^2)$ and so tends to zero, meaning a return to the CDM regime. This is the case at late times, on large scales and for heavier scalar masses.

Fig. 4.1 shows the evolution of c_s^2 at different scales, computed using a modified version of the publicly available `CLASS` Boltzmann code[3] [123].

---

[3] `https://github.com/lesgourg/class_public`

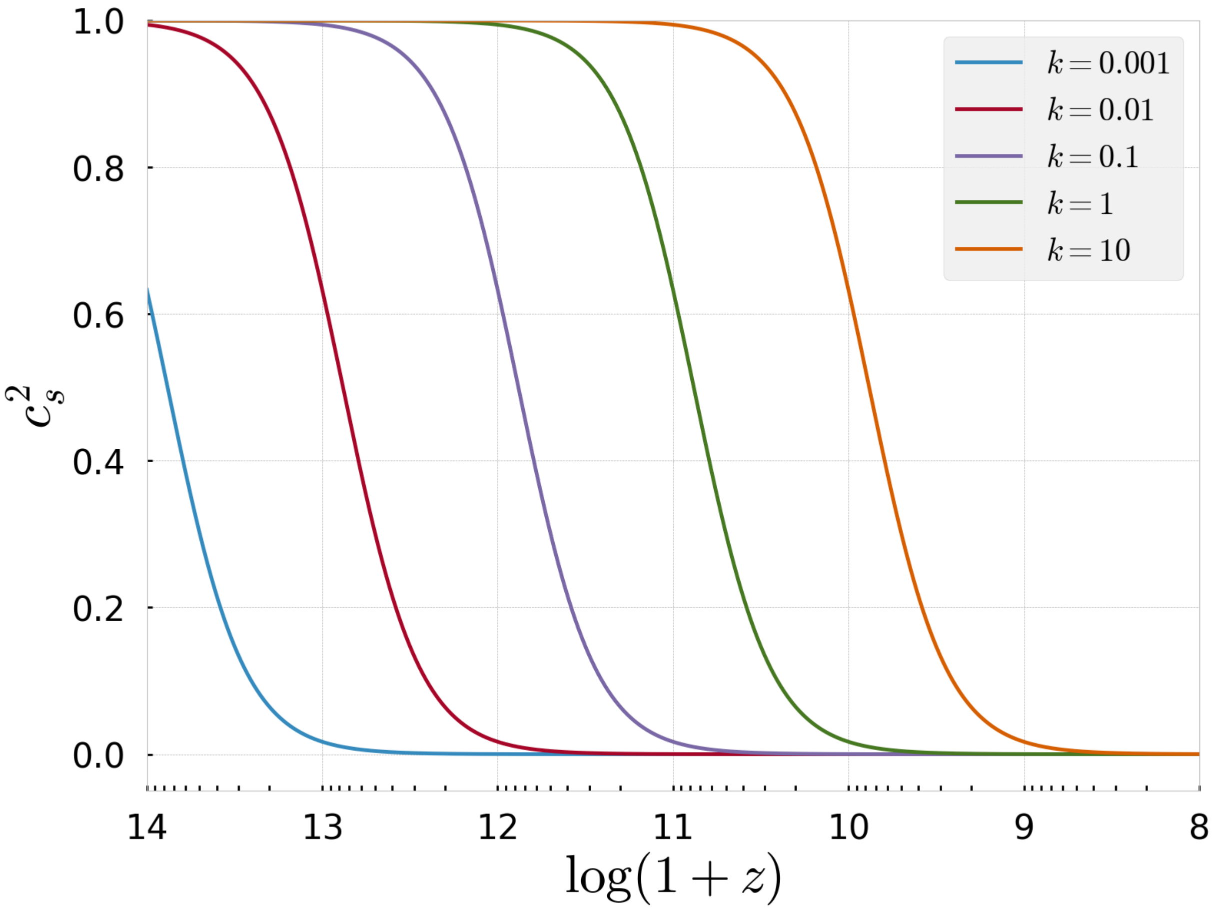

Figure 4.1: Plot of the evolution of the sound speed c_s^2 for different values of wavenumber k in units of h Mpc^{-1}. The mass of the scalar field DM is fixed at $m = 10^{-19}$ eV, and the other cosmological parameters are chosen to match the Planck 2018 ΛCDM best-fit values.

In practice, one needs masses of order around 10^{-20}eV or smaller [124] to have a sizeable effect on cosmological observables. The most notable effect is a reduction in the matter power spectrum at small scales – the impact on the CMB is much smaller. Figures 4.2, 4.3 show the angular and matter power spectra for various axion masses. In order to compute the aforementioned observables, we need to solve for the evolution of $\langle \delta\rho \rangle$ and $\langle v \rangle$. To do this, we need to change back to either synchronous or Newtonian gauge, as these are the gauges used in Boltzmann solvers. The sound speed in Eq. (4.43) essentially defines a pressure perturbation in the comoving gauge as a multiple of the energy density perturbation.

To go from an arbitrary gauge (denoted by superscript X) to the comoving gauge

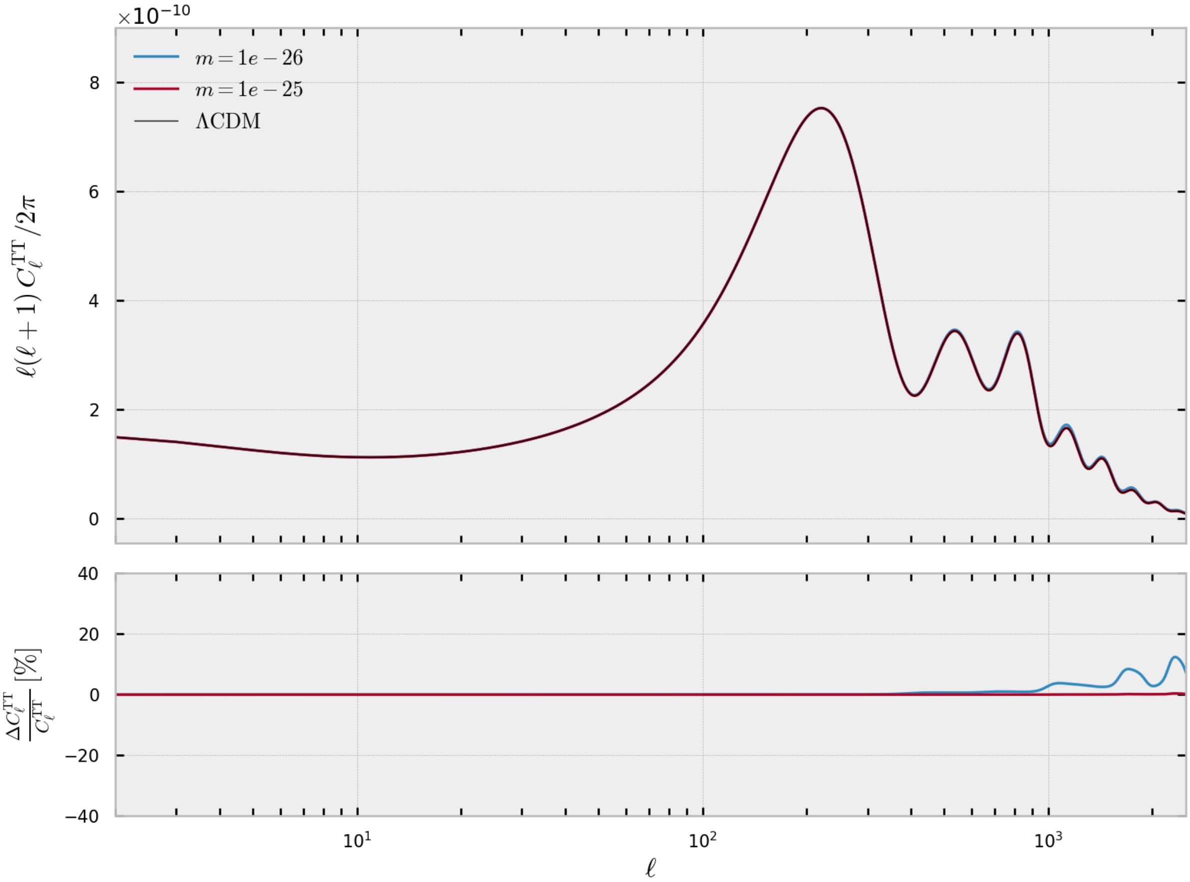

Figure 4.2: Plot of the TT CMB power spectrum for ultra-light scalar field dark matter compared to ΛCDM. DM masses are in eV. All other cosmological parameters are set to the best-fit values for Planck 2018 ΛCDM. The impact of such a DM is only noticeable on the CMB for extremely light fields.

(superscript C) requires the following transformation [46]:

$$\xi'_{X\to C} = -v^X \tag{4.44}$$

$$\xi^0_{X\to C} = (v^X - B^X). \tag{4.45}$$

This means that to go from the synchronous gauge (superscript S) to the conformal gauge requires (since $B^S{=}0$):

$$\xi'_{S\to C} = -v^S \tag{4.46}$$

$$\xi^0_{S\to C} = v^S. \tag{4.47}$$

We can now write down the gauge transformation for the perturbed pressure, energy

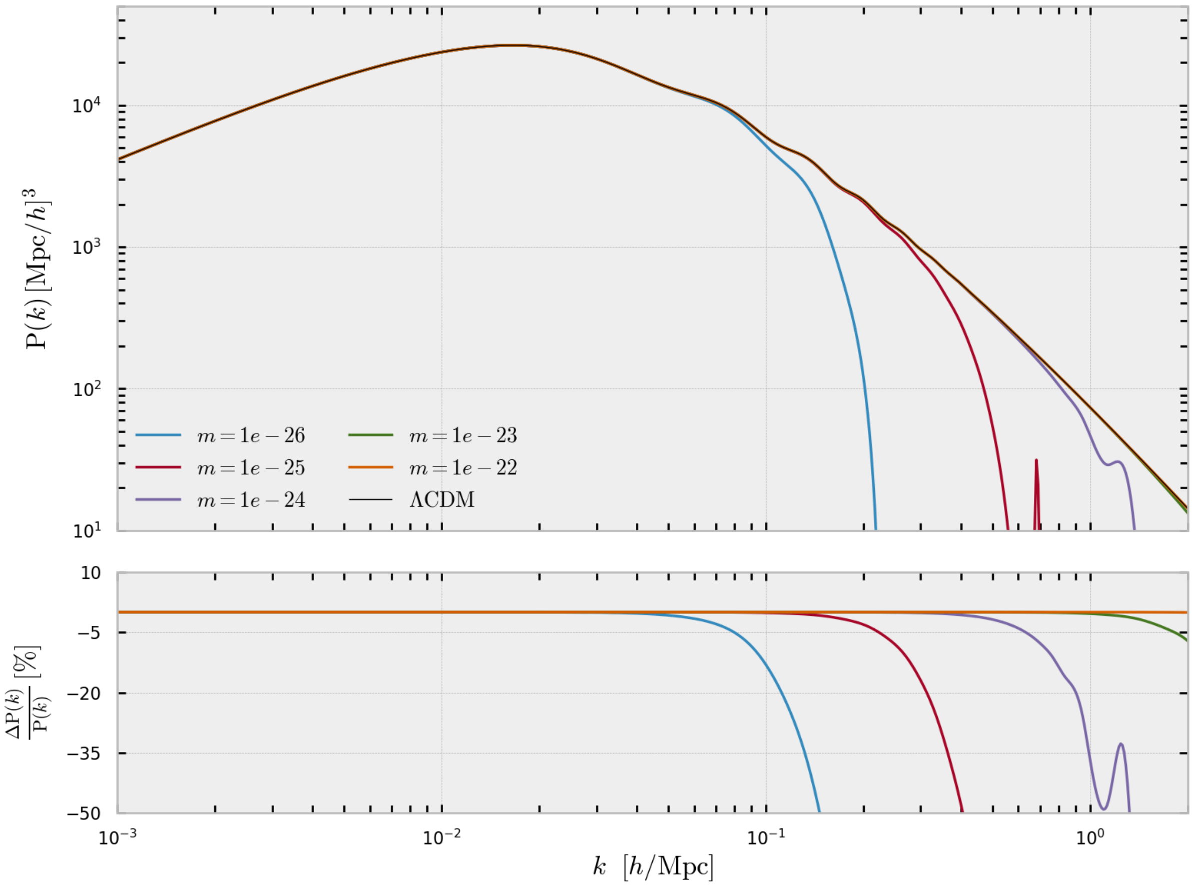

Figure 4.3: Plot of the matter power spectrum for ultra-light scalar field dark matter compared to ΛCDM. DM masses are in eV. All other cosmological parameters are set to the best-fit values for Planck 2018 ΛCDM.

density and velocity following Section 2.3. It is then possible to invert these gauge transformations and go from comoving gauge to synchronous gauge by realising that

$$\xi'_{C\to S} = -\xi'_{S\to C} \tag{4.48}$$
$$\xi^0_{C\to S} = -\xi^0_{S\to C}. \tag{4.49}$$

Writing the equations for $\delta\rho$ and v in synchronous gauge, we need to obtain $\langle\delta p^S\rangle$ from $\langle\delta p^C\rangle$ which is proportional to $\langle\delta\rho^C\rangle$. We have the following expression for $\langle\delta p^S\rangle$ [125]:

$$\begin{aligned}\langle\delta p^S\rangle &= \langle\delta p^C\rangle + p'\langle v^S\rangle\\ &= c_s^2\langle\delta\rho^C\rangle + c_{\mathrm{ad}}^2\rho'\langle v^S\rangle\\ &= c_s^2\langle\delta\rho^S\rangle + 3\mathcal{H}(\langle\rho\rangle + \langle p\rangle)(c_s^2 - c_{\mathrm{ad}}^2)\langle v^S\rangle\end{aligned} \tag{4.50}$$

where we have defined the adiabatic sound speed as $c_{\text{ad}}^2 \equiv \langle \dot{p} \rangle / \langle \dot{\rho} \rangle$ and used

$$\langle \delta\rho^C \rangle = \langle \delta\rho^S \rangle - \rho' \langle v^S \rangle. \tag{4.51}$$

In the end we get the following equations for the oscillation averaged scalar fluid perturbations in synchronous gauge, where we omit angle brackets and the S subscript for ease of notation:

$$\delta\rho' = -3\mathcal{H}\delta\rho(1+c_s^2) - (\rho+p)(\frac{1}{2}h' + kv) - 9\mathcal{H}^2(\rho+p)(c_s^2 - c_{\text{ad}^2})v \tag{4.52}$$

$$(\rho+p)v' = -(\rho+p)'v - 4\mathcal{H}(\rho+p)v + k[c_s^2\delta\rho + 3\mathcal{H}(\rho+p)(c_s^2 - c_{\text{ad}}^2)v] \tag{4.53}$$

The most studied candidates for scalar field dark matter are the so-called axions and axion-like particles[4]. These include the QCD axion [88], which was developed as a solution to the strong CP problem, and string theory axions which arise naturally when compactifying down to four dimensions [126]. Technically these axions are pseudoscalars, but in terms of cosmology the difference is not relevant. In this work, we will study scalar fields without considering their embedding into fundamental theories, but rather as proof-of-concept toy-models to explore low-energy, late-time cosmological phenomena.

4.2 Interactions between dark energy and dark matter

So far we have discussed ways to model dark energy and dark matter beyond the ΛCDM description, leading to observable differences. We now generalise our approach and consider interactions between the two dark components of the universe. In the standard case, it is assumed that DE and DM only interact through gravity, however it is possible to imagine that the two are part of a dark sector which involves some further interactions between the two. These dark sectors have been extensively studied from a particle physics point of view [127] as well as from a cosmological phenomenology point of view [101,128]. Not only can such an interaction yield new observable signatures, some models also attempt to solve cosmological tensions and theoretical problems such as the coincidence problem.

The simplest way to implement such interactions is to introduce some energy transfer

---

[4] We will use axion and ALP interchangeably.

between the DM and DE species in the following way:

$$\dot{\rho}_{\rm DE} + 3H\rho_{\rm DE}(1+w_{\rm DE}) = Q \tag{4.54}$$
$$\dot{\rho}_{\rm DM} + 3H\rho_{\rm DM} = -Q, \tag{4.55}$$
$$\tag{4.56}$$

where the opposite signs of Q in the two equations ensures conservation of total energy-momentum.

The specific form of Q is model-dependent, and it is common to take a phenomenological approach by simply assuming a coupling Q and studying its effect on observables [100]. It is common in this approach to choose $Q \propto H\rho_{\rm DM}$, $Q \propto H\rho_{\rm DE}$, or a linear combination of the two [101]. Although this method yields interesting phenomenology, it does not provide any hints at the microscopic physics of DE or DM. This can be improved with coupled quintessence [129], which couples a dark energy scalar field ϕ to a dark matter fluid[5]. In this framework, the interaction between DE and DM leads to an exchange of energy between the two. One motivation for this form of coupling is that it is a simple form which arises naturally in string theory or certain scalar-tensor theories [130].

The equations in this case are:

$$\ddot{\phi} + 3H\dot{\phi} + V_{,\phi} = \beta\rho_{\rm DM} \tag{4.57}$$
$$\dot{\rho}_{\rm DM} + 3H\rho_{\rm DM} = -\beta\rho_{\rm DM}\dot{\phi}, \tag{4.58}$$

where β is a coupling constant. The potential is not specified, although the exponential potential is commonly used. These equations can be derived from an action by introducing a conformal coupling between DE and DM[6]. Consider the following

$$\mathcal{S} = \int d^4x\sqrt{-g}\left(\frac{M_{\rm Pl}^2}{2}R - \frac{1}{2}g^{\mu\nu}\partial_\mu\phi\partial_\nu\phi - V(\phi)\right) + \mathcal{S}_{\rm SM} + \mathcal{S}_{\rm DM}, \tag{4.59}$$

where $\mathcal{S}_{\rm SM}$ denotes the Lagrangian containing the standard model fields propagating in geodesics of the metric $g_{\mu\nu}$. $\mathcal{S}_{\rm DM}$ contains the Lagrangian for the DM fluid, but propagates on the conformal metric $\tilde{g}_{\mu\nu}$:

$$\mathcal{S}_{\rm DM} = \int d^4x\sqrt{-\tilde{g}}\mathcal{L}_{\rm DM}, \tag{4.60}$$

---

[5] Note that in the original coupled quintessence paper the scalar field also couples to baryons.

[6] We will consider these interactions in more detail in the following chapters.

where

$$\tilde{g}_{\mu\nu} \equiv C(\phi) g_{\mu\nu}, \tag{4.61}$$

and $C(\phi)$ is the conformal factor.

Varying the above action we get the following modified Klein-Gordon equation:

$$\nabla^\mu \nabla_\mu \phi = V_{,\phi} - \frac{C_{,\phi}}{2C} T_{\mathrm{DM}}, \tag{4.62}$$

where we have defined the EM tensor in the following way:

$$T^{\mathrm{DM}}_{\mu\nu} \equiv -2 \frac{1}{\sqrt{-g}} \frac{\delta(\sqrt{-\tilde{g}} \mathcal{L}_{\mathrm{DM}})}{\delta g^{\mu\nu}}, \tag{4.63}$$

and defined its trace $T_{\mathrm{DM}} \equiv T^{\mathrm{DM}\ \mu}_{\mu}$. Conservation of energy-momentum tells us that

$$\nabla^\mu (T^\phi_{\mu\nu} + T^{\mathrm{DM}}_{\mu\nu}) = 0, \tag{4.64}$$

where $T^\phi_{\mu\nu}$ is the standard EM tensor for a scalar field defined in Eq. (4.3). Plugging Eq. (4.62) into the above, we get the following conservation equation for the DM:

$$\nabla^\mu T^{\mathrm{DM}}_{\mu\nu} = \frac{C_{,\phi}}{2C} T_{\mathrm{DM}} \nabla_\nu \phi. \tag{4.65}$$

For a rigorous treatment see [131] (this result holds only for DM). Choosing $C = e^{2\beta\phi}$ yields exactly Eqs. (4.57). In this case the conformal coupling can be interpreted as introducing a time-varying mass to the DM: $m_{\mathrm{DM}} \propto C(\phi)$.

It is also possible to obtain a similar set of coupled quintessence equations from a conformal coupling using a scalar field dark matter – see [132, 133] and Chapter 7.

4.3 Summary

In this chapter we introduced scalar fields in the context of cosmology in order to describe DE and DM beyond ΛCDM. Both formulations are similar, with the main difference being that DE is described by a slowly rolling scalar field, while a DM scalar field must be oscillating in a quadratic potential. In the case of DM, we used a fluid approximation to derive the equation of state and the sound speed at background and linear perturbation level respectively. We then discussed the coupled quintessence scenario, in which DM and DE exchange energy via an interaction term. This scenario generally involves a DE scalar field interacting with a fluid DM component, but in the rest of this thesis we will focus on models where both DE and DM are scalar fields.

Chapter 5

A hybrid model for the dark sector

5.1 Introduction

We have seen in the previous chapters how successful the ΛCDM is when it comes to fitting the observed cosmological data. However, we have also seen that this model has many shortcomings, one of them being the origin of DM and DE.

There is a plethora of phenomenological proposals for DM, motivated by theories beyond the standard model of particle physics. Candidates for DM range from weakly interacting massive particles to light scalar fields; see, e.g. [124, 126, 134–141] and references therein. DE is often seen as a separate issue, not related to DM. However, we saw in Chapter 4 that it is common to consider a dark sector made up of two interacting components for DM and DE. Whilst most of these models rely on a phenomenological description of DM – that is, DM is a perfect fluid – some approaches involve two fundamental scalar fields as DM and DE [132, 142–147].

In this chapter, we explore new phenomenology in the dark sector by considering two interacting scalar fields for DM and DE. This interaction is driven by a shared potential V, which will take the well-known form of the hybrid inflation potential [37]. This choice leads to a hierarchy of masses for DM and DE, which we discuss in more detail in the next section. The DM field is identified with the heavier field, and its mass is set by the expectation value of the DE field, corresponding to the flat direction of the potential. We will show that the DE field is limited to evolving very slowly under these conditions. One consequence of the theory proposed is that the current period of accelerated expansion is transient. In the future, both fields will settle at a local minimum, for which the potential energy vanishes. The subsequent evolution of the universe is then determined by other factors, such as the curvature of space.

The motivation for this work is twofold: first, we wish to bridge the gap between a two-field system and the more traditionally studied field-fluid scenario. To do this, we apply time-averaging to the field-field equations of motion. The second motivation is to find a simple setup (that of hybrid inflation) which yields interesting physics in the dark sector, with possible implications for the ultimate fate of the universe.

The chapter is organised as follows: In Section 5.2, we present the model. The conditions on the model parameter are discussed in Section 5.3. To study the cosmological background dynamics and calculate the evolution of perturbations, we develop a fluid description for the DM field in Section 5.4. In Section 5.5, we describe the evolution of the universe and the predictions for the CMB anisotropies and large-scale structures spectra. The results and phenomenology of the model are discussed in Section 5.6. We conclude in Section 5.7.

5.2 Model

In this section, we discuss the field contents of the model studied in this chapter. The set-up under consideration is based on that of hybrid inflation [37] with the addition of the standard model fields and is defined through the following action:

$$\begin{aligned} S &= \int d^4x\sqrt{-g}\left[\frac{1}{2}\mathrm{M}_{\mathrm{Pl}}^2 R - \frac{1}{2}(\partial\phi)^2 - \frac{1}{2}(\partial\chi)^2 - V(\phi,\chi)\right] \\ &+ S_{\mathrm{SM}}. \end{aligned} \tag{5.1}$$

We aim to have ϕ playing the role of DE and χ being DM. The standard model fields are accounted for in the action S_{SM}. The term $V(\phi,\chi)$ stands for the effective interaction potential, given in analogy to the one in hybrid inflation as

$$V(\phi,\chi) = \frac{\lambda}{4}(M^2-\chi^2)^2 + \frac{1}{2}g^2\phi^2\chi^2 + \frac{1}{2}\mu^2\phi^2 \tag{5.2}$$

$$\equiv V_0 - \frac{1}{2}\lambda M^2\chi^2 + \frac{1}{4}\lambda\chi^4 + \frac{1}{2}g^2\phi^2\chi^2 + \frac{1}{2}\mu^2\phi^2, \tag{5.3}$$

where M and μ are mass scales, g and λ are dimensionless coupling constants and $V_0 \equiv \frac{1}{4}\lambda M^4$ is the scale of the potential. See Fig. 5.1 for a plot of the potential for a given set of parameter values. For ϕ and χ to play the role of DE and DM, respectively, appropriate choices of the parameter values have to be made. We will discuss this in-depth in the next section. The global minimum of the potential is at

$\chi = \pm M$ and $\phi = 0$, for which the potential energy vanishes. Note that our set-up differs from [148], where ϕ and χ play the role of DM and DE, respectively. Consequently, the physical interpretation of the fields, their dynamics and the choices of parameters change significantly.

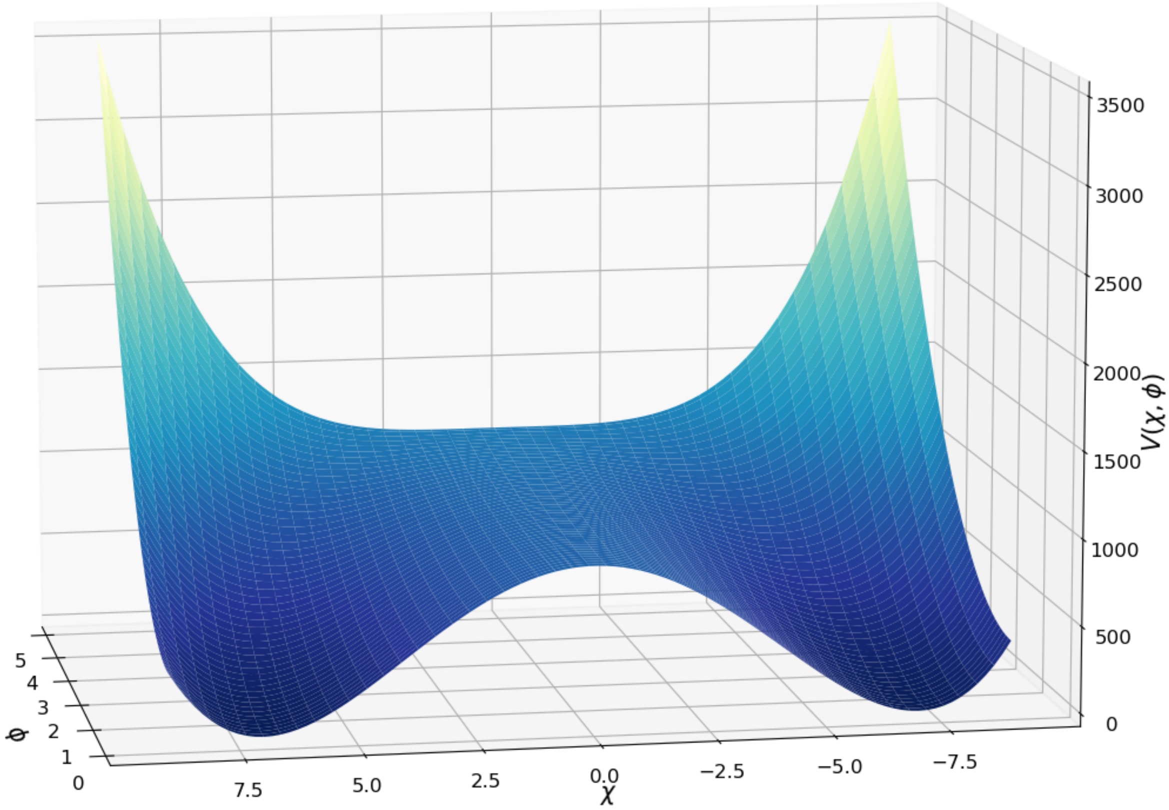

Figure 5.1: Hybrid inflation potential, plotted with $\lambda = 1.5$, $M = 7$, $g = 1.7$ and $\mu = 4$, all in Planck units.

The effective masses of the DM scalar field χ and of the DE scalar field ϕ are determined by the second order derivatives of the potential, given by

$$m_\chi^2 \equiv \frac{\partial^2 V}{\partial \chi^2} = g^2\phi^2 - \lambda M^2 + 3\lambda\chi^2, \tag{5.4}$$

and

$$m_\phi^2 \equiv \frac{\partial^2 V}{\partial \phi^2} = g^2\chi^2 + \mu^2, \tag{5.5}$$

respectively.

We consider a spatially flat universe described by the FLRW metric. The equations of motion for each scalar field read

$$\ddot{\phi} + 3H\dot{\phi} = -(g^2\chi^2 + \mu^2)\phi, \tag{5.6}$$

$$\ddot{\chi} + 3H\dot{\chi} = -\lambda\chi^3 + (\lambda M^2 - g^2\phi^2)\chi, \tag{5.7}$$

and the Friedmann equations are

$$\dot{H} = -\frac{1}{2\mathrm{M}_{\mathrm{Pl}}^2}(\rho + P), \tag{5.8}$$

$$H^2 = \frac{1}{3\mathrm{M}_{\mathrm{Pl}}^2}\rho, \tag{5.9}$$

where ρ and P are the collective energy density and pressure of both scalar fields, baryons, and radiation expressed as

$$\rho = \frac{1}{2}\dot{\phi}^2 + \frac{1}{2}\dot{\chi}^2 + V(\phi, \chi) + \rho_b + \rho_\gamma, \tag{5.10}$$

$$P = \frac{1}{2}\dot{\phi}^2 + \frac{1}{2}\dot{\chi}^2 - V(\phi, \chi) + p_\gamma, \tag{5.11}$$

respectively. For convenience, we split the energy density contributions of each scalar field into two different quantities:

$$\rho_\chi = \frac{1}{2}\dot{\chi}^2 - \frac{1}{2}\lambda M^2\chi^2 + \frac{1}{4}\lambda\chi^4 + \frac{1}{2}g^2\phi^2\chi^2, \tag{5.12}$$

$$\rho_\phi = \frac{1}{2}\dot{\phi}^2 + V_0 + \frac{1}{2}\mu^2\phi^2, \tag{5.13}$$

It is important to emphasise that this splitting is a choice and has no impact on the underlying physics so long as the sum of both parts is equal to the whole energy density of the scalar fields system. The particular choice in Eq. (5.12) is such that all oscillating terms (i.e. those containing χ) are grouped to obtain the effective pressureless behaviour needed for structure formation in the matter domination era. The ϕ-field is expected to behave like a cosmological constant at late times. Nevertheless, we will see that the evolution may still differ at early times, driven by the interaction with the χ-field.

Under this scenario, if ϕ is displaced sufficiently far from the origin, then χ will oscillate around zero. There is an abrupt transition in the shape of the potential when the effective DM mass, given by Eq. (5.4), changes from positive to negative. Using Eq. (5.4) and assuming that χ has decayed enough as it oscillates around 0 so as to ignore the quartic term in the potential, this transition happens approximately when ϕ

reaches a critical value given by

$$|\phi_c| \approx \frac{\sqrt{\lambda}M}{g}. \tag{5.14}$$

For $\phi > \phi_c$, χ behaves as dark matter, and ϕ is a dynamical dark energy component, slowly rolling down its potential. Moreover, the dynamics of ϕ are mainly determined by the dominant constant scale in the potential, V_0, and the interaction with χ. However, when ϕ approaches the critical value ϕ_c, χ quickly drops and starts oscillating around $\chi = \pm M$. Simultaneously, $V(\phi, \chi)$ drops to zero leading to a sudden decay of dark energy and implying that the epoch of DE domination is just a transient phenomenon in this theory.

5.3 Conditions on model parameters

In this section, we examine the necessary conditions to fulfil the scenario described above. In other words, we look for constraints on the free parameters g, M and λ. For ϕ to play the role of DE, the field needs to roll slowly, and the potential energy needs to be of order $\rho_{\text{DE},0}$, the DE density today. Thus, we demand that $V_0 = \frac{1}{4}\lambda M^4 \approx 10^{-47}\text{GeV}^4$. The contribution from the μ^2–term cannot be larger than this because it also affects the dark energy density. Thus, the mass scale M is of order 10^{-3}eV, as expected in models with DE.

On the other hand, for χ to behave like dark matter, it must oscillate in a quadratic potential from the early universe onwards [117]. Firstly to prevent the damping term in Eq. (5.7) from withholding the oscillations, $m_\chi \approx g\phi \gg H$ must hold. Secondly, we need to ensure that the quadratic term dominates over the quartic one in Eq. (5.3), which translates into the condition $g^2\phi^2 - \lambda M^2 \gg \frac{1}{2}\lambda\chi^2$. As discussed below, ϕ does not change significantly during the cosmological evolution, and the value of ϕ today must be large, ($\phi_0 \gtrsim 10\ \text{M}_{\text{Pl}}^2$). Therefore, the mass of the χ-field, $m_\chi = g\phi$, is large unless g is exceedingly small.

At some time t_i in the early universe, $H \approx m_\chi$, at which point the field starts to oscillate rapidly around 0 as the expansion rate becomes smaller than the mass. To estimate the temperature of this transition, we assume that the universe is in the radiation-dominated epoch after an inflationary phase. During this period,

$$H^2 = \frac{1}{3\text{M}_{\text{Pl}}^2}\frac{\pi^2}{30}g_*(T)T^4,$$

with $g_*(T)$ being the effective number of relativistic degrees of freedom at a temperature T (which is of the order of several hundred in theories beyond the standard model). Therefore we infer that the oscillations happen at a temperature

$$T \approx 10^{15} \left(\frac{g}{10^{-7}}\right)^{1/2} \left(\frac{\phi_i}{10\mathrm{M}_{\mathrm{Pl}}^2}\right)^{1/2} \left(\frac{g_*}{100}\right)^{-1/4} \mathrm{GeV}.$$

This corroborates the assumption that the field starts to oscillate very early on in the radiation dominated epoch, almost immediately after a period of inflation in this framework. Below we will derive the evolution for the χ–field (Eq. (5.40)), which allows us to find the initial field amplitude χ_i in the very early universe. Using the fact that $\rho_{\mathrm{DM},0} \approx g^2\phi_0^2\chi_0^2 \approx 4 \times 10^{-47}$ GeV^4 (where the 0 indicates the present time) and that the amplitude evolves as $\chi(t) = \chi_i(a_i/a)^{3/2} = \chi_i(T/T_i)^{3/2}$, we find, using the expression for the temperature above

$$\frac{\chi_i}{\mathrm{GeV}} \approx 1.4 \cdot 10^6 \left(\frac{g}{10^{-7}}\right)^{-1/4} \left(\frac{\phi_0}{10\mathrm{M}_{\mathrm{Pl}}^2}\right)^{-1/4} \left(\frac{g_*}{100}\right)^{-3/8}.$$

This is the initial field amplitude the χ-field must have after inflation in order to predict the right amount of DM today (emphasising again that we assume that the field χ is responsible for all DM).

As the model is currently formulated, during inflation the ϕ–field is light. The only requirement is that its field excursion is large ($\phi \gtrsim 10$ M$_{\mathrm{Pl}}$), so that in the radiation dominated epoch the mass of the χ–field also remains large and, as we will see in Section 5.4, the coupling between χ and ϕ is small enough. Since ϕ is light during inflation it is subject to quantum fluctuations, which are of order $H_{\mathrm{inf}}/2\pi$, where H_{inf} is the expansion rate during inflation. But the ϕ–field is a (almost) flat direction and subdominant during the radiation and matter dominated epoch. Therefore the quantum fluctuations will not result in large isocurvature modes in the DE sector. However, the situation with the χ–field is more delicate. If ϕ is light during inflation, i.e. $g\phi < H_{\mathrm{inf}}$, then the quantum fluctuations of χ are also of the order $H_{\mathrm{inf}}/2\pi$, resulting in potentially large isocurvature modes with an amplitude [149]

$$A_I = \frac{(H_{\mathrm{inf}}^2/\mathrm{M}_{\mathrm{Pl}}^2)}{\pi^2(\chi_{\mathrm{inf}}^2/\mathrm{M}_{\mathrm{Pl}}^2)},$$

where χ_{inf} is the value of χ during inflation, which has to be of order 10^6 GeV for $g \approx 10^{-7}$. As it is the case for axion–like fields, there are ways to evade isocurvature bounds. We consider two of these briefly: Firstly, the field χ is heavy during inflation, so that $g\phi > H_{\rm inf}$. In this case, the isocurvature modes are suppressed. The challenge with this option is that at the end of inflation the field amplitude needs to be large enough so that the χ–field can play the role of DM (or at least be a non–negligible part of the DM sector). Alternatively, the dynamics of χ during inflation is non–standard, either by coupling χ to gravity (as in e.g. [150]) or by coupling χ directly to the inflaton field. In this case, the dark sector is bigger than just the fields ϕ and χ we consider here and it would be interesting to study this option further, also from the model–building perspective. For the rest of the chapter, however, we are dealing with the post–inflation period and assume that the isocurvature perturbations can be kept small.

For the numerical study in the following sections, we select initial conditions, taken at $z_i = 10^{14}$, such that $\phi_i \gg \phi_c$, i.e. $g\phi_i \gg \sqrt{\lambda}M$ from Eq. (5.14) and since $m_\chi \gg H$ we have

$$g\phi_i \gg H, \tag{5.15}$$

where a subscript i denotes quantities evaluated at the initial redshift z_i in the numerical simulations. On the other hand, as previously argued, ϕ must be rolling slowly so that $m_\phi^2 \ll H^2$. Assuming that μ is small compared to $g\chi$, the following constraint is obtained from Eq. (5.5):

$$g^2\chi^2 \ll H^2. \tag{5.16}$$

In the original hybrid inflation setting, it is well-understood that the oscillations of χ around the minimum do not play an important role since the potential is dominated by V_0 in the early stages of inflation. This is required in order to get a period of quasi de-Sitter expansion – it is 'quasi' in the sense that the exponential expansion must end at some point, to make way for radiation domination as is widely accepted in the big bang scenario. The energy scale of inflation is rather high, with $H \sim 10^{14}\,$GeV [151] and it is therefore natural to have V_0 dominate over the oscillating part in that case. In our late-time scenario, the oscillations of χ around 0 are expected to dominate the field dynamics in the early universe and at later times as well. Again, this is reasonable since in our model V_0 has to match the very small observational prediction for the cosmological constant $\rho_\Lambda \sim 10^{-47}\,{\rm GeV}^4$ [8]. This leaves a wide range of initial conditions for the χ field to dominate the potential in the early and late universe. During the matter-dominated epoch, the χ-field dominates the dynamics. As we will describe in more detail in the next section, the DM fractional energy density will eventually start to decrease. At the same time, the universe keeps expanding, and the ϕ-field keeps slowly varying until, finally, DE dominates the evolution, driven by the potential energy. Therefore, at early times we require

$$\frac{1}{2}\mu^2\phi^2 + V_0 \ll \frac{1}{2}g^2\phi^2\chi^2, \tag{5.17}$$

warranting a period of matter domination. From this, we infer

$$\begin{aligned}\rho_\chi &= \frac{1}{2}\dot{\chi}^2 + \frac{1}{2}m_\chi^2\chi^2 \\ &\approx m_\chi^2\chi^2,\end{aligned} \tag{5.18}$$

where we have used that $m_\chi \approx g\phi$ and relied on the fact that the rapidly oscillating χ-field is approximately pressureless when averaged over several oscillation periods. Note that because of how slowly ϕ is evolving, the effective DM mass is nearly constant. Solving for χ^2 and replacing in Eq. (5.16) leads to

$$g^2\frac{\rho_\chi}{m_\chi^2} \ll H^2. \tag{5.19}$$

During the matter-dominated era, when χ stands as the predominant contribution, the Friedmann equation can be approximated as

$$H^2 \approx \frac{\rho_\chi}{3\mathrm{M}_{\mathrm{Pl}}^2}. \tag{5.20}$$

Therefore, from Eq. (5.19), we arrive at the following condition

$$1 \ll \frac{1}{3}\left(\frac{\phi}{\mathrm{M}_{\mathrm{Pl}}}\right)^2, \tag{5.21}$$

where we have employed $m_\chi \approx g\phi$. The inequality above can only be satisfied if the ϕ-field is trans-Planckian, that is, if $\phi \gg \mathrm{M}_{\mathrm{Pl}}$. Therefore, ϕ must be at least of the order of the Planck scale to satisfy the constraint in Eq. (5.21) and fulfil the scenario intended in this theory. This condition is required in many inflationary models [151] and is still a debated subject in the literature. Indeed, in a quantum theory of gravity, one expects the presence of Planck-suppressed operators in the Lagrangian of the form $\frac{\phi^{4+n}}{\mathrm{M}_{\mathrm{Pl}}v^n}$ for $n \geq 1$; for large field values, these higher-order operators cannot be ignored in the quantum theory, which can lead to problems [152]. Since we are not concerned with a UV complete theory of quantum gravity in this work, we will accept that ϕ can take large values, up to and above the order of the Planck scale. Consequently, unless g is exceedingly small, this results in a considerably large DM mass, in direct contrast with models with ultralight and light scalar fields as DM candidates [90, 124, 153]. We remark that this can potentially be accommodated in the WIMPzilla scenario, proposed and analysed in [138] and [154], which considers heavy weakly interacting DM and shows that such particles can be created in large enough quantities in the early universe through e.g. gravitational production.

It is useful to note that in the previous paragraph we have assumed that the χ field makes up the entire dark matter content of the universe. However it may be the case that DM is actually made up of different components. Assuming that ρ_χ is only a fraction of the total DM energy density $\rho_{\rm DM}$, Eq. (5.15) becomes

$$1 \ll \frac{1}{3}\left(\frac{\rho_{\rm DM}}{\rho_\chi}\right)\left(\frac{\phi}{\rm M_{Pl}}\right)^2 . \tag{5.22}$$

It is therefore possible to ease the large-field constraint by considering cases where ρ_χ only makes up a small fraction of the whole DM content. However, one would need a comparatively small contribution due to the power of 2 in Eq. (5.22), making this model less relevant phenomenologically.

Another necessary condition for χ to be a viable DM particle candidate is that the scalar field must be stable. This means that the χ field does not decay efficiently into the ϕ field, since this decay channel is kinematically allowed due to the mass scale difference between the fields. We must therefore check that the decay rate Γ for this interaction is smaller than the Hubble rate of expansion when averaged over the oscillation time scale, i.e. $\Gamma < H$. Indeed, if the universe is expanding at a faster rate than the fields can interact, then the decay will not happen enough to change the energy of the fields significantly. The relevant interaction term in the Lagrangian is $\frac{1}{2}g^2\phi^2\chi^2$. This can be represented by a Feynman diagram associated to the following Feynman rule [155] shown in Fig. 5.2.

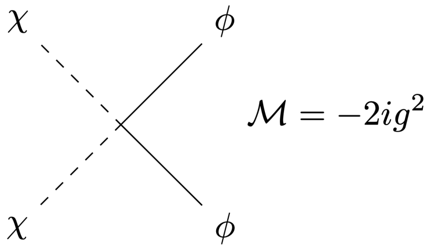

Figure 5.2: Feynman diagram for the two-to-two scattering interaction between ϕ and χ. $\mathcal{M}$ is the quantum amplitude associated with the corresponding interacting process.

The decay rate for a dark matter particle is given by $\Gamma = n\overline{\sigma v}$ [45], where n is the number density of the decaying particle, σ is the interaction cross-section and v is the particle velocity. The over-line denotes thermal averaging (usually denoted by angle brackets in the literature). It is straightforward to obtain the number density for the χ field,

$$n_\chi = m_\chi \langle \chi^2 \rangle, \tag{5.23}$$

where we averaged χ^2 over an oscillation cycle, as is required to see that the scalar field indeed behaves like dark matter. To calculate the thermally averaged cross-section, we follow the approach in [156, 157] and expand $\overline{\sigma v}$ in powers of x^{-1} where $x \equiv m_\chi/T$ and T is the temperature of the universe:

$$\overline{\sigma v}(x) = \sigma v|_{s=4m_\chi^2} + 6m_\chi^2 \left.\frac{\partial(\sigma v)}{\partial s}\right|_{s=4m_\chi^2} x^{-1} + \mathcal{O}(x^{-2}), \tag{5.24}$$

where s is a Mandelstam variable $s = (p_1 + p_2)^2$ and p_1 and p_2 are the four-momenta of both incoming particles. Let us clarify on why we evaluate at $s = 4m_\chi^2$: first, notice that expanding around small x^{-1} corresponds to the non-relativistic limit where $T << m_\chi$, which is equivalent to an expansion around $v = 0$ where v is the relative velocity $v = |\vec{v_1} - \vec{v_2}|$. It is easiest to work in the centre of mass frame, in which case one can write $p_1 = (E, \vec{p})$, $p_2 = (E, -\vec{p})$ and so

$$\begin{aligned} s = 4E^2 &= 4(m_\chi^2 + |\vec{p}|^2) \\ &\approx 4m_\chi^2\left(1 + \frac{v^2}{4}\right) \end{aligned} \tag{5.25}$$

where we have used the fact that the particles are non-relativistic in the second line. Note the factor of $\frac{1}{4}$ comes from the definition of the relative velocity in the centre of mass frame, where $v \approx 2\frac{|\vec{p}|}{m_\chi}$. Expanding around $v = 0$ is therefore analogous to expanding around $s = 4m_\chi^2$. In the following we will only take the above expansion to zeroth order. The calculation of this term is straightforward using the following general formula for a two-to-two scattering process [158, 159]

$$\sigma v = \frac{1}{16\pi\left((s - (m_1^2 + m_2^2)\right)\sqrt{\lambda_{12}}} \int_{t_1}^{t_0} dt |\mathcal{M}(s,t)|^2, \tag{5.26}$$

where $t = (p_1 - p_3)^2$ and $u = (p_1 - p_4)^2$ are the remaining two Mandelstam variables, p_3

and p_4 are the four-momenta of the outgoing particles, and

$$t_0 = \frac{1}{4s}\left[(m_1^2 - m_2^2 - m_3^2 + m_4^2)^2 - (\sqrt{\lambda_{12}} - \sqrt{\lambda_{34}})^2\right] \tag{5.27}$$

$$t_1 = \frac{1}{4s}\left[(m_1^2 - m_2^2 - m_3^2 + m_4^2)^2 - (\sqrt{\lambda_{12}} + \sqrt{\lambda_{34}})^2\right] \tag{5.28}$$

and

$$\lambda_{ij} \equiv (s - m_i^2 - m_j^2)^2 - 4m_i^2 m_j^2. \tag{5.29}$$

In our case, $m_{1,2} = m_\chi$ and $m_{3,4} = m_\phi$. This leads to

$$\overline{\sigma v} \approx \frac{g^4\sqrt{m_\chi^2 - m_\phi^2}}{8\pi m_\chi^3} \tag{5.30}$$

$$\approx \frac{g^4}{8\pi m_\chi^2} \tag{5.31}$$

$$\tag{5.32}$$

where we have used the fact that $m_\chi \gg m_\phi$ in the second line. The decay rate is therefore given by

$$\Gamma(\chi\chi \to \phi\phi) = \frac{g^4\langle\chi^2\rangle}{8\pi m_\chi}. \tag{5.33}$$

Due to the direct dependence of the amplitude on the χ field, and the fact that $\langle\chi^2\rangle \propto a^{-3}$ (see Section 5.4 for more details), we conclude that $\Gamma \propto a^{-3}$, while H scales as $a^{-3/2}$ and a^{-2} during matter and radiation dominated epochs respectively. This implies that the decay width drops much more rapidly than the expansion rate over the history of the universe. Consequently, for any sensible values of $g \leq 1$, the DM field will remain stable.

A final remark before we discuss the cosmological evolution of the system is whether quantum corrections to the potential can spoil the considerations above. In general, quantum corrections to the tree–level potential are expected to be of order $\mathrm{M}_{\mathrm{Pl}}^2$ (choosing M_{Pl} to be the natural cut–off). In supersymmetric theories, however, the corrections are of order $\ln(\phi/\mathrm{M}_{\mathrm{Pl}})$ [160]. These ln–corrections can be kept small if the coupling constants are small, which is a natural case for the model considered here.

5.4 Fluid approximation and dynamics

Since simulation of the oscillations in the χ-field are computationally expensive, we wish to find reasonable approximations allowing for the study of the cosmological evolution. More precisely, we recast our framework as an interacting quintessence model through a fluid description of the DM field χ. Despite its similarities with other scalar-field models of DM, one crucial difference in this scenario is that the mass of the DM field evolves as the DE field is slowly rolling. As seen in Section 4.1.3 it is a well-known result that one can describe its dynamics according to an oscillating envelope with amplitude $\mathcal{A}(t) \propto a^{-\frac{3}{2}}$. Employing the Wentzel-Kramer-Brillouin (WKB) approximation, we can solve for the dynamics of the oscillating scalar field χ using the conditions derived in the previous section ($g\phi \gg H$ and $\dot{\phi}/\phi \ll 1$). We want to solve

$$\ddot{\chi} + 3H\dot{\chi} + g^2\phi^2\chi = 0. \tag{5.34}$$

We set

$$\chi = e^{iA(t)} \tag{5.35}$$

and plug this into Eq. (5.34) to get

$$\dot{A}^2 - i\ddot{A} - 3Hi\dot{A} - g^2\phi^2 = 0. \tag{5.36}$$

Assuming that $\ddot{A} \ll g^2\phi^2$, we can find the following approximate solution for $\dot{A}$:

$$\dot{A} \approx \pm g\phi + \frac{3}{2}iH. \tag{5.37}$$

Taking the derivative and plugging back into Eq. (5.36), we get

$$\dot{A} = \frac{3}{2}iH \pm g\phi\left[1 \pm \frac{\dot{\phi}}{2g\phi^2}\right], \tag{5.38}$$

which can be integrated:

$$A \approx A_0 + i\frac{3}{2}\ln\left(\frac{a}{a_i}\right) \pm g\phi(t - t_i) + \frac{i}{2}\ln\left(\frac{\phi}{\phi_i}\right). \tag{5.39}$$

We therefore arrive at a solution of the form

$$\chi(t) = \chi_i\left(\frac{\phi_i}{\phi}\right)^{1/2}\left(\frac{a_i}{a}\right)^{3/2}\sin\left(g\phi\left(t - t_i\right)\right). \tag{5.40}$$

where χ_i is the initial amplitude of χ. Since ϕ is evolving slowly, the ratio ϕ_i/ϕ is practically constant, meaning that the χ-field behaves like pressureless dust according to $\rho_\chi \propto \chi^2 \propto a^{-3}$. Taking the expression for ρ_χ in Eq. (5.18), we gather that the energy density of DM averaged over an oscillation period is roughly given by

$$\langle \rho_\chi \rangle \approx \rho_{\chi,i} \left(\frac{\phi}{\phi_i} \right) \left(\frac{a_i}{a} \right)^3 , \tag{5.41}$$

where $\rho_{\chi,i} = \frac{1}{2} g^2 \phi_i^2 \chi_i^2$ is the energy density of χ at $t = t_i$.

For simplicity, since we will be considering time–scales much larger than the oscillation span, we drop the bracket notation henceforth, and oscillation-averaged quantities will always be implied. It is worth pointing out that the (averaged) density in Eq. (5.41) depends linearly on ϕ. Therefore, we obtain the following continuity equation for the oscillation-averaged interacting fluid:

$$\dot{\rho_\chi} + 3H\rho_\chi = \frac{\dot{\phi}}{\phi} \rho_\chi . \tag{5.42}$$

In this context, the equation of motion for the DE field is recast as

$$\ddot{\phi} + 3H\dot{\phi} = -\frac{1}{\phi} \rho_\chi . \tag{5.43}$$

The previous equation is entirely equivalent to a continuity equation for DE, assuming a perfect fluid description for the field as well, with $\rho_\phi \approx \dot{\phi}^2/2 + V_0$ and $p_\phi \approx \dot{\phi}^2/2 - V_0$:

$$\dot{\rho_\phi} + 3H(\rho_\phi + P_\phi) = -\frac{\dot{\phi}}{\phi} \rho_\chi , \tag{5.44}$$

following conservation of the total energy density of both ϕ and χ, as required by the general covariance of Einstein's equations. According to the approximation in Eq. (5.41), Eq. (5.43) becomes

$$\frac{1}{a^3} \frac{d}{dt} \left(a^3 \dot{\phi} \right) = -\frac{\rho_{\chi,i}}{\phi_i} \left(\frac{a_i}{a} \right)^3 , \tag{5.45}$$

which, when integrated with respect to time, yields the following expression for the rate of change of the field, $\dot{\phi}$:

$$\dot{\phi} = \left(\frac{a_i}{a} \right)^3 \left(K_i - \frac{\rho_{\chi,i}}{\phi_i} t \right) , \tag{5.46}$$

where $K_i \equiv \dot{\phi}_i + \frac{\rho_{\chi,i}}{\phi_i} t_i$ is an integration constant and $\dot{\phi}_i$ is the initial field velocity, that is when $a(t_i) = a_i$. Hence, provided that the relation between a and t is known, the behaviour of ϕ is fully determined. As verified in the previous section, the fluid approximation yields a suitable description after inflation since the χ-field starts oscillating around 0 after this period has ended, and radiation becomes the dominant contributor in the universe at $t = t_i$. Consequently, solving Eq. (5.46) in the radiation-dominated epoch, during which $a(t) \propto t^{1/2}$, we obtain

$$\phi(t) = \phi_i + C_i - A_i \left(\frac{t}{t_i}\right)^{\frac{1}{2}} - B_i \left(\frac{t}{t_i}\right)^{-\frac{1}{2}}, \tag{5.47}$$

where $C_i \equiv 2\left(\frac{\rho_{\chi,i}}{\phi_i} t_i^2 + K_i t_i\right)$, $A_i \equiv 2\frac{\rho_{\chi,i}}{\phi_i} t_i^2$ and $B_i \equiv 2K_i t_i$ are constants. Therefore during this period, the energy density of ϕ scales according to

$$\rho_\phi \propto \dot{\phi}^2 \propto a^{-1}. \tag{5.48}$$

Eq. (5.47) sets the field's evolution until the matter-radiation equality at $t_{\rm eq}$. When the matter-dominated era begins, $a(t) \propto t^{2/3}$ which leads to the following solution of Eq. (5.46):

$$\phi(t) = \phi_{\rm eq} + C_{\rm eq} - A_{\rm eq} \ln\left(\frac{t}{t_{\rm eq}}\right) - B_{\rm eq} \left(\frac{t}{t_{\rm eq}}\right)^{-1}, \tag{5.49}$$

where equivalently $C_{\rm eq} \equiv t_{\rm eq} K_{\rm eq}$, $A_{\rm eq} \equiv t_{\rm eq}^2 \frac{\rho_{\chi,{\rm eq}}}{\phi_{\rm eq}}$, and $B_{\rm eq} \equiv t_{\rm eq} K_{\rm eq}$ are constants depending on initial conditions taken at radiation-matter equality, denoted by the subscript 'eq'. The constant $K_{\rm eq}$ is defined in analogy to K_i in Eq. (5.46), with each quantity taken at time $t_{\rm eq}$ instead of t_i. Since the field is slow-rolling, it is reasonable to assume $\dot{\phi}_{\rm eq} \ll t_{\rm eq}\rho_{\chi,{\rm eq}}/\phi_{\rm eq}$, resulting in $B_{\rm eq} \approx t_{\rm eq} A_{\rm eq}$. It is worth noting that Eq. (5.49) implies that $\dot{\phi} \propto a^{-\frac{3}{2}}$ since $t \propto a^{\frac{3}{2}}$ during matter domination. Moreover, considering that the coupling to DM is the main driver of the field's dynamics and accordingly $\dot{\phi}^2 \gg V_0$, we arrive at

$$\rho_\phi \propto \dot{\phi}^2 \propto a^{-3}. \tag{5.50}$$

It is noteworthy that, during this regime, the DE component scales with ordinary matter and CDM. This scaling is not a general feature of interacting dark energy models with a constant potential, making this model novel in this regard. Solutions of this kind are relevant to address the cosmic coincidence problem of ΛCDM concerning the comparable magnitude for the energy density of DE (Λ in the standard model) and CDM at present [161–164]. In the Section 5.6, we illustrate and analyse the dynamics in this regime through numerical simulations.

The form of the coupling term on the right-hand side of Eq. (5.42) implies that ϕ must be large up until the current cosmological era, in line with the discussion in Section 5.3, as required to avoid drastic deviations from the ΛCDM case. Albeit counter-intuitive at first glance, this framework hinges on the fact that ϕ is rolling slowly as $\dot{\phi}/(\phi H) \ll 1$, which we have also confirmed numerically, implying that $\phi > M_{\rm Pl}$, according to Eq. (5.21).

From a mathematical point of view, the result of the fluid approximation of the system considered here is analogous to encapsulating the effect of a 5th–force, mediated by a dark energy scalar field, in a conformally rescaled metric that determines the geodesics for the dark matter particles $\widetilde{g}_{\mu\nu}$, as given in Section 4.2 by

$$\widetilde{g}_{\mu\nu} = C\left(\phi\right) g_{\mu\nu}, \tag{5.51}$$

in terms of the gravitational metric $g_{\mu\nu}$, with the conformal factor identified as

$$C(\phi) = \frac{\phi^2}{M_{\rm Pl}^2} \quad \text{for } |\phi| > |\phi_c|, \tag{5.52}$$

see Eq. (5.14) for definition of the critical field value. The transformation is always invertible as $|\phi| > |\phi_c|$. Note that the fluid approximation will break down well before ϕ can approach 0. Moreover, it follows that $C\left(\phi\right) > 0$ and the Lorentzian signature of the metric is preserved, avoiding any instabilities related to metric singularities. In this framework, the form of the energy transfer function for the fluid approximation is recovered and reads:

$$Q = -\frac{C_{,\phi}}{2C}\rho_\chi = -\frac{\rho_\chi}{\phi}. \tag{5.53}$$

By modelling both components of the dark sector as perfect fluids, it is possible to rewrite the relevant dynamical equations, such as the conservation relations. We use conformal time in our numerical work. The equations for the DM and DE fluids read

$$\rho_\chi' + 3\mathcal{H}\rho_\chi = -Q\phi' = \frac{\phi'}{\phi}\rho_\chi, \tag{5.54}$$

$$\rho_\phi' + 3\mathcal{H}\left(\rho_\phi + p_\phi\right) = Q\phi' = -\frac{\phi'}{\phi}\rho_\chi. \tag{5.55}$$

These equations lay out the energy exchange between the fluids, with the direction directly related to the sign of ϕ'/ϕ. If this ratio is positive, it is DE sourcing the DM component, while if it is negative, there will be an energy flow from ϕ to the dark matter fluid. Regardless of the initial conditions chosen, we find that ϕ and ϕ' always have opposite signs. Consequently, this model exhibits a unidirectional energy transfer from the χ fluid to the ϕ-field. The modified Klein-Gordon equation encodes the same information:

$$\phi'' + 2\mathcal{H}\phi' = -\frac{a^2}{\phi}\rho_\chi = a^2 Q, \tag{5.56}$$

and can be numerically integrated for different realisations of the system yielding particular solutions for the dynamical evolution of the model.

For numerical purposes, the only free model-specific parameters are the initial conditions for the DE scalar field $\phi_i = \phi\left(\tau_i\right)$ and $\phi'_i = \phi'\left(\tau_i\right)$ and the scale of the hybrid potential V_0. It is important to note that the parameters in the potential energy in Eq. (5.2) drop out completely from the calculation, meaning we do not need to choose their values to solve the system numerically so long as we assume that they satisfy the constraints derived in Section 5.3. However, we set μ equal to zero for simplicity since it does not contribute up to current times. Without loss of generality, we compute V_0 through a shooting method for the fiducial value of the present DE relative energy density: $\Omega^0_\phi = \rho^0_\phi/(3\mathrm{M}^2_{\mathrm{Pl}} H^2_0)$. Moreover, and as previously mentioned, the value of ϕ'_i has no impact on the dynamics as the scalar field is quickly driven towards the minimum deep in the radiation-dominated epoch where its contribution is negligible. For this reason, and without loss of generality, in the numerical study, we always take $\phi'_i = 0$. In this way, the analysis presented can be focused on the effects of varying the only free parameter: the initial condition for the scalar field ϕ_i. We will focus only on scenarios for which $\phi_i > 0$, as the solutions for $\phi_i < 0$ would lead to the same dynamics starting from the opposite side of the symmetric potential.

5.5 Cosmological perturbations and observables

Following the discussion on the background evolution, we now map the cosmological perturbations onto an interacting DE model. We are interested in studying the modifications to the gravitational interaction in contrast to ΛCDM and assessing the measurable imprints left by the approximations made at the background level. For this purpose, we consider perturbations in the Newtonian gauge [165], corresponding to the following line element

$$ds^2 = a^2(\tau)\left[-\left(1+2\Psi\right)d\tau^2 + \left(1-2\Phi\right)\delta_{ij}dx^i dx^j\right], \tag{5.57}$$

where $\Psi(\tau,\vec{x})$ and $\Phi(\tau,\vec{x})$ are the conventional Newtonian scalar potentials. For the remainder of this section, a δ denotes perturbed quantities, and since we are dealing with a system of scalar fields, the anisotropic stress vanishes. Moreover, we work in Fourier space, such that the mapping $\nabla^2 \to -k^2$ holds for the spatial derivatives of the respective quantities.

The equations of motion for $\delta\phi$ and $\delta\rho_\chi$ in the coupled DE framework are

$$\delta\phi'' + 2\mathcal{H}\delta\phi' + k^2\delta\phi = \left(\Psi' + 3\Phi'\right)\phi' + 2a^2 Q\Psi + a^2\delta Q, \tag{5.58}$$

$$\delta'_\chi = -(\theta_\chi - 3\Phi') + \frac{Q}{\rho_\chi}\phi'\delta_\chi - \frac{Q}{\rho_\chi}\delta\phi' - \frac{\theta'}{\rho_\chi}\delta Q, \tag{5.59}$$

where we have defined the density contrast $\delta_\chi = \delta\rho_\chi/\rho_\chi$, θ_χ is the DM velocity perturbation and the perturbed coupling δQ is given by

$$\delta Q = \frac{\rho_\chi\delta\phi - \phi\delta\rho_\chi}{\phi^2}. \tag{5.60}$$

It is worth remarking that in Eq. (5.59), both the equation of state $w_\chi = \frac{p_\chi}{\rho_\chi}$ and the sound speed $c_s^2 = \frac{\delta p_\chi}{\delta\rho_\chi}$ of the DM fluid were set to zero. The former assumption is motivated by the study of the background dynamics in the previous section, while the latter is justified when looking at the explicit form of the sound speed for an oscillating scalar field, which under this approximation becomes [124],

$$c_s^2 = \frac{k^2/(4m_\chi^2 a^2)}{1 + k^2/(4m_\chi^2 a^2)}. \tag{5.61}$$

This equation strictly holds for an uncoupled scalar field, but since the coupling considered here is small, it captures the essential physics. Since m_χ is required to be considerably large in our model and we are considering scales $k \ll 2m_\chi a$, it is a reasonable assumption to take $c_s^2 = 0$, which we have also confirmed numerically.

To better appreciate the influence of the coupling on the evolution of the density matter perturbations, we look at scales in the sub-horizon limit ($k \gg \mathcal{H}$) together with the quasi-static approximation. The latter relies on the matter and field perturbations being the main contributors to the time variation of the gravitational potentials. In practice, this implies neglecting the time derivatives of the perturbations and metric potentials, leading to the following simplification for the equation of motion for δ_χ (neglecting the contribution of baryons) [166, 167]:

$$\delta''_\chi + \mathcal{H}_{\text{eff}}\delta'_\chi \simeq 4\pi G_{\text{eff}}\rho_\chi\delta_\chi, \tag{5.62}$$

where we have defined the effective Hubble term

$$\mathcal{H}_{\text{eff}} = \mathcal{H}\left(1 + \frac{Q}{\rho_\chi}\frac{\phi'}{\mathcal{H}}\right), \tag{5.63}$$

which involves an additional friction contribution related to the changes to the background expansion evolution, and the effective gravitational constant, which in the small-scale limit (large k) becomes dominant and is given simply as

$$G_{\text{eff}} \simeq G_N\left(1 + 2\mathrm{M}_{\mathrm{Pl}}^2\frac{Q^2}{\rho_\chi^2}\right), \tag{5.64}$$

as expected according to the general results for scalar-tensor gravity models under a conformal transformation [168–170].

5.6 Phenomenology

In this section, we explore the dynamics of DM and DE, discuss the main signatures left by the hybrid dark sector on the cosmological observables, and compare the predictions against ΛCDM. As expected, the qualitative features of the model are in line with standard coupled quintessence scenarios with constant effective interactions [129, 130] (see [8, 171–181] for recent studies). Nevertheless, there are distinct quantitative signatures due to the slow-rolling of the scalar field, on which we wish to focus. For illustration purposes, we consider four different realisations of the evolution of the model, characterised by $\phi_i/\mathrm{M}_{\mathrm{Pl}} = \{8, 10, 15, 20\}$, with ϕ_i being the free parameter responsible for setting not only the initial dynamics of the scalar field but also the strength of the coupling in the dark sector. The initial velocity is kept constant at $\phi'_i = 0$ since it has no significant impact on the overall dynamics, as we will verify in more detail below. The cosmological parameters are fixed to standard Planck 2018 fiducial values for a ΛCDM cosmology [8]: $H_0 = 67.56$ km/s/Mpc for the Hubble parameter, and $\Omega_b h^2 = 0.022$ and $\Omega_c h^2 = 0.12$ for the relative energy density of the baryon and dark matter fluids, with $h = H_0/100$. The Friedmann constraint sets the scale of the potential. For the perturbative analysis, we assume Gaussian adiabatic initial conditions, a scalar power spectrum with an amplitude of curvature fluctuations $A_s = 2.215 \times 10^{-9}$ at the pivot scale $k_{\text{piv}} = 0.05\ \mathrm{Mpc}^{-1}$, and with spectral index $n_s = 0.962$. Moreover, and without

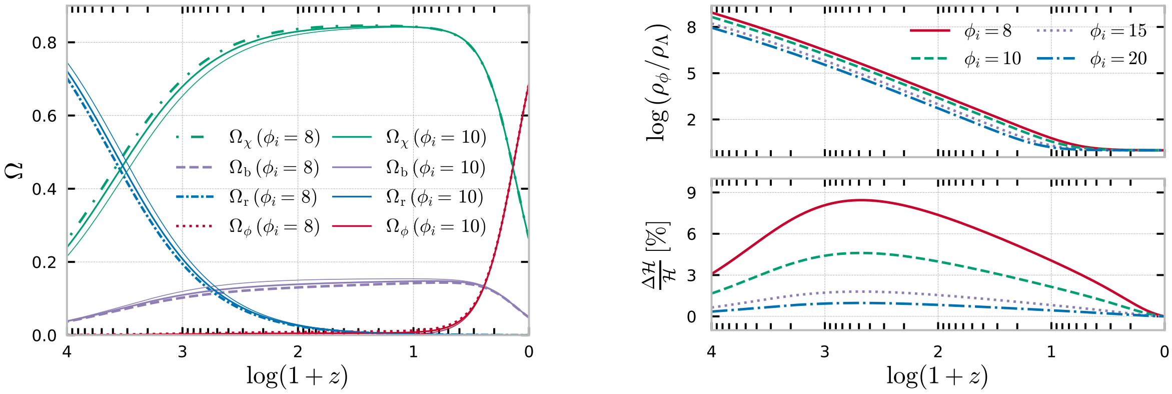

Figure 5.3: *Left panel:* Redshift evolution of the relative energy densities Ω_i of the dark matter fluid χ, baryons, radiation and the scalar field ϕ for the hybrid model. ϕ_i values are given in Planck units. *Right panel:* Ratio of the dark energy density (*top panel*) and fractional deviations in the Hubble rate (*bottom panel*) in the hybrid coupled model with respect to the standard model as a function of redshift $1 + z$, for different values of ϕ_i.

loss of generality, we assume vanishing initial conditions for the scalar field perturbation and its corresponding velocity, that is, $\delta\phi_i = \delta\phi_i' = 0$. To calculate the evolution of the background and cosmological perturbations, we adapted the publicly available `CLASS` code[1] [123, 182, 183] for our purposes.

5.6.1 Background evolution

Since the potential $V(\phi, \chi)$ is constant in the fluid approximation, in the absence of the coupling the field remains static, making its evolution indistinguishable from a cosmological constant. However, when the coupling is turned on, the interaction between DM and DE drives the evolution of the DE field, as shown in the left panel of Fig. 5.4. When the coupling becomes relevant – at the end of the radiation domination epoch – the field ϕ begins to evolve slowly and its energy density starts to track that of the DM to which it couples. During this phase, the scalar field behaves effectively like a pressureless fluid, although contrary to the DM field it is not oscillating. This scaling regime ends when the kinetic energy of the field becomes comparable to its potential energy, set by V_0, i.e. when $\phi'^2 \approx a^2 V_0$. The transition out of this regime is also influenced by the initial value of the field ϕ_i, as it sets the value of ϕ' (see Eq. (5.46)). A higher value of ϕ_i leads to dynamics which are closer to ΛCDM, and therefore the field exits the scaling

---

[1] https://github.com/lesgourg/class_public

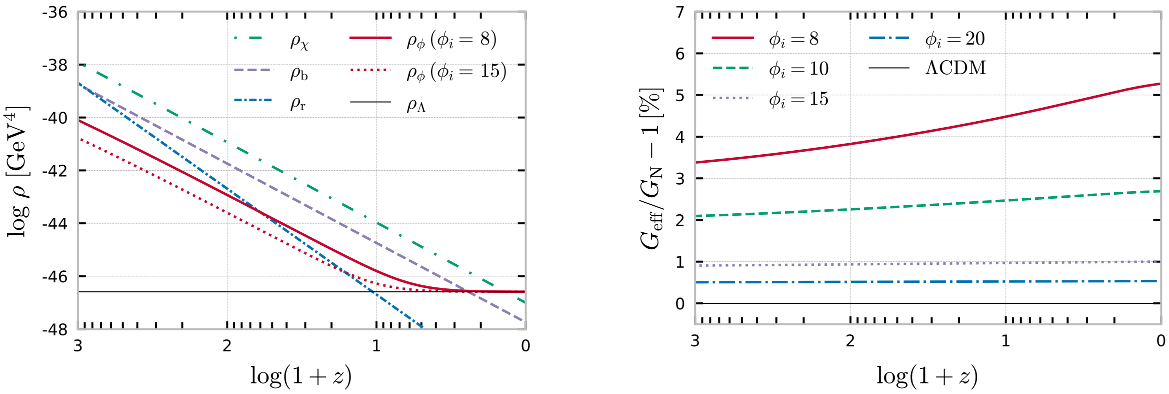

Figure 5.4: *Left panel:* Evolution of the energy densities ρ of the dark matter fluid χ, baryons, radiation and the scalar field ϕ for $\phi_i = 8$ $\mathrm{M_{Pl}}$. To appreciate the differences, we also include ρ_ϕ for the $\phi_i = 15$ $\mathrm{M_{Pl}}$ case and ρ_Λ for the standard model for completeness. *Right panel:* Percentage deviations of the effective gravitational constant, as defined in Eq. (5.64), with respect to the standard G_N for $\phi_i = \{8, 10, 15, 20\}$ $\mathrm{M_{Pl}}$.

regime earlier (see right panel of Fig. 5.3 and left panel of Fig. 5.4). On the other hand, ϕ' is rapidly adjusted, regardless of the initial velocity, as the field is driven down the effective potential. This means that ϕ'_i only sets the start of the scaling period, which happens earlier for higher initial velocities. Since this transition happens during radiation domination, it does not change the background dynamics of the model as both DM and DE are subdominant during that epoch. A similar effect has been identified in [184], driven by a significant acceleration of the scalar field instead. When the $\phi-$field exits the matter-scaling regime, it heads towards a cosmological constant-like attractor solution, where it will keep slowly rolling down until the fluid approximation breaks down.

The impact of the coupling is also evident in the amplification of ρ_ϕ during the scaling regime for higher coupling values (smaller ϕ_i). This leads to slightly earlier matter-dark energy equality. The DM density is also increased in these cases, to compensate for DM losing energy to DE. This results in an earlier radiation-matter equality, as can be seen in the left panel of Fig. 5.3.

In the lower right panel of Fig. 5.3, we show the percentage deviations in the Hubble rate $H(z)$ for the hybrid model compared to ΛCDM. Despite fixing H_0 to its ΛCDM value, we observe up to a 9% increase in $H(z)$ for the lowest value of ϕ_i considered. This increase is only present during matter-domination, and is due to the enhanced densities ρ_χ and ρ_ϕ. It will be useful to refer to this result when studying the growth of matter perturbations at different scales. We now turn our attention to the evolution of

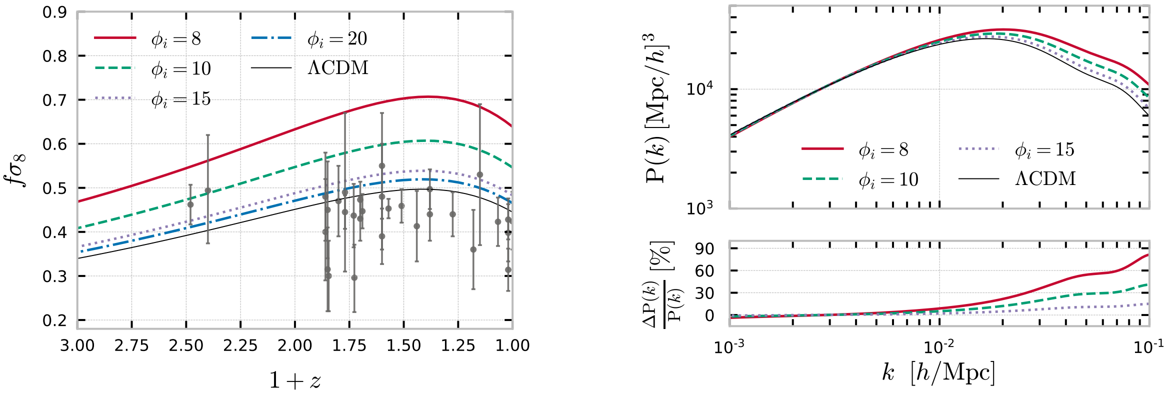

Figure 5.5: *Left panel:* Evolution of the cosmological observable $f\sigma_8$ (defined in Eq. (5.67)) with redshift $1+z$ for the hybrid coupled model with a range of ϕ_i values and for the ΛCDM case. The redshift distortion space data points and corresponding error bars correspond to the compilation presented in [28]. *Right panel:* The matter power spectrum as a function of Fourier scales k (*top panel*) and corresponding percentage deviations (*bottom panel*), for the hybrid coupled model with respect to the ΛCDM case (thin black solid line).

cosmological perturbations.

5.6.2 Cosmological perturbations

The linear growth rate $f(z,k)$, of the total matter perturbation (i.e. both baryons and DM) δ_m, parametrises their evolution and is defined by

$$f(z,k) = \frac{1}{\mathcal{H}} \frac{\delta'_m(z,k)}{\delta_m(z,k)}, \tag{5.65}$$

where

$$\delta_m(z,k) = \frac{\Omega_b \delta_b + \Omega_{\mathrm{DM}} \delta_{\mathrm{DM}}}{\Omega_b + \Omega_{\mathrm{DM}}}. \tag{5.66}$$

In the above equation, the b subscript stands for baryons. The departure in the evolution of $f(z,k)$ in the hybrid model in contrast with ΛCDM coincides with the onset of the matter-dominated era when the coupling in the dark sector becomes important. The combined variable $f\sigma_8$ is directly connected to data since it is a scale-independent physical quantity that can be statistically constrained by observations of the growth of structures at different redshifts [185] and is expressed as

$$f\sigma_8(z, k_{\sigma_8}) = \frac{\sigma_8(0, k_{\sigma_8})}{\mathcal{H}} \frac{\delta'_m(z, k_{\sigma_8})}{\delta_m(0, k_{\sigma_8})}, \tag{5.67}$$

where σ_8 is the root mean square mass fluctuation amplitude for spheres of size $8h^{-1}$ Mpc (or equivalently for Fourier scales $k_{\sigma_8} = 0.125h$ Mpc^{-1}), parametrised as

$$\sigma_8(z, k_{\sigma_8}) = \sigma_8(0, k_{\sigma_8}) \frac{\delta_m(z, k_{\sigma_8})}{\delta_m(0, k_{\sigma_8})}, \tag{5.68}$$

and it is generally used to set the amplitude of the matter power spectrum at present $\sigma_8^0 \equiv \sigma_8(0, k_{\sigma_8})$.

Observations of redshift-space distortions (RSD) are a probe for the evolution of the matter perturbations. This effect arises from a Doppler shift ascribed to changes in the peculiar velocities of galaxies moving in clusters. Hence it can be used as a probe for the linear growth of structures and is observed as an additional contribution to the expansion redshift, with the redshift distribution of galaxies appearing 'distorted'.

The left panel of Fig. 5.5 shows how $f\sigma_8$ evolves with redshift for different coupling values. In all cases with non-zero coupling, we see an enhancement in the linear growth of matter perturbations which is maximised for the lowest values of ϕ_i. This can be traced back to the modifications in the expansion history discussed above. For context, we also include observational data of RSD[2] from the compilation in [28] (see references therein) which include observations from various surveys. As is visible in the plots, the enhancement in linear growth $f\sigma_8$ in the hybrid model goes in the wrong direction to match the data optimally. Indeed, by fixing the primordial perturbations amplitude A_s, a higher $f\sigma_8$ means a higher σ_8. In these conditions, we conclude that the model may struggle to address the S_8 tension, although only a more thorough analysis could confirm this since the data analysis implicitly assumes the ΛCDM model.

The right panel of Fig. 5.5 plots the matter power spectrum $P(k)$ (top) and the relative deviations from ΛCDM (bottom). On large scales (low k), we find a small suppression, while on smaller scales (higher k) the power is significantly enhanced. For the smallest value of ϕ_i, the deviation reaches 81% at $k = 10^{-1}h$Mpc^{-1} – at this scale, the linear approximation starts to break down as non-linear effects become important. This scale-dependent behaviour is expected: the modified gravitational constant affects the growth of perturbations more strongly on small scales, especially for low ϕ_i. The slight suppression at large scales can be explained by the changes in the expansion rate $H(z)$. A higher $H(z)$ leads to a larger friction term in Eq. (5.63), which inhibits the growth of matter perturbations. This effect dominates over the fifth-force only on the largest scales, and is negligible for large values of ϕ_i. Lastly, we note that the turnover

---

[2] https://gitlab.com/federicomarulli/CosmoBolognaLib

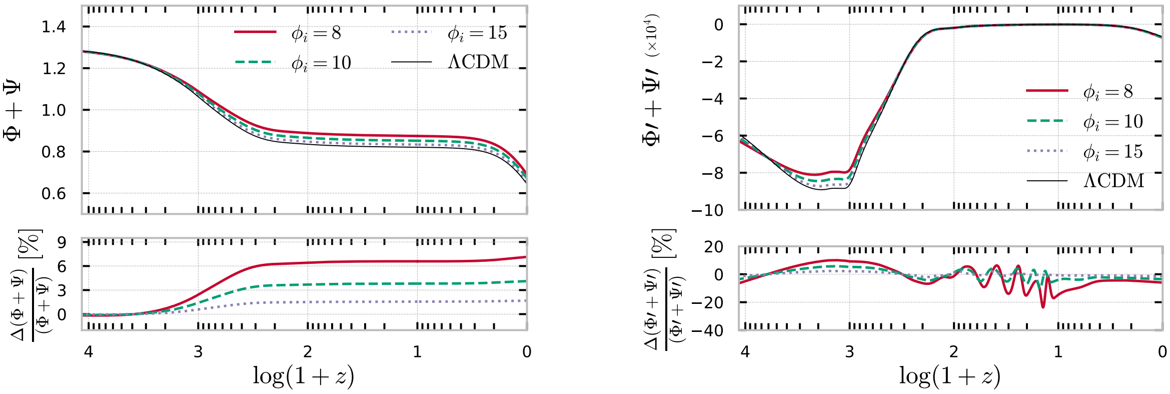

Figure 5.6: Redshift evolution of the sum of the gravitational potentials, $\Phi + \Psi$, (*top left panel*) and the corresponding derivative with respect to conformal time, $\Phi' + \Psi'$ (*top right panel*) for the hybrid coupled model with $\phi_i = \{8, 10, 15\}$ $\mathrm{M_{Pl}}$ and for the ΛCDM case, including the percentage deviations from the standard model (*bottom panels*).

scale in the matter power spectrum is shifted towards smaller scales compared to ΛCDM. This is due to the change of radiation-matter equality towards larger redshifts.

In the left panel of Fig. 5.6, we present the redshift evolution of the gravitational potentials $\Phi + \Psi$ (top) along with their relative deviations from ΛCDM (bottom), for a representative intermediate scale $k = 0.01$ Mpc^{-1}. The most significant deviations occur during the matter-dominated era, which is when the expansion rate varies most from ΛCDM and ρ_ϕ scales like matter. We show the lensing power spectrum $C_\ell^{\phi\phi}$, which depends on the lensing potential $\phi_{lens} = \Phi + \Psi$ via its source term in the line-of-sight integral, in the left panel of Fig. 5.7. We find that $C_\ell^{\phi\phi}$ is enhanced across all angular scales, which is consistent with the increased lensing potential. This boost could help explain the excess lensing signal observed in Planck temperature data, as mentioned in Chapter 3. Physically, this enhancement can be explained by the evolution of the matter density contrast δ_m, which increases due to the stronger effective gravitational interaction between DM particles (as seen in Fig. 5.4).

Similar features are imprinted in the CMB TT power spectrum, shown in the right panel of Fig. 5.7. The dominant contribution to the modifications arises from the ISW effect, which is sourced by the derivative of the lensing potential (see right panel of Fig. 5.6). This includes both an early contribution – resulting in an increase of the time-derivative due to earlier onset of matter domination – and a late-time contribution – induced by the non-trivial dynamics of the dark sector, leading to changes in the lensing of the CMB by large scale structures. The late-time ISW effect also tends to suppress

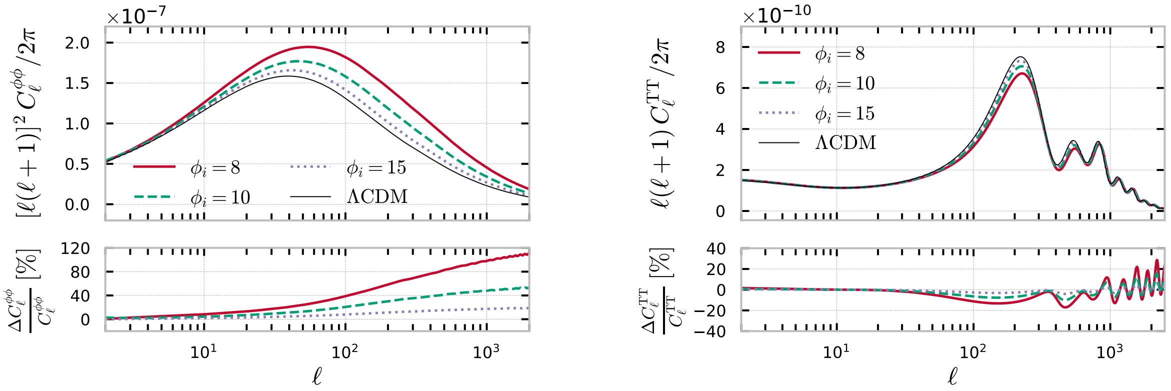

Figure 5.7: Lensing (*top left panel*) and TT (*top right panel*) power spectra as a function of the angular scale ℓ for the hybrid coupled model with $\phi_i = \{8, 10, 15\}$ $\mathrm{M_{Pl}}$ and for the ΛCDM case, along with the fractional deviations from the standard model (*bottom panels*).

$\Phi' + \Psi'$ at low redshifts. We also observe a suppression in the amplitude of the peaks and troughs of the TT spectrum, along with a narrowing of their widths. These changes are associated with the decrease of the baryon to DM energy density ratio ρ_b/ρ_ϕ (due to increased DM density) around recombination, which is a well-known signature in the literature [176, 186]. This effect induces a degeneracy between the coupling strength (i.e. ϕ_i) and H_0, as both parameters impact the amplitude and position of the first acoustic peak. Additionally, the shift of the peaks to higher multipoles is a consequence of the modified expansion history. In particular, the change in distance to the last scattering surface leads to a smaller value for the sound horizon at the drag epoch compared to ΛCDM. In both panels of Fig. 5.7, the increased Hubble rate leads to a systematic shift in power towards smaller angular scales.

5.7 Conclusions

In this chapter, we have proposed a hybrid model for the dark sector, in which DM and DE originate from two interacting scalar fields. We employed a form of potential commonly used in hybrid inflation to model the DM–DE system. The cosmology in this setup is studied in considerable detail. The heavy scalar field quickly oscillates from deep inside the radiation-dominated epoch and consequently behaves like pressureless DM. We have shown that, once the heavy field starts to oscillate rapidly, the two scalar fields can be described by a DM fluid coupled to a slowly evolving DE field.

To finish, we highlight the following predictions of the model proposed:

- We find that the DE field must have a large field value today ($\phi > \mathrm{M_{Pl}}$) so that the fluid description is valid. Consequently, the coupling between DM and DE is relatively small today, and the DM is very heavy (similar to DM in the WIMPZilla scenario). At the same time, the energy scales in the potential are significantly reduced compared to the Planck scale. The mass scale M is of order eV or so, depending on the coupling constant λ. The fact that this model requires super-Planckian field excursions, like in inflationary scenarios, provides a challenge to model building in theories beyond the standard model. But it is interesting to note that the model proposed here combines two mass scales: the small mass scale M and the large field excursions for the DE field ϕ.

- Another prediction of the model is that the epoch of dark energy domination is transient. In future, the DM field becomes light and will no longer behave like a pressureless fluid. Both scalar fields will settle at the true minimum of the potential (at $\phi = 0$ and $\chi = \pm M$). The universe's future will then depend on whether space is closed. If the universe is closed, the expansion will stop and collapse, opening up the possibility of a bounce in the long-distant future.

As we have seen, if the coupling is large enough today, the DE field leaves distinct signatures on the temperature-temperature power spectrum of CMB anisotropies and in the growth of structures encoded in the matter power spectrum. These characteristic changes can be tested against current and future observational data. A more thorough and detailed study is highly desirable, resorting to different independent data sets and sampling the remaining relevant cosmological parameters. We will describe this work in the next chapter.

Chapter 6

Alleviating cosmological tensions with a hybrid dark sector

6.1 Introduction

In the last chapter we introduced a hybrid dark sector model to describe a shared origin for DM and DE. Starting from two scalar fields, we derived a one-parameter extension to ΛCDM adding a coupling between DE and DM. The coupling is inversely proportional to the initial value of the DE field ϕ_i. This parameter governs the coupling strength between DM and DE, mediating the energy transfer from the DM fluid to the DE field. The interaction modifies the expansion history and offers a potential resolution to the Hubble and S_8 tensions while aligning with recent preferences for dynamical dark energy [13, 187–193]. In this chapter, we constrain the hybrid model using current cosmological data, assuming adiabatic initial conditions for the cosmological perturbations.

The chapter is organised as follows. After introducing the model in Section 6.2, we detail the methodology followed in this analysis and present and discuss the results in Section 6.3. We conclude our work in Section 6.4, where we also present an outlook for future directions of investigation.

6.2 A hybrid model for the dark sector

As introduced in Chapter 5, the hybrid dark sector model is a coupled scalar field model based on the hybrid inflation potential. After averaging out the fast oscillations of the χ

DM field, we are left with a DM fluid ρ_c[1] interacting with a DE scalar ϕ, whose evolutions are described by Eqs. (5.42), (5.43) respectively. The coupling between DM and DE is proportional to $1/\phi$, meaning the system's modified dynamics are fully determined by the initial value of the DE field, ϕ_i. As shown in Chapter 5, the DE scalar field is invariably driven towards the minimum of the potential at very early stages when its contribution is effectively negligible for the cosmological evolution. For this reason, the initial velocity of the DE scalar field $\dot{\phi}_i$ does not have a relevant impact on the dynamics, and so, without loss of generality, we always set $\dot{\phi}_i = 0$. This model is thus a one-parameter extension of the ΛCDM model.[2] For the data analysis in the following sections, we sample the initial value of the coupling parameter $1/\phi_i$, which is more intuitive and defines a compact parameter range. In the limit $1/\phi_i \to 0$, ΛCDM is recovered. Larger coupling values (corresponding to ϕ_i closer to the theoretical limit in Eq. (5.21)) lead to greater deviations from standard cosmology.

We demonstrate the main effect of the coupling in Fig. 6.1, showing deviations from ΛCDM by introducing the following reparametrization of the background DE density [167, 194]:

$$\rho_{\phi,\text{eff}}(a) = \rho_\phi + \rho_c(a) - \rho_{c,0}a^{-3}. \tag{6.1}$$

The quantity $\rho_{\phi,\text{eff}}$ describes an effective dark energy fluid, which includes the DE component plus the non-standard component of DM arising due to the interaction in the dark sector, effectively mimicking an uncoupled dark sector at the level of the background. In other words, it encloses the deviation from the standard ΛCDM evolution in a single component. The evolution of $\rho_{\phi,\text{eff}}$ is given by

$$\dot{\rho}_{\phi,\text{eff}} + 3H\rho_{\phi,\text{eff}}(1 + w_{\phi,\text{eff}}) = 0 \ , \tag{6.2}$$

where we have defined the effective equation of state

$$w_{\phi,\text{eff}} = \frac{p_\phi}{\rho_{\phi,\text{eff}}}. \tag{6.3}$$

This effective equation of state is the equation of state of DE, assuming an uncoupled DM species, as it is usually taken as given when analysing low-redshift data such as supernovae. In Figure 6.1, we show the equation of state parameter of this effective dark

---

[1] In this chapter we refer to the DM fluid as ρ_c rather than ρ_χ in order to align with the ΛCDM notation.

[2] In this framework, V_0 is merely the scale of the potential, not a true degree of freedom, that is used to numerically enforce the closure relation $\sum_i \Omega_i = 1$ through a shooting method.

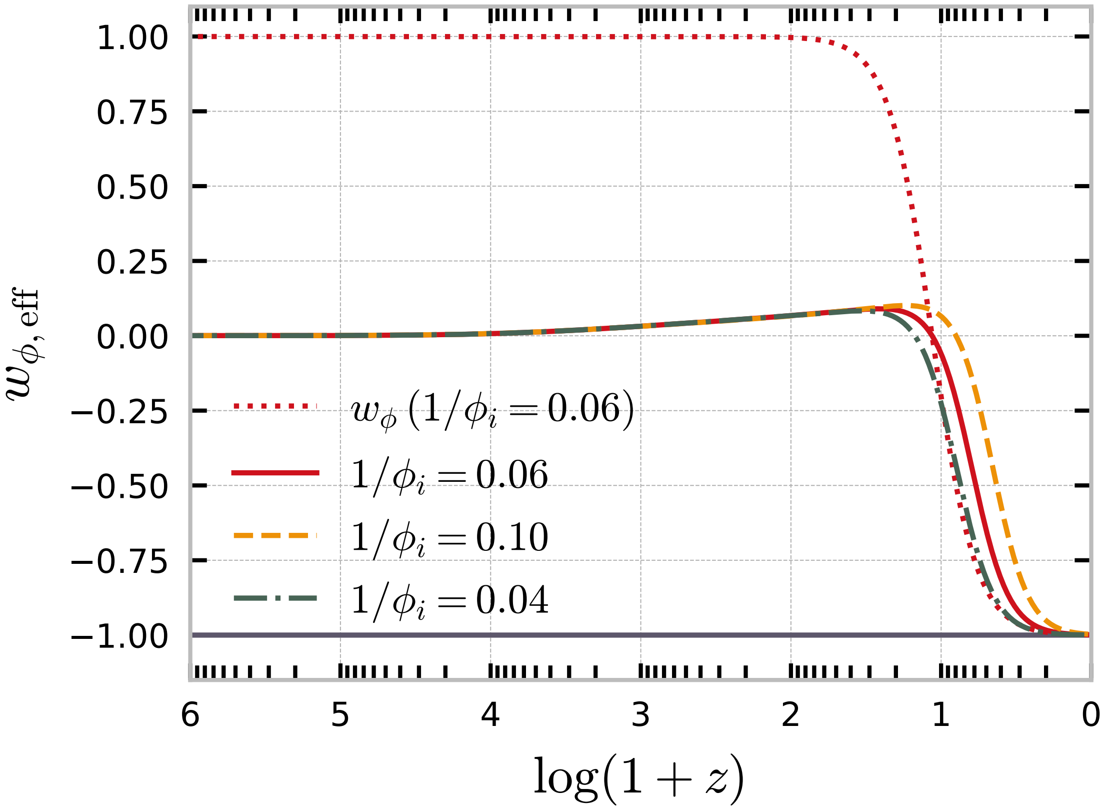

Figure 6.1: Effective DE equation of state parameter for different values of ϕ_i. All cosmological parameters are fixed to the mean values for the hybrid model under the Pl18+DESI data combination (see Section 6.3.1) for various values of the coupling parameter $1/\phi_i$. We also show the equation of state parameter for the ϕ DE scalar field for the Pl18+DESI scenario in the red dotted line.

energy sector, supposing standard CDM evolution.

The effective DE behaviour can be investigated from the individual evolutions of ρ_c and ρ_ϕ: as described in Chapter 5, the ρ_ϕ component tracks the DM during the matter domination era until its kinetic part decays enough for the constant potential to take over, at which point it transitions to a cosmological constant. The ρ_c component starts as standard CDM at early times, then diluting faster than a^{-3} when the ϕ field starts to evolve, and the coupling turns on. As a result, the effective DE field behaves as an additional DM component at early times until matter domination. At this point, the effective EoS becomes positive and $\rho_{\phi,\mathrm{eff}}$ is dominated by the ρ_c contribution. At late times, the EoS transitions back to that of a cosmological constant. This means that, effectively, a fraction of the DM energy density becomes DE at late times. Although it resembles tracking dark energy (e.g. [195]), it is also different from such models as the DE field does not always scale with the dominant component in this effective description.

It is also important to note that the coupling constant g present in the potential in Eq. (5.3) is absent from the effective fluid equations (see Chapter 5 for more details), meaning that its value cannot be constrained under this fluid approximation. This, in turn, implies that the masses of DM and DE are not constrained in this model, as they depend linearly on g. Conversely, in Section 6.3.2, we will use our best-fit results to derive an upper limit on g.

The dynamics of the hybrid model also introduce modifications at the level of the linear perturbations in comparison to ΛCDM. We refer to Chapter 5 for the complete derivation of the perturbation equations and a discussion of the evolution of cosmological perturbations in this model. This work aims to constrain the hybrid model with cosmological data, which is the focus of the remainder of the chapter.

6.3 Analysis

6.3.1 Methodology and datasets

We implement the relevant equations for the hybrid model in our modified version of the Einstein-Boltzmann solver code `CLASS`. We perform a Markov Chain Monte Carlo (MCMC) analysis by interfacing the solver with the publicly available sampler `Monte Python`[3] [196, 197] to confront the hybrid model with recent cosmological data. Cosmological and nuisance parameters are varied according to Cholesky's parameter decom-

---

[3] https://github.com/brinckmann/montepython_public

Parameter	Prior
$\Omega_b h^2$	$[0.005, 0.1]$
$\Omega_c h^2$	$[0.001, 0.99]$
$100\theta_s$	$[0.5, 10]$
τ_{reio}	$[0.02, 0.08]$
n_s	$[0.7, 1.3]$
$\log(10^{10} A_s)$	$[1.7, 5.0]$
$1/\phi_i$	$[0, 1]$

Table 6.1: Flat priors on the cosmological and model parameters sampled in this work.

position [198]. We consider chains to be converged with the Gelman-Rubin convergence criterion $R - 1 < 0.01$ [199]. The corresponding chains are treated and analysed using the `GetDist`[4] Python package [200].

We assume wide uniform priors for the set of sampled cosmological parameters

$$\{\Omega_b h^2, \Omega_c h^2, 100\theta_s, \tau_{\rm reio}, n_s, \log(10^{10} A_s)\}$$

in the range detailed in Table 6.1. These are the standard ΛCDM parameters, namely the physical density of baryonic matter today, the physical density of dark matter today, the angular scale of the sound horizon at the time of last scattering, the optical depth to reionisation, the scalar spectral index, and the amplitude of the primordial scalar power spectrum at the pivot scale $k_{\rm pivot} = 0.05\,{\rm Mpc}^{-1}$. Regarding the free parameter of the hybrid model, the initial condition of the dark energy scalar field ϕ_i, we opt for sampling over its inverse $1/\phi_i$ to reduce the impact of the diverging parameter space in which the model reduces to the ΛCDM limit ($\phi_i \gg 1$), with a uniform prior covering the range of validity of the model's assumptions. The other independent parameters are fixed to their Planck best-fit values [8], including the assumption of two massless and one massive neutrino species with $m_\nu = 0.06\,{\rm eV}$. Although not explicitly listed, a large number of nuisance parameters are varied simultaneously, following the respective collaboration recommendations.

Our baseline datasets are the ones listed below:

- **Planck 2018 (Pl18)**: The Planck-2018 CMB high-ℓ TTTEEE, low-ℓ TTEE, and lensing likelihoods [5, 8, 201]. Specifically, this includes the high-ℓ `Plik` likelihood for TT over the range $30 \leq \ell \leq 2508$, and for TE and EE within $30 \leq \ell \leq 1996$, combined with the low-ℓ TT and EE likelihoods for $2 \leq \ell \leq 29$, based on the

---

[4] https://github.com/cmbant/getdist

`Commander` algorithm and the `SimAll` likelihood (see references above for detail on these likelihoods). Although newer versions of the Planck likelihood have been developed [106, 107], we use the baseline collaboration likelihood and expect only slightly tighter constraints with alternative likelihoods, which will not impact our main results.

- **DESI**: The BAO measurements obtained from the first year of Dark Energy Spectroscopic Instrument (DESI) observations. These data are based on galaxy and quasar observations [202] as well as Lyman-α tracers [203], as detailed in Table I of Ref. [13]. Covering an effective redshift range of approximately $z \sim 0.1 - 4.1$, the measurements include the transverse comoving distance (d_M/r_d), the Hubble horizon (d_H/r_d), and the angle-averaged distance (d_V/r_d), each normalised to the comoving sound horizon at the drag epoch, r_d. The appropriate correlations between measurements of d_M/r_d and d_H/r_d are considered in the computations.

- **Pantheon+ (SN)**: The Pantheon+ catalogue distance modulus measurements derived from 1701 light curves of 1550 Type Ia supernovae (SNeIa), detected spectroscopically, spanning a redshift range of $0.001 < z < 2.26$. The data, compiled in the Pantheon+ sample [55, 204], include observed magnitudes post-processed for systematic effects, with residual corrections and marginalisation over nuisance parameters [205]. These can be translated into uncalibrated luminosity distances of the SNeIa.

- **Pantheon+ with SH0ES R22 (SH0ES)**: In our analysis, we consider the Pantheon+ sample with and without the SH0ES Cepheid host distance anchors as calibrators [14], typically employed to address degeneracies in the $M - H_0$ plane (where M is the absolute magnitude, see Section 3.3.2).

Our baseline dataset is Planck 2018, denoted as "Pl18", to which we incrementally add other combinations to assess the constraints imposed by each dataset on the model. Separate combinations with DESI BAO and Pantheon+ data are referred to as "Pl18+DESI" and "Pl18+SN", respectively, while the full addition of background data to the CMB is denoted as "Pl18+DESI+SN". Finally, whenever the SH0ES Cepheid anchors are considered, the "SN" data is represented as "SH0ES", and the inclusion of all datasets is denoted as "Pl18+DESI+SH0ES".

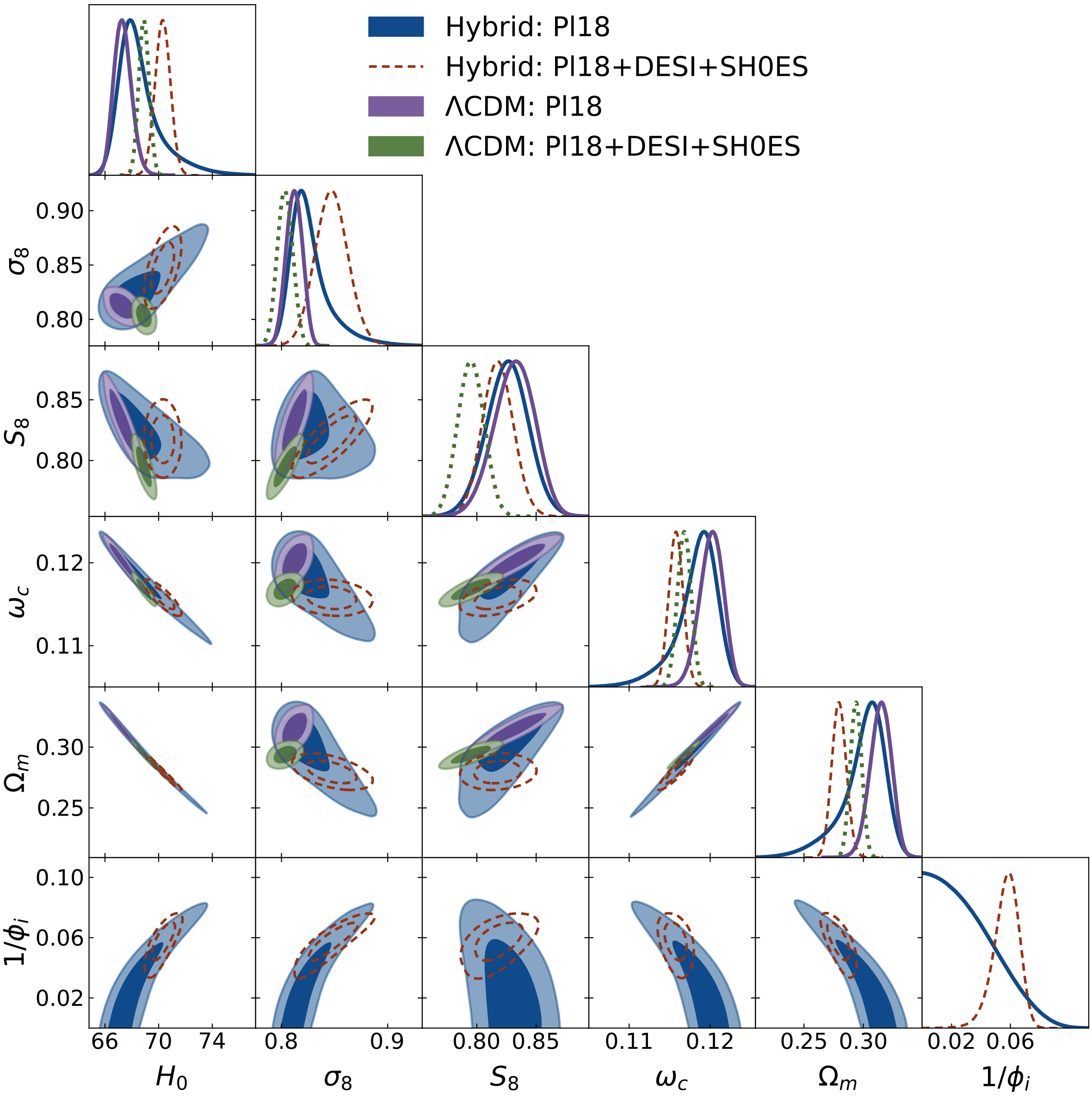

Figure 6.2: One-dimensional posterior probability distribution functions and two-dimensional contours at 68% and 95% CL for the parameters of interest in the hybrid model and the standard ΛCDM model for reference, for the minimal Pl18 dataset and the full combination Pl18+DESI+SH0ES, as indicated in the legend and listed in Section 6.3.1.

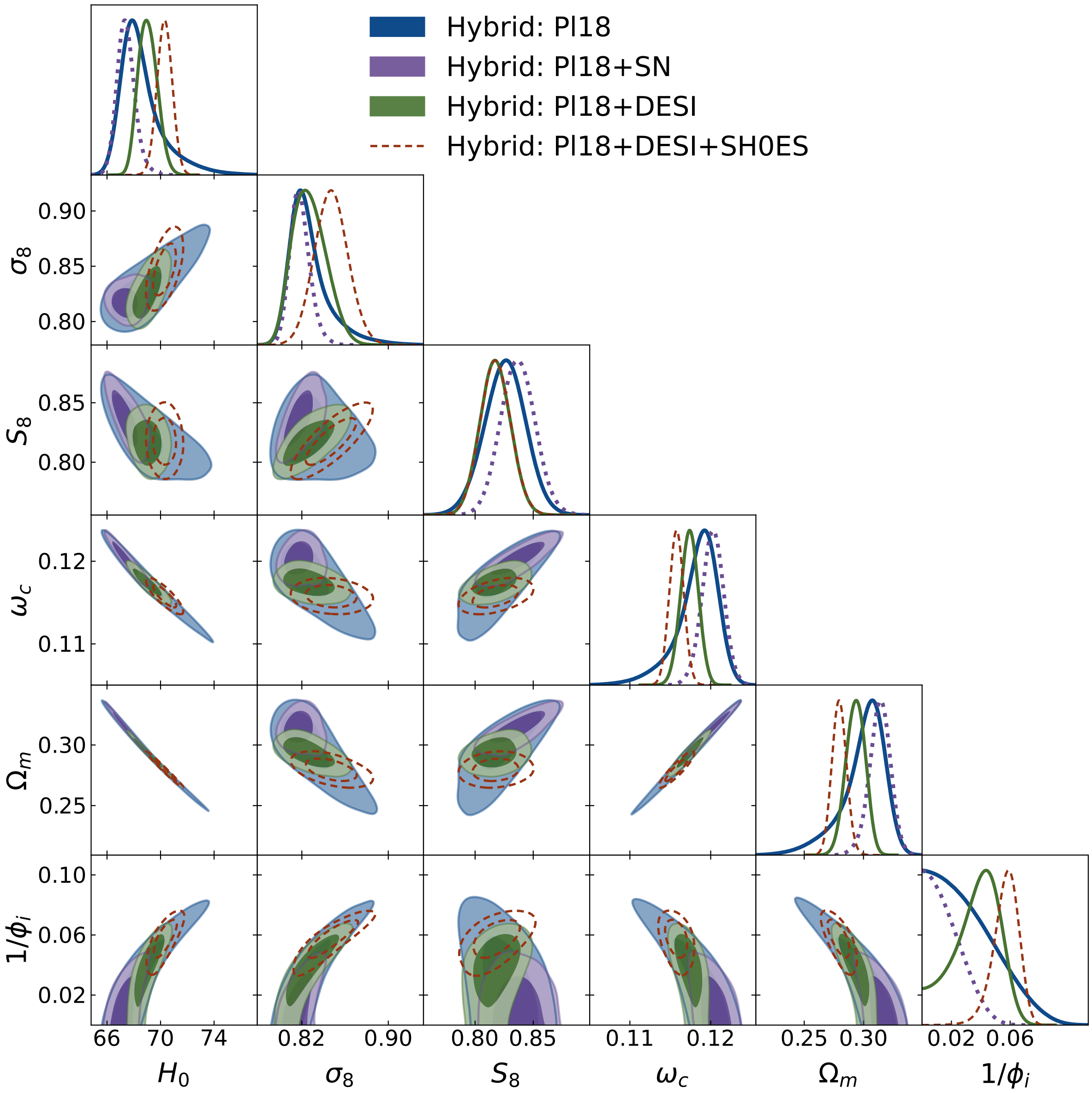

Figure 6.3: One-dimensional posterior probability distribution functions and two-dimensional contours at 68% and 95% CL for the parameters of interest in the hybrid model for incremental dataset combinations, as indicated in the legend and listed in Section 6.3.1.

Parameter	**Pl18**	**Pl18+SN**	**Pl18+SH0ES**	**Pl18+DESI**	**Pl18+DESI+SN**	**Pl18+DESI+SH0ES**
$\omega_{\rm b}$	0.02236 ± 0.00015	0.02231 ± 0.00014	0.02237 ± 0.00015	0.02240 ± 0.00015	0.02239 ± 0.00015	0.02237 ± 0.00015
$\omega_{\rm c}$	$0.1184^{+0.0029}_{-0.0016}$	0.1202 ± 0.0014	0.1139 ± 0.0014	0.1174 ± 0.0011	0.11820 ± 0.00099	0.11577 ± 0.00089
$100\theta_s$	1.04187 ± 0.00030	1.04182 ± 0.00029	1.04190 ± 0.00030	1.04193 ± 0.00030	1.04194 ± 0.00029	1.04188 ± 0.00029
$\tau_{\rm reio}$	0.0548 ± 0.0077	0.0539 ± 0.0077	0.0558 ± 0.0079	0.0557 ± 0.0079	0.0557 ± 0.0077	0.0554 ± 0.0078
n_s	0.9660 ± 0.0045	0.9640 ± 0.0041	0.9683 ± 0.0041	0.9677 ± 0.0040	0.9673 ± 0.0039	0.9670 ± 0.0041
$\log 10^{10} A_s$	3.047 ± 0.016	3.046 ± 0.016	3.049 ± 0.016	3.047 ± 0.016	3.047 ± 0.016	3.048 ± 0.016
$1/\phi_i$	< 0.0390	< 0.0220	$0.0661^{+0.0095}_{-0.0073}$	$0.037^{+0.019}_{-0.012}$	$0.029^{+0.017}_{-0.015}$	$0.0570^{+0.0096}_{-0.0070}$
Best-fit:	[0.0054]	[0.0019]	[0.0676]	[0.0455]	[0.0341]	[0.0591]
σ_8	$0.8263^{+0.0095}_{-0.021}$	$0.8185^{+0.0079}_{-0.010}$	0.858 ± 0.017	$0.827^{+0.013}_{-0.018}$	$0.821^{+0.010}_{-0.015}$	0.847 ± 0.015
H_0	$68.55^{+0.80}_{-1.8}$	$67.42^{+0.59}_{-0.72}$	71.49 ± 0.87	$69.04^{+0.65}_{-0.76}$	$68.51^{+0.51}_{-0.63}$	70.30 ± 0.56
Ω_m	$0.300^{+0.021}_{-0.011}$	$0.3138^{+0.0093}_{-0.0084}$	0.2669 ± 0.0091	0.2934 ± 0.0080	$0.2997^{+0.0073}_{-0.0065}$	0.2796 ± 0.0061
S_8	0.826 ± 0.018	0.837 ± 0.015	0.809 ± 0.014	0.817 ± 0.013	0.821 ± 0.013	0.818 ± 0.013
$\Delta\chi^2_{\rm min}$	0.14	0.08	-16.32	-2.8	-1.06	-12.76
$\log B_{\rm M,\Lambda CDM}$	-3.3	-3.6	4.5	-2.0	-2.8	2.5
$Q_{\rm DMAP}^{\rm SH0ES}$	$--$	4.78	$--$	$--$	4.65	$--$

Table 6.2: Observational constraints at a 68% confidence level on the independent and derived cosmological parameters using different dataset combinations for the hybrid model, as detailed in Section 6.3.1. $\Delta\chi^2_{\rm min}$ represents the difference in the best-fit χ^2 of the profile likelihood global minimisation, and $\log B_{\rm M,\Lambda CDM}$ indicates the ratio of the Bayesian evidence, both computed with respect to ΛCDM. The value of $Q_{\rm DMAP}^{\rm SH0ES}$ is calculated according to Eq. (6.4). For reference, the same results for ΛCDM are given in Table B.1 of Appendix B.

6.3.2 Results

In this section, we discuss the constraints placed by each dataset combination on the hybrid model in direct comparison with the ΛCDM model. Table 6.2 summarises the results of the analysis described in Section 6.3.1 for the Pl18, Pl18+SN, Pl18+SH0ES, Pl18+DESI, Pl18+DESI+SN, Pl18+DESI+SH0ES datasets at the 68% confidence level (CL). The corresponding 1D and 2D marginalised posterior distributions are depicted in Figs. 6.2, 6.3 for relevant parameters and key data combinations at 68% and 95% CL. Similar tables for the same datasets in the ΛCDM model can be found in Appendix B.

To determine the model preference in terms of the fit to each data combination, we report the difference in the value of the minimum χ^2 with respect to the ΛCDM model, $\Delta\chi^2_{\rm min} = \chi^2_{\rm min,\,Hybrid} - \chi^2_{\rm min,\,\Lambda CDM}$, computed through a global minimisation approach using the simulated-annealing optimiser `Procoli`[5] package [206] – see Appendix B for more detail. A negative value of $\Delta\chi^2_{\rm min}$ indicates a better fit for the hybrid model, while a positive value suggests otherwise. Additionally, we report on the Bayesian evidence

---

[5] https://github.com/tkarwal/procoli

$\log B_{\mathrm{M},\Lambda\mathrm{CDM}}$ test for model comparison, for which we employed the public `MCEvidence`[6] code [207, 208]. The greater the evidence for the hybrid model relative to ΛCDM, the larger the Bayes factor ratio (the difference of the logarithms) will be. Furthermore, if its value is negative, there is no evidence supporting the hybrid model over ΛCDM for a given dataset, while the opposite holds if it is positive.

Finally, the *difference of the maximum a posteriori* (DMAP) metric tension for H_0 given a particular dataset D is [209]

$$Q^{\mathrm{SH0ES}}_{\mathrm{DMAP,\,D}} = \sqrt{\chi^2_{\mathrm{min}}(\mathrm{D} + M_B) - \chi^2_{\mathrm{min}}(\mathrm{D})}, \tag{6.4}$$

and is used to assess the compatibility between the constraints derived for the model under the dataset D and the SH0ES prior on the value of H_0.[7] This method has the added benefit of being insensitive to prior volume effects, and the global maximum likelihood values are derived directly from `Procoli`.

At the end of Table 6.2, we list the $\Delta\chi^2_{\mathrm{min}}$ values and the associated Bayesian evidence compared to ΛCDM for all the data combinations, and also the $Q^{\mathrm{SH0ES}}_{\mathrm{DMAP,\,D}}$ tension for the relevant cases. In Table B.2 of Appendix B, we list in detail the χ^2_{min} values associated with each likelihood for the different models and data combinations used in this study.

We summarise our main findings below, based on the results in the above figures and tables.

Starting with the baseline CMB Pl18 dataset, we note that the fit is similar to ΛCDM as evidenced by $\Delta\chi^2_{\mathrm{min}} = 0.14$. There is no preference for a non-zero value of $1/\phi_i$ at 1σ, as $1/\phi_i < 0.0390$. The constraints on other parameters are overall similar to ΛCDM as can be seen in Fig. 6.2, but the large tail in the distribution due to the weak constraint on $1/\phi_i$ leads to small deviations, as well as a worse Bayesian evidence (this is exacerbated by the fact that we have one extra parameter in the theory). However, we observe a positive (negative) correlation between $1/\phi_i$ and H_0 (S_8), which hints at the potential of this model to alleviate cosmological tensions. Note that the H_0 correlation remains for all dataset combinations whilst the S_8 correlation weakens as additional datasets are introduced (see Fig. 6.3).

Adding BAO data from DESI to Pl18 improves the constraining power by breaking

---

[6] https://github.com/yabebalFantaye/MCEvidence

[7] The formulation of the DMAP metric tension in Eq. (6.4) is only valid for datasets differing by one degree of freedom. Since when imposing the SH0ES calibration as listed in Section 6.3.1 we consider only a sub-sample of the supernovae in the entire Pantheon+ catalogue, we opt instead for replacing the full SH0ES likelihood with the Pantheon+ sample plus a Gaussian prior on the absolute magnitude calibration M_B of the supernovae in SH0ES [14]. We use this approximation for the sole purpose of computing $Q^{\mathrm{SH0ES}}_{\mathrm{DMAP,\,D}}$, and we have confirmed that it does not impact the results.

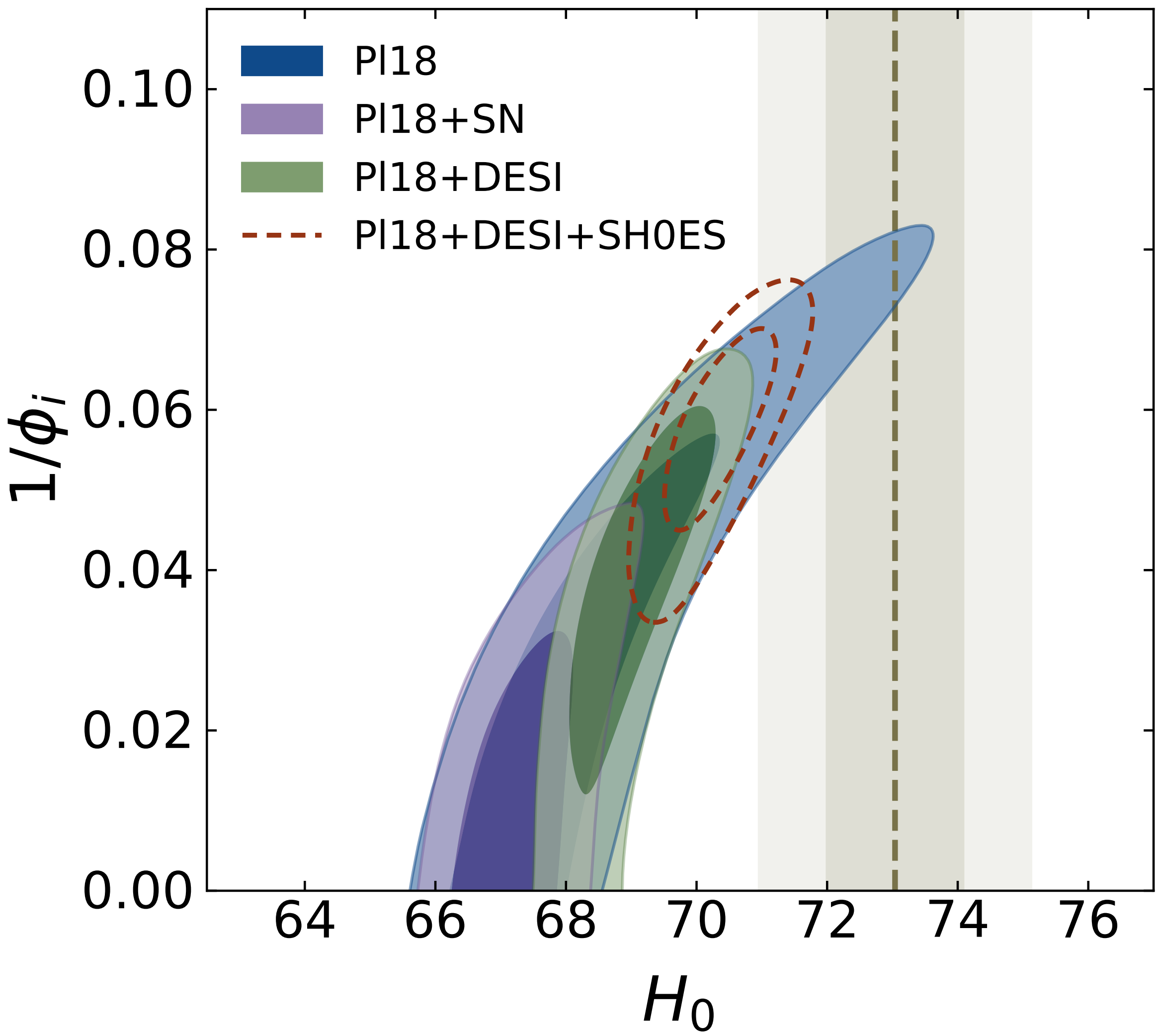

Figure 6.4: 2D contours at 68% and 95% CL for the initial condition of the scalar field $1/\phi_i$ and the Hubble parameter H_0 (in units of km/s/Mpc). The results are inferred considering different combinations of Planck 2018, DESI BAO distance, and SN distance moduli data. The grey dashed line and band represent the value of H_0 measured by the SH0ES collaboration and the respective uncertainties.

geometrical degeneracies in the CMB. Moreover, it is known that DESI favours dynamical DE at late times [13] and this preference shows up here too. The coupling is detected at 2σ level, with $1/\phi_i = 0.037^{+0.025}_{-0.033}$ at 95% CL. This can be seen in Fig. 6.3 as a defined peak in the 1D posterior for $1/\phi_i$. Consequently, this leads to narrower constraints on other cosmological parameters. The hybrid model fits this data combination better than the baseline, with $\Delta\chi^2_{\rm min} = -2.8$, but this is not enough to favour it over ΛCDM in terms of Bayesian evidence.

The combination of Pl18+SN provides a similar fit to ΛCDM, with narrower constraints and a slight aversion to a non-zero coupling, with $1/\phi_i < 0.0220$. However, adding the SH0ES prior changes things, increasing H_0 and providing a 3σ detection of the coupling with $1/\phi_i = 0.066^{+0.019}_{-0.028}$ at 99% CL.

Considering Pl18+DESI+SN, we see that the constraints are close to those of Pl18 + DESI. However, there is a decrease in the degree of preference for a non-zero coupling, with only a 1σ detection: $1/\phi_i = 0.029^{+0.017}_{-0.015}$ at 68% CL. This can be explained by the addition of SN, which prefer a value closer to zero for the coupling. The addition of the SH0ES prior once again increases the value of H_0 and leads to a 3σ detection for the coupling with $1/\phi_i = 0.057^{+0.019}_{-0.029}$ at 99% CL.

It is important to note that the SH0ES prior in both cases increases the quality of the fit drastically, with $\Delta\chi^2_{\rm min} = -16.32$ for Pl18+SH0ES and $\Delta\chi^2_{\rm min} = -12.76$ for Pl18+DESI+SH0ES. The Bayesian evidence increases, leading to a strong to moderate preference for the hybrid model over ΛCDM according to Jeffreys' scale. However, the $Q^{\rm SH0ES}_{\rm DMAP}$ indicator shows that there is still a large residual tension between the datasets. The breakdown of $\chi^2_{\rm min}$ in Table B.2 shows that the tension is indeed hidden in a worsened fit to the Pl18 and DESI likelihoods compared to the case without the SH0ES calibration. With respect to ΛCDM, there is a better fit to Pl18 and SH0ES in the hybrid case but a worse fit to DESI.

Overall, the hybrid model leads to a slight alleviation of the H_0 tension, with $Q^{\rm SH0ES}_{{\rm DMAP},\,Pl18+SN} = 4.78\sigma$ and $Q^{\rm SH0ES}_{\rm DMAP,\,Pl18+DESI+SN} = 4.65\sigma$, compared to $Q^{\rm SH0ES}_{\rm DMAP,\,Pl18+SN} = 6.25\sigma$ and $Q^{\rm SH0ES}_{\rm DMAP,\,Pl18+DESI+SN} = 5.76\sigma$ for ΛCDM. This means the hybrid model provides only a mild reduction of the H_0 tension. The H_0 tension is of the same order regardless of the inclusion of DESI in the baseline dataset because the posteriors obtained are compatible at 1σ, and the value of H_0 predicted is too low in both cases compared to SH0ES. Once the SH0ES calibration is added to the analysis, the predicted value of $H_0 \sim 70$ is a compromise between the two incompatible values (the value preferred by SH0ES and the value preferred by the datasets without the prior), reflecting the tension

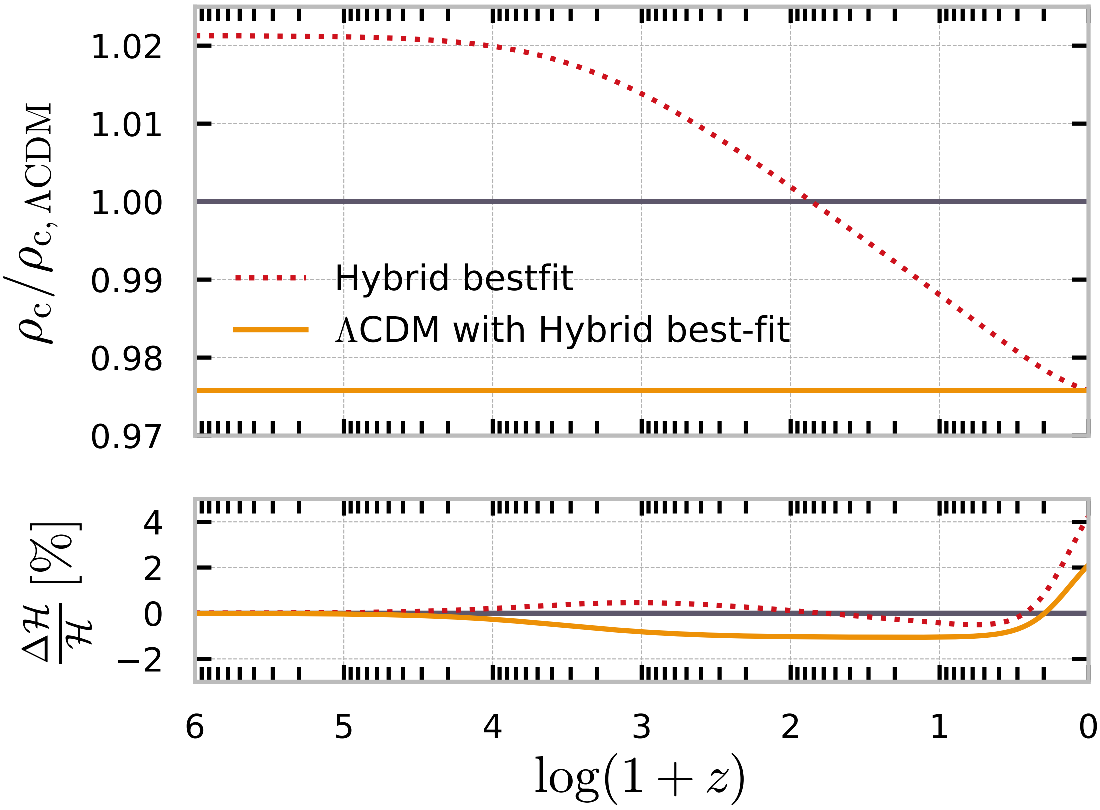

Figure 6.5: *Top panel*: Redshift evolution of the dark matter energy density for the hybrid model and ΛCDM model, with cosmological parameters fixed to the best-fit of the hybrid model under the Pl18+DESI+SH0ES dataset combination in both cases. The corresponding baseline case of the ΛCDM best-fit is shown in grey for reference. *Bottom panel*: Percent relative deviations in the value of the Hubble rate with respect to the ΛCDM Pl18+DESI+SH0ES best-fit for the same scenarios.

in the datasets under the model under consideration. This effect is illustrated in Fig. 6.4, where we display the 2D contours for the model parameter $1/\phi_i$ and H_0 for the incremental datasets used in this analysis.

We can explore the origin of the correlation between $1/\phi_i$ and H_0 by looking at the behaviour of $\omega_{\mathrm{c}} \equiv \Omega_c h^2$ shown in Fig. 6.3. Indeed, there is a negative correlation between $1/\phi_i$ and ω_c, i.e. a stronger interaction leads to smaller values for ω_c. A smaller ω_{c} allows to compensate the larger h, yielding an overall smaller Ω_m, which helps in keeping the angular diameter distance to recombination (and therefore the angular size of the sound horizon) fixed. Note that this mechanism is different from regular dynamical dark energy, which requires a phantom behaviour [109].

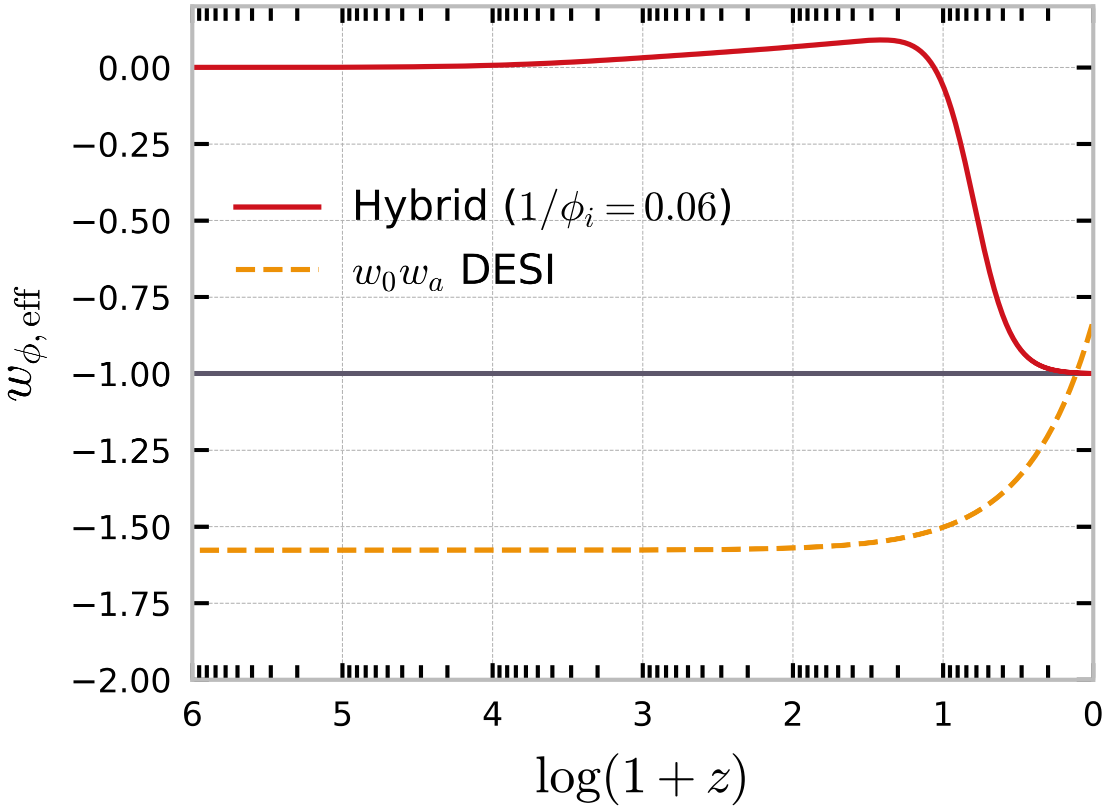

Figure 6.6: Redshift evolution of the effective EoS parameter of DE in the hybrid model with the Pl18+DESI+SH0ES best-fit compared with the EoS parameter for DE reported by the DESI collaboration for a CPL $w_0 w_a$ parametrisation $w(a) = w_0 + (1-a)w_a$ [29,30] under Pl18+DESI+SN with best-fit values $w_0 = -0.827$ and $w_a = -0.75$ [13].

In Fig. 6.5, we illustrate the impact of the interaction on the evolution of the DM density. We fix cosmological parameters to the best-fit values obtained with the Pl18+DESI+SH0ES dataset combination for the hybrid model. We divide the DM density by the DM density in ΛCDM, for the best-fit values from the ΛCDM analysis. We can see that if our model behaved like ΛCDM, this would lead to an overall reduction in DM density due to lower ω_c. However, we can see that in the hybrid model this ratio is redshift-dependent. At early times, we have a higher ρ_c and at late times the ratio becomes smaller than in ΛCDM. This can be explained by considering Eq. (6.3): this tells us that there is an additional redshift-dependent component to DM, on top of the traditional CDM component. This extra component starts decaying quicker than normal DM (see Fig. 6.1) which leads to a lower value today. It is interesting to note that the early enhancement in ρ_c in the hybrid model can explain the higher preferred value for σ_8. However, S_8 is suppressed as Ω_m is smaller.

From the results obtained from the combination of Planck 2018 and DESI BAO distance measurements, there is some evidence to support the interaction between DE and DM through the hybrid fluid approximation. Indeed, it is known that DESI data tends to bring the physical matter density down in ΛCDM. This leads to a slight disagreement between DESI and Pl18 ($\sim 2\sigma$) under ΛCDM. As a result, the time-dependence of ρ_c in the hybrid model is favoured when DESI is added to the baseline dataset, with $\Delta\chi^2_{\rm min} = 0.14$ in Pl18 going to $\Delta\chi^2_{\rm min} = -2.8$ for Pl18+DESI. However, this is not supported by Pantheon+ data, which favours a larger Ω_m than DESI. In the analysis reported by the DESI collaboration [13] for minimal parametrisations of dynamical dark energy, a considerable preference in favour of phantom dark energy over ΛCDM (with the combination of Planck 2018, DESI, and SNIa data) was reported and has been the focus of multiple studies. In the context of the hybrid model, the preference for a late-time effective phantom-like behaviour for DE is replaced by the coupled dark sector with a non-vanishing detection of $1/\phi_i > 0$ exceeding the 95% CL. The phenomenological difference in the dynamics of DE under the hybrid model compared to the CPL [29, 30] parametrisation highlighted in the DESI Y1 data release [13] is illustrated in Fig. 6.6 with $w_{\phi,\rm eff}$ as defined in Eq. (6.3), mimicking DE in an uncoupled dark sector. We stress that in that case, $w_{\phi,\rm eff}$ never becomes phantom. This suggests an alternative explanation to the mild discrepancy between DESI and Pl18. However, this behaviour does not help reconcile Pl18+DESI data with the (uncalibrated) SNe, which favour larger Ω_m and a phantom DE behaviour [210, 211]. Future BAO and SNe data are thus crucial for the fate of the hybrid model.

Finally, using the fact that $m_\chi \approx g\phi$ in conjunction with our best-fit results, we can put an upper limit on the coupling constant g. For Planck+DESI+SH0ES, we find the best-fit value $\phi_i = 16.92\,\mathrm{M_{Pl}}$. Requiring that the DM mass is smaller than the Planck mass yields the most conservative upper limit on the value of g. However, another conservative requirement is ensuring that the DM is not oscillating during inflation: requiring $m_\chi \lesssim 10^{12}$ GeV leads to $g \lesssim 10^{-8}$. Stronger upper limits on the DM mass will put more stringent constraints on the value of the coupling constant g.

6.4 Conclusions

In this chapter, we have explored the predictions of the hybrid model proposed in Chapter 5 and its fit to currently available datasets, namely Planck 2018 CMB data, the Pantheon+ catalogue of SN distance moduli – with and without the Cepheid calibration from SH0ES – and the recent BAO distance measurements by the DESI collaboration. From the phenomenological side, this model has interesting features derived from a Lagrangian formulation with a fluid description motivated by the physics of the dark sector. The model extends the standard ΛCDM framework by introducing one single additional parameter, the initial value of the DE scalar field ϕ (ϕ_i), which governs the strength of the interaction between dark matter and dark energy ($\propto 1/\phi_i$). On the observational side, the main effect of this coupling is to provide a non-trivial time dependence to the dark matter and dark energy densities as the effective DE field transitions from behaving like DM at early times to regular DE at late times. As a result, the dynamics of the scalar field and the dark sector interaction induce a negative correlation between the physical density of dark matter ω_c and the coupling parameter. This correlation helps accommodate the tendency of the DESI data to bring the matter density down in ΛCDM, leading to a better fit to this dataset in the hybrid model. At the same time, this is also entangled with a positive correlation between $1/\phi_i$ and H_0 (required to preserve the angular diameter distance to recombination), making it possible to alleviate the Hubble tension slightly.

Our main conclusions regarding the hybrid model in light of CMB, BAO and SNe data are as follows:

- For Pl18 alone, the hybrid model is virtually indistinguishable from ΛCDM in terms of the quality of the fit ($\Delta\chi^2_{\rm min} \simeq 0$), and we derive an upper bound on the initial field value $1/\phi_i < 0.0390$.

- When DESI data are included, the hybrid model provides a better fit than ΛCDM, thanks to the ability to accommodate the lower Ω_m favoured by DESI. The inclusion of (uncalibrated) Pantheon+ data, however, reduces the relative improvement in χ^2, and the Bayesian evidence comparison remains inconclusive for most combinations, often favouring ΛCDM due to the increased prior volume.

- The hybrid model demonstrates potential to slightly alleviate the Hubble tension, with a relaxation of the constrain to H_0, allowing for values closer to those from SH0ES measurements when combining all datasets. However, the alleviation is insufficient to eliminate the tensions, estimated to be 4.65σ in the hybrid model down from 5.76σ in ΛCDM.

- The coupling parameter $1/\phi_i$ correlates positively with σ_8 due to the additional DM contribution at early times, but the decrease in Ω_m at late times dominates, yielding a slightly smaller S_8.

Overall, while the hybrid model offers promising avenues for addressing theoretical questions related to the nature of the dark sector and observational issues such as the cosmological tensions, whether it provides a better fit to available data in comparison with ΛCDM is dataset-dependent, and significant challenges remain in reconciling all the observational incompatibilities within this framework. Nevertheless, the ability to introduce time dependence in the DM (and DE) densities is an interesting phenomenological feature of the model, which helps address DESI measurements and accommodate larger H_0 values. In this study, we focused on purely adiabatic initial conditions. The impact of isocurvature modes on the constraints is worth investigating in future work.

In light of these results, we highlight the importance of phenomenological models of the dark sector, which, through their inherent dynamics, can address the cosmological tensions under specific regimes. We emphasise the need to investigate the phenomenological predictions of such models and assess these against the available observational data.

Chapter 7

Scalar field dark matter with time-varying equation of state

7.1 Introduction

So far, we have focussed our discussion of DM on heavy scalar fields. We now approach the problem of modelling DM from a different angle, namely that of axion-like particles, or fuzzy dark matter. Ultralight scalars often emerge in particle physics and string theory compactifications, where axion-like particles arise as Kaluza-Klein zero modes of anti-symmetric tensor fields [212–214]. Arguments based on measurements of CMB anisotropies constrain the mass of these ultralight fields to be $m_\phi \gtrsim 10^{-24}$ eV [124, 140, 215–217], while observations of the Lyman-α forest extend this lower bound to about $m_\phi \sim 10^{-21}$ eV [218–222], assuming these particles account for over 30% of the total dark matter content. Albeit less widely agreed upon, studies on the kinematics of ultra-faint dwarf galaxies further bring the lower limit to around $m_\phi \sim 10^{-19}$ eV [223–225]. Other probes include galaxy clustering [226, 227], weak lensing measurements [228, 229] and 21 cm observations [230–232]. It should be noted that the analyses mentioned above often rely on the assumption that the ultralight DM makes up the whole of DM and interacts solely through gravitational means.

The other dark ingredient of the standard model of cosmology is the cosmological constant Λ, the simplest realisation of dark energy in the form of a background energy component which accounts for the current accelerated expansion of the universe. Given that the value of the cosmological constant has to be very small, alternative candidates for DE have been proposed, including slowly evolving scalar fields [113, 114, 130, 233, 234], three-form fields [235] and other more exotic proposals (see [73, 195, 236] for reviews on dark energy models). If DE is a dynamical degree of freedom, couplings to other types of matter fields are generally expected unless a particular symmetry forbids such interactions [237]. Constraints coming from solar system probes [238] suggest that the coupling of a slowly rolling DE scalar field to the standard model fields has to be much weaker than gravity, as the field's small mass results in a very large interaction range. On the other hand, these constraints can be relaxed for couplings to DM only, derived based on model-dependent cosmological observations. Some interacting dark energy (IDE) models may address shortcomings of the ΛCDM model such as the Hubble tension [21, 100, 102, 103, 239, 240], providing a guiding direction and framework for further study. Of particular interest are a class of models in which the DM-DE coupling is directly proportional to the energy density of dark energy, as studied for example in Refs. [1, 241–252].

Given our ignorance about the theoretical origins of DM and DE, it is essential to keep an open mind about their properties and whether they interact directly. Here, we will keep the same philosophy developed in the past chapters – namely to consider a common origin for DM and DE at the Lagrangian level. We will consider two interacting scalar fields, one light, oscillating DM field and one lighter, slowly-varying DE field. Our work aims to study the properties of scalar field DM. The novelty with respect to the previous literature is twofold. First, unlike the typical approach to coupled DM/DE models, where dark matter is a perfect fluid, here it is a fast oscillating field at the minimum of its potential (for similar discussions, see [132, 253, 254]). Secondly, the interaction is mediated not by dark energy but by the fast oscillating dark matter field, whereas dark energy is slowly varying. Still, we expect our results to hold even if DE is a cosmological constant (but coupled to DM) or a three-form field [235]. We will see in Section 7.5 that in the specific case of a conformal transformation, the interaction is proportional to the averaged energy density of dark energy, which provides nice motivation for the phenomenologically studied models.

This chapter is organised as follows: we motivate and describe the proposed framework in Section 7.2. In this section, we also collect the field equations and useful relations, which will be relevant to the subsequent calculations. In Section 7.3, we derive an effective fluid-field description, a valid approximation from the onset of the DM field quick oscillations around the minimum of an effective potential. The treatment of the associated fluid-field cosmological perturbations is discussed in Section 7.4. In Section 7.5, we provide concrete realisations of the model. We summarise our findings in Section 7.6.

7.2 Model

The action we consider, inspired by effective field theories (EFT), contains two interacting scalar fields and is given by

$$\begin{aligned}\mathcal{S} &= \int d^4x\sqrt{-g}\left(\frac{M_{\rm Pl}^2}{2}\mathcal{R}-\frac{1}{2}g^{\mu\nu}\partial_\mu\phi\partial_\nu\phi-U(\phi)-\frac{1}{2}g^{\mu\nu}\partial_\mu\chi\partial_\nu\chi-V(\chi)\right) \\ &- \int d^4x\sqrt{-g}\left(\phi Q_0\left(\chi,X^{(\chi)}\right)+\frac{1}{2}\phi^2Q_1\left(\chi,X^{(\chi)}\right)+...\right)+\mathcal{S}_{\rm SM},\end{aligned} \tag{7.1}$$

where $\mathcal{R}$ is the Ricci-scalar and $M_{\rm Pl}\equiv 1/\sqrt{8\pi G}$ is the reduced Planck mass. In the action above, $\mathcal{S}_{\rm SM}$ denotes the Lagrangian containing the standard model fields. Q_0 and Q_1 are coupling functions, depending on the slowly varying DE field χ and its kinetic term $X^{(\chi)}=-\frac{1}{2}g^{\mu\nu}\partial_\mu\chi\partial_\nu\chi$. The dots denote higher-order terms, which we assume are negligible in the following. This action can be thought of as a general formulation for an interacting DM-DE scalars system, where the interaction term is expanded order-by-order in the DM field ϕ.

The equation of motion for the dark matter field ϕ reads

$$\nabla^\mu\nabla_\mu\phi = U_{,\phi}+Q_0+\phi Q_1\ , \tag{7.2}$$

while the equation of motion for the dark energy field χ is

$$\begin{aligned}&\left(1-\phi Q_{0,X}-\frac{1}{2}\phi^2Q_{1,X}\right)\nabla^\mu\nabla_\mu\chi = \\ -\nabla^\mu\chi\nabla_\mu&\left(1-\phi Q_{0,X}-\frac{1}{2}\phi^2Q_{1,X}\right)+V_{,\chi}+\phi Q_{0,\chi}+\frac{1}{2}\phi^2Q_{1,\chi}.\end{aligned} \tag{7.3}$$

The Einstein equations for this system take the form

$$G_{\mu\nu}=\kappa^2\left(T^{(\phi)}_{\mu\nu}+T^{(\rm SM)}_{\mu\nu}+T^{(\chi)}_{\mu\nu}+T^{(\rm coup)}_{\mu\nu}\right), \tag{7.4}$$

where $T^{(\rm coup)}_{\mu\nu}$ is the contribution of the coupling terms to the total energy-momentum tensor. We identify, as is customary, $T^{(\phi)}_{\mu\nu}$ with the energy-momentum tensor of DM and $T^{(\chi)}_{\mu\nu}+T^{(\rm coup)}_{\mu\nu}\equiv T^{\rm DE}_{\mu\nu}$ as the DE energy-momentum tensor[1].

For pedagogical reasons, we specialise to the case in which the functions Q_0 and Q_1

---

[1] If we were to include the coupling terms into the definition of the energy-momentum tensor for DM, the effective potential would have a minimum at negative values of the potential, a situation we want to avoid, as this can lead to negative energy density for DM. This problem does not exist with the split performed here.

are only functions of the field χ and do not depend on the kinetic term $X^{(\chi)}$. This is done to simplify the DE equations of motion, but it is important to note that our core results regarding the DM dynamics do not change based on this choice. In this case, the covariant definitions of the EM tensors are as follows:

$$T_{\mu\nu}^{(\phi)} = \nabla_\mu\phi\nabla_\nu\phi - g_{\mu\nu}\left(\frac{1}{2}g^{\alpha\beta}\nabla_\alpha\phi\nabla_\beta\phi + V(\phi)\right), \tag{7.5}$$

$$T_{\mu\nu}^{(\chi)} = \nabla_\mu\chi\nabla_\nu\chi - g_{\mu\nu}\left(\frac{1}{2}g^{\alpha\beta}\nabla_\alpha\chi\nabla_\beta\chi + U(\chi)\right), \tag{7.6}$$

$$T_{\mu\nu}^{(\mathrm{coup})} = -g_{\mu\nu}\left(\phi Q_0\left(\chi\right) + \frac{1}{2}\phi^2 Q_1\left(\chi\right) + ...\right). \tag{7.7}$$

Since ϕ plays the role of DM, we assume that ϕ has the potential $U(\phi) = \frac{1}{2}m^2\phi^2$. Concerning χ, we assume it is a DE field that evolves very slowly on time scales much larger than the oscillations of ϕ. Hence, $V(\chi)$ will be a typical quintessential potential, e.g. of exponential form. We assume a flat FLRW spacetime. The Friedmann equation is given by

$$H^2 = \frac{1}{3M_{\mathrm{Pl}}^2}\left(\rho_\phi + \rho_{\mathrm{DE}} + \rho_{\mathrm{SM}}\right), \tag{7.8}$$

where we have defined

$$\rho_\phi = \frac{1}{2}\dot{\phi}^2 + U(\phi), \tag{7.9}$$

$$\rho_{\mathrm{DE}} = \frac{1}{2}\dot{\chi}^2 + V(\chi) + \phi Q_0 + \frac{1}{2}\phi^2 Q_1, \tag{7.10}$$

and the pressure components pick up a minus sign in front of non-kinetic terms.

The modified Klein-Gordon equation for the ϕ and χ fields read

$$\ddot{\phi} + 3H\dot{\phi} + m^2\phi = -Q(t) \equiv -Q_0(\chi) - Q_1(\chi)\phi\ , \tag{7.11}$$

and

$$\ddot{\chi} + 3H\dot{\chi} + V_\chi = -\phi Q_{0,\chi} - \frac{1}{2}\phi^2 Q_{1,\chi}. \tag{7.12}$$

We note that the modified Klein-Gordon equation in Eq. (7.11) for the DM field ϕ can be written in the form

$$\dot{\rho_\phi} + 3H(\rho_\phi + P_\phi) = -(Q_0 + Q_1\phi)\dot{\phi}. \tag{7.13}$$

This concludes the derivation of the relevant equations for this theory. In the next section we will use them to derive a fluid-field description for the system.

7.3 Towards a fluid-field description

We now seek to solve the equations derived in the previous section to study the evolution of both the DM and DE species. The main difference and challenge of our model compared to interacting quintessence models is that the coupling described here by $Q(t)$ depends on ϕ, which must rapidly oscillate for ϕ to behave like DM. Therefore, we have to perform an analysis based on the time-averaged character of the field over a period of oscillation to extract its average evolution and make the equations more manageable.

From Eq. (7.11), the equation of motion for ϕ can be recast into

$$\ddot{\phi} + 3H\dot{\phi} + m_{\mathrm{eff}}^2(t)\phi = -Q_0(t), \tag{7.14}$$

where we have defined the effective mass

$$m_{\mathrm{eff}}^2(t) \equiv m^2 + Q_1(t). \tag{7.15}$$

Before solving these equations, we want to stress that the following analysis hinges on the form of Eq. (7.11) and that the functions Q_0 and Q_1 are slowly varying. The exact form of Q_0 and Q_1 does not play a role in the overall phenomenology of the DM.

We will be interested in the case where $m > H$ and the scalar field is under-damped, allowing for the oscillations to begin before the DM-dominated epoch begins. To solve Eq. (7.14) we employ an ansatz for ϕ:

$$\phi(t) = \phi_{\mathrm{osc}}(t) + A(t), \tag{7.16}$$

where ϕ_{osc} is the solution to the homogeneous version of the Klein-Gordon equation:

$$\ddot{\phi}_{\mathrm{osc}} + 3H\dot{\phi}_{\mathrm{osc}} + m_{\mathrm{eff}}^2(t)\phi_{\mathrm{osc}} = 0, \tag{7.17}$$

while $A(t)$ solves

$$\ddot{A} + 3H\dot{A} + m_{\mathrm{eff}}^2(t)A = -Q_0(t). \tag{7.18}$$

On the basis that A is sourced by a slowly-evolving function, Q_0, we make the assumption that $A(t)$ itself is slowly varying such that $\ddot{A}, 3H\dot{A} \ll m_{\mathrm{eff}}^2 A$ and thus, we can neglect the first two terms of the above equation. This results in an approximated analytical solution for A:

$$A(t) \approx -\frac{Q_0(t)}{m_{\text{eff}}^2(t)}. \tag{7.19}$$

Making use of the WKB approximation (as in Chapter 5), we find the following solution for ϕ_{osc}:

$$\phi_{\text{osc}}(t) = \left(\frac{a_0}{a}\right)^{3/2} \left(\frac{m_0}{m_{\text{eff}}}\right)^{1/2} \left(\phi_+ \sin\left(m_{\text{eff}} t\right) + \phi_- \cos\left(m_{\text{eff}} t\right)\right), \tag{7.20}$$

where m_0 is the effective mass taken at $t = t_0$, and ϕ_+ and ϕ_- are constants. We can then average ϕ over one oscillation period to get

$$\langle \phi \rangle = A, \tag{7.21}$$

and for its velocity

$$\langle \dot{\phi} \rangle = \dot{A}. \tag{7.22}$$

Likewise, the variance of these quantities becomes,

$$\langle \phi^2 \rangle = \frac{1}{2}(\phi_+^2 + \phi_-^2) \left(\frac{m_0}{m_{\text{eff}}}\right) \left(\frac{a_0}{a}\right)^3 + A^2, \tag{7.23}$$

$$\langle \dot{\phi}^2 \rangle = \frac{1}{2} m_{\text{eff}}^2 (\phi_+^2 + \phi_-^2) \left(\frac{m_0}{m_{\text{eff}}}\right) \left(\frac{a_0}{a}\right)^3, \tag{7.24}$$

where in the last line we have ignored an $\dot{A}^2$ term, since under our assumptions $\dot{A} \ll m_{\text{eff}} A$.

The above expressions are crucial to the final results shown in this section. For standard uncoupled scalar field DM, both the field value and its derivative average out to zero. These equations encode that, in our case, the field does not oscillate around zero; instead, its averaged value is shifted by A due to the interaction. Therefore, the average energy density and pressure of the field are

$$\langle \rho_\phi \rangle = \frac{1}{4}(\phi_+^2 + \phi_-^2) \left(\frac{m_0}{m_{\text{eff}}}\right) \left(\frac{a_0}{a}\right)^3 (m_{\text{eff}}^2 + m^2) + \frac{m^2 A^2}{2}, \tag{7.25}$$

and

$$\langle p_\phi \rangle = \frac{1}{4}(\phi_+^2 + \phi_-^2) \left(\frac{m_0}{m_{\text{eff}}}\right) \left(\frac{a_0}{a}\right)^3 (m_{\text{eff}}^2 - m^2) - \frac{m^2 A^2}{2}, \tag{7.26}$$

respectively. Here, we clearly see that the interaction between DM and DE results in a change in the DM pressure, causing its departure from zero. The pressure can also be expressed as

$$\langle p_\phi \rangle = \left(\langle \rho_\phi \rangle - \frac{m^2 A^2}{2} \right) \frac{m_{\text{eff}}^2 - m^2}{m_{\text{eff}}^2 + m^2} - \frac{m^2 A^2}{2}, \tag{7.27}$$

in which case the equation of state becomes

$$w_\phi \equiv \frac{\langle p_\phi \rangle}{\langle \rho_\phi \rangle} = \left(1 - \frac{m^2 A^2}{2\langle \rho_\phi \rangle} \right) \frac{m_{\text{eff}}^2 - m^2}{m_{\text{eff}}^2 + m^2} - \frac{m^2 A^2}{2\langle \rho_\phi \rangle}. \tag{7.28}$$

Provided the kinetic energy of the dark energy field is small compared to its potential, Q_1 is positive and $m_{\text{eff}} > m$. This means that the equation of state of dark matter starts by being positive in its early stages. Around matter-dark energy equality, the equation of state begins to decrease and, in fact, becomes increasingly negative, as illustrated in Section 7.5. The very late-time occurrence of this transition is ascribed to the dependence of the coupling on the dark energy density, implying that the coupling only has a significant impact on w_ϕ when DE begins to dominate.

Differentiating the averaged density, Eq. (7.25), we obtain

$$\frac{d\langle \rho_\phi \rangle}{dt} + 3H \left(\langle \rho_\phi \rangle + \langle p_\phi \rangle \right) = \frac{3H}{4} (\phi_+^2 + \phi_-^2) \left(\frac{m_0}{m_{\text{eff}}} \right) \left(\frac{a_0}{a} \right)^3 (m_{\text{eff}}^2 - m^2) + m^2 A \dot{A}, \tag{7.29}$$

or equivalently

$$\frac{d}{dt} \langle \rho_\phi \rangle + 3H \left(\langle \rho_\phi \rangle - \frac{m^2 A^2}{2} \right) = m^2 A \dot{A}. \tag{7.30}$$

Had we done the time-averaging of Eq. (7.13) directly, we would conclude that, in fact

$$\frac{d\langle \rho_\phi \rangle}{dt} = \langle \dot{\rho}_\phi \rangle. \tag{7.31}$$

We now define an effective equation of state parameter for DM as

$$w_{\text{eff}} = -\frac{1}{\langle \rho_\phi \rangle} \left(\frac{m^2 A^2}{2} + \frac{m^2 A \dot{A}}{3H} \right), \tag{7.32}$$

such that Eq. (7.30) becomes

$$\langle \dot{\rho}_\phi \rangle + 3H \langle \rho_\phi \rangle (1 + w_{\text{eff}}) = 0. \tag{7.33}$$

Finally, and for completeness, the equation of motion for the dark energy field, obtained by substituting Eqs. (7.21) and (7.22) into Eq. (7.12), yields

$$\ddot{\chi} + 3H\dot{\chi} + V_{,\chi} = \frac{Q_0}{m_{\text{eff}}^2} Q_{0,\chi} - \frac{2\langle\rho_\phi\rangle + \frac{Q_0^2}{m_{\text{eff}}^2}}{2\left(m_{\text{eff}}^2 + m^2\right)} Q_{1,\chi}. \tag{7.34}$$

It is worth noting that the last term on the r.h.s depends on the DM energy density, which, in principle, could be large. Therefore, it is a requirement that $\frac{Q_{1,\chi}}{m_{\text{eff}}^2 + m^2}$ is small enough to avoid this coupling term driving the evolution of the χ field, which would invalidate our assumption that DE is slowly rolling.

7.4 Perturbations

We now turn to the study of linear perturbations for our model. This will lead up to the derivation of the sound speed, which is crucial to solving the fluid-scalar field equations of motion.

We follow the approach developed in [122] and described in Chapter 4 to compute the sound speed, considering only scalar perturbations. We adopt the following conventions for the metric scalar perturbations in a general gauge:

$$\delta g_{00} = -2\Phi, \tag{7.35}$$

$$\delta g_{i0} = a\nabla_i B, \tag{7.36}$$

$$\delta g_{ij} = -2a^2(\delta_{ij}\Psi - \nabla_i\nabla_j E), \tag{7.37}$$

where Φ, Ψ, B and E are the four scalar degrees of freedom which can be expanded and decomposed in independently evolving Fourier modes k. This results in the following equations of motion for the perturbations of the scalar fields $\delta\chi$ and $\delta\phi$:

$$\begin{aligned}\delta\ddot{\chi} + 3H\delta\dot{\chi} + \left(\frac{k^2}{a^2} + V_{,\chi\chi}\right)\delta\chi = {}& \dot{\chi}\left(\dot{\Phi} + 3\dot{\Psi} - \frac{k}{a}B + \dot{E}\right) \\ & + 2(\ddot{\chi} + 3H\dot{\chi})\Phi - \delta\phi\, Q_{0,\chi} - \phi\, Q_{0,\chi\chi}\,\delta\chi \\ & - \phi\,\delta\phi\, Q_{1,\chi} - \tfrac{1}{2}\phi^2 Q_{1,\chi\chi}\,\delta\chi.\end{aligned} \tag{7.38}$$

and

$$\delta\ddot{\phi} + 3H\delta\dot{\phi} + \frac{k^2}{a^2}\delta\phi + m^2\delta\phi = \dot{\phi}\left(\dot{\Phi} + 3\dot{\Psi} - \frac{k}{a}B + \dot{E}\right) + 2(\ddot{\phi} + 3H\dot{\phi})\Phi - \delta Q. \tag{7.39}$$

Here, we have defined δQ as the perturbation of the coupling function. As for the background evolution, we can expand it as

$$\delta Q = \delta Q_0 + \phi\delta Q_1 + \delta\phi Q_1, \tag{7.40}$$

such that Eq. (7.39) becomes

$$\delta\ddot{\phi}+3H\delta\dot{\phi}+\frac{k^2}{a^2}\delta\phi+m_{\text{eff}}^2\delta\phi = \dot{\phi}\left(\dot{\Phi}+3\dot{\Psi}-\frac{k}{a}B+\dot{E}\right)+2(\ddot{\phi}+3H\dot{\phi})\Phi-\delta Q_0-\phi\delta Q_1. \tag{7.41}$$

The exact form of δQ_0 and δQ_1 depends on the details of the model.

The perturbed perfect fluid quantities are defined in terms of the time-averaged oscillating DM scalar field and its perturbation [111]:

$$\delta\rho = \langle\dot{\phi}\delta\dot{\phi} - \dot{\phi}^2\Phi + m^2\phi\delta\phi\rangle, \tag{7.42}$$

$$\delta p = \langle\dot{\phi}\delta\dot{\phi} - \dot{\phi}^2\Phi - m^2\phi\delta\phi\rangle, \tag{7.43}$$

$$\frac{a}{k}(\rho+p)(v-B) = \langle\dot{\phi}\delta\phi\rangle. \tag{7.44}$$

It should be understood that the fluid variables are themselves time-averaged quantities. Bringing together Eqs. (7.41)-(7.44), we arrive at the following expressions for the perturbed continuity equations:

$$\delta\dot{\rho} + 3H(\delta\rho+\delta p) = (\rho+p)\left(3\dot{\Psi}+\dot{E}-\frac{k}{a}v\right) - \langle\delta Q\dot{\phi}\rangle - \langle Q\delta\dot{\phi}\rangle, \tag{7.45}$$

$$\frac{1}{a^4(\rho+p)}\frac{d}{dt}[a^4(\rho+p)(v-B)] = \frac{k}{a}\Phi + \frac{k}{a(\rho+p)}[\delta p - \langle Q\delta\phi\rangle]. \tag{7.46}$$

For convenience and to simplify the calculations, we consider the axion-comoving gauge[2], which amounts to setting $B = v$. Thus, in this context, Eq. (7.46) reduces to

$$\Phi = -\frac{\delta p}{\rho+p} + \frac{\langle Q\delta\phi\rangle}{\rho+p}. \tag{7.47}$$

Analogous to background fluid-field treatment, we specify the following ansatz for the perturbation of the ϕ field:

$$\delta\phi(k,t) = \delta\phi_+(k,t)\sin(m_{\text{eff}}t) + \delta\phi_-(k,t)\cos(m_{\text{eff}}t) + \delta\mathcal{A}(t). \tag{7.48}$$

---

[2] The name of the gauge is used in the literature [97, 122], but we note here that ϕ is not necessarily an axion field but a generic DM scalar field.

It is important to note that $\delta\mathcal{A}(t)$ is not just the perturbation of $A(t)$ defined in Eq. (7.19), as will be shown explicitly below.

For the rest of the calculation, we will assume a quasi-static approximation following [122] and our calculation in Chapter 4, and will also be discarding derivatives of A and $\delta\mathcal{A}$ on similar grounds. In axion comoving gauge we have $\langle\dot{\phi}\delta\phi\rangle = 0$ from Eq. (7.44), which implies

$$a^{-\frac{3}{2}}\left(\frac{m_0}{m_{\rm eff}}\right)^{\frac{1}{2}} m_{\rm eff}[\delta\phi_+\phi_- - \delta\phi_-\phi_+] + \dot{A}\delta\mathcal{A} = 0 \tag{7.49}$$

and so leads to the following useful relation:

$$\delta\phi_+\phi_- = \delta\phi_-\phi_+ \tag{7.50}$$

after discarding small A terms. Now we can solve Eq. (7.41) to leading order in H/m since the field oscillates if $m \gg H$. This implies assuming that metric perturbations vary only on cosmological time scales $t \sim H^{-1} \gg m^{-1}$. We start by substituting the ansatz in Eq. (7.48) into Eq. (7.41). Splitting the equation into oscillating and non-oscillating terms, we get:

$$\delta\ddot{\mathcal{A}} + \frac{k^2}{a^2}\delta\mathcal{A} + m_{\rm eff}^2\delta\mathcal{A} = -\delta Q_0 - \delta Q_1 A \tag{7.51}$$

for the non-oscillating terms which, in the quasi-static approximation, yields

$$\delta\mathcal{A} = -\frac{\delta Q_0 + \delta Q_1 A}{\frac{k^2}{a^2} + m_{\rm eff}^2} = -\frac{\delta Q_0 - \frac{Q_0}{m_{\rm eff}^2}\delta Q_1}{\frac{k^2}{a^2} + m_{\rm eff}^2}. \tag{7.52}$$

Grouping the oscillating terms in powers of H/m and considering only leading order, we obtain:

$$\Phi = -\frac{1}{2}\left(\frac{a}{a_0}\right)^{3/2}\left(\frac{m_0}{m_{\rm eff}}\right)^{-1/2}\frac{\delta\phi_+}{\phi_+}\frac{k^2}{m_{\rm eff}^2 a^2} - \frac{1}{2m_{\rm eff}^2}\delta Q_1, \tag{7.53}$$

which can be compared to Eq. (4.33). To compute the perturbed pressure and energy density we will need the following time averaged quantities (up to leading order in H/m):

$$\langle\dot{\phi}\delta\dot{\phi}\rangle = \frac{a^{-\frac{3}{2}}}{2}\left(\frac{m_0}{m_{\rm eff}}\right)^{\frac{1}{2}} m_{\rm eff}^2(\delta\phi_+\phi_+ + \delta\phi_-\phi_-) \tag{7.54}$$

$$\langle\phi\delta\phi\rangle = \frac{a^{-\frac{3}{2}}}{2}\left(\frac{m_0}{m_{\rm eff}}\right)^{\frac{1}{2}}(\delta\phi_+\phi_+ + \delta\phi_-\phi_-) + A\delta\mathcal{A}. \tag{7.55}$$

Replacing these expressions, as well as Eq. (7.53) into the perturbed fluid equations for δp and $\delta\rho$, Eqs. (7.42) and (7.43) we arrive at

$$\begin{aligned} \delta p &= \frac{a^{-\frac{3}{2}}}{2}\left(\frac{m_0}{m_{\text{eff}}}\right)^{\frac{1}{2}}(\phi_+^2+\phi_-^2)\frac{\delta\phi_+}{\phi_+}m_{\text{eff}}^2\left[\frac{1}{2}\frac{k^2}{a^2m_{\text{eff}}^2}+\frac{Q_1}{m_{\text{eff}}^2}\right] \\ &- m^2A\delta\mathcal{A}+\frac{a^{-3}}{4}\left(\frac{m_0}{m_{\text{eff}}}\right)(\phi_+^2+\phi_-^2)\delta Q_1, \qquad (7.56) \\ \delta\rho &= \frac{a^{-\frac{3}{2}}}{2}\left(\frac{m_0}{m_{\text{eff}}}\right)^{\frac{1}{2}}(\phi_+^2+\phi_-^2)\frac{\delta\phi_+}{\phi_+}m_{\text{eff}}^2\left[\frac{1}{2}\frac{k^2}{a^2m_{\text{eff}}^2}+2-\frac{Q_1}{m_{\text{eff}}^2}\right] \\ &+ m^2A\delta\mathcal{A}+\frac{a^{-3}}{4}\left(\frac{m_0}{m_{\text{eff}}}\right)(\phi_+^2+\phi_-^2)\delta Q_1. \qquad (7.57)\end{aligned}$$

From here, and using Eq. (7.53), we can compute the pressure perturbation, given by

$$\delta p = c_s^2\delta\rho - m^2A\delta\mathcal{A}(1+c_s^2)+\frac{1}{2}\frac{\rho+p}{m_{\text{eff}}^2}\delta Q_1(1-c_s^2), \qquad (7.58)$$

where we have defined the effective sound speed

$$c_s^2 = \frac{\frac{1}{2}\frac{k^2}{a^2m_{\text{eff}}^2}+\frac{Q_1}{m_{\text{eff}}^2}}{\frac{1}{2}\frac{k^2}{a^2m_{\text{eff}}^2}+2-\frac{Q_1}{m_{\text{eff}}^2}} = \frac{\frac{1}{2}\frac{k^2}{a^2m^2}+\frac{Q_1}{m^2}}{\frac{1}{2}\frac{k^2}{a^2m^2}+2+\frac{Q_1}{m^2}}, \qquad (7.59)$$

and the second equality follows from the definition of m_{eff}^2 in Eq. (7.15). It is important to note that this effective sound speed is akin to that of the non-interacting axion, presented in [97,122] and Chapter 4. See also [145,255] for calculations of non-standard axion sound-speed. Accordingly, and as expected, Eq. (7.59) reduces to that case in the limit where Q_1 is zero.

Furthermore, according to Eq. (7.58), in contrast to the non-interacting case, the pressure perturbation is not precisely proportional to the density perturbation. This can be interpreted as a non-adiabatic contribution to the pressure perturbation caused by the interaction with the dark energy scalar field [132,143,256,257].

7.5 Concrete model examples

In this section, we provide two concrete examples for obtaining equations of motion for the DM field of the same form as Eq. (7.11).

7.5.1 Conformal coupling

This setup is inspired by that of field theories of dark energy, such as coupled quintessence [129,130,132,253,254,258], but with the role of the fields for DM and DE swapped. That is, we treat ϕ in the action below as a dark matter scalar field, and the dark energy sector is coupled conformally to the DM sector, resulting in the following effective action for this model:

$$\mathcal{S} = \int d^4x\sqrt{-g}\left(\frac{M_{\rm Pl}^2}{2}\mathcal{R} - \frac{1}{2}g^{\mu\nu}\partial_\mu\phi\partial_\nu\phi - U(\phi)\right) + \mathcal{S}_{\rm SM} + \mathcal{S}_{\rm DE}. \tag{7.60}$$

In what follows, we assume that the DE sector can be described by a slowly evolving scalar field χ, described by the action

$$\mathcal{S}_{\rm DE} = \int d^4x\sqrt{-\tilde{g}}\left(\frac{1}{2}\tilde{g}^{\mu\nu}\partial_\mu\chi\partial_\nu\chi - V(\chi)\right)\ , \tag{7.61}$$

where the metric $\tilde{g}$ is related to the metric g via a conformal transformation of the form $\tilde{g}_{\mu\nu} = C(\phi)g_{\mu\nu}$. Rewriting $\mathcal{S}_{\rm DE}$ in terms of the metric $g_{\mu\nu}$ results in

$$\mathcal{S}_{\rm DE} = \int d^4x\sqrt{-g}\left(\frac{C(\phi)}{2}g^{\mu\nu}\partial_\mu\chi\partial_\nu\chi - C^2(\phi)V(\chi)\right). \tag{7.62}$$

In contrast to models such as coupled quintessence, in which C depends on the dark energy field, the function C in this framework is dependent on dark matter properties.

The equation of motion for the DE field χ is derived from the corresponding variation of the action in Eq. (7.60) and reads

$$\nabla^\mu\nabla_\mu\chi - C\frac{dV}{d\chi} = -\frac{\nabla_\alpha C}{C}\nabla^\alpha\chi. \tag{7.63}$$

The equation for the DM field ϕ is derived in an analogous manner and yields

$$\nabla^\mu\nabla_\mu\phi - \frac{\partial U}{\partial\phi} = Q, \tag{7.64}$$

where the coupling Q was defined as

$$\begin{aligned} Q &= \nabla_\mu\left(\frac{\partial L_\chi}{\partial(\nabla_\mu\phi)}\right) - \frac{\partial L_\chi}{\partial\phi} \\ &= \frac{C_{,\phi}}{2C}\left[Cg^{\alpha\beta}\nabla_\alpha\chi\nabla_\beta\chi + 4C^2U\right]. \end{aligned} \tag{7.65}$$

The Einstein equations result from variation of the action with the gravitational metric $g_{\mu\nu}$, resulting in

$$R_{\mu\nu} - \frac{1}{2}Rg_{\mu\nu} = \kappa^2 \left(T^{(\phi)}_{\mu\nu} + T^{(\chi)}_{\mu\nu} + T^{(\mathrm{SM})}_{\mu\nu}\right), \tag{7.66}$$

where $R_{\mu\nu}$ is the Ricci tensor, $\kappa \equiv 1/M_{\mathrm{Pl}}$ and $T^{(i)}_{\mu\nu}$ are the energy-momentum tensors for each i-th fluid, which for the dark sector scalar fields ϕ and χ read

$$T^{(\phi)}_{\mu\nu} = \nabla_\mu\phi\nabla_\nu\phi - g_{\mu\nu}\left(\frac{1}{2}g^{\alpha\beta}\nabla_\alpha\phi\nabla_\beta\phi + V(\phi)\right), \tag{7.67}$$

$$T^{(\chi)}_{\mu\nu} \;\;=\;\; C\nabla_\mu\chi\nabla_\nu\chi - g_{\mu\nu}\left(\frac{C}{2}g^{\alpha\beta}\nabla_\alpha\chi\nabla_\beta\chi + C^2U(\chi)\right), \tag{7.68}$$

respectively, and obey the following conservation equations:

$$\nabla^\mu T^{(\phi)}_{\mu\nu} = Q\nabla_\nu\phi, \quad \nabla^\mu T^{(\chi)}_{\mu\nu} = -Q\nabla_\nu\phi, \tag{7.69}$$

which are physically equivalent to the modified Klein-Gordon equations.

For the background cosmology, we consider the case of a flat Friedmann-Lemaître-Robertson-Walker universe, for which the field equations read

$$\ddot{\phi} + 3H\dot{\phi} + U_{,\phi} = \frac{1}{2}C_{,\phi}\dot{\chi}^2 - 2CC_{,\phi}V, \tag{7.70}$$

$$\ddot{\chi} + \left(3H + \frac{C_{,\phi}}{C}\dot{\phi}\right)\dot{\chi} + CV_{,\chi} = 0. \tag{7.71}$$

The energy densities ρ_ϕ and ρ_χ and the corresponding pressures p_ϕ and p_χ are given by

$$\rho_\phi = \frac{1}{2}\dot{\phi}^2 + U(\phi), \quad p_\phi = \frac{1}{2}\dot{\phi}^2 - U(\phi), \tag{7.72}$$

$$\rho_\chi = \frac{1}{2}C\dot{\chi}^2 + C^2V(\chi), \quad p_\chi = \frac{1}{2}C\dot{\chi}^2 - C^2V(\chi). \tag{7.73}$$

The Friedmann equations, which govern the expansion of the universe and which can be derived from Einstein's equations, Eq. (7.66), read

$$H^2 = \frac{\kappa^2}{3}\left[\frac{1}{2}\dot{\phi}^2 + U(\phi) + \frac{1}{2}C(\phi)\dot{\chi}^2 + C(\phi)^2V(\chi)\right], \tag{7.74}$$

$$\dot{H} = -\frac{\kappa^2}{2}\left[\dot{\phi}^2 + C(\phi)\dot{\chi}^2\right]. \tag{7.75}$$

Finally, the modified Klein-Gordon equations for ϕ and χ, Eqs. (7.63) and (7.63), become

$$\dot{\rho}_\phi + 3H\left(\rho_\phi + p_\phi\right) = -\frac{C_{,\phi}}{2C}\left(\rho_\chi - 3p_\chi\right)\dot{\phi}, \tag{7.76}$$

$$\dot{\rho}_\chi + 3H\left(\rho_\chi + p_\chi\right) = \frac{C_{,\phi}}{2C}\left(\rho_\chi - 3p_\chi\right)\dot{\phi}. \tag{7.77}$$

Since we wish for ϕ to behave as dark matter and χ as dark energy, in this analysis, we focus on the following self-interacting scalar field potentials:

$$V(\chi) = V_0 e^{-\kappa\lambda\chi}, \tag{7.78}$$

$$U(\phi) = \frac{1}{2}m^2\phi^2. \tag{7.79}$$

The function Q defined in Eq. (7.65) can be written as

$$Q = \frac{C_{,\phi}}{2C}\left(\rho_\chi - 3p_\chi\right), \tag{7.80}$$

for a field-dependent conformal function C. The form of this Q is proportional to the energy density of DE, providing a concrete theoretical realisation for a widely studied class of phenomenological interacting DE models (see [100] and references therein) which was previously missing. This means that the equation of motion for the ϕ field is of the form

$$\ddot{\phi} + 3H\dot{\phi} + m^2\phi = -Q(t). \tag{7.81}$$

Choosing a polynomial form for $C(\phi)$ will yield a similar form to that described in Eq. (7.1). From there, it is straightforward to read off the specific forms of Q_0 and Q_1, after which we can directly apply the results of Sections 7.3 and 7.4. Concretely, we now choose

$$C(\phi) = 1 + 2\kappa\beta\phi, \tag{7.82}$$

for the conformal coupling where β is a dimensionless constant and we use $\kappa \equiv \frac{1}{M_{\rm Pl}}$.

With our choice of $C(\phi)$, we can decompose the source term above as

$$Q(t) = Q_0(t) + Q_1(t)\phi, \tag{7.83}$$

where the functions Q_0, Q_1 are of the specific form:

$$\begin{aligned} Q_0(\chi, X^{(\chi)}) &= 4\kappa\beta V(\chi) - 2\kappa\beta X^{(\chi)} && (7.84)\\ Q_1(\chi) &= 8\kappa^2\beta^2 V(\chi). && (7.85)\end{aligned}$$

In an FLRW spacetime, the above coupling functions reduce to

$$\begin{aligned} Q_0(t) &= -\kappa\beta(\dot{\chi}^2 - 4V), && (7.86)\\ Q_1(t) &= 8\kappa^2\beta^2 V. && (7.87)\end{aligned}$$

The equation of motion for ϕ can then be recast into

$$\ddot{\phi} + 3H\dot{\phi} + m_{\text{eff}}^2(t)\phi = -Q_0(t), \tag{7.88}$$

as in Section 7.3. After time-averaging the DM field, the DE equation of motion becomes

$$\ddot{\chi} + \left(3H + \frac{2\kappa\beta\dot{A}}{1 + 2\beta\kappa A}\right)\dot{\chi} + V_{,\chi}\,(1 + 2\beta\kappa A) = 0, \tag{7.89}$$

which is different to Eq. (7.34) due to the extra kinetic contribution in Q_0. However, the differences in DE dynamics can easily be kept small whilst yielding the same changes in the DM dynamics.

Here we prove that the relation between Q_0 and Q_1 from Eqs. (7.86), (7.87) implies that the EoS transitions to negative values around DM-DE equality. Indeed, from Eq. (7.28), we see that $w_\phi < 0$ when

$$\langle\rho_\phi\rangle < \frac{1+Z}{Z}\,\frac{m^2A^2}{2}, \tag{7.90}$$

where $Z = (m_{\text{eff}}^2 - m^2)/(m_{\text{eff}}^2 + m^2) \approx Q_1/2m^2$. As $A \approx -Q_0/m^2$, it turns out that $w_\phi < 0$ when $\langle\rho_\phi\rangle$ drops below

$$\langle\rho_\phi\rangle < \frac{Q_0^2}{Q_1} \approx V \approx \rho_\chi\,. \tag{7.91}$$

Consequently, the DM pressure becomes appreciably negative only at very low redshift.

At linear perturbative level, the equation of motion for $\delta\phi$ is the same as that presented in Section 7.4. For completeness, the corresponding equation for $\delta\chi$ is

$$\begin{aligned}\delta\ddot{\chi} + \left(3H + \frac{C_{,\phi}}{C}\,\dot{\phi}\right)\delta\dot{\chi} + \left(\frac{k^2}{a^2} + C(\phi)\,V_{,\chi\chi}\right)\delta\chi \\ = \dot{\chi}\left(\dot{\Phi} + 3\dot{\Psi} - \frac{k}{a}B + \dot{E}\right) - 2C(\phi)\,V_{,\chi}\,\Phi - C_{,\phi}\,V_{,\chi}\,\delta\phi \\ - \frac{C_{,\phi}}{C}\,\dot{\chi}\,\delta\dot{\phi} - \left(\frac{C_{,\phi}}{C}\right)_{,\phi}\dot{\phi}\,\dot{\chi}\,\delta\phi.\end{aligned} \tag{7.92}$$

In contrast to our discussion in the previous sections, here Q_0 contains a dependency on the kinetic term $X^{(\chi)}$ which comes out of the conformal coupling. The difference brought by the kinetic dependence comes in the form of a modified equation of motion for the DE χ field. We have checked explicitly that this extra kinetic term does not spoil our initial assumption that χ is slow-rolling. We leave it for future work to study the modified dynamics of the DE in these models, and the effect of a kinetic coupling.

It is important to note that any model, such as the conformal coupling described above, that admits a Q_0 that depends on the kinetic term $X^{(\chi)}$ can be potentially problematic. Indeed, since the ϕ field is oscillating, the kinetic term for the χ field can become negative if the Q_0 contribution is larger than 1, which can lead to instabilities in the $\delta\chi$ perturbations. However, since the oscillations are on much smaller timescales than the evolution of the χ perturbations, we would expect that instabilities do not grow due to the kinetic term becoming negative only briefly every oscillation cycle. Since we do not study this in detail, we will keep to scenarios where strictly $2\kappa\beta\phi < 1$ in order to avoid possible instabilities. In this scenario, it is natural to think of the linear conformal coupling as a first order Taylor expansion of an exponential conformal coupling, which are common in the literature. This restriction on ϕ, it turns out, is quite limiting. To see this, let us first estimate the initial value of the ϕ field, ϕ_i when it starts rolling, at around $H \approx m$. To do this, we assume that the field will start rolling during the radiation epoch, which is required for ϕ to make up all of DM. Starting from

$$\rho_{\phi,0} \approx \frac{1}{2}\phi_i^2 m^2 a_i^3, \tag{7.93}$$

and writing $m \approx H$ as $m \approx H_{eq}\left(a_{eq}/a_i\right)^2$ where the subscript eq indicates a quantity evaluated at matter-radiation equality, we get the following approximation for the initial value:

$$\phi_i \approx \sqrt{2}\rho_{\phi,0}^{1/2} H_{eq}^{-3/4} a_{eq}^{-3/2} m^{-1/4}. \tag{7.94}$$

Setting the condition $2\kappa\beta\phi_i < 1$ ensures that the condition holds at all times, as ϕ only decays over time once it starts oscillating. Plugging in some numbers [259] we are left with

$$\beta \lessapprox 10^{-19} \left(\frac{m}{\text{eV}}\right)^{1/4} \text{eV}^{-1}. \tag{7.95}$$

Now we can estimate the maximum value for the non-zero equation of state of DM today in this model using Eqs. (7.28), (7.84):

$$w_{\phi,0} \approx \frac{16\beta^2 V^2}{m^2 \rho_{\phi,0}}. \tag{7.96}$$

Plugging in numbers once more [259], we get this upper limit on $w_{\phi,0}$:

$$w_{\phi,0} \lessapprox 10^{-47} \left(\frac{m}{\text{eV}}\right)^{-3/2}. \tag{7.97}$$

Even for the lightest possible scalar field DM currently allowed, we get an incredibly small value for $w_{\phi,0}$ which would be completely indistinguishable from ΛCDM. This means that unless there is an additional physical process which ‘turns on’ the conformal coupling at a later time – when ϕ has already decayed to a small enough number – this model cannot produce any different physics to ΛCDM. We will not study further any extensions of this model trying to address these limitations, but still highlight its usefulness in providing a concrete implementation of Eq. (7.1) as well as a physical motivation for phenomenological interactive DE models. Instead, we will now study the simplest model described by Eq. (7.1).

7.5.2 Minimal Λ scenario

We now move on to a much simpler model, which will serve as an approximate toy-model to develop an intuition of the possible physical effects derived in Sections 7.3 and 7.4.

We will take the 0th-order approximation of our framework. Let us consider a quasi-static χ field. This means that DE behaves almost as a cosmological constant, and that Q_0 and Q_1 are also very slowly varying. In this scenario, we have checked that the back reaction of the coupling onto the χ field dynamics is minimal, meaning that the DE stays slowly evolving. In this context, it is then sensible to approximate χ as a cosmological constant, and Q_0 and Q_1 as constants also. We can then follow our previous results and simply plug in constant Q_0 and Q_1. One can then solve for the background evolution assuming χ is non-dynamical (i.e. a cosmological constant)[3].

To illustrate the physics of this minimal model, we produce a modified version of the `CLASS` code to solve for the dynamics. Note that all values of Q_0 and Q_1 in the plots are given in `CLASS` units. To convert to SI units, multiply Q_0 by 10^{-31} eV^3 and multiply Q_1 by 4×10^{-59} eV^2. Fig. 7.1 shows the evolution of the field's equation of state parameter w_ϕ from Eq. (7.28). From this, we see that the DM equation of state parameter is positive at early time and becomes negative around DM-DE equality. It is important to note that the effective equation of state, from Eq. (7.32), is strictly negative in this model, as $\dot{A} = 0$. Since it is w_{eff} that dictates the actual evolution of the DM component according to Eq. (7.33), the DM in this model will behave like CDM (at background level) for most of the expansion history, until it starts diluting slower around DM-DE equality due to the negative effective EoS. We will study this model in more detail in Chapter 8.

The effect of the coupling on the DM sound speed can be appreciated in Figs. 7.2 and 7.3. At early times, the k^2/a^2m^2 term dominates, and we get a similar behaviour to that of the non-interacting case. On the other hand, at late times, when $k^2/a^2m^2 \ll Q_1$, the sound speed becomes practically constant, according to $c_s^2 \approx \frac{Q_1}{2m^2}$. As expected, in the absence of the coupling, c_s^2 falls to zero at small redshifts.

---

[3] We will study this model and its perturbations in more detail in the next chapter.

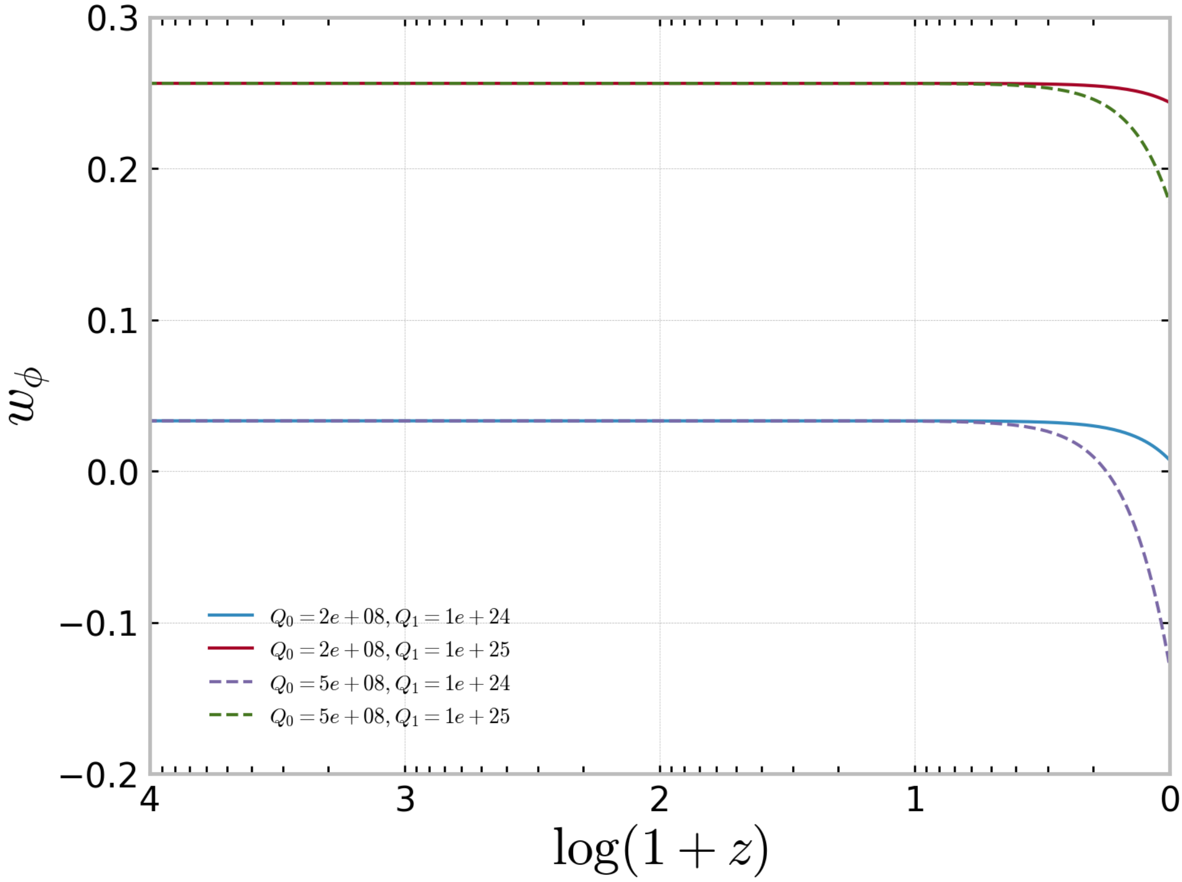

Figure 7.1: Evolution of the equation of state of dark matter w_ϕ defined in Eq. (7.28), for the minimal Λ model. The model parameters used in this illustrative example are $m = 10^{-17}$ eV as well as the remaining Planck ΛCDM best-fit parameters. Different curves are shown for different values of Q_0 and Q_1.

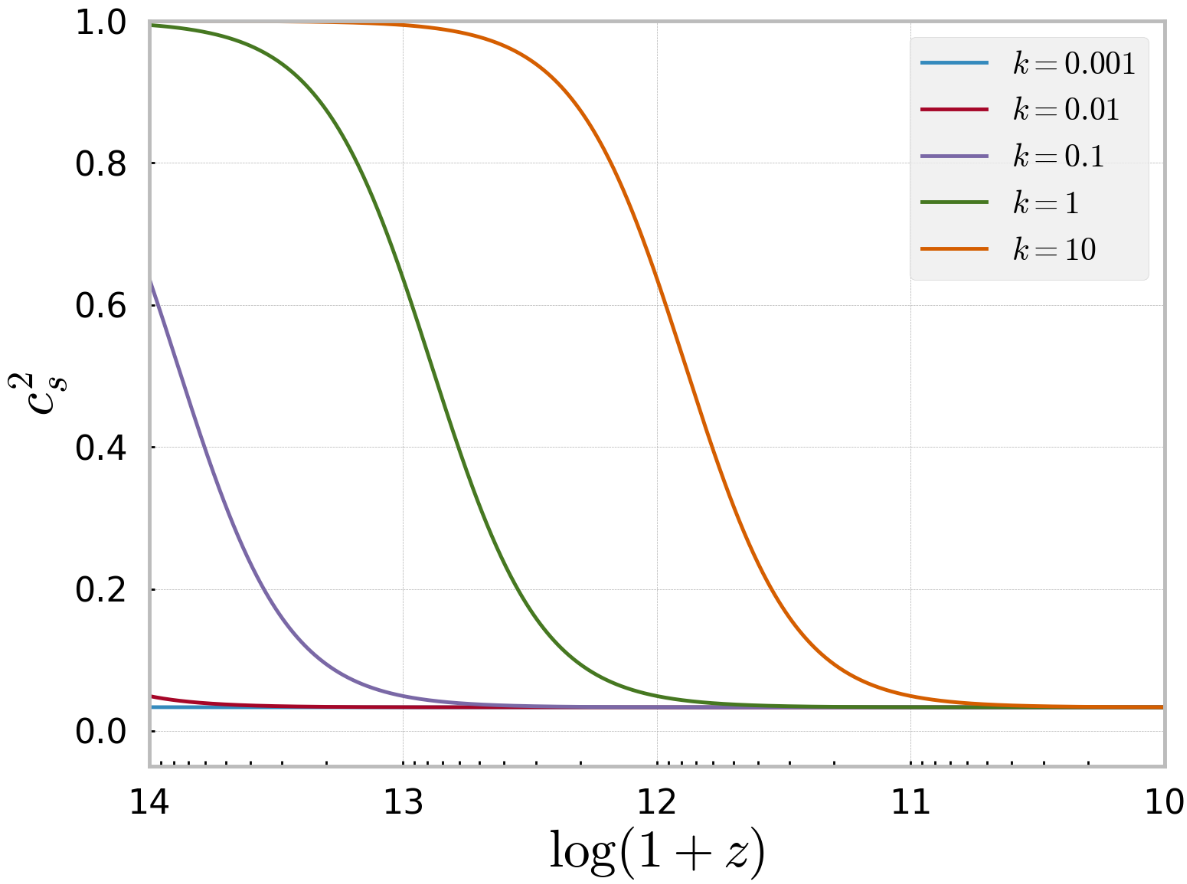

Figure 7.2: Evolution of the effective sound speed in terms of redshift z, as defined in Eq. (7.59), for a set of k values $\{0.001, 0.01, 0.1, 1, 10\}$ (in Mpc^{-1}), and the following set of parameters: $m = 10^{-17}$eV, $Q_0 = 0$, $Q_1 = 10^{24}$ and all other parameters fixed to Planck ΛCDM best-fit.

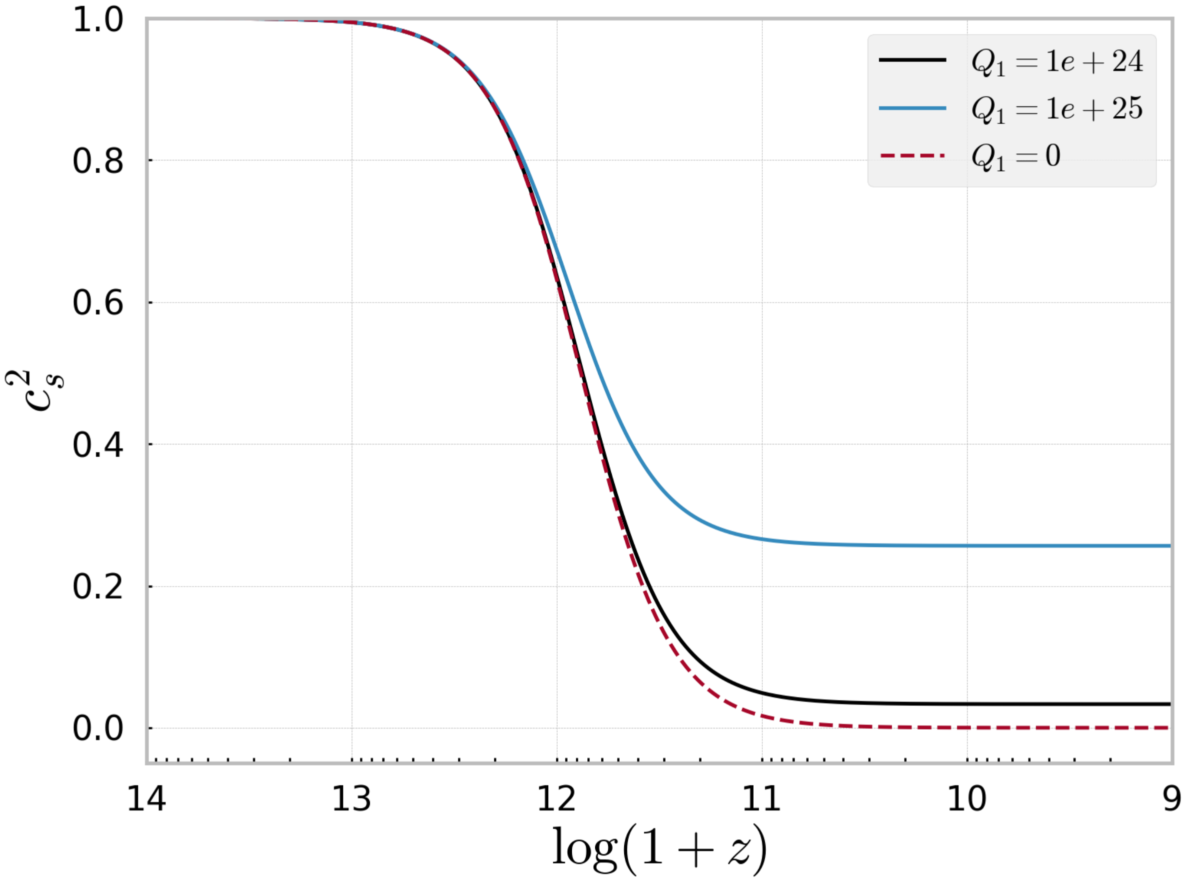

Figure 7.3: Evolution of the effective sound speed for two values of Q_1, defined in Eq. (7.59), compared with a non-coupled standard axion, with the same parameters used as in Fig. 7.2 and $k = 10$ Mpc^{-1}.

7.6 Summary and conclusions

In this chapter, we have introduced a novel model of the dark sector consisting of scalar field dark matter interacting with quintessence dark energy. The couplings between the dark matter scalar field ϕ and the slowly evolving dark energy field χ is mediated by interactions of the form $\phi O(\chi, X^{(\chi)})$ and $\phi^2 O(\chi, X^{(\chi)})$. The aim of our work is to study whether the properties of the DM scalar field, such as the equation of state and the adiabatic sound speed, change in the presence of such couplings. Furthermore, as a result of these couplings, we have found an effective theory of interacting dark matter and dark energy in which the coupling term is linked to the energy density of DE rather than DM. Our framework not only offers a theoretical basis for many extensively studied models of interacting dark energy found in the existing literature, e.g. in [239,242,246,251,252,260–262], but also introduces significant differences. In our setup, the coupling between DM and DE offsets the oscillations of the scalar field, resulting in a non-zero average for its equation of state parameter. By averaging over these rapid oscillations, we have derived a fluid-field description of the system, revealing a non-zero average value for the field determined by the coupling. Consequently, the effective DM fluid exhibits a non-zero physical pressure, starkly contrasting with standard IDE models. This physical pressure transitions from slightly positive at early times to negative after DM-DE equality. The main observational effect most likely comes from the change in the DM equation of state at very late times, at a redshift smaller than the redshift of the DE-DM equality. Thus, our work carries implications in the context of searches for non-standard CDM physics and provides theoretical support for such models (see [263–266]). Notably, the non-standard equation of state of DM impacts the analysis and interpretation of cosmological observational data, such as Pantheon+ [55] or the recently published DESI data [13].

At the linear perturbation level, we have computed the pressure perturbation and sound speed of the averaged DM fluid. Our findings reveal terms proportional to the density perturbation $\delta\rho$ plus non-adiabatic pressure terms depending on the perturbation of the DE scalar field. Notably, due to the coupling, the adiabatic term deviates from the standard axion scalar field scenario. This results in an effective sound speed that remains non-zero across all scales, unlike the uncoupled case where it vanishes at small k. Consequently, we anticipate a slight power suppression in the matter power spectrum at all scales within the interacting scenario considered here. Furthermore, the influence of non-adiabatic pressure contributions on observables in this context warrants further investigation, as well as the changes to the properties of DE, such as the sound speed [267, 268] and the full evolution of perturbations in the DE field. A comprehensive study of these points requires a full implementation of the theory in publicly available Boltzmann codes such as `CLASS` or `CAMB`[4] [269].

Finally, we have studied two realisations of our framework, first using a conformal coupling to obtain Lagrangian of the correct form, and then considering a minimal model of DM coupling to a cosmological constant instead of a DE scalar field. The conformal coupling provides motivation for phenomenological DE models, although further study is needed to determine if the model is stable for observationally relevant parameter values. The minimal model provides a robust 0th-order approximation for our formalism, which makes it much simpler to study whilst showcasing the main physical effects expected from the model – i.e. a modified EoS and sound-speed. We will study the minimal model in more detail, as well as constrain its parameters using cosmological data, in Chapter 8.

---

[4] https://github.com/cmbant/CAMB

Chapter 8

Cosmological constraints on late-time negative pressure dark matter

8.1 Introduction

We have seen throughout this thesis that interaction between DM and DE at the scalar field level can yield interesting phenomenology. In the previous chapter, we discussed a model where the interaction leads to minimal modifications to the DE dynamics, whilst introducing new physics in the DM sector. This is a less explored approach, as traditional DE-DM interactions assume a standard CDM and a modified DE sector [100, 101]. It is important to study such models as alternative to the traditional interacting dark energy scenarios, especially in light of current cosmological tensions. For more analyses of non-standard DM, see [263, 265, 266, 270]. In this chapter we will study in detail the simplest model described by the framework introduced in Chapter 7. That is, we will treat the DE scalar field as being constant, thus behaving like a cosmological constant. We will therefore take Q_0 to be a constant, and we will set $Q_1 = 0$. These choices, although seemingly drastic, manage to capture the core physics whilst greatly reducing computational complexity. We refer to this minimal model as ΛQDM, which is a one-parameter extension to ΛCDM. We will first derive the equations of motion for ΛQDM, then study its evolution by implementing these equations in the `CLASS` Boltzmann-solver. This will allow us to understand the dynamics of the model both at linear and perturbation level. Next, we will perform an analysis of the model against available cosmological data, using the `Cobaya` package to interface a MCMC algorithm with the `CLASS` solver. In essence, this determines a set of best-fit parameters for the model, as well as a measure of the goodness of fit which we compare to ΛCDM. This chapter is organised as follows: in Section 8.2 we describe the ΛQDM model, in Section 8.3 we study the phenomenology of the model, Section 8.4 describes the data analysis and Section 8.5 outlines the conclusions of the work.

8.2 The interacting ΛQDM model

We build upon the minimal model described in the previous chapter. We start with Eq. (7.1) and consider a slowly varying χ field. As a 0^{th} order approximation, we consider χ as a constant, as well as Q_0 and Q_1. Since we are interested in the simplest model, and the Q_1 term is higher order in ϕ, we will simply set Q_1 to 0 for this analysis. This makes this model a one-parameter extension to ΛCDM, as we will discuss in more detail later. The minimal model aims to capture the essential physical effects of the fully covariant formulation of Chapter 7 whilst distilling the complexity down.

The minimal ΛQDM model can be formulated by taking Eqs. (7.9), (7.10) and demoting χ to a constant Λ:

$$\rho_\phi = \frac{1}{2}\dot{\phi}^2 + \frac{1}{2}m^2\phi^2 \tag{8.1}$$

$$\rho_\Lambda = \Lambda + \phi Q_0. \tag{8.2}$$

At background level, the equation of motion for ϕ is

$$\ddot{\phi} + 3H\dot{\phi} + m^2\phi = -Q_0. \tag{8.3}$$

Following Section 7.3, we define

$$A = -\frac{Q_0}{m^2}. \tag{8.4}$$

Solving for ϕ and averaging over a period of oscillation, we get the fluid equation of motion:

$$\dot{\rho}_\phi + 3H\rho_\phi(1 + w_\phi) = 0, \tag{8.5}$$

where

$$w_\phi = -\frac{m^2A^2}{2\rho_\phi} = -\frac{Q_0^2}{2m^2\rho_\phi}. \tag{8.6}$$

It should be understood that the above quantities are now period-averaged. Time-averaging the DE energy density leads to

$$\rho_\Lambda = \Lambda - \frac{Q_0^2}{m^2}, \tag{8.7}$$

which is just a constant offset that can be reabsorbed into the definition of Λ. At background level, then, the only modification to the ΛCDM is the time-varying equation of state w_ϕ, which becomes negative at late-time as ρ_ϕ dilutes[1].

At the perturbation level, the equations in general gauge for $\delta\phi$ are the same as Eq. (7.39), with $\delta Q = 0$ since Q_0 is constant and $Q_1 = 0$:

$$\delta\ddot{\phi} + 3H\delta\dot{\phi} + \frac{k^2}{a^2}\delta\phi + m^2\delta\phi = \dot{\phi}\left(\dot{\Phi} + 3\dot{\Psi} - \frac{k}{a}B + \dot{E}\right) + 2(\ddot{\phi} + 3H\dot{\phi})\Phi, \tag{8.8}$$

$$\delta\dot{\rho}_\phi + 3H(\delta\rho_\phi + \delta p_\phi) = (\rho_\phi + p_\phi)\left(3\dot{\Psi} + \dot{E} - \frac{k}{a}v\right) - Q_0\langle\delta\dot{\phi}\rangle. \tag{8.9}$$

$$\frac{1}{a^4(\rho_\phi + p_\phi)}\frac{d}{dt}[a^4(\rho_\phi + p_\phi)(v - B)] = \frac{k}{a}\Phi + \frac{k}{a(\rho_\phi + p_\phi)}[\delta p_\phi - Q_0\langle\delta\phi\rangle]. \tag{8.10}$$

Since there is no slowly-evolving driving term on the rhs of Eq. (8.8), we choose the following ansatz for $\delta\phi$:

$$\delta\phi(k,t) = \delta\phi_+(k,t)\sin(mt) + \delta\phi_-(k,t)\cos(mt), \tag{8.11}$$

which is equivalent to setting $\delta\mathcal{A} = 0$ in Eq. (7.48). Following the procedure described in Section 7.4, the averaged pressure perturbation is

$$\langle\delta p_\phi\rangle = c_s^2\langle\delta\rho_\phi\rangle, \tag{8.12}$$

where

$$c_s^2 = \frac{\frac{1}{2}\frac{k^2}{a^2m^2}}{\frac{1}{2}\frac{k^2}{a^2m^2} + 2}, \tag{8.13}$$

which is the standard sound speed for scalar field dark matter and ultralight axion-like particles. Next, we discuss the perturbed equations of motion in synchronous gauge. As discussed in Appendix A, we have to convert all comoving-gauge-specific quantities to the synchronous or Newtonian gauge. We choose to adopt the comoving gauge in this study, without loss of generality. The pressure perturbation becomes (dropping the ϕ

---

[1] Note that the asymptotic future behaviour of ρ_ϕ is that of a cosmological constant, and so $w_\phi \to -1$ instead of growing forever.

subscript for clarity):

$$\delta p^S = c_s^2 \delta\rho^S + 3\mathcal{H}\rho(1+w_\phi)c_s^2 v^S \tag{8.14}$$

where we have used the fact that the adiabatic sound speed is 0 since p is constant, and the S, C superscripts stand for synchronous and axion comoving gauges respectively. The perturbed field quantities are

$$\langle \delta\phi^S \rangle = \langle \delta\phi^C \rangle + \langle \dot{\phi} \rangle v^S = 0, \tag{8.15}$$

$$\langle \delta\dot{\phi}^S \rangle = \langle \delta\dot{\phi}^C \rangle + \langle \ddot{\phi} \rangle v^S = 0, \tag{8.16}$$

since A is constant and $\delta\mathcal{A} = 0$.

Thus, the perturbation equations in the synchronous gauge are

$$\delta\rho' = -3\mathcal{H}\delta\rho(1+c_s^2) - \rho(1+w_\phi)(\frac{1}{2}h' + kv) - 9\mathcal{H}^2\rho(1+w_\phi)c_s^2 v, \tag{8.17}$$

$$v' = -(1-3c_s^2)\mathcal{H}v + k\frac{c_s^2}{\rho(1+w_\phi)}\delta\rho, \tag{8.18}$$

which correspond exactly to a generalised dark matter component with no adiabatic sound speed [111,271]. For definitions of terms above see Section 2.3.3. We adopt initial conditions derived in [272], namely

$$\delta_i = -\frac{1}{4}(1+w_\phi)\frac{4-3c_s^2}{4-6w_\phi+3c_s^2}(k\tau_i)^2 \tag{8.19}$$

$$v_i = -\frac{1}{4}\frac{c_s^2}{4-6w_\phi+3c_s^2}(k\tau_i)^3, \tag{8.20}$$

where τ_i is the initial conformal time used in the numerical simulation.

8.3 Cosmological observables/ Phenomenology

In this section we implement the above equations numerically by modifying the `CLASS` code. At the background level, the only difference with ΛCDM comes from the non-zero CDM equation of state, which turns on at late times. At linear perturbations level, there are two effects to take into account: the equation of state, and the sound-speed. We will see that for the allowed scalar field DM mass range, the sound-speed shows very little impact on observables.

8.3.1 Background evolution

We study first in detail the background evolution of the model. In this case, it is interesting to note that the mass m only enters the equation of motion in the ratio Q_0/m, meaning this ratio is the only parameter at background level. For our numerical analysis, we will set $m = 10^{-17}$eV, and vary the value of Q_0. Other cosmological parameters are fixed to their ΛCDM values. It is worth mentioning that the values of Q_0 for which a sizeable effect on the dynamics is produced is quite narrow. Indeed, Q_0 values from $Q_0 = 0$ (the ΛCDM limit) to around $Q_0 = 10^{-24}$ eV^3 (i.e. $Q_0 = 10^7$ in `CLASS` units) do not change the EoS in a meaningful way. On the other hand, values of $Q_0 > 10^{-21}$ eV^3 – while technically allowed – require prohibitively large values of Ω_c today, making them non-viable.

We can get an idea of the overall behaviour of the model by looking at the evolution of ρ_ϕ. In Fig. 8.1, we show the ratio of ρ_ϕ to ρ_{CDM} in ΛCDM - or equivalently $\rho_\phi(Q_0 = 0)$. It is clear to see that the modifications to the expansion history happen at redshifts $z < 1$, as expected from the evolution of the equation of state. At late time, the equation of state becomes negative, which means the energy density decays slower than a^{-3}. Due to the way the `CLASS` code works, initial values of $\rho_{\phi,i}$ will be obtained via a shooting procedure in order to recover the correct energy density today. This explains why the energy density in the past becomes smaller for large values of Q_0. In reality, in order to match ρ_ϕ to the ΛCDM around recombination, one would need to increase the present energy density $\rho_{\phi,0}$. Since the main effect of the coupling is to slow down the decay of ρ_ϕ, the expected physical result should be a higher DM density today. The model parameters used in this illustrative example are $m = 10^{-17}$ eV as well as the remaining Planck ΛCDM best-fit parameters. Values of Q_0 are shown in `CLASS` units, see Chapter 7 for conversion factor.

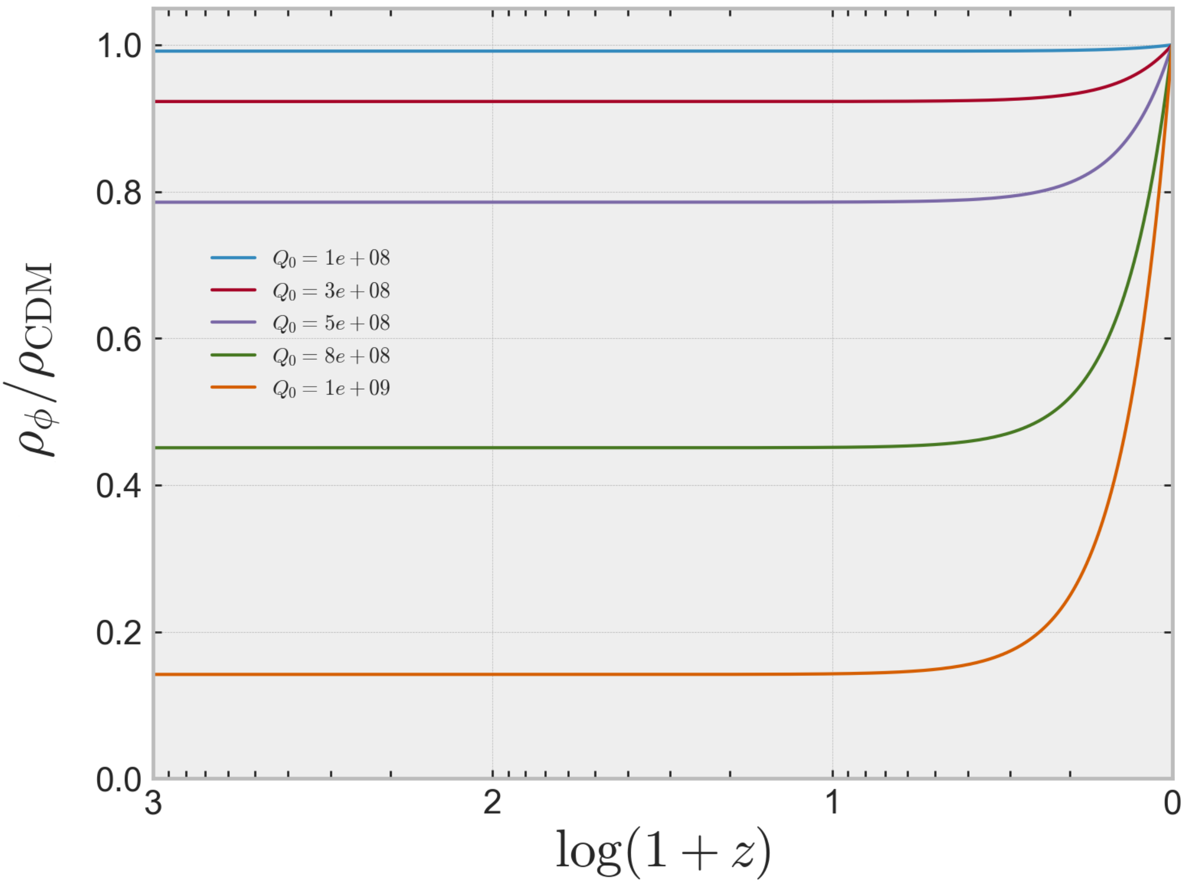

Figure 8.1: Evolution of the ratio of DM energy density in ΛQDM and ΛCDM for different values of Q_0.

Another consequence of having lower ρ_ϕ at early time is evidenced in the relative abundances of the different components of the universe. At early time, there is less dark matter and so radiation-matter equality occurs later than in ΛCDM. At late time, since ρ_ϕ behaves increasingly like a DE component, the matter-DE equality occurs earlier. Overall, this leads to a shortening of the matter domination era.

Finally, we can see the effect of the coupling on the Hubble rate in Fig. 8.2: keeping H_0 constant, we see a decrease in H during matter domination for large couplings, which directly follows from the lower ρ_ϕ. The effect of the coupling is minimal during radiation domination, so H goes back to its ΛCDM value at early-time. Note again that this effect is due to fixing H_0 to its ΛCDM value. Changing this, along with $\rho_{\phi,0}$ would modify the expansion history in different ways. We will study the correlation between the model parameters in more detail in Section 8.4.

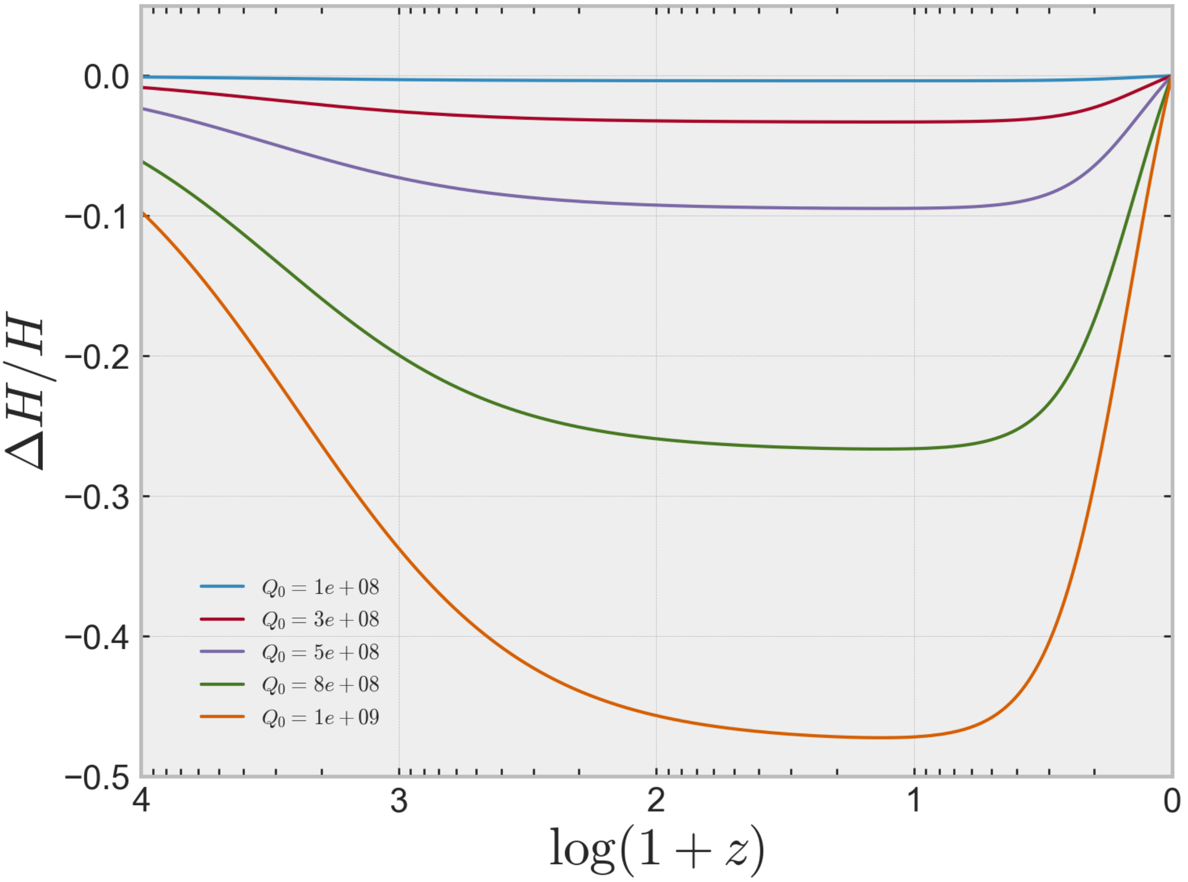

Figure 8.2: Evolution of the fractional difference in H between ΛQDM and ΛCDM, for different values of Q_0.

8.3.2 Cosmological perturbations

We now turn our attention to the linear perturbations of the model. At this level, the degeneracy between Q_0 and m is broken due to the equation of state c_s^2, which contains m on its own. This means in principle that we need two parameters to describe the model's perturbation. However, we have seen in Section 4.1.3 that the impact of a non-zero sound-speed for ultralight scalar field dark matter on the matter power spectrum is small, and indistinguishable in the CMB. The effect on the perturbations of this model can be separated into a contribution from the EoS, which depends on Q_0/m and one from the sound-speed which depends on m. Since we have shown that the sound-speed does not contribute in this case[2], we can simply go back to the same treatment we used at background level by fixing m and varying Q_0.

Both the density and velocity perturbations are suppressed in our model as Q_0 in-

---

[2] We have checked that this is the case in the ΛQDM model also.

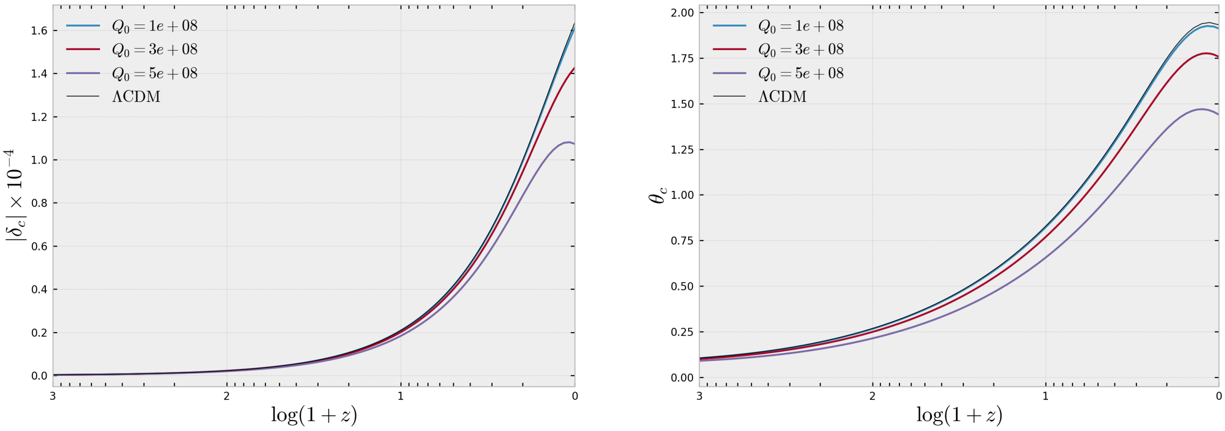

Figure 8.3: *Left*: Evolution of the density contrast for DM in ΛQDM and ΛCDM for different values of Q_0. *Right*: Evolution of the DM velocity potential in ΛQDM and ΛCDM for the same values of Q_0 as *left*. For both plots $k = 0.1$ Mpc^{-1}.

creases. A similar phenomenon is also observed in the Newtonian potentials (Fig. 8.4). This is a direct result of a lower ρ_ϕ (and therefore lower H) during matter domination. The suppression is also due to the earlier transition to DE domination, which tends to reduce the growth of DM perturbations.

Let us now focus on the observables arising due to perturbations. The most important of these is the CMB temperature power spectrum, shown in Fig. 8.5. As Q_0 increases, the CMB peaks are enhanced, in particular the first, and shifted. Again, this is primarily a consequence of lower ρ_c around recombination. The lower value leads to a increase in the angular scale of the sound horizon as well as an increase in the angular diameter distance to last scattering, therefore shifting the peaks to higher ℓ values. Another consequence of higher Q_0 and smaller ρ_ϕ is an increase in the power in the acoustic peaks, as in ΛCDM [64]: less DM means radiation-matter equality occurs later, meaning the photon perturbations are enhanced and the early ISW effect is enhanced. Increasing $\rho_{\phi,0}$ can compensate for the low ρ_ϕ at early times caused by a high Q_0. Such an increase of DM density during matter domination, so as to match the abundance of ΛCDM, would lead to an increase of H, which would flatten the $\Delta H/H$ curve. It follows, then, that the effect of increasing the coupling can be almost entirely negated by increasing the present DM density. This leaves the CMB similar to ΛCDM. It is therefore reasonable to expect a strong correlation between Q_0 and the fractional CDM energy density today $\Omega_{c,0}$ when we later compare our model to real data.

The lensing power spectrum, shown in Fig. 8.6, exhibits a decrease in power for higher Q_0. Since the source term for lensing include the lensing potential $\phi_{\text{lens}} = \Phi + \Psi$,

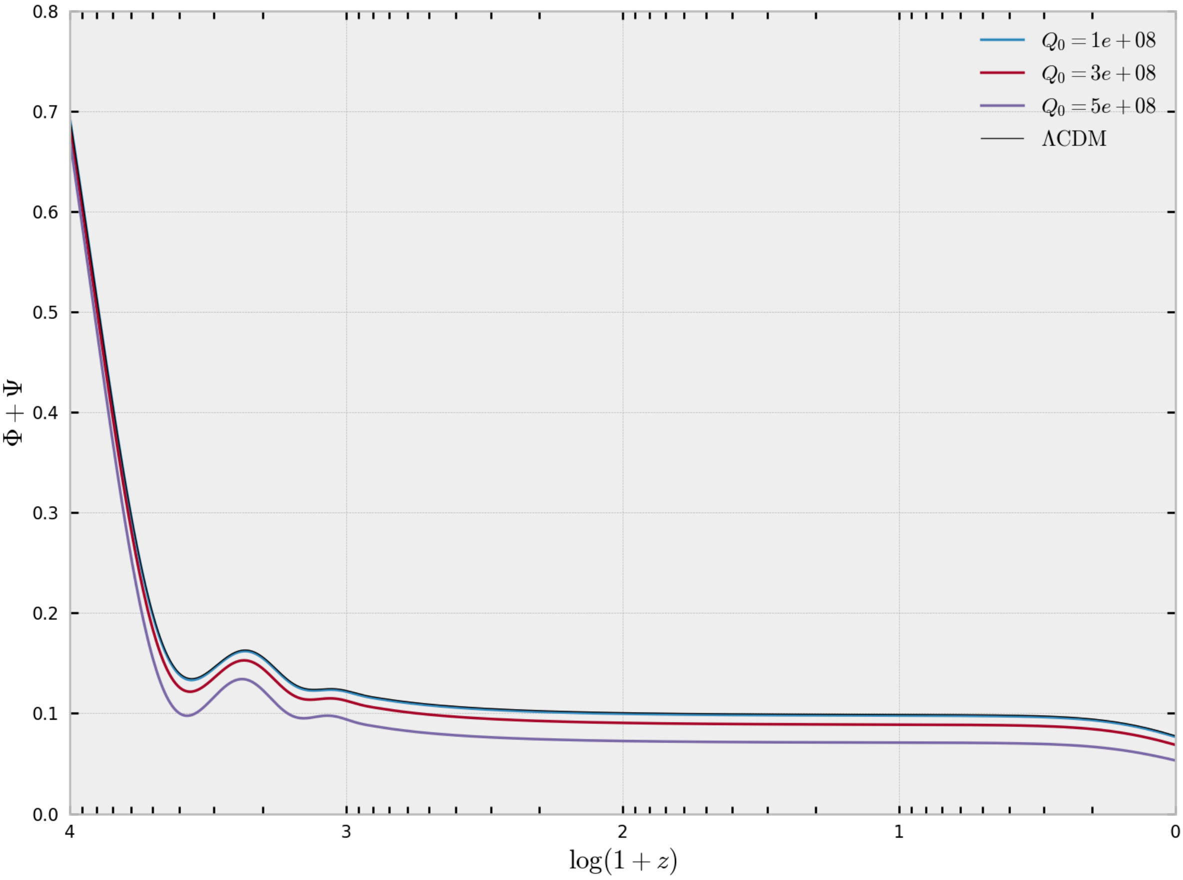

Figure 8.4: Plot of the lensing potential $\Phi + \Psi$ in ΛQDM and ΛCDM for different values of Q_0, and $k = 0.1$ Mpc^{-1}.

its behaviour mirrors that of $\Phi + \Psi$ from Fig. 8.4: As the DM perturbations are smaller from around recombination, due mainly to lower H and lower ρ_ϕ, the lensing potential is smaller and therefore the lensing power is also lower. In practice this implies less structure formation, which can also be observed by looking at the matter power spectrum in Fig. 8.7.

Whilst these simulations give us an idea of the physics at play in this model, and the effect of the coupling, the conclusions presented should be taken with a grain of salt. Since we are fixing parameters to their ΛCDM values, the model does not fit observations well and therefore overcompensates at earlier times - by reducing ρ_ϕ and H during matter domination. In practice, we will study the effects of the best-fit model after comparing it to data. This will allow us to discuss degeneracies and correlations in the parameter space, and make sense of the non-trivial effects of varying multiple cosmological parameters at the same time.

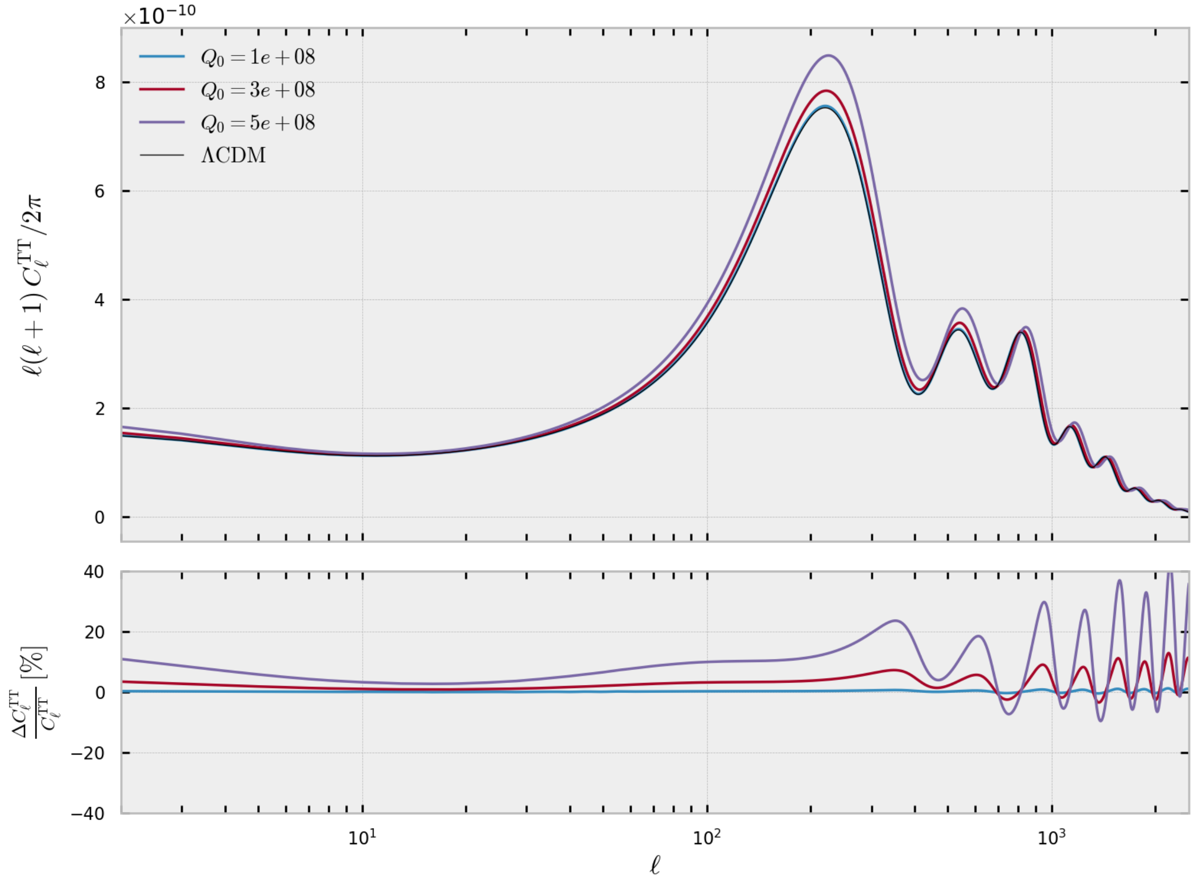

Figure 8.5: *Top panel*: temperature power spectra against angular scale ℓ for various values of Q_0 in ΛQDM and for ΛCDM. *Bottom panel*: fractional difference between ΛQDM and ΛCDM values for $C_\ell^{\rm TT}$.

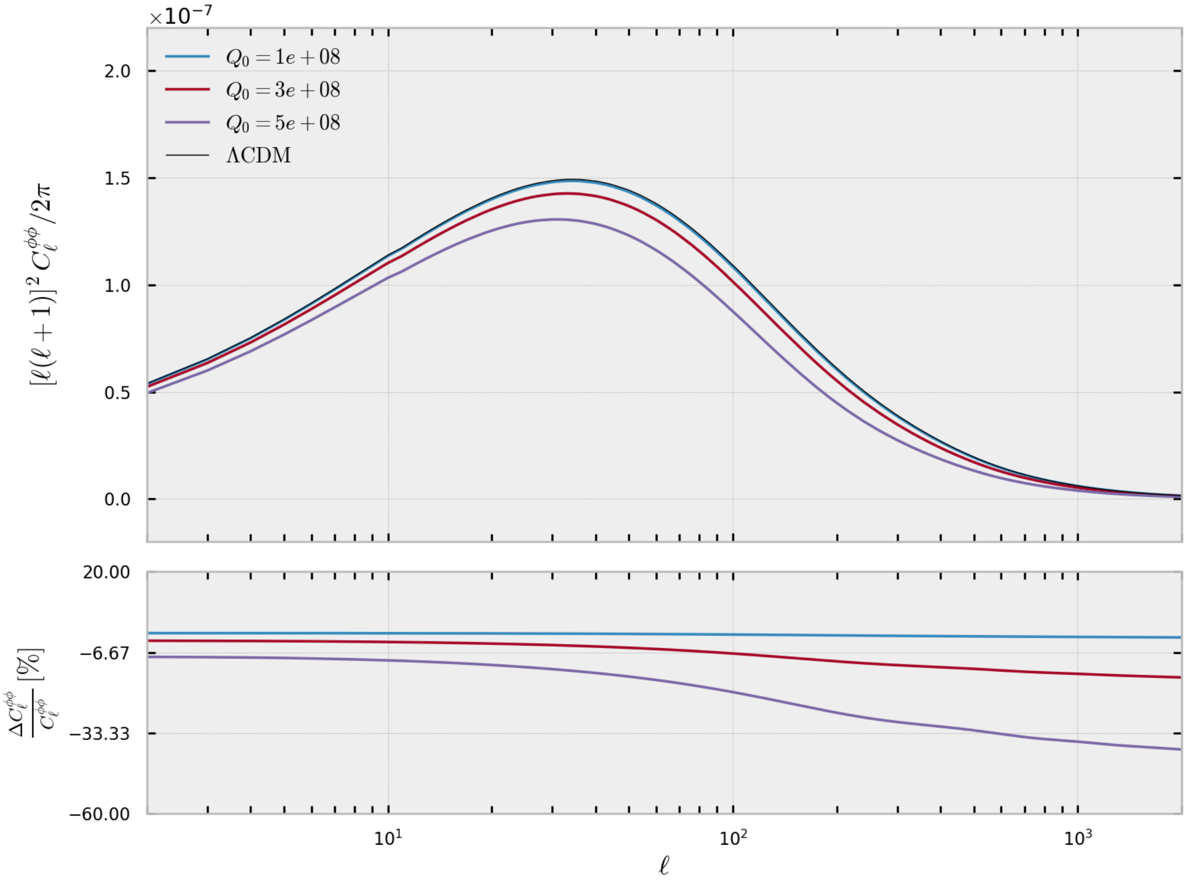

Figure 8.6: *Top panel*: lensing power spectra against angular scale ℓ for various values of Q_0 in ΛQDM and for ΛCDM. *Bottom panel*: fractional difference between ΛQDM and ΛCDM values for $C_\ell^{\phi\phi}$.

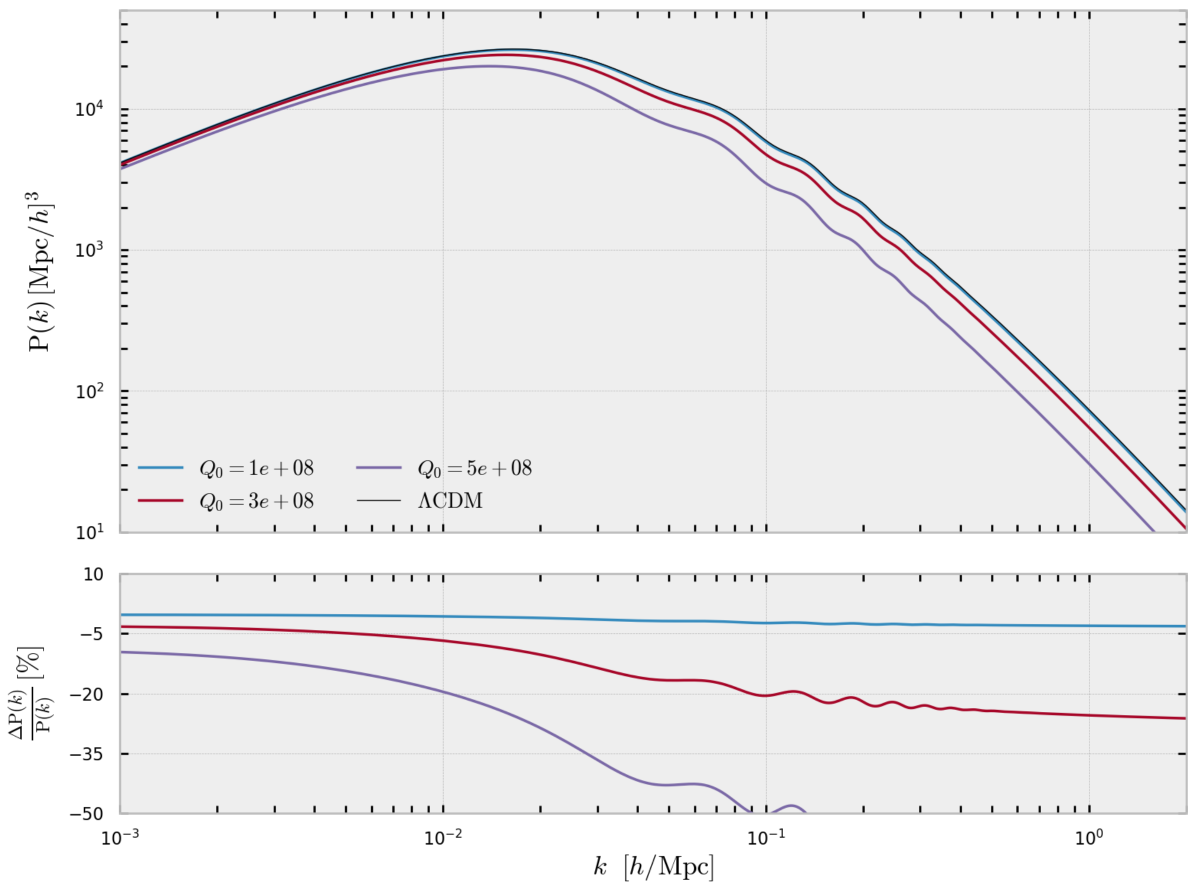

Figure 8.7: *Top panel*: matter power spectra against wave number k for various values of Q_0 in ΛQDM and for ΛCDM. *Bottom panel*: fractional difference between ΛQDM and ΛCDM values for $P(k)$.

8.4 Constraints on model parameters

8.4.1 Methodology and datasets

Using our modified `CLASS` code, we perform a MCMC anaysis using the publicly available sampler `Cobaya` to establish how well our model fits cosmological data. Cosmological and nuisance parameters are varied according to Cholesky's parameter decomposition. We consider chains to be converged with the Gelman-Rubin convergence criterion $R - 1 < 0.03$. The obtained chains are analysed using the `GetDist` Python package.

We assume standard ΛCDM priors as shown in Table 8.1. Note that we choose to vary H_0 instead of θ_s; these two approaches are equivalent as far as the `CLASS` code is concerned. For Q_0, we opt for a flat prior on a rescaled version of the parameter, $10^{-8} \times Q_0$. Note that this is in `CLASS` units. The reason for this rescaling is that most of the values of Q_0, from 0 to around $\sim 10^7$, show no effect on any cosmological observables. This implies most of the parameter space is simply equivalent to ΛCDM. In order to reduce the ΛCDM-like parameter volume, we rescale the extra parameter so that more weight is put on the phenomenologically distinct part of the parameter space. As stated in the previous section, we can fix the mass of the scalar field m and vary Q_0; we set $m = 10^{-17}$ eV without loss of generality. The other independent parameters are fixed to their Planck best-fit values [8], including the assumption of two massless and one massive neutrino species with $m_\nu = 0.06\,\text{eV}$. Although not explicitly listed, a large number of nuisance parameters are varied simultaneously, following the respective collaboration recommendations.

Parameter	Prior
$\Omega_b h^2$	$[0.005, 0.1]$
$\Omega_c h^2$	$[0.001, 0.99]$
H_0	$[20, 100]$
τ_{reio}	$[0.02, 0.08]$
n_s	$[0.7, 1.3]$
$\log(10^{10} A_s)$	$[1.7, 5.0]$
$10^{-8} Q_0$	$[0, 8]$

Table 8.1: Flat priors on the cosmological and model parameters sampled in this work.

We use the following datasets:

- **Planck PR4 (PR4)**: The latest Planck CMB release, introduced in [107]. It includes the large-scale low-l TT likelihood `Commander` and low-l EE likelihood `simAll` from Planck 2018 release. Both of these are in the range $2 \leq l \leq 29$. The high-l likelihood for TT, EE and TE spectra is the NPIPE `CamSpec` likelihood [106], in the range $30 \leq l \lesssim 2500$. The PR4 lensing likelihood is also included, as described in [273].

- **DESI**: As described in Section 6.3.1.
- **Pantheon+ (SN)**: As described in Section 6.3.1.
- **Pantheon+ with SH_0ES R22 (SH0ES)**: As described in Section 6.3.1.

We will use different combinations of datasets starting with our baseline of Planck PR4, which we refer to as PR4. We then consider Planck PR4 and Pantheon+ (PR4+SN), PR4 and DESI (PR4+DESI), PR4 and Pantheon+ and DESI (PR4+SN+DESI) and finally we combine all datasets including the H_0 prior: PR4+DESI+SH0ES.

8.4.2 Results

We now discuss the constraints on the model parameters imposed by the various dataset combinations, and compare them to ΛCDM. We quantify the goodness of fit for each dataset by using the difference in χ^2 between our model and ΛCDM: $\Delta\chi^2_{\rm min} = \chi^2_{\rm min,\Lambda QDM} - \chi^2_{\rm min,\,\Lambda CDM}$. A negative value of $\Delta\chi^2_{\rm min}$ indicates a better fit for the Q_0 model compared to ΛCDM. These chi-squared values are obtained using the `minimizer` method from `Cobaya`. From here on we will refer to ρ_ϕ as ρ_c in order to compare to the ΛCDM values.

We show the 68% confidence intervals for the ΛQDM parameters and $\Delta\chi^2$ values in Table 8.2 (see Appendix C for the same table for ΛCDM). Fig. 8.8 shows the posterior distributions comparing the ΛQDM and ΛCDM models for the PR4 and PR4+DESI+SH0ES. Fig. 8.9 shows the posterior distributions for the ΛQDM model for all dataset combinations except PR4+DESI+SH0ES.

As a general observation, all datasets seem to agree with our earlier hypothesis that Q_0 and Ω_c should be highly correlated, whilst Q_0 and H_0 are not. That is to say, an increase in Q_0 can be compensated by an increase in ω_c. In turn, this increase in ω_c leads to the CDM energy density at recombination $\rho_{c,\rm rec}$ being close to its ΛCDM value, and H will also be unchanged during that time. The resulting cosmology is therefore close to ΛCDM as far as the CMB and other late time background probes are concerned. We will discuss later what other data could be included to narrow down the constraints. Another interesting result, which is consistent across all datasets, is a lower preferred

Parameter	**PR4**	**PR4+SN**	**PR4+DESI**	**PR4+DESI+SN**	**PR4+DESI+SH0ES**
$\omega_{\rm b}$	0.02216 ± 0.00013	0.02214 ± 0.00013	0.02227 ± 0.00013	0.02225 ± 0.00013	0.02233 ± 0.00012
$\omega_{\rm c}$	$0.141^{+0.012}_{-0.025}$	$0.139^{+0.011}_{-0.024}$	$0.137^{+0.010}_{-0.023}$	$0.139^{+0.013}_{-0.025}$	$0.138^{+0.012}_{-0.025}$
$\tau_{\rm reio}$	0.0523 ± 0.0072	0.0514 ± 0.0069	0.0573 ± 0.0071	$0.0561^{+0.0064}_{-0.0073}$	0.0591 ± 0.0071
n_s	0.9620 ± 0.0042	0.9614 ± 0.0041	0.9659 ± 0.0037	0.9650 ± 0.0037	0.9673 ± 0.0036
$\log 10^{10} A_s$	3.037 ± 0.014	3.036 ± 0.014	3.045 ± 0.014	3.043 ± 0.013	3.048 ± 0.014
H_0	67.18 ± 0.46	67.04 ± 0.44	67.87 ± 0.36	67.73 ± 0.35	68.12 ± 0.35
$10^{-8} Q_0$	$--$	< 4.91	< 4.83	$--$	$--$
σ_8	$0.714^{+0.10}_{-0.060}$	$0.722^{+0.098}_{-0.055}$	$0.721^{+0.098}_{-0.053}$	$0.712^{+0.10}_{-0.062}$	$0.716^{+0.10}_{-0.087}$
Ω_m	$0.361^{+0.028}_{-0.056}$	$0.359^{+0.026}_{-0.053}$	$0.346^{+0.023}_{-0.050}$	$0.353^{+0.028}_{-0.055}$	$0.345^{+0.026}_{-0.054}$
S_8	$0.777^{+0.056}_{-0.033}$	$0.783^{+0.054}_{-0.030}$	$0.768^{+0.053}_{-0.028}$	$0.766^{+0.056}_{-0.033}$	$0.761^{+0.056}_{-0.031}$
$\Delta\chi^2_{\rm min}$	0.78	0.26	1.38	0.98	2.88

Table 8.2: Observational constraints at 68% confidence level on the independent and derived cosmological parameters using all dataset combinations for the ΛQDM model, as detailed in Section 8.4.1. $\Delta\chi^2_{\rm min}$ values are also included, computed as explained in Section 8.4.1.

value for σ_8 and S_8. This makes sense from our previous analysis as we saw in Fig. 8.7 that higher Q_0 values led to smaller matter power spectra. Due to its degeneracy with ω_c, Q_0 is largely unconstrained – see Table 8.2. Other parameters, including A_s, n_s, $\tau_{\rm reio}$, ω_b, remain unchanged by the addition of the late-time negative EoS for DM. The baseline dataset, i.e. including only PR4 CMB data, reveals an almost equal preferred value of H_0 compared to ΛCDM, $H_0 = 67.18 \pm 0.46$. At the same time, the mean value for ω_c increases to $\omega_c = 0.141^{+0.012}_{-0.025}$ and S_8 decreases to $S_8 = 0.777^{+0.056}_{-0.033}$. The overall behaviour of parameters under a change of dataset in ΛQDM is consistent with that observed in ΛCDM. For example, the value of the best-fit H_0 decreases when considering PR4+SN, but increases when including DESI data, with the highest value predictably obtained for the full dataset combination PR4+DESI+SN+SH0ES. Both in ΛCDM and ΛQDM, DESI data prefers lower values of ω_c and S_8, while Pantheon+ prefers slightly higher values of ω_c and S_8. This can explain why the fit, as evidenced by the $\Delta\chi^2_{\rm min}$ values, is worsened when adding DESI data, as our model tends to increase ω_c rather than reduce it. Combining PR4+DESI+SN leads to only a slight increase in ω_c and S_8 compared to PR4+DESI.

Overall, judging by the $\Delta\chi^2$ values, ΛQDM is generally indistinguishable from, or fits slightly worse than ΛCDM. The fit is in particular worse for datasets which naturally prefer a higher (lower) value for H_0 (ω_c), such as PR4+DESI and PR4+DESI+SH0ES.

As we will see below, the ΛQDM model breaks the degeneracy between H_0 and ω_c (see Fig. 8.8). This means that it is not possible to adjust the H_0 parameter in ΛQDM in order to lower ω_c, leading to a still high value of ω_c in ΛQDM which worsens the fit.

Whilst the ΛQDM model does show preference for a lower value of S_8, as shown in Fig. 8.10, a full analysis using LSS data would be needed to establish the degree to which the S_8 tension is addressed in this model. What is more, since Q_0 is unconstrained, S_8 correspondingly can take a range of values. It is possible that adding LSS data may break the degeneracy between Q_0 and Ω_c, but we leave this analysis for future work.

There are two main reasons why the model does not depart much from ΛCDM, and thus does not alleviate the Hubble tension. First, due to the correlation between ω_c and Q_0, the correlation between ω_c and H_0 completely disappears compared to ΛCDM. This can be explained by the fact that the value of ω_c at recombination is tightly constrained by the first peak of the CMB in this model, as in ΛCDM. Since Ω_c at recombination is adjusted by varying $\Omega_{c,0}$ and Q_0, H_0 does not have any freedom to vary. This leads into the second reason, which is that the changes to the physics are focussed on very late times, $z < 1$. This reduces the ability to imprint new signatures into the CMB, as the only possible effect is the late-time ISW, which we have checked deviates minimally from ΛCDM in this model. What is more, the late time probes DESI and Pantheon+ lack constraining power at low enough redshifts, and therefore do not contribute much to the total χ^2 value. It is interesting to note the preference in this model for higher ω_c, which seems to agree with supernovae data. It would be interesting to use alternative SN datasets, such as DESY5 which prefers even higher CDM densities compared to Pantheon+ [274].

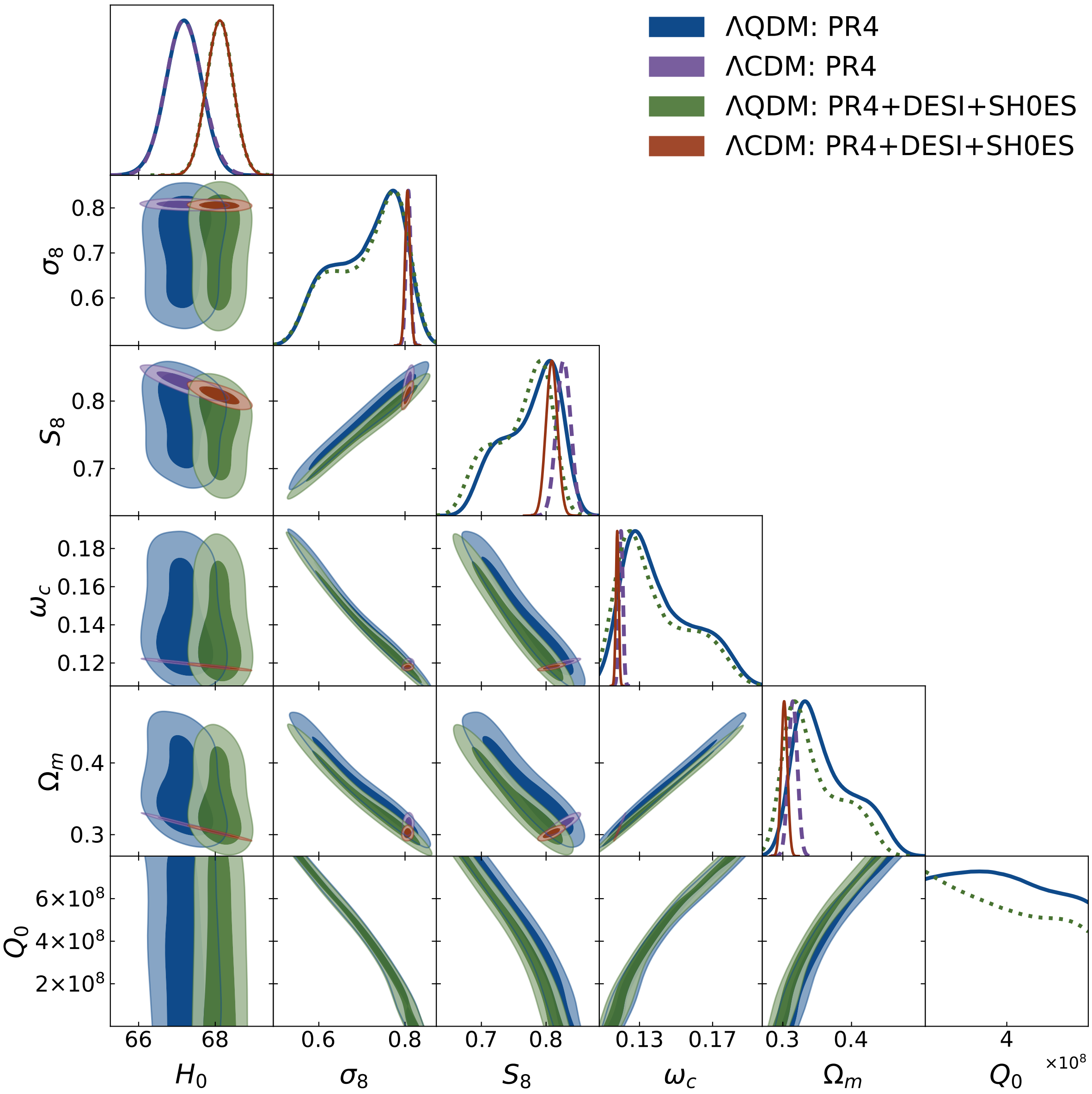

Figure 8.8: One-dimensional posterior probability distribution functions and two-dimensional contours at 68% and 95% CL for the parameters of interest in the ΛQDM model and the standard ΛCDM model for reference, for the PR4 dataset and the full combination PR4+DESI+SH0ES.

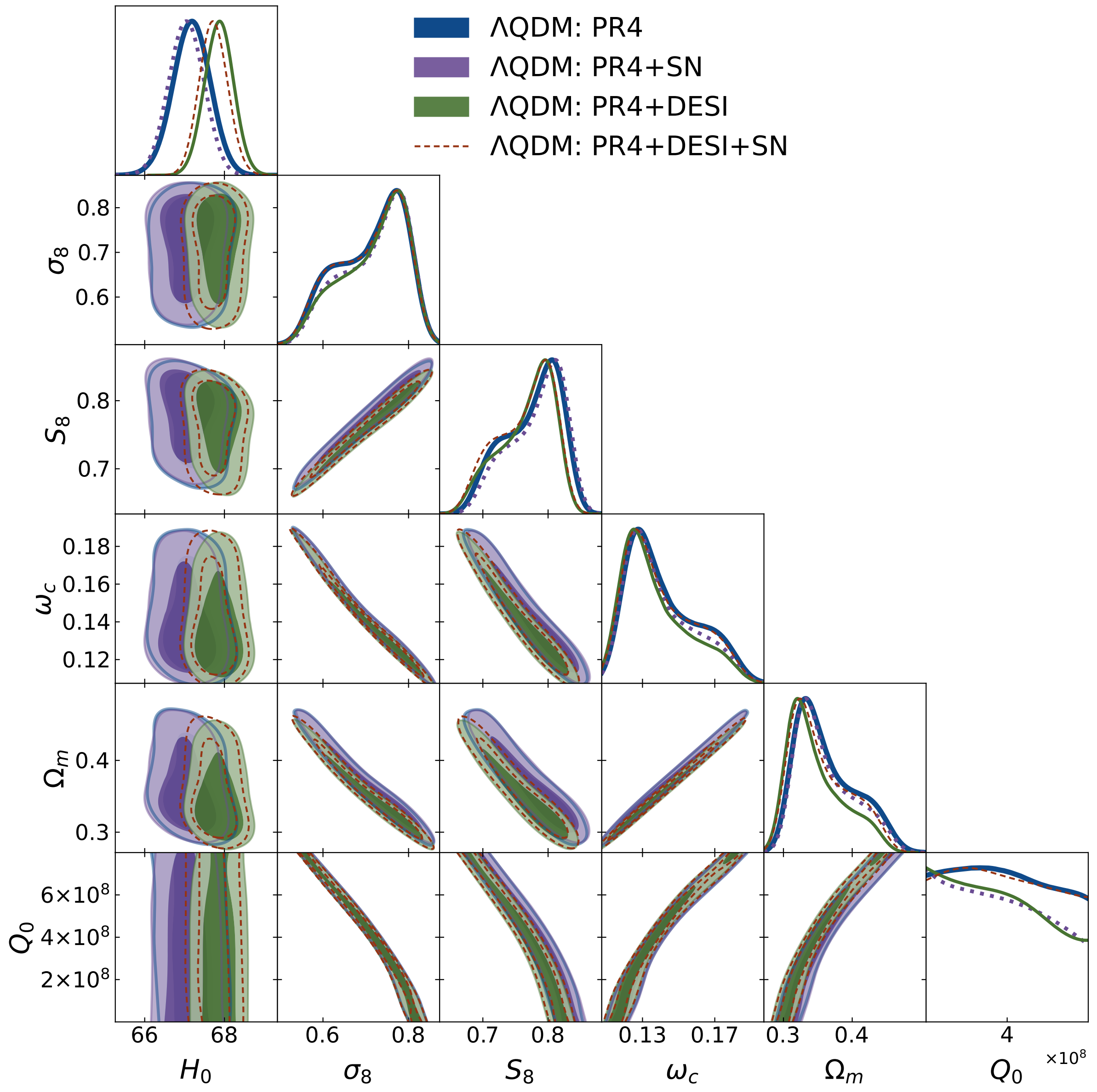

Figure 8.9: One-dimensional posterior probability distribution functions and two-dimensional contours at 68% and 95% CL for the parameters of interest in the ΛQDM model for incremental dataset combinations, as indicated in the legend and listed in Section 8.4.1.

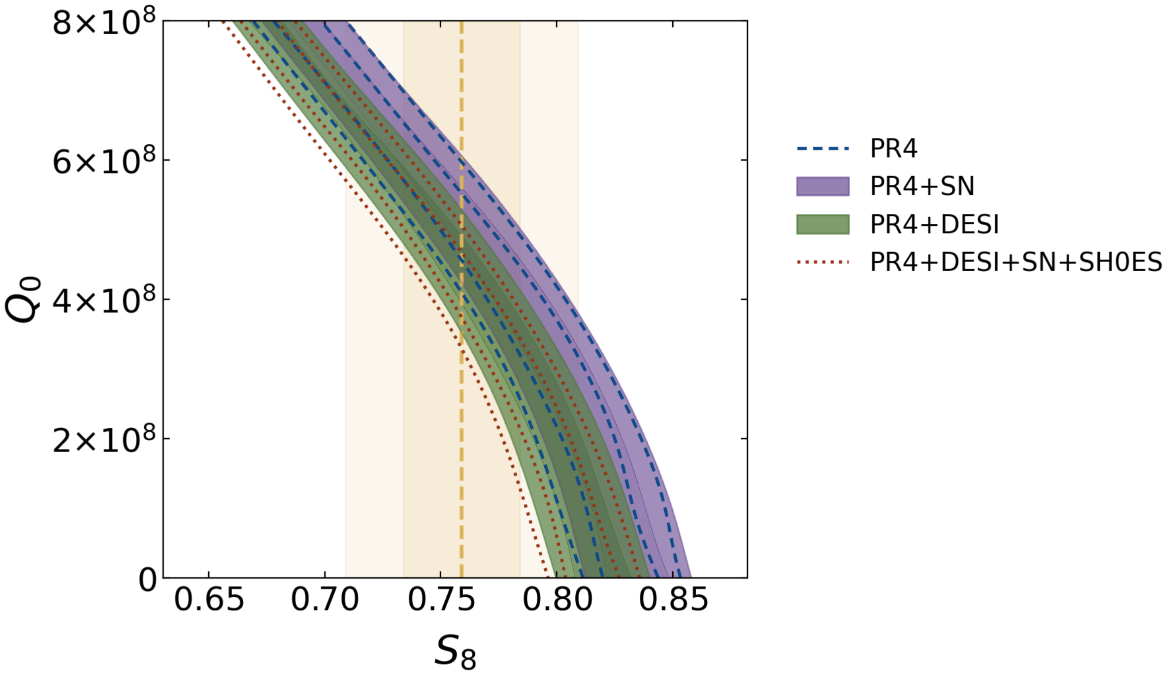

Figure 8.10: 2D contours at 68% and 95% CL for Q_0 and the S_8 parameter in the ΛQDM. The results are inferred considering different combinations of Planck PR4, DESI BAO distance, and SN distance moduli data. The yellow dashed line and band represent the value of S_8 from DESY3 and the corresponding uncertainties.

8.5 Conclusions

In this chapter we have studied in detail the ΛQDM model, both in terms of its cosmological observables and how well it fits cosmological datasets – including Planck PR4, DESI and Pantheon+. The Q_0 model is the simplest extension to ΛCDM based on the EFT of interacting DM-DE described in Chapter 7. In this model, we consider only the linear interaction between the DM and DE fields – we set $Q_0 \neq 0$ and $Q_1 = 0$ – and the dynamics of the DE scalar field are approximated at 0^{th} order – i.e. as a cosmological constant – and so Q_0 is a constant. Although this is a much simplified model, it is important to note that the key physics of the model described in Section 7.3 are still present here, namely the equation of state of DM becomes negative at late time, around DM-DE equality.

We studied the background and linear perturbation dynamics of the model, as well as cosmological observables. At the background level, the negative EoS leads the DM to decay more slowly at late times. This implies that, for H_0 and Ω_c fixed to ΛCDM values, the energy density of DM ρ_c is lower in the past, leading to a lower H_0. This effect is also seen in the perturbations, leading to an enhancement in the CMB first peak, and a decrease in the matter power spectrum. The effects of the coupling are only relevant when Q_0 is large enough to match the DE scale. This corresponds roughly to $Q_0 > 5 \times 10^7$ in `CLASS` units. We then constrained this model by comparing it to a wide range of cosmological datasets including CMB, BAO and Supernovae data. From the data analysis, it is clear that Q_0 and Ω_c are strongly correlated, to the point where any increase in Q_0 can be balanced by an increase in Ω_c today. A related correlation arises for clustering with S_8 decreasing as Q_0 increases. H_0 is entirely uncorrelated to Q_0 and its value is consistent with that obtained in ΛCDM. The fit of the Q_0 model is slightly worse than that of ΛCDM, as estimated with the $\Delta\chi^2$ values. We suspect that using LSS data, such as redshift space distortion, could break some degeneracies and provide better constraints on Q_0. It would also be interesting to use alternate SN data such as DESY5 to see if the preference for higher ω_c is enhanced.

Overall, this work showcases how a simple model for very-late-time interactions in the dark sector based on a Lagrangian description can lead to interesting phenomenology, especially reducing the preferred value of S_8.

Chapter 9

Conclusions

In this thesis, we gave an introduction to modern cosmology, with a focus on dark sector dynamics, its observational signatures and viability in light of new data. In particular, we focused on novel scalar field models for DM and DE, including interactions. These models have not been studied extensively in the literature, even though they provide interesting theoretical and phenomenological implications. Indeed, two-scalar field models can be thought of as toy-models for low-energy realisations of unifying theories, such as string theory – which commonly predicts multiple interacting scalar fields [214]. Whilst adopting a top-down approach – starting from a high-energy theory and working out the cosmology – is attractive, they are often restrictive and less well understood. We bridge the gap in our approach by starting from a Lagrangian formulation and computing the cosmological evolution of the DM and DE components, agnostic of any fundamental theory.

We started with a brief review of the background material as well as the current literature in scalar field dark sectors. In Chapter 2 we introduced GR and the basics of physical cosmology. In Chapter 3 we discussed the relevant observational probes in the historical development of cosmology as well as the standard model ΛCDM, elaborating on its successes and limitations. In Chapter 4 we covered essential elements from the literature pertaining to scalar fields in cosmology, involving DE and DM models as well as their interactions. From Chapter 5 onwards, we present new results found as part of the doctoral research.

Chapter 5 provides a novel model for an interacting dark sector based on two scalar fields and the hybrid inflation potential. We start from the two-scalars description and average out the rapid oscillations of the DM field, to end up with a DM fluid interacting with a DE scalar ϕ. The coupling is proportional to the DM energy density and $1/\phi$, which was not previously studied as a phenomenological coupling. We solve for the evolution of this system both analytically and numerically, obtaining observables such as the CMB and matter power spectra. We also find that in this model, the mass of the DM field is typically large and the DE domination is transient – there is a phase transition in the future at which point the DE scalar decays completely.

In Chapter 6 we confront the hybrid dark sector model against modern cosmological data, including CMB, BAO and supernovae. We find a preference for a non-zero coupling when including the SH0ES prior, which also yields a higher value for H_0, reducing the tension to 4.65σ in the hybrid model compared to 5.76σ in ΛCDM. The coupling parameter $1/\phi_i$ also leads to a smaller value for S_8. These results highlight the potential of late time modifications to ΛCDM, and motivate adopting a more top-down approach which can lead to new and interesting phenomenology.

In Chapter 7 we propose a new framework to study interacting DM and DE scalar fields based on effective field theory. Starting from a Lagrangian, we show that averaging over the fast-oscillations of the DM scalar leads to a DM fluid with non-zero equation of state. This is a novel result, as interacting DM-DE models usually assume cold DM with modified DE dynamics. The equation of state in this model is typically positive at early times and becomes negative around matter-DE equality. We also compute the sound-speed of DM perturbations in this framework, which we find to be different to the standard result for non-interacting axions, leading to a suppression of power in the matter power spectrum on all scales. We also study two realisations of the framework. A conformal coupling depending on the fast-oscillating DM field is used, which we show is equivalent to the EFT approach. This leads to a coupling proportional to $\rho_{\rm DE}$, providing theoretical motivation for a wide class of phenomenological models, although the parameter values can potentially lead to instabilities. We also study a $0^{\rm th}$-order approximation of our framework by considering the DE field to be a constant.

We investigate further the minimal DE-DM EFT interacting model in Chapter 8, computing its observables and performing data-analysis to compare its fit to ΛCDM. We set $Q_1 = 0$, naming the model ΛQDM. This model is very similar to ΛCDM apart from its evolution during DE domination, when the EoS of DM becomes negative. At the level of the CMB, this effect can be compensated by increasing Ω_c at present time. Running the data-analysis, we find that Q_0 is strongly positively correlated with Ω_c and negatively correlated with S_8. This means that the ΛQDM prefers lower values of S_8, in line with the S_8 tension, however H_0 remains unchanged compared to ΛCDM. The fit of this model is slightly worse than ΛCDM when including DESI BAO measurements, as these tend to prefer lower values for Ω_c. The parameter Q_0 is not well constrained with this combination of datasets, although new LSS data could break degeneracies.

To conclude, our investigation of two-scalar field interacting dark sectors has shown that rich phenomenology can be found when considering more fundamental models. We hope that further theoretical questioning and cosmological data will be able to shed light on the dark sector, potentially solving observational tensions at the same time.

Bibliography

[1] van de Bruck, C., Poulot, G. & Teixeira, E. M. Scalar field dark matter and dark energy: a hybrid model for the dark sector. *JCAP* **07**, 019 (2023). 2211.13653.

[2] Teixeira, E. M., Poulot, G., van de Bruck, C., Di Valentino, E. & Poulin, V. Alleviating cosmological tensions with a hybrid dark sector (2024). 2412.14139.

[3] Poulot, G., Teixeira, E. M., van de Bruck, C. & Nunes, N. J. Scalar field dark matter with time-varying equation of state (2024). 2404.10524.

[4] Adam, R. *et al.* Planck 2015 results. I. Overview of products and scientific results. *Astron. Astrophys.* **594**, A1 (2016). 1502.01582.

[5] Aghanim, N. *et al.* Planck 2018 results. I. Overview and the cosmological legacy of Planck. *Astron. Astrophys.* **641**, A1 (2020). 1807.06205.

[6] Alam, S. *et al.* Completed SDSS-IV extended baryon oscillation spectroscopic survey: cosmological implications from two decades of spectroscopic surveys at the Apache Point observatory. *Phys. Rev. D* **103**, 083533 (2021). 2007.08991.

[7] Hubble, E. A relation between distance and radial velocity among extra-galactic nebulae. *Proc. Nat. Acad. Sci.* **15**, 168–173 (1929).

[8] Aghanim, N. *et al.* Planck 2018 results. VI. Cosmological parameters. *Astron. Astrophys.* **641**, A6 (2020). [Erratum: Astron.Astrophys. 652, C4 (2021)], 1807.06209.

[9] Kamionkowski, M. & Riess, A. G. The Hubble tension and early dark energy. *Ann. Rev. Nucl. Part. Sci.* **73**, 153–180 (2023). 2211.04492.

[10] Aiola, S. *et al.* The Atacama Cosmology Telescope: DR4 maps and cosmological parameters. *JCAP* **12**, 047 (2020). 2007.07288.

[11] Henning, J. W. *et al.* Measurements of the temperature and E-Mode polarization of the CMB from 500 square degrees of SPTpol data. *Astrophys. J.* **852**, 97 (2018). `1707.09353`.

[12] Hinshaw, G. *et al.* Nine-year Wilkinson Microwave Anisotropy Probe (WMAP) observations: cosmological parameter results. *ApJS* **208**, 19 (2013). `1212.5226`.

[13] Adame, A. G. *et al.* DESI 2024 VI: cosmological constraints from the measurements of baryon acoustic oscillations. *JCAP* **02**, 021 (2025). `2404.03002`.

[14] Riess, A. G. *et al.* A comprehensive measurement of the local value of the Hubble constant with 1 km s^1 Mpc^1 uncertainty from the Hubble space telescope and the SH0ES team. *Astrophys. J. Lett.* **934**, L7 (2022). `2112.04510`.

[15] Riess, A. G. *et al.* JWST validates HST distance measurements: selection of supernova subsample explains differences in JWST estimates of local H $_0$. *Astrophys. J.* **977**, 120 (2024). `2408.11770`.

[16] Freedman, W. L. *et al.* Status report on the Chicago-Carnegie Hubble program (CCHP): measurement of the Hubble constant using the Hubble and James Webb space telescopes. *Astrophys. J.* **985**, 203 (2025). `2408.06153`.

[17] Wong, K. C. *et al.* H0LiCOW – XIII. A 2.4 per cent measurement of H0 from lensed quasars: 5.3σ tension between early- and late-Universe probes. *Mon. Not. Roy. Astron. Soc.* **498**, 1420–1439 (2020). `1907.04869`.

[18] Pesce, D. W. *et al.* The megamaser cosmology project. XIII. Combined Hubble constant constraints. *Astrophys. J. Lett.* **891**, L1 (2020). `2001.09213`.

[19] Kourkchi, E. *et al.* Cosmicflows-4: the calibration of optical and infrared Tully–Fisher relations. *Astrophys. J.* **896**, 3 (2020). `2004.14499`.

[20] Blakeslee, J. P., Jensen, J. B., Ma, C.-P., Milne, P. A. & Greene, J. E. The Hubble constant from infrared surface brightness fluctuation distances. *Astrophys. J.* **911**, 65 (2021). `2101.02221`.

[21] Di Valentino, E. *et al.* In the realm of the Hubble tension—a review of solutions. *Class. Quant. Grav.* **38**, 153001 (2021). `2103.01183`.

[22] Dutcher, D. *et al.* Measurements of the E-mode polarization and temperature-E-mode correlation of the CMB from SPT-3G 2018 data. *Phys. Rev. D* **104**, 022003 (2021). 2101.01684.

[23] Secco, L. F. *et al.* Dark Energy Survey Year 3 results: cosmology from cosmic shear and robustness to modeling uncertainty. *Phys. Rev. D* **105**, 023515 (2022). 2105.13544.

[24] Asgari, M. *et al.* KiDS-1000 cosmology: cosmic shear constraints and comparison between two point statistics. *Astron. Astrophys.* **645**, A104 (2021). 2007.15633.

[25] Abbott, T. M. C. *et al.* DES Y3 + KiDS-1000: consistent cosmology combining cosmic shear surveys. *Open J. Astrophys.* **6**, 2305.17173 (2023). 2305.17173.

[26] Heymans, C. *et al.* KiDS-1000 cosmology: multi-probe weak gravitational lensing and spectroscopic galaxy clustering constraints. *Astron. Astrophys.* **646**, A140 (2021). 2007.15632.

[27] Lange, J. U. *et al.* Constraints on S8 from a full-scale and full-shape analysis of redshift-space clustering and galaxy–galaxy lensing in BOSS. *Mon. Not. Roy. Astron. Soc.* **520**, 5373–5393 (2023). 2301.08692.

[28] Marulli, F. *et al.* C3 cluster clustering cosmology I. New constraints on the cosmic growth rate at z $\sim$ 0.3 from redshift-space clustering anisotropies. *Astrophys. J.* **920**, 13 (2021). 2010.11206.

[29] Chevallier, M. & Polarski, D. Accelerating universes with scaling dark matter. *Int. J. Mod. Phys. D* **10**, 213–224 (2001). gr-qc/0009008.

[30] Linder, E. V. Exploring the expansion history of the universe. *Phys. Rev. Lett.* **90**, 091301 (2003). astro-ph/0208512.

[31] Einstein, A. Zur allgemeinen relativitätstheorie. *Sitzungsber. Preuss. Akad. Wiss. Berlin (Math. Phys.)* **1915**, 778–786 (1915).

[32] Friedmann, A. Über die krümmung des raumes. *Zeitschrift fur Physik* **10**, 377–386 (1922). https://doi.org/10.1007/BF01332580.

[33] Lemaître, G. A homogeneous universe of constant mass and increasing radius accounting for the radial velocity of extra-galactic nebulae. *MNRAS* **91**, 483–490 (1931). https://doi.org/10.1093/mnras/91.5.483.

[34] Robertson, H. P. Kinematics and world-structure. *ApJ* **82**, 284 (1935). https://doi.org/10.1086/143726.

[35] Walker, A. G. On Milne's theory of world-structure. *Proceedings of the London Mathematical Society* **42**, 90–127 (1937). https://doi.org/10.1112/plms/s2-42.1.90.

[36] Turner, M. S. The road to precision cosmology. *Ann. Rev. Nucl. Part. Sci.* **72**, 1–35 (2022). http://dx.doi.org/10.1146/annurev-nucl-111119-041046.

[37] Linde, A. D. Hybrid inflation. *Phys. Rev. D* **49**, 748–754 (1994). astro-ph/9307002.

[38] Carroll, S. M. *Spacetime and Geometry: An Introduction to General Relativity* (Cambridge University Press, 2019).

[39] Misner, C. W., Thorne, K. S. & Wheeler, J. A. *Gravitation* (W. H. Freeman, San Francisco, 1973).

[40] Wald, R. M. *General Relativity* (Chicago Univ. Pr., Chicago, USA, 1984).

[41] Lovelock, D. The Einstein tensor and its generalizations. *J. Math. Phys.* **12**, 498–501 (1971). https://doi.org/10.1063/1.1665613.

[42] O'Raifeartaigh, C. & Mitton, S. Interrogating the legend of Einstein's 'biggest blunder'. *Physics in Perspective* **20**, 318–341 (2018). http://dx.doi.org/10.1007/s00016-018-0228-9.

[43] Straumann, N. Minimal assumptions leading to a Robertson–Walker model of the Universe. *Helv. Phys. Acta, v. 47, no. 3, pp. 379-383* (1974). https://www.osti.gov/biblio/4240052.

[44] Pandey, B. & Sarkar, S. Testing homogeneity in the sloan digital sky survey data release twelve with shannon entropy. *Mon. Not. Roy. Astron. Soc.* **454**, 2647–2656 (2015). https://dx.doi.org/10.1093/mnras/stv2166.

[45] Baumann, D. *Cosmology* (Cambridge University Press, 2022).

[46] Kurki-Suonio, H. Cosmological perturbation theory i (2024). https://www.mv.helsinki.fi/home/hkurkisu/cpt/CosPer.pdf.

[47] Ma, C.-P. & Bertschinger, E. Cosmological perturbation theory in the synchronous and conformal Newtonian gauges. *Astrophys. J.* **455**, 7–25 (1995). astro-ph/9506072.

[48] Liddle, A. R. & Lyth, D. H. *Cosmological inflation and large scale structure* (Cambridge University Press, 2000).

[49] de Sitter, W. Einstein's theory of gravitation and its astronomical consequences, First Paper. *Mon. Not. Roy. Astron. Soc.* **76**, 699–728 (1916). https://doi.org/10.1093/mnras/76.9.699.

[50] Peebles, P. J. E. *Principles of Physical Cosmology* (Princeton University Press, 2020).

[51] Bertone, G. & Hooper, D. History of dark matter. *Rev. Mod. Phys.* **90**, 045002 (2018). https://link.aps.org/doi/10.1103/RevModPhys.90.045002.

[52] Rubin, V. C. Dark matter in spiral galaxies. *Scientific American* **248**, 96–106 (1983). https://doi.org/10.1038/scientificamerican0683-96.

[53] Perlmutter, S. *et al.* Measurements of Ω and Λ from 42 high redshift supernovae. *Astrophys. J.* **517**, 565–586 (1999). astro-ph/9812133.

[54] Riess, A. G. *et al.* Observational evidence from supernovae for an accelerating universe and a cosmological constant. *Astron. J.* **116**, 1009–1038 (1998). astro-ph/9805201.

[55] Brout, D. *et al.* The Pantheon+ analysis: cosmological constraints. *Astrophys. J.* **938**, 110 (2022). 2202.04077.

[56] Abbott, T. M. C. *et al.* Dark Energy Survey Year 3 results: cosmological constraints from galaxy clustering and weak lensing. *Phys. Rev. D* **105**, 023520 (2022). 2105.13549.

[57] Rubin, D. *et al.* Union through unity: cosmology with 2000 sne using a unified bayesian framework. *Astrophys. J.* **986**, 231 (2025). https://doi.org/10.3847/1538-4357/adc0a5.

[58] Penzias, A. A. & Wilson, R. W. A Measurement of excess antenna temperature at 4080 Mc/s. *ApJ* **142**, 419–421 (1965). https://doi.org/10.1086/148307.

[59] Dicke, R. H., Peebles, P. J. E., Roll, P. G. & Wilkinson, D. T. Cosmic blackbody radiation. *Astrophys. J.* **142**, 414–419 (1965). `https://doi.org/10.1086/148306`.

[60] Mather, J. C. *et al.* Measurement of the cosmic microwave background spectrum by the COBE FIRAS instrument. *ApJ* **420**, 439 (1994). `https://doi.org/10.1086/173574`.

[61] Balkenhol, L. *et al.* Measurement of the CMB temperature power spectrum and constraints on cosmology from the SPT-3G 2018 TT, TE, and EE dataset. *Phys. Rev. D* **108**, 023510 (2023). `2212.05642`.

[62] Ryden, B. *Introduction to cosmology* (Cambridge University Press, 1970).

[63] Durrer, R. *The Cosmic Microwave Background* (Cambridge University Press, Cambridge, 2008).

[64] Dodelson, S. *Modern Cosmology* (Academic Press, Amsterdam, 2003).

[65] Seljak, U. & Zaldarriaga, M. A line of sight integration approach to cosmic microwave background anisotropies. *Astrophys. J.* **469**, 437–444 (1996). `astro-ph/9603033`.

[66] Giannantonio, T. & Crittenden, R. The effect of reionization on the CMB-density correlation. *Mon. Not. Roy. Astron. Soc.* **381**, 819 (2007). `0706.0274`.

[67] Sugiyama, N., Silk, J. & Vittorio, N. Reionization and cosmic microwave anisotropies. *ApJ* **419**, L1 (1993). `astro-ph/9310051`.

[68] Ade, P. A. R. *et al.* Detection of B-mode polarization at degree angular scales by BICEP2. *Phys. Rev. Lett.* **112**, 241101 (2014). `1403.3985`.

[69] Ade, P. A. R. *et al.* Joint analysis of BICEP2/*Keck* array and *Planck* data. *Phys. Rev. Lett.* **114**, 101301 (2015). `1502.00612`.

[70] Bassett, B. A. & Hlozek, R. Baryon aoustic oscillations (2009). `0910.5224`.

[71] Eisenstein, D. J. *et al.* Detection of the baryon acoustic peak in the large-scale correlation function of SDSS luminous red galaxies. *Astrophys. J.* **633**, 560–574 (2005). `astro-ph/0501171`.

[72] Shoji, M., Jeong, D. & Komatsu, E. Extracting angular diameter distance and expansion rate of the universe from two-dimensional galaxy power spectrum at high redshifts: baryon acoustic oscillation fitting versus full modeling. *Astrophys. J.* **693**, 1404 (2009). `https://doi.org/10.1088/0004-637X/693/2/1404`.

[73] Amendola, L. & Tsujikawa, S. *Dark Energy: Theory and Observations* (Cambridge University Press, 2015).

[74] Schöneberg, N. The 2024 BBN baryon abundance update. *JCAP* **06**, 006 (2024). `2401.15054`.

[75] Peebles, P. J. *The large-scale structure of the universe* (Princeton University Press, 1980).

[76] Ratra, B. & Vogeley, M. S. The beginning and evolution of the universe. *Publ. Astron. Soc. Pac.* **120**, 235–265 (2008). `0706.1565`.

[77] Guth, A. H. The inflationary universe: a possible solution to the horizon and flatness problems. *Phys. Rev. D* **23**, 347–356 (1981). `https://doi.org/10.1103/PhysRevD.23.347`.

[78] Kofman, L., Linde, A. D. & Starobinsky, A. A. Reheating after inflation. *Phys. Rev. Lett.* **73**, 3195–3198 (1994). `hep-th/9405187`.

[79] Carniani, S. *et al.* Spectroscopic confirmation of two luminous galaxies at a redshift of 14. *Nature* **633**, 318–322 (2024). `2405.18485`.

[80] Weinberg, S. The cosmological constant problem. *Rev. Mod. Phys.* **61**, 1–23 (1989). `https://link.aps.org/doi/10.1103/RevModPhys.61.1`.

[81] Martin, J. Everything you always wanted to know about the cosmological constant problem (but were afraid to ask). *Comptes Rendus Physique* **13**, 566–665 (2012). `1205.3365`.

[82] Velten, H. E. S., vom Marttens, R. F. & Zimdahl, W. Aspects of the cosmological "coincidence problem". *Eur. Phys. J. C* **74**, 3160 (2014). `1410.2509`.

[83] Sivanandam, N. Is the cosmological coincidence a problem? *Phys. Rev. D* **87**, 083514 (2013). `1203.4197`.

[84] De Felice, A. & Tsujikawa, S. f(R) theories. *Living Rev. Rel.* **13**, 3 (2010). `1002.4928`.

[85] Tsujikawa, S. Quintessence: a review. *Class. Quant. Grav.* **30**, 214003 (2013). `1304.1961`.

[86] Young, B.-L. A survey of dark matter and related topics in cosmology. *Front. Phys. (Beijing)* **12**, 121201 (2017). `https://doi.org/10.1007/s11467-016-0583-4`. [Erratum: Front.Phys.(Beijing) 12, 121202 (2017)].

[87] Steigman, G. & Turner, M. S. Cosmological constraints on the properties of Weakly Interacting Massive Particles. *Nucl. Phys. B* **253**, 375–386 (1985). `https://doi.org/10.1016/0550-3213(85)90537-1`.

[88] Peccei, R. D. & Quinn, H. R. CP conservation in the presence of instantons. *Phys. Rev. Lett.* **38**, 1440–1443 (1977). `https://doi.org/10.1103/PhysRevLett.38.1440`.

[89] Adams, C. B. *et al.* Axion dark matter. In *Snowmass 2021* (2022). `2203.14923`.

[90] Hu, W., Barkana, R. & Gruzinov, A. Cold and fuzzy dark matter. *Phys. Rev. Lett.* **85**, 1158–1161 (2000). `astro-ph/0003365`.

[91] Vázquez, J. A., Padilla, L. E. & Matos, T. Inflationary cosmology: from theory to observations. *Rev. Mex. Fis. E* **17**, 73–91 (2020). `1810.09934`.

[92] Turok, N. A critical review of inflation. *Classical and Quantum Gravity* **19**, 3449 (2002). `https://doi.org/10.1088/0264-9381/19/13/305`.

[93] Ferreira, P. G., Wolf, W. J. & Read, J. The spectre of underdetermination in modern cosmology. *Philosophy of Physics* (2025). `2501.06095`.

[94] Brandenberger, R. & Peter, P. Bouncing cosmologies: progress and problems. *Found. Phys.* **47**, 797–850 (2017). `1603.05834`.

[95] Bojowald, M. Quantum cosmology: a review. *Rept. Prog. Phys.* **78**, 023901 (2015). `1501.04899`.

[96] Poulin, V., Smith, T. L. & Karwal, T. The ups and downs of early dark energy solutions to the Hubble tension: a review of models, hints and constraints circa 2023. *Phys. Dark Univ.* **42**, 101348 (2023). `2302.09032`.

[97] Poulin, V., Smith, T. L., Karwal, T. & Kamionkowski, M. Early dark energy can resolve the Hubble tension. *Phys. Rev. Lett.* **122**, 221301 (2019). `1811.04083`.

[98] Vagnozzi, S. New physics in light of the H_0 tension: an alternative view. *Phys. Rev. D* **102**, 023518 (2020). `1907.07569`.

[99] Sekiguchi, T. & Takahashi, T. Early recombination as a solution to the H_0 tension. *Phys. Rev. D* **103**, 083507 (2021). `2007.03381`.

[100] Di Valentino, E., Melchiorri, A., Mena, O. & Vagnozzi, S. Interacting dark energy in the early 2020s: a promising solution to the H_0 and cosmic shear tensions. *Phys. Dark Univ.* **30**, 100666 (2020). `1908.04281`.

[101] Di Valentino, E. *et al.* The cosmoverse white paper: addressing observational tensions in cosmology with systematics and fundamental physics. *Physics of the Dark Universe* **49**, 101965 (2025). `https://www.sciencedirect.com/science/article/pii/S221268642500158X`.

[102] Schöneberg, N. *et al.* The H0 Olympics: a fair ranking of proposed models. *Phys. Rept.* **984**, 1–55 (2022). `2107.10291`.

[103] Abdalla, E. *et al.* Cosmology intertwined: a review of the particle physics, astrophysics, and cosmology associated with the cosmological tensions and anomalies. *JHEAp* **34**, 49–211 (2022). `2203.06142`.

[104] Di Valentino, E. *et al.* Cosmology intertwined III: $f\sigma_8$ and S_8. *Astropart. Phys.* **131**, 102604 (2021). `2008.11285`.

[105] Di Valentino, E., Melchiorri, A. & Silk, J. Cosmological constraints in extended parameter space from the Planck 2018 legacy release. *JCAP* **01**, 013 (2020). `1908.01391`.

[106] Rosenberg, E., Gratton, S. & Efstathiou, G. CMB power spectra and cosmological parameters from Planck PR4 with CamSpec. *Mon. Not. Roy. Astron. Soc.* **517**, 4620–4636 (2022). `2205.10869`.

[107] Tristram, M. *et al.* Cosmological parameters derived from the final Planck data release (PR4). *Astron. Astrophys.* **682**, A37 (2024). `2309.10034`.

[108] Louis, T. *et al.* The Atacama Cosmology Telescope: DR6 power spectra, likelihoods and ΛCDM parameters (2025). `2503.14452`.

[109] Raveri, M. *Resolving the Hubble tension at late times with dark energy*, 503–515 (Springer Nature Singapore, Singapore, 2024). https://doi.org/10.1007/978-981-99-0177-7_27.

[110] Ellis, G., Maartens, R. & MacCallum, M. *Relativistic cosmology* (Cambridge University Press, United Kingdom, 2012).

[111] Hu, W. Structure formation with generalized dark matter. *Astrophys. J.* **506**, 485–494 (1998). astro-ph/9801234.

[112] Kurki-Suonio, H. Cosmological perturbation theory ii (2024). https://www.mv.helsinki.fi/home/hkurkisu/cpt/CosPer2.pdf.

[113] Ratra, B. & Peebles, P. J. E. Cosmological consequences of a rolling homogeneous scalar field. *Phys. Rev. D* **37**, 3406 (1988). https://doi.org/10.1103/PhysRevD.37.3406.

[114] Peebles, P. J. E. & Ratra, B. Cosmology with a time variable cosmological constant. *Astrophys. J. Lett.* **325**, L17 (1988). https://doi.org/10.1086/185100.

[115] Copeland, E. J., Liddle, A. R. & Wands, D. Exponential potentials and cosmological scaling solutions. *Phys. Rev. D* **57**, 4686–4690 (1998). gr-qc/9711068.

[116] Weiss, N. Possible origins of a small nonzero cosmological constant. *Phys. Lett. B* **197**, 42–44 (1987). https://doi.org/10.1016/0370-2693(87)90338-8.

[117] Turner, M. S. Coherent scalar field oscillations in an expanding universe. *Phys. Rev. D* **28**, 1243 (1983). https://doi.org/10.1103/PhysRevD.28.1243.

[118] Gorbunov, D. S. & Rubakov, V. A. *Introduction to the theory of the early universe* (World Scientific Publishing Company, 2011). https://www.worldscientific.com/doi/pdf/10.1142/7873.

[119] Liddle, A. R. & Scherrer, R. J. A classification of scalar field potentials with cosmological scaling solutions. *Phys. Rev. D* **59**, 023509 (1999). astro-ph/9809272.

[120] Scherrer, R. J. Exact general solutions for cosmological scalar field evolution in a background-dominated expansion. *Phys. Rev. D* **105**, 103502 (2022). 2202.01132.

[121] Passaglia, S. & Hu, W. Accurate effective fluid approximation for ultralight axions. *Phys. Rev. D* **105**, 123529 (2022). 2201.10238.

[122] Hwang, J.-c. & Noh, H. Axion as a cold dark matter candidate. *Phys. Lett. B* **680**, 1–3 (2009). 0902.4738.

[123] Lesgourgues, J. The cosmic linear anisotropy solving system (class) i: overview (2011). 1104.2932.

[124] Hlozek, R., Grin, D., Marsh, D. J. E. & Ferreira, P. G. A search for ultralight axions using precision cosmological data. *Phys. Rev. D* **91**, 103512 (2015). 1410.2896.

[125] Poulin, V., Smith, T. L., Grin, D., Karwal, T. & Kamionkowski, M. Cosmological implications of ultralight axionlike fields. *Phys. Rev. D* **98**, 083525 (2018). 1806.10608.

[126] Marsh, D. J. E. Axion cosmology. *Phys. Rept.* **643**, 1–79 (2016). 1510.07633.

[127] Baker, O., Afanasev, A., Lagouri, T., Pan, J. & Weber, C. Particle physics of the dark sector. *Symmetry* **14**, 2238 (2022). https://doi.org/10.3390/sym14112238.

[128] Abdalla, E. & Marins, A. The dark sector cosmology. *Int. J. Mod. Phys. D* **29**, 2030014 (2020). 2010.08528.

[129] Amendola, L. Coupled quintessence. *Phys. Rev. D* **62**, 043511 (2000). astro-ph/9908023.

[130] Wetterich, C. The cosmon model for an asymptotically vanishing time dependent cosmological 'constant'. *Astron. Astrophys.* **301**, 321–328 (1995). hep-th/9408025.

[131] Koivisto, T. Growth of perturbations in dark matter coupled with quintessence. *Phys. Rev. D* **72**, 043516 (2005). astro-ph/0504571.

[132] Carrillo González, M. & Trodden, M. Field theories and fluids for an interacting dark sector. *Phys. Rev. D* **97**, 043508 (2018). [Erratum: Phys.Rev.D 101, 089901 (2020)], 1705.04737.

[133] Bolotin, Y. L., Kostenko, A., Lemets, O. A. & Yerokhin, D. A. Cosmological evolution with interaction between dark energy and dark matter. *Int. J. Mod. Phys. D* **24**, 1530007 (2014). 1310.0085.

[134] Jungman, G., Kamionkowski, M. & Griest, K. Supersymmetric dark matter. *Phys. Rept.* **267**, 195–373 (1996). hep-ph/9506380.

[135] Bertone, G., Hooper, D. & Silk, J. Particle dark matter: evidence, candidates and constraints. *Phys. Rept.* **405**, 279–390 (2005). hep-ph/0404175.

[136] Holman, R., Lazarides, G. & Shafi, Q. Axions and the dark mater of the universe. *Phys. Rev. D* **27**, 995 (1983). https://doi.org/10.3390/sym14112238.

[137] Blumenthal, G. R., Faber, S. M., Primack, J. R. & Rees, M. J. Formation of galaxies and large scale structure with cold dark matter. *Nature* **311**, 517–525 (1984). https://doi.org/10.1038/311517a0.

[138] Chung, D. J. H., Kolb, E. W. & Riotto, A. Superheavy dark matter. *Phys. Rev. D* **59**, 023501 (1998). hep-ph/9802238.

[139] Ballesteros, G., Redondo, J., Ringwald, A. & Tamarit, C. Unifying inflation with the axion, dark matter, baryogenesis and the seesaw mechanism. *Phys. Rev. Lett.* **118**, 071802 (2017). 1608.05414.

[140] Hlozek, R., Marsh, D. J. E. & Grin, D. Using the full power of the cosmic microwave background to probe axion dark matter. *Mon. Not. Roy. Astron. Soc.* **476**, 3063–3085 (2018). 1708.05681.

[141] Roszkowski, L., Sessolo, E. M. & Trojanowski, S. WIMP dark matter candidates and searches—current status and future prospects. *Rept. Prog. Phys.* **81**, 066201 (2018). 1707.06277.

[142] Arbey, A. Dark fluid: a complex scalar field to unify dark energy and dark matter. *Phys. Rev. D* **74**, 043516 (2006). astro-ph/0601274.

[143] Johnson, J. P. & Shankaranarayanan, S. Cosmological perturbations in the interacting dark sector: mapping fields and fluids. *Phys. Rev. D* **103**, 023510 (2021). 2006.04618.

[144] Smith, A. *et al.* A minimal axio-dilaton dark sector. *JCAP* **2025**, 023 (2025). https://doi.org/10.1088/1475-7516/2025/07/023.

[145] Aboubrahim, A. & Nath, P. Interacting ultralight dark matter and dark energy and fits to cosmological data in a field theory approach. *JCAP* **09**, 076 (2024). 2406.19284.

[146] Garcia-Arroyo, G., Ureña López, L. A. & Vázquez, J. A. Interacting scalar fields: dark matter and early dark energy. *Phys. Rev. D* **110**, 023529 (2024). 2402.08815.

[147] Rahimy, S., Teixeira, E. M. & Zavala, I. Deciphering coupled scalar dark sectors. *Phys. Rev. D* **112**, 043512 (2025). https://link.aps.org/doi/10.1103/8hgv-l6ph.

[148] Axenides, M. & Dimopoulos, K. Hybrid dark sector: locked quintessence and dark matter. *JCAP* **07**, 010 (2004). hep-ph/0401238.

[149] Marsh, D. J. E., Grin, D., Hlozek, R. & Ferreira, P. G. Tensor interpretation of BICEP2 results severely constrains axion dark matter. *Phys. Rev. Lett.* **113**, 011801 (2014). 1403.4216.

[150] Folkerts, S., Germani, C. & Redondo, J. Axion dark matter and Planck favor non-minimal couplings to gravity. *Phys. Lett. B* **728**, 532–536 (2014). 1304.7270.

[151] Dimopoulos, K. *Introduction to cosmic inflation and dark energy* (CRC Press-Taylor & Francis Group, 2020).

[152] Baumann, D. The physics of inflation (2011). https://www.icts.res.in/sites/default/files/baumann_icts_dec2011.pdf.

[153] Hui, L., Ostriker, J. P., Tremaine, S. & Witten, E. Ultralight scalars as cosmological dark matter. *Phys. Rev. D* **95**, 043541 (2017). 1610.08297.

[154] Kolb, E. W., Chung, D. J. H. & Riotto, A. WIMPzillas! *AIP Conf. Proc.* **484**, 91–105 (1999). hep-ph/9810361.

[155] Wysozka, S. R. J., Kielanowski, P., Longoria, E. U. & Mercado, L. V. Two interacting scalar fields: practical renormalization (2021). https://arxiv.org/abs/2104.09681.

[156] Gondolo, P. & Gelmini, G. Cosmic abundances of stable particles: improved analysis. *Nucl. Phys.* **B360**, 145–179 (1991). https://doi.org/10.1016/0550-3213(91)90438-4.

[157] Srednicki, M., Watkins, R. & Olive, K. A. Calculations of relic densities in the early universe. *Nucl. Phys. B* **310**, 693 (1988). https://doi.org/10.1016/0550-3213(88)90099-5.

[158] Tanabashi, M. *et al.* Review of particle physics. *Phys. Rev.* **D98**, 030001 (2018).

[159] Norbury, J. W., Dick, F., Norman, R. B. & Maung Maung, K. Cross-sections from scalar field theory. *Canadian Journal of Physics* **88**, 149–156 (2010). https://doi.org/10.1139/P10-002.

[160] Lyth, D. H. & Riotto, A. Particle physics models of inflation and the cosmological density perturbation. *Phys. Rept.* **314**, 1–146 (1999). hep-ph/9807278.

[161] Ferreira, P. G. & Joyce, M. Cosmology with a primordial scaling field. *Phys. Rev. D* **58**, 023503 (1998). astro-ph/9711102.

[162] Bahamonde, S. *et al.* Dynamical systems applied to cosmology: dark energy and modified gravity. *Phys. Rept.* **775-777**, 1–122 (2018). 1712.03107.

[163] van de Bruck, C., Mifsud, J., Mimoso, J. P. & Nunes, N. J. Generalized dark energy interactions with multiple fluids. *JCAP* **11**, 031 (2016). 1605.03834.

[164] Teixeira, E. M., Nunes, A. & Nunes, N. J. Conformally coupled tachyonic dark energy. *Phys. Rev. D* **100**, 043539 (2019). 1903.06028.

[165] Mukhanov, V. F., Feldman, H. A. & Brandenberger, R. H. Theory of cosmological perturbations. Part 1. Classical perturbations. Part 2. Quantum theory of perturbations. Part 3. Extensions. *Phys. Rept.* **215**, 203–333 (1992). https://doi.org/10.1016/0370-1573(92)90044-Z.

[166] van de Bruck, C. & Morrice, J. Disformal couplings and the dark sector of the universe. *JCAP* **04**, 036 (2015). 1501.03073.

[167] van de Bruck, C. & Teixeira, E. M. Dark D-Brane cosmology: from background evolution to cosmological perturbations. *Phys. Rev. D* **102**, 103503 (2020). 2007.15414.

[168] Mifsud, J. & Van De Bruck, C. Probing the imprints of generalized interacting dark energy on the growth of perturbations. *JCAP* **11**, 001 (2017). 1707.07667.

[169] Tsujikawa, S. Matter density perturbations and effective gravitational constant in modified gravity models of dark energy. *Phys. Rev. D* **76**, 023514 (2007). 0705.1032.

[170] Amendola, L. Linear and non-linear perturbations in dark energy models. *Phys. Rev. D* **69**, 103524 (2004). astro-ph/0311175.

[171] Barros, B. J., Amendola, L., Barreiro, T. & Nunes, N. J. Coupled quintessence with a ΛCDM background: removing the σ_8 tension. *JCAP* **01**, 007 (2019). 1802.09216.

[172] Gómez-Valent, A., Pettorino, V. & Amendola, L. Update on coupled dark energy and the H_0 tension. *Phys. Rev. D* **101**, 123513 (2020). 2004.00610.

[173] Teixeira, E. M., Nunes, A. & Nunes, N. J. Disformally coupled quintessence. *Phys. Rev. D* **101**, 083506 (2020). 1912.13348.

[174] Amendola, L. Dark energy and the Boomerang data. *Phys. Rev. Lett.* **86**, 196–199 (2001). astro-ph/0006300.

[175] Pettorino, V., Amendola, L., Baccigalupi, C. & Quercellini, C. Constraints on coupled dark energy using CMB data from WMAP and SPT. *Phys. Rev. D* **86**, 103507 (2012). 1207.3293.

[176] Pettorino, V. Testing modified gravity with Planck: the case of coupled dark energy. *Phys. Rev. D* **88**, 063519 (2013). 1305.7457.

[177] Xia, J.-Q. New limits on coupled dark energy from Planck. *JCAP* **11**, 022 (2013). 1311.2131.

[178] van de Bruck, C., Mifsud, J. & Morrice, J. Testing coupled dark energy models with their cosmological background evolution. *Phys. Rev. D* **95**, 043513 (2017). 1609.09855.

[179] Van De Bruck, C. & Mifsud, J. Searching for dark matter - dark energy interactions: going beyond the conformal case. *Phys. Rev. D* **97**, 023506 (2018). 1709.04882.

[180] Ade, P. A. R. *et al.* Planck 2015 results. XIV. Dark energy and modified gravity. *Astron. Astrophys.* **594**, A14 (2016). 1502.01590.

[181] Agrawal, P., Obied, G. & Vafa, C. H_0 tension, swampland conjectures, and the epoch of fading dark matter. *Phys. Rev. D* **103**, 043523 (2021). 1906.08261.

[182] Blas, D., Lesgourgues, J. & Tram, T. The cosmic linear anisotropy solving system (class). part ii: approximation schemes. *JCAP* **2011**, 034–034 (2011). `http://dx.doi.org/10.1088/1475-7516/2011/07/034`.

[183] Lesgourgues, J. The cosmic linear anisotropy solving system (class) iii: comparision with camb for lambdacdm (2011). 1104.2934.

[184] Pettorino, V. & Baccigalupi, C. Coupled and extended quintessence: theoretical differences and structure formation. *Phys. Rev. D* **77**, 103003 (2008). `0802.1086`.

[185] Linder, E. V. Cosmic growth and expansion conjoined. *Astropart. Phys.* **86**, 41–45 (2017). `1610.05321`.

[186] Amendola, L., Pettorino, V., Quercellini, C. & Vollmer, A. Testing coupled dark energy with next-generation large-scale observations. *Phys. Rev. D* **85**, 103008 (2012). `1111.1404`.

[187] Giarè, W. Dynamical dark energy beyond planck? constraints from multiple cmb probes, desi bao, and type-ia supernovae. *Phys. Rev. D* **112**, 023508 (2025). `https://link.aps.org/doi/10.1103/ss37-cxhn`.

[188] Cortês, M. & Liddle, A. R. Interpreting DESI's evidence for evolving dark energy. *JCAP* **12**, 007 (2024). `2404.08056`.

[189] Patel, V., Chakraborty, A. & Amendola, L. The prior dependence of the DESI results (2024). `2407.06586`.

[190] Giarè, W., Sabogal, M. A., Nunes, R. C. & Di Valentino, E. Interacting dark energy after desi baryon acoustic oscillation measurements. *Phys. Rev. Lett.* **133**, 251003 (2024). `https://link.aps.org/doi/10.1103/PhysRevLett.133.251003`.

[191] Giarè, W., Najafi, M., Pan, S., Di Valentino, E. & Firouzjaee, J. T. Robust preference for dynamical dark energy in DESI BAO and SN measurements. *JCAP* **10**, 035 (2024). `2407.16689`.

[192] Berghaus, K. V., Kable, J. A. & Miranda, V. Quantifying scalar field dynamics with DESI 2024 Y1 BAO measurements. *Phys. Rev. D* **110**, 103524 (2024). `2404.14341`.

[193] Efstathiou, G. Evolving dark energy or supernovae systematics? *Mon. Not. Roy. Astron. Soc.* **538**, 875–882 (2025). `2408.07175`.

[194] Das, S., Corasaniti, P. S. & Khoury, J. Superacceleration as the signature of a dark sector interaction. *Phys. Rev. D* **73** (2006). `http://dx.doi.org/10.1103/PhysRevD.73.083509`.

[195] Copeland, E. J., Sami, M. & Tsujikawa, S. Dynamics of dark energy. *Int. J. Mod. Phys. D* **15**, 1753–1936 (2006). `hep-th/0603057`.

[196] Brinckmann, T. & Lesgourgues, J. MontePython 3: boosted MCMC sampler and other features. *Phys. Dark Univ.* **24**, 100260 (2019). 1804.07261.

[197] Audren, B., Lesgourgues, J., Benabed, K. & Prunet, S. Conservative constraints on early cosmology with monte python. *JCAP* **2013**, 001 (2013). https://doi.org/10.1088/1475-7516/2013/02/001.

[198] Lewis, A. Efficient sampling of fast and slow cosmological parameters. *Phys. Rev. D* **87**, 103529 (2013). 1304.4473.

[199] Gelman, A. & Rubin, D. B. Inference from tterative simulation using multiple sequences. *Statistical Science* **7**, 457–472 (1992). https://doi.org/10.1214/ss/1177011136.

[200] Lewis, A. GetDist: a Python package for analysing Monte Carlo samples. *JCAP* **08**, 025 (2025). 1910.13970.

[201] Aghanim, N. *et al.* Planck 2018 results. V. CMB power spectra and likelihoods. *Astron. Astrophys.* **641**, A5 (2020). 1907.12875.

[202] Adame, A. G. *et al.* DESI 2024 III: baryon acoustic oscillations from galaxies and quasars. *JCAP* **04**, 012 (2025). 2404.03000.

[203] Adame, A. G. *et al.* DESI 2024 IV: Baryon Acoustic Oscillations from the Lyman alpha forest. *JCAP* **01**, 124 (2025). 2404.03001.

[204] Scolnic, D. *et al.* The Pantheon+ analysis: the full data set and light-curve release. *Astrophys. J.* **938**, 113 (2022). 2112.03863.

[205] Brout, D. *et al.* The Pantheon+ analysis: SuperCal-fragilistic cross calibration, retrained SALT2 light-curve model, and calibration systematic uncertainty. *Astrophys. J.* **938**, 111 (2022). 2112.03864.

[206] Karwal, T. *et al.* Procoli: profiles of cosmological likelihoods (2024). 2401.14225.

[207] Heavens, A. *et al.* Marginal likelihoods from Monte Carlo Markov chains (2017). 1704.03472.

[208] Heavens, A. *et al.* No evidence for extensions to the standard cosmological model. *Phys. Rev. Lett.* **119**, 101301 (2017). 1704.03467.

[209] Raveri, M. & Hu, W. Concordance and discordance in cosmology. *Phys. Rev. D* **99**, 043506 (2019). 1806.04649.

[210] Ó Colgáin, E. & Sheikh-Jabbari, M. M. DESI and SNe: dynamical dark energy, Ω_m tension or systematics? *MNRAS* **542**, L24–L30 (2025). 2412.12905.

[211] Dhawan, S., Popovic, B. & Goobar, A. The axis of systematic bias in sn ia cosmology and implications for desi 2024 results. *Mon. Not. Roy. Astron. Soc.* **540**, 1626–1634 (2025). https://doi.org/10.1093/mnras/staf779. https://academic.oup.com/mnras/article-pdf/540/2/1626/63212391/staf779.pdf.

[212] Green, M. B., Schwarz, J. H. & Witten, E. *Superstring theory. Vol. 1: Introduction*. Cambridge Monographs on Mathematical Physics (1988).

[213] Svrcek, P. & Witten, E. Axions in string theory. *JHEP* **06**, 051 (2006). hep-th/0605206.

[214] Arvanitaki, A., Dimopoulos, S., Dubovsky, S., Kaloper, N. & March-Russell, J. String axiverse. *Phys. Rev. D* **81**, 123530 (2010). 0905.4720.

[215] Amendola, L. & Barbieri, R. Dark matter from an ultra-light pseudo-Goldsone-boson. *Phys. Lett. B* **642**, 192–196 (2006). hep-ph/0509257.

[216] Hložek, R. *et al.* Future CMB tests of dark matter: ultralight axions and massive neutrinos. *Phys. Rev. D* **95**, 123511 (2017). 1607.08208.

[217] Farren, G. S., Grin, D., Jaffe, A. H., Hložek, R. & Marsh, D. J. E. Ultralight axions and the kinetic Sunyaev-Zel'dovich effect. *Phys. Rev. D* **105**, 063513 (2022). 2109.13268.

[218] Iršič, V., Viel, M., Haehnelt, M. G., Bolton, J. S. & Becker, G. D. First constraints on fuzzy dark matter from Lyman-α forest data and hydrodynamical simulations. *Phys. Rev. Lett.* **119**, 031302 (2017). 1703.04683.

[219] Armengaud, E., Palanque-Delabrouille, N., Yèche, C., Marsh, D. J. E. & Baur, J. Constraining the mass of light bosonic dark matter using SDSS Lyman-α forest. *Mon. Not. Roy. Astron. Soc.* **471**, 4606–4614 (2017). 1703.09126.

[220] Kobayashi, T., Murgia, R., De Simone, A., Iršič, V. & Viel, M. Lyman-α constraints on ultralight scalar dark matter: Implications for the early and late universe. *Phys. Rev. D* **96**, 123514 (2017). 1708.00015.

[221] Nori, M., Murgia, R., Iršič, V., Baldi, M. & Viel, M. Lyman α forest and non-linear structure characterization in fuzzy dark matter cosmologies. *Mon. Not. Roy. Astron. Soc.* **482**, 3227–3243 (2019). 1809.09619.

[222] Rogers, K. K. & Peiris, H. V. Strong bound on canonical ultralight axion dark matter from the Lyman-alpha forest. *Phys. Rev. Lett.* **126**, 071302 (2021). 2007.12705.

[223] Hayashi, K., Ferreira, E. G. M. & Chan, H. Y. J. Narrowing the mass range of fuzzy dark matter with ultrafaint dwarfs. *Astrophys. J. Lett.* **912**, L3 (2021). 2102.05300.

[224] Dalal, N. & Kravtsov, A. Excluding fuzzy dark matter with sizes and stellar kinematics of ultrafaint dwarf galaxies. *Phys. Rev. D* **106**, 063517 (2022). 2203.05750.

[225] Goldstein, I. S., Koushiappas, S. M. & Walker, M. G. Viability of ultralight bosonic dark matter in dwarf galaxies. *Phys. Rev. D* **106**, 063010 (2022). 2206.05244.

[226] Laguë, A. *et al.* Constraining ultralight axions with galaxy surveys. *JCAP* **01**, 049 (2022). 2104.07802.

[227] Rogers, K. K. *et al.* Ultra-light axions and the S $_8$ tension: joint constraints from the cosmic microwave background and galaxy clustering. *JCAP* **06**, 023 (2023). 2301.08361.

[228] Dentler, M. *et al.* Fuzzy dark matter and the Dark Energy Survey Year 1 data. *Mon. Not. Roy. Astron. Soc.* **515**, 5646–5664 (2022). 2111.01199.

[229] Kunkel, A., Chiueh, T. & Schäfer, B. M. A weak lensing perspective on non-linear structure formation with fuzzy dark matter. *Mon. Not. Roy. Astron. Soc.* **527**, 10538–10556 (2023). 2211.01523.

[230] Hotinli, S. C., Marsh, D. J. E. & Kamionkowski, M. Probing ultralight axions with the 21-cm signal during cosmic dawn. *Phys. Rev. D* **106**, 043529 (2022). 2112.06943.

[231] Bauer, J. B., Marsh, D. J. E., Hložek, R., Padmanabhan, H. & Laguë, A. Intensity mapping as a probe of axion dark matter. *Mon. Not. Roy. Astron. Soc.* **500**, 3162–3177 (2020). 2003.09655.

[232] Flitter, J. & Kovetz, E. D. Closing the window on fuzzy dark matter with the 21-cm signal. *Phys. Rev. D* **106**, 063504 (2022). 2207.05083.

[233] Wetterich, C. Cosmology and the fate of dilatation symmetry. *Nucl. Phys. B* **302**, 668–696 (1988). 1711.03844.

[234] Caldwell, R. R., Dave, R. & Steinhardt, P. J. Cosmological imprint of an energy component with general equation of state. *Phys. Rev. Lett.* **80**, 1582–1585 (1998). astro-ph/9708069.

[235] Koivisto, T. S. & Nunes, N. J. Coupled three-form dark energy. *Phys. Rev. D* **88** (2013). http://dx.doi.org/10.1103/PhysRevD.88.123512.

[236] Li, M., Li, X.-D., Wang, S. & Wang, Y. Dark energy. *Commun. Theor. Phys.* **56**, 525–604 (2011). 1103.5870.

[237] Carroll, S. M. Quintessence and the rest of the world. *Phys. Rev. Lett.* **81**, 3067–3070 (1998). astro-ph/9806099.

[238] Will, C. M. The confrontation between general relativity and experiment. *Living Rev. Rel.* **17**, 4 (2014). 1403.7377.

[239] Di Valentino, E., Melchiorri, A. & Mena, O. Can interacting dark energy solve the H_0 tension? *Phys. Rev. D* **96**, 043503 (2017). 1704.08342.

[240] Yang, W., Pan, S., Di Valentino, E., Mena, O. & Melchiorri, A. 2021-H0 odyssey: closed, phantom and interacting dark energy cosmologies. *JCAP* **10**, 008 (2021). 2101.03129.

[241] Honorez, L. L., Reid, B. A., Mena, O., Verde, L. & Jimenez, R. Coupled dark matter-dark energy in light of near universe observations. *JCAP* **2010**, 029–029 (2010). http://dx.doi.org/10.1088/1475-7516/2010/09/029.

[242] Gavela, M. B., Lopez Honorez, L., Mena, O. & Rigolin, S. Dark coupling and gauge invariance. *JCAP* **11**, 044 (2010). 1005.0295.

[243] He, J.-H., Wang, B. & Abdalla, E. Stability of the curvature perturbation in dark sectors' mutual interacting models. *Phys. Lett. B* **671**, 139–145 (2009). 0807.3471.

[244] Valiviita, J., Majerotto, E. & Maartens, R. Instability in interacting dark energy and dark matter fluids. *JCAP* **07**, 020 (2008). 0804.0232.

[245] Yang, W., Pan, S. & Mota, D. F. Novel approach toward the large-scale stable interacting dark-energy models and their astronomical bounds. *Phys. Rev. D* **96**, 123508 (2017). 1709.00006.

[246] Gavela, M. B., Hernandez, D., Lopez Honorez, L., Mena, O. & Rigolin, S. Dark coupling. *JCAP* **07**, 034 (2009). [Erratum: JCAP 05, E01 (2010)], 0901.1611.

[247] Yang, W., Pan, S., Mena, O. & Di Valentino, E. On the dynamics of a dark sector coupling. *JHEAp* **40**, 19–40 (2023). 2209.14816.

[248] Yang, W., Mena, O., Pan, S. & Di Valentino, E. Dark sectors with dynamical coupling. *Phys. Rev. D* **100**, 083509 (2019). 1906.11697.

[249] Yang, W., Di Valentino, E., Mena, O., Pan, S. & Nunes, R. C. All-inclusive interacting dark sector cosmologies. *Phys. Rev. D* **101**, 083509 (2020). 2001.10852.

[250] Nunes, R. C., Vagnozzi, S., Kumar, S., Di Valentino, E. & Mena, O. New tests of dark sector interactions from the full-shape galaxy power spectrum. *Phys. Rev. D* **105**, 123506 (2022). 2203.08093.

[251] Di Valentino, E., Melchiorri, A., Mena, O. & Vagnozzi, S. Nonminimal dark sector physics and cosmological tensions. *Phys. Rev. D* **101**, 063502 (2020). 1910.09853.

[252] Giarè, W. *et al.* Tightening the reins on nonminimal dark sector physics: interacting dark energy with dynamical and nondynamical equation of state. *Phys. Rev. D* **110**, 063527 (2024). `https://link.aps.org/doi/10.1103/PhysRevD.110.063527`.

[253] Beyer, J. & Wetterich, C. Small scale structures in coupled scalar field dark matter. *Phys. Lett. B* **738**, 418–423 (2014). 1407.0141.

[254] Beyer, J., Nurmi, S. & Wetterich, C. Coupled dark energy and dark matter from dilatation anomaly. *Phys. Rev. D* **84**, 023010 (2011). 1012.1175.

[255] Cembranos, J. A. R., Maroto, A. L. & Núñez Jareño, S. J. Cosmological perturbations in coherent oscillating scalar field models. *JHEP* **03**, 013 (2016). 1509.08819.

[256] Christopherson, A. J. & Malik, K. A. The non-adiabatic pressure in general scalar field systems. *Physics Letters B* **675**, 159–163 (2009). `http://dx.doi.org/10.1016/j.physletb.2009.04.003`.

[257] Koshelev, N. Non-adiabatic perturbations in multi-component perfect fluids. *JCAP* **2011**, 021–021 (2011). http://dx.doi.org/10.1088/1475-7516/2011/04/021.

[258] Sá, P. M. Late-time evolution of the universe within a two-scalar-field cosmological model. *Phys. Rev. D* **103**, 123517 (2021). 2103.01693.

[259] Kolb, E. W. & Turner, M. S. *The early universe*, vol. 69 (Taylor and Francis, 2019).

[260] Caldera-Cabral, G., Maartens, R. & Schaefer, B. M. The growth of structure in interacting dark energy models. *JCAP* **07**, 027 (2009). 0905.0492.

[261] Zhao, Y. *et al.* Constraining interacting dark energy models with the halo concentration–mass relation. *Mon. Not. Roy. Astron. Soc.* **523**, 5962–5971 (2023). 2212.02050.

[262] Zhai, Y. *et al.* A consistent view of interacting dark energy from multiple CMB probes. *JCAP* **07**, 032 (2023). 2303.08201.

[263] Ilić, S., Kopp, M., Skordis, C. & Thomas, D. B. Dark matter properties through cosmic history. *Phys. Rev. D* **104**, 043520 (2021). 2004.09572.

[264] Pan, S., Yang, W., Di Valentino, E., Mota, D. F. & Silk, J. IWDM: the fate of an interacting non-cold dark matter — vacuum scenario. *JCAP* **07**, 064 (2023). 2211.11047.

[265] Naidoo, K., Jaber, M., Hellwing, W. A. & Bilicki, M. Dark matter solution to the H0 and S8 tensions, and the integrated Sachs-Wolfe void anomaly. *Phys. Rev. D* **109**, 083511 (2024). 2209.08102.

[266] Khurshudyan, M. & Elizalde, E. Constraints on prospective deviations from the cold dark matter model using a Gaussian process. *Galaxies* **12**, 31 (2024). 2402.08630.

[267] Skordis, C., Pourtsidou, A. & Copeland, E. Parametrized post-friedmannian framework for interacting dark energy theories. *Phys. Rev. D* **91** (2015). http://dx.doi.org/10.1103/PhysRevD.91.083537.

[268] Linton, M. S., Pourtsidou, A., Crittenden, R. & Maartens, R. Variable sound speed in interacting dark energy models. *JCAP* **2018**, 043–043 (2018). http://dx.doi.org/10.1088/1475-7516/2018/04/043.

[269] Lewis, A., Challinor, A. & Lasenby, A. Efficient computation of CMB anisotropies in closed FRW models. *Astrophys. J.* **538**, 473–476 (2000). `astro-ph/9911177`.

[270] Balázs, C. *et al.* Cosmological constraints on decaying axion-like particles: a global analysis. *JCAP* **12**, 027 (2022). `2205.13549`.

[271] Kopp, M., Skordis, C. & Thomas, D. B. Extensive investigation of the generalized dark matter model. *Phys. Rev. D* **94**, 043512 (2016). `1605.00649`.

[272] Ballesteros, G. & Lesgourgues, J. Dark energy with non-adiabatic sound speed: initial conditions and detectability. *JCAP* **10**, 014 (2010). `1004.5509`.

[273] Carron, J., Mirmelstein, M. & Lewis, A. CMB lensing from Planck PR4 maps. *JCAP* **09**, 039 (2022). `2206.07773`.

[274] Abbott, T. M. C. *et al.* The Dark Energy Survey: cosmology results with ∼1500 new high-redshift type Ia supernovae using the full 5 yr data set. *Astrophys. J. Lett.* **973**, L14 (2024). `2401.02929`.

[275] Bellini, E. *et al.* Comparison of Einstein-Boltzmann solvers for testing general relativity. *Phys. Rev. D* **97**, 023520 (2018). `1709.09135`.

[276] Hobson, M. P., Jaffe, A. H., Liddle, A. R., Mukherjee, P. & Parkinson, D. *Bayesian Methods in Cosmology* (Cambridge University Press, 2009).

[277] Trotta, R. Bayesian methods in cosmology (2017). `1701.01467`.

[278] Padilla, L. E., Tellez, L. O., Escamilla, L. A. & Vazquez, J. A. Cosmological parameter inference with Bayesian statistics. *Universe* **7**, 213 (2021). `1903.11127`.

[279] Liddle, A. R. Statistical methods for cosmological parameter selection and estimation. *Ann. Rev. Nucl. Part. Sci.* **59**, 95–114 (2009). `0903.4210`.

[280] Christensen, N., Meyer, R., Knox, L. & Luey, B. Bayesian methods for cosmological parameter estimation from cosmic microwave background measurements. *Classical and Quantum Gravity* **18**, 2677 (2001). `https://doi.org/10.1088/0264-9381/18/14/306`.

[281] Metropolis, N., Rosenbluth, A. W., Rosenbluth, M. N., Teller, A. H. & Teller, E. Equation of state calculations by fast computing machines. *The Journal of Chemical Physics* **21**, 1087–1092 (1953). `https://doi.org/10.1063/1.1699114`.

[282] Hastings, W. K. Monte carlo sampling methods using markov chains and their applications. *Biometrika* **57**, 97–109 (1970). `https://doi.org/10.1093/biomet/57.1.97`.

[283] Torrado, J. & Lewis, A. Cobaya: Code for Bayesian Analysis of hierarchical physical models. *JCAP* **05**, 057 (2021). `2005.05290`.

[284] Jeffreys, H. *The Theory of Probability.* Oxford Classic Texts in the Physical Sciences (1939).

Appendix A

Numerical and statistical methods

Here we describe the numerical and statistical methods used in this thesis.

A.1 Einstein-Boltzmann solvers

In order to make accurate predictions in cosmology, we need powerful numerical methods to solve the relevant equations. These are the Einstein-Boltzmann equations, which include the evolution of perturbations described in the main text as well as equations governing the thermodynamics of the universe [64]. Numerical solvers tailored for this purpose are usually referred to as Einstein-Boltzmann codes. The two state of the art examples are[1] `CAMB` [269] and `CLASS` [123]. In this work we use `CLASS`, which is written in `C`. `CLASS` is easily modifiable to add new interactions, particles or fluids to the standard cosmology. Generally, one needs to modify the `input.c`, `background.c` and `perturbations.c` modules. This includes adding new parameters to be read by the program, and then modifying the background and perturbations equations and quantities. Running `CLASS` then only requires a set of parameters (at the minimum one needs to provide the ΛCDM parameters) and extra precision options are available. Note that the perturbation equations can be given either in Newtonian or synchronous gauge. In this thesis we will adopt the synchronous gauge without loss of generality.

A.2 Statistical methods

Cosmology is a unique branch of science in the sense that observations are non-repeatable. Indeed, we only have one universe to observe, and so we must make the most of this to

---

[1] For a comparison of the two, see for example [275].

extract physical information from observations. To do this requires a good understanding of statistics and probability.

A.2.1 Bayesian inference

We will follow a Bayesian approach to statistics and probability, which relies on the following philosophy: the *parameters* of the theoretical model underlying the physics of the universe are fundamentally unknown, and we must try to estimate them – i.e. assign a probability distribution – as best as possible using the available *data*. In the Bayesian context the data is fixed, in contrast to the frequentist approach where the parameters are fixed and the data can be repeated. We will need three quantities when discussing Bayesian inference, given a set of parameters $\boldsymbol{\vartheta}$ and a set of data points $\boldsymbol{d}$:

- The *posterior* distribution $p(\boldsymbol{\vartheta}|\boldsymbol{d})$ is the probability of the model parameters being a certain value, given the observed data. It is the central quantity that needs to be calculated in cosmology, as it allows us to make predictions about different models.

- The *prior* distribution $p(\boldsymbol{\vartheta})$ is the probability of the model. This is an essential part of the Bayesian approach, which describe our beliefs about the model prior to the experiment. In practice, the prior could be influenced by previous experiments or by theoretical considerations.

- The *likelihood* distribution $p(\boldsymbol{d}|\boldsymbol{\vartheta})$ is the probability of the data, given the model parameters. In general this is constructed as a Gaussian distribution, assuming the apparatus is subject to random Gaussian noise. The likelihood is also sometimes written as $\mathcal{L}(\boldsymbol{d};\boldsymbol{\vartheta})$.

- The *evidence* $p(\boldsymbol{d}) = \int p(\boldsymbol{d}|\boldsymbol{\vartheta})p(\boldsymbol{\vartheta})d\boldsymbol{\vartheta}$, also called marginal likelihood, is a normalisation factor describing the probability of the data. Since it is independent of the model parameters, it does not play a role in determining the best-fit parameters. It is however important in the context of Bayesian model selection, as we will see below.

The above four quantities come together in the fundamental equation of Bayesian statistics, Bayes' theorem [276–278]:

$$p(\boldsymbol{\vartheta}|\boldsymbol{d}) = \frac{p(\boldsymbol{\vartheta})p(\boldsymbol{d}|\boldsymbol{\vartheta})}{p(\boldsymbol{d})}, \tag{A.1}$$

which states that the posterior distribution is proportional to the product of the prior and the likelihood. The aim of the game, then, is to calculate the likelihood, and therefore the posterior, in order to find the model parameters corresponding to the maximum probability.

As we will be dealing with high dimensional likelihoods, it is often convenient to deal with the one-dimensional posterior distribution for a given model parameter θ_i, assuming a total of j parameters. This is obtained by *marginalisation*, i.e. integrating the posterior over all other parameters:

$$p(\vartheta_i|\boldsymbol{d}) = \int \cdots \int p(\boldsymbol{\vartheta}|\boldsymbol{d}) d\vartheta_1 \dots d\vartheta_{i-1} d\vartheta_{i+1} \dots d\vartheta_j. \tag{A.2}$$

Finally, we will often quote confidence intervals. Generally we will consider 1σ, 2σ and 3σ (standard deviation), which means the true value of a parameter is within the interval 68%, 95% and 99.7% of the time for a Gaussian distribution.

A.2.2 Markov-Chain Monte-Carlo methods

When dealing with cosmological data, it can be computationally expensive to calculate the likelihood [279] which usually takes a non-analytical form. This is exacerbated by a high parameter dimensionality. Exploring the parameter space efficiently is therefore a priority when considering Bayesian inference. Indeed, simply drawing a grid including all parameters, and calculating the likelihood at all points, would be prohibitively expensive in most cases, due to potential high dimensionality, multi-modality (i.e. the likelihood has several peaks) or degeneracies between parameters (meaning one parameter might leave the likelihood unchanged along a particular trajectory in parameter space). All of these arguments lead to the need for a clever algorithm to determine the posterior. Here we will focus on Markov Chain Monte Carlo (MCMC) methods, which were first suggested for cosmology in [280]. An MCMC algorithm is designed to explore a probability distribution using random sampling (the Monte Carlo part), where each new step depends only on the previous one (the Markov Chain part). The output of such an algorithm is a *chain*, which is a list of steps containing a realisation of the model (i.e. a list of parameters) and their associated likelihood/posterior probability. It is then simple to reconstruct the whole distribution – either by considering the density of parameters in the chains or the associated posterior value directly – and marginalisation does not require any integration in this case.

The most commonly used algorithm is the Metropolis-Hastings [281, 282] algorithm which follows the following simple rules:

1. Select a starting point $\boldsymbol{\vartheta}^{(0)}$ within the parameter space.
2. Propose a next step in parameter space $\boldsymbol{\vartheta}^{(c)}$. The function responsible for such a step is called the *proposal distribution* $q(\boldsymbol{\vartheta}^{(0)}, \boldsymbol{\vartheta}^{(c)})$ must obey the *detailed balanced condition*, meaning that moving back to the starting point is equally likely compared to moving away from it. The proposal distribution is usually chosen to be Gaussian.
3. Evaluate the posterior at $\boldsymbol{\vartheta}^{(c)}$. If the probability at the new point is higher, accept the new point. If it is lower, calculate the acceptance ratio

   $$\alpha = \frac{p(\boldsymbol{\vartheta}^{(0)}|\boldsymbol{d})}{p(\boldsymbol{\vartheta}^{(c)}|\boldsymbol{d})}. \tag{A.3}$$

   Generate a random number μ in the interval $[0, 1)$. Accept the step iff $\mu \leq \alpha$. In case of rejection, create a new point in the chain equal to the previous. Either way, a new point in the chain is created at each step.
4. Return to step 1 until reaching termination condition.

The termination condition in the Metropolis-Hastings algorithm is usually taken to be *convergence*. Conceptually, if running several chains for the same model and data, all chains should eventually reach the same distribution. Formally this is quantified by the Gelman-Rubin [199] criterion R. It is common to consider chains with $R - 1 \leq 0.01$ as converged.

We implement the MCMC algorithm using the `MontePython` [196] and `cobaya` [283] codes, which interface the Einstein-Boltzmann solver with MCMC algorithms.

A.2.3 Evaluating goodness of fit

Once we have a (marginalised) posterior distribution, which tells us the best-fit parameters for our model, an important question still remains: does my model actually fit the data well? In the Bayesian sense, this question has no absolute answer, and can only be answered in relation to a different model. That is, we can only say that a model fits the data better or worse compared to another model.

In the case of a purely Gaussian likelihood, maximising the likelihood/posterior (and therefore obtaining the best-fit value) corresponds to minimising the chi-squared statistic, obtained in the following way:

$$\chi^2 \equiv -2 \log \mathcal{L}. \tag{A.4}$$

Note that this is only a good estimate of fit for likelihoods close to Gaussian. The chi-squared can be used to compare two models in the following way: the model with the smaller minimum chi-squared, and therefore larger maximum likelihood, is a better fit to the data. This is usually quantified with the $\Delta\chi^2$ quantity, defined for two models A and B as

$$\Delta\chi^2 \equiv \chi^2_{min}(A) - \chi^2_{min}(B). \tag{A.5}$$

If $\Delta\chi^2 < 0$, model A is a better fit to the data, and vice versa for $\Delta\chi^2 > 0$.

Another model comparison approach relies on the evidence. The ratio of probabilities for models A and B given the data is given by Bayes' theorem as

$$\frac{p(A|\boldsymbol{d})}{p(B|\boldsymbol{d})} = \frac{p(A)p(\boldsymbol{d}|A)}{p(B)p(\boldsymbol{d}|B)} \tag{A.6}$$

where $p(A)$ is the prior for model A and $p(\boldsymbol{d}|A)$ is simply the evidence for model A and accordingly for model B. Assuming we have no prior bias for one given model, the fraction becomes the Bayes factor

$$B_{A,B} = \frac{p(\boldsymbol{d}|A)}{p(\boldsymbol{d}|B)}, \tag{A.7}$$

which is used for model selection. Due to the marginalisation needed to obtain the evidence, the Bayes factor includes both goodness of fit as well as number of parameters to select a model, following the principle of Occam's razor. In general, $B_{A,B} > 1$ implies a preference for model A and $B_{A,B} < -1$ prefers model B. Values between $-1 < B_{A,B} < 1$ lead are inconclusive. A full interpretation of Bayes factor values can be obtained using Jeffreys' scale [284].

In order to analyse the chains to compute the above quantities, as well as to produce plots, we use the `GetDist` [200] package.

Appendix B

Extra constraints from hybrid dark sector and ΛCDM models

In this appendix, we provide results for the dataset combinations considered in Chapter 6 for the ΛCDM model. Table B.1 follows the same organisation as Table 6.2, with the results pertaining to the ΛCDM model for the Pl18, Pl18+SN, Pl18+SH0ES, Pl18+DESI, Pl18+DESI+SN, Pl18+DESI+SH0ES datasets.

Parameter	**Pl18**	**Pl18+SN**	**Pl18+SH0ES**	**Pl18+DESI**	**Pl18+DESI+SN**	**Pl18+DESI+SH0ES**
$\omega_{\rm b}$	0.02235 ± 0.00015	0.02231 ± 0.00015	0.02264 ± 0.00014	0.02249 ± 0.00013	0.02246 ± 0.00013	0.02265 ± 0.00013
$\omega_{\rm c}$	0.1202 ± 0.0014	0.1207 ± 0.0013	0.1169 ± 0.0011	0.11817 ± 0.00094	0.11862 ± 0.00091	0.11678 ± 0.00083
$100\theta_s$	1.04187 ± 0.00030	1.04182 ± 0.00029	1.04221 ± 0.00028	1.04206 ± 0.00028	1.04203 ± 0.00028	1.04223 ± 0.00028
$\tau_{\rm reio}$	0.0543 ± 0.0078	0.0536 ± 0.0077	0.0591 ± 0.0079	0.0572 ± 0.0078	0.0565 ± 0.0077	0.0595 ± 0.0078
n_s	0.9647 ± 0.0045	0.9635 ± 0.0042	0.9729 ± 0.0039	0.9697 ± 0.0038	0.9686 ± 0.0036	0.9733 ± 0.0035
$\log 10^{10} A_s$	3.045 ± 0.016	3.045 ± 0.016	3.048 ± 0.016	3.046 ± 0.016	3.046 ± 0.016	3.048 ± 0.016
σ_8	0.8118 ± 0.0074	0.8125 ± 0.0074	0.8026 ± 0.0074	0.8066 ± 0.0071	0.8078 ± 0.0071	0.8030 ± 0.0071
H_0	67.29 ± 0.61	67.08 ± 0.56	68.86 ± 0.49	68.21 ± 0.42	68.01 ± 0.40	68.91 ± 0.38
Ω_m	0.3150 ± 0.0085	0.3179 ± 0.0078	0.2944 ± 0.0062	0.3024 ± 0.0055	0.3050 ± 0.0053	0.2936 ± 0.0047
S_8	0.832 ± 0.016	0.836 ± 0.015	0.795 ± 0.013	0.810 ± 0.012	0.815 ± 0.012	0.794 ± 0.011
$Q_{\rm DMAP}^{\rm SH0ES}$	$--$	6.25	$--$	$--$	5.76	$--$

Table B.1: Observational constraints at a 68% confidence level on the independent and derived cosmological parameters using different dataset combinations for the ΛCDM model, as detailed in Section 6.3.1. The value of $Q_{\rm DMAP}^{\rm SH0ES}$ is calculated according to Eq. (6.4).

We provide a breakdown of the χ^2 fit for each model and data combination considered through a profile likelihood analysis performed with `Procoli` [206]. In Table B.2, we list the overall and individual dataset best-fit χ^2 values for the ΛCDM model and the hybrid

Data	Model	Total χ^2	Pl18	DESI	SN	SH0ES
Pl18	ΛCDM	2766.53	2766.53	-	-	-
	Hybrid	2766.55	2766.55	-	-	-
Pl18+DESI	ΛCDM	2783.32	2768.82	14.50	-	-
	Hybrid	2780.51	2767.64	12.87	-	-
Pl18+DESI+SN	ΛCDM	4195.78	2768.03	15.69	1412.06	-
	Hybrid	4194.54	2767.28	14.14	1413.12	-
Pl18+DESI+SH0ES	ΛCDM	4105.02	2773.33	12.85	-	1318.84
	Hybrid	4092.07	2768.53	14.38	-	1309.16
Pl18+SN	ΛCDM	4177.11	2766.79	-	1410.32	-
	Hybrid	4177.03	2766.65	-	1410.38	-
Pl18+SH0ES	ΛCDM	4091.93	2772.62	-	-	1319.31
	Hybrid	4075.63	2769.23	-	-	1306.40

Table B.2: Best-fit χ^2-values of overall and individual datasets considered in this work for the ΛCDM and hybrid models for various likelihood combinations.

model, as detailed in Section 6.3.1.

Appendix C

Constraints on ΛCDM from Planck PR4 and additional datasets

In this appendix, we provide results from the dataset combinations considered in Chapter 8 for the ΛCDM model. Table C.1 follows the same organisation as Table 8.2, with the results pertaining to the ΛCDM model for the PR4, PR4+SN, PR4+DESI, PR4+DESI+SN, PR4+DESI+SH0ES datasets.

Parameter	**PR4**	**PR4+SN**	**PR4+DESI**	**PR4+DESI+SN**	**PR4+DESI+SH0ES**
ω_b	0.02216 ± 0.00014	0.02213 ± 0.00013	0.02226 ± 0.00012	0.02224 ± 0.00013	0.02232 ± 0.00012
ω_c	0.1198 ± 0.0011	0.1201 ± 0.0010	0.11833 ± 0.00081	0.11861 ± 0.00080	0.11782 ± 0.00076
τ_reio	0.0525 ± 0.0072	0.0517 ± 0.0071	0.0573 ± 0.0071	0.0564 ± 0.0070	$0.0592^{+0.0066}_{-0.0075}$
n_s	0.9625 ± 0.0040	0.9616 ± 0.0039	0.9661 ± 0.0036	0.9654 ± 0.0036	0.9675 ± 0.0036
$\log 10^{10} A_s$	3.037 ± 0.014	3.036 ± 0.014	3.045 ± 0.014	3.043 ± 0.014	3.048 ± 0.014
H_0	67.19 ± 0.47	67.06 ± 0.44	67.86 ± 0.36	67.74 ± 0.36	68.12 ± 0.34
σ_8	0.8075 ± 0.0055	0.8078 ± 0.0054	0.8062 ± 0.0057	0.8065 ± 0.0056	0.8059 ± 0.0057
Ω_m	0.3146 ± 0.0065	0.3164 ± 0.0062	0.3053 ± 0.0048	0.3070 ± 0.0048	0.3021 ± 0.0045
S_8	0.827 ± 0.011	0.830 ± 0.010	0.8133 ± 0.0090	0.8158 ± 0.0090	0.8087 ± 0.0087

Table C.1: Observational constraints at 68% confidence level on the independent and derived cosmological parameters using all dataset combinations for the ΛCDM model, as detailed in Section 8.4.1.